UC Riverside
UC Riverside Electronic Theses and Dissertations

Title
Data-Driven Integration of Renewable Energy in Smart Grid

Permalink
https://escholarship.org/uc/item/42n5t5wb

Author
Kabir, Farzana

Publication Date
2022

Copyright Information
This work is made available under the terms of a Creative Commons Attribution-NonCommercial-ShareAlike License, availalbe at https://creativecommons.org/licenses/by-nc-sa/4.0/

Peer reviewed|Thesis/dissertation

eScholarship.org
Powered by the California Digital Library
University of California

UNIVERSITY OF CALIFORNIA
RIVERSIDE

Data-Driven Integration of Renewable Energy in Smart Grid

A Dissertation submitted in partial satisfaction
of the requirements for the degree of

Doctor of Philosophy

in

Electrical Engineering

by

Farzana Kabir

March 2022

Dissertation Committee:

Dr. Nanpeng Yu, Chairperson
Dr. Weixin Yao
Dr. Salman Asif

Copyright by
Farzana Kabir
2022

The Dissertation of Farzana Kabir is approved:

Committee Chairperson

University of California, Riverside

Acknowledgments

As I am close to the end of my Ph.D., I feel extremely grateful to all the people who made this journey possible. First and foremost, I would like to express my sincere gratitude to my advisor Professor Nanpeng Yu for extending me the opportunity to begin my Ph.D. here. His knowledge, insights, attention to detail and honest feedback made him an exceptional mentor. He has been supportive and patient throughout the time. I greatly appreciate the time, care, and attention with which he guided me. It has helped me become a better researcher. I want to sincerely thank Professor Weixin Yao for his wonderful collaboration and guidance. His expertise has been a big contributing factor in my research. He has been very encouraging and wonderful to work with. A special thanks to my committee member Dr. Salman Asif for providing valuable discussions and feedback during the development of this dissertation.

I want to thank my fellow labmates for their help and cooperation. I would like to specially mention my coauthor and friend Yuanqi Gao. You have been a wonderful collaborator and friend. Discussing research problems with you has been a great experience. I am thankful to all my teachers and tutors who taught me, inspired me, and encouraged me to pursue higher education. I would like to remember my late father who would have been the happiest to see me finish my Ph.D. A special thanks to my mother who sacrificed a lot for me and loved me unconditionally. I would not be where I am today without them. Thanks to all my sisters for loving and supporting me. Thanks to all of my extended family, in-laws, and friends for the love and encouragement. Thanks to all of you, I was able to have a great family life and social life despite the busy schedule.

And last but not the least, I would like to thank my husband and life partner, Shafiur Rahman. It was quite fun to share this journey with you. You have been very patient and understanding. You took a lot of stress off of me and kept me in good humor. It would have been a lot harder without you.

In dedication to my father Shamsul Kabir and my mother Saima Kabir for all their sacrifices, love and support

ABSTRACT OF THE DISSERTATION

Data-Driven Integration of Renewable Energy in Smart Grid

by

Farzana Kabir

Doctor of Philosophy, Graduate Program in Electrical Engineering
University of California, Riverside, March 2022
Dr. Nanpeng Yu, Chairperson

Renewable energy is an environment-friendly and economically attractive source of electricity generation. However, substantial grid integration of renewable energy is challenging as the power generation from renewables is weather-dependent, highly intermittent, and uncontrollable. To address these challenges, we exploited machine learning and data analytic techniques to develop frameworks and algorithms for integrating renewables into the grid.

Distribution grid planning, control, and optimization require accurate estimation of solar photovoltaic generation and electric load in the system. Most small residential solar PV systems are installed behind-the-meter making only the net load readings available to the utilities. We developed an unsupervised framework for estimating solar PV generation of individual customers by disaggregating the net load readings. Next, we developed an unsupervised framework for joint disaggregation of the net load readings of a group of customers. Our algorithms synergistically combined a physical PV system performance model for individual solar PV generation estimation with a statistical model for load estimation.

High solar PV penetration in the distribution grids gives rise to frequent voltage

fluctuations due to the intermittent nature of solar PV production. The slow operating conventional voltage regulating devices, therefore, need to be supplemented with fast operating real and reactive power control of smart inverters. Complete and accurate information about distribution network topology and line parameters needed for traditional model-based Volt-Var optimization methods is often unavailable. To tackle these challenges, we developed a two timescale Volt-Var control framework with model-based slow timescale control and a reinforcement learning-based fast timescale smart inverter control. The proposed framework does not rely on any distribution network secondary feeder information but requires primary feeder information. Next, we proposed a completely model-free reinforcement learning-based two timescale Volt-Var control framework that does not rely on any distribution network primary or secondary feeder topology or parameter information.

Natural and anthropogenic aerosols have a great influence on meteorological variables which in turn impacts the reservoir inflow and ultimately hydropower generation. We developed a comprehensive framework to quantify the impact of aerosols on reservoir inflow by integrating the physical Weather Research and Forecasting Model with chemistry (WRF-Chem) and a statistical dynamic regression model. We quantified the impact of aerosols on hydropower generation and revenue by incorporating the hydropower operation optimization toolbox into the framework.

Lastly, we developed a data-driven framework for the predictive maintenance of distribution transformers to increase the reliability of the distribution system. We utilized readily available data such as the transformers' specification, loading, location, and weather.

Contents

List of Figures

List of Tables

Chapter 1

Introduction

1.1 Background and Motivation

Renewable energy is a promising alternative to limited reserves of fossil fuel-based energy. Since it is environmentally friendly, it can reduce greenhouse gas emissions and ultimately mitigate the impacts of climate change brought about by the use of fossil fuels in the energy sector. In the electricity sector, renewable energy is also becoming increasingly economically attractive. More than half of the new renewable power generation capacity added in 2019 achieved lower power costs than the cheapest new coal plants [9]. These factors coupled with favorable government policies led to the rise in the adoption of renewable energy in the electricity sector. The share of renewables in electricity supply rose from 19% in 2008 to 26% in 2019 [21]. Driven by low operating costs, larger installed capacity, and priority dispatch, only renewable-based power generation experienced a growth in demand during the coronavirus pandemic, whereas demand for other energies fell [17].

Solar, wind, and hydropower are the three biggest sources of renewable-based electricity generation. As the weather is the main determinant for hydropower, wind, and solar PV, the production of renewable electricity largely depends on the availability of natural resources. These forms of renewable energy sources can be exploited in most parts of the world. Hydropower, wind, and solar PV together accounted for over 85% of all renewable electricity generation in 2019 [21].

Solar energy is the largest energy resource available on earth. Solar energy technologies fall into two broad categories: photovoltaic (PV) and concentrating solar power (CSP). Solar photovoltaic systems convert direct and diffuse solar radiation into electricity through a photovoltaic process using semiconductor devices. CSP uses reflective surfaces to focus sunlight into a beam to heat a working fluid in a receiver. The receiver transfers the heat to a conventional engine generator—such as a steam turbine—that generates electricity. PV technology is very modular and therefore is a very suitable option for off-grid rural electrification. It is possible to extract solar energy from photovoltaic (PV) including rooftop, ground-mounted, and building integrated PV systems. Moreover, the cost of the solar PV installation is rapidly dropping [376]. Since 2010, the cost of photovoltaic solar energy has dropped by 82% [9]. As such, solar energy provides people in developing countries with access to electricity, improves their quality of life, and facilitates energy independence. Residential and commercial PV adoptions are increasing rapidly around the world [16, 376]. Solar photovoltaics (PV) is projected to constitute 46% of total renewable generation by 2050, increasing from only 13% in 2018 [103]. Solar energy is highly intermittent due to cloud cover and shading, fluctuating up to 15% of their nameplate ratings within one-minute intervals [370].

Hydropower is the most mature source of renewable power. Hydropower converts the potential energy of water by converting it into electricity. The most common form of hydropower uses a dam on a river to retain a large reservoir of water which is released through turbines to generate power. On the other hand, “run of the river” systems have little or no water storage; water is diverted from the river and directed through a pipeline to a turbine. Hydroelectric power plants have a high level of operational flexibility and storage capability. Therefore, they play a key role in supporting the integration of increasing amounts of wind and solar energy. Hydropower generation constituted about 16% of the world’s generated electricity and about 60% of renewable electricity generation in 2019 [21]. However, the share of hydro in the total generation is expected to decrease by 2050, due to the spike in energy demand in other renewable technologies [25].

Renewable energy integration into the electric grid focuses on incorporating renewable energy, distributed generation, energy storage, thermally activated technologies, and demand response into the electric distribution and transmission system. Substantial grid integration of renewables is challenging as the power generation from solar and wind is weather-dependent, highly intermittent, and uncontrollable. Traditional power systems have been designed to handle the variable nature of loads. This additional supply-side variability and uncertainty can pose new challenges for utilities and system operators. Specifically, the high penetration of PV in the distribution system poses several challenges in the distribution system operation and planning [317]. For example, in the United States, the ANSI Standard C84.1 [11] states that the voltage of residential loads should remain within five percent of its nominal value (120 V) under normal operating conditions. Solar

PV generation may cause feeder overvoltage and inadequate voltage compensation by the voltage regulator. The high variability of PV generation causes voltage fluctuations in the feeder. Therefore, it is very challenging to maintain an appropriate feeder-wide voltage profile when the PV penetration is high. Moreover, during light load and high PV generation, there might be reverse power flow which may cause temporary and transient overvoltage and problems for protection systems and voltage regulators. Distributing the PV's surplus power can exceed the ampacity ratings of the feeder. Masked load from PV can exacerbate cold load pickup problem and can cause overloading of the circuit elements if the PV disconnects. Additionally, PV generation increases the fault current levels and may cause the fault current level to exceed the interrupting rating.

One important mitigation strategy to address the renewable energy integration challenge is to have accurate knowledge of the amount of renewable generation in the transmission and distribution network. Specifically, there is a lack of visibility into the solar PV generation because most of the solar PV systems are installed 'behind-the-meter' in the distribution system. The advanced metering infrastructure (AMI) measurements only provide net load data which equals the load consumption minus solar PV generation. The lack of visibility into the behind-the-meter solar generation brings many operational and planning challenges to the distribution system operators. It is therefore necessary to estimate the solar PV generation by disaggregating the available net load data of the consumers for performing the distribution grid operation and control. This research also helps reduce the uncertainty of variable renewable generation by assisting in solar power forecasting.

The next renewable energy integration strategy is to design and operate the electric grid so that it can accommodate the additional variability and uncertainty of renewables. To achieve this objective, it is necessary to modernize the grid with the installation of supporting hardware like smart meters, smart inverters, and new control devices such as remotely controllable switches, on-load tap changers, capacitor banks, etc. These devices can reliably collect consumption and generation data in real-time and react fast to the variable distributed generation, making the grid ”smart”. The smart grid facilitates two-way communication among generators, transmitters, and customers with digital communications technology. The smart grid also facilitates control systems and computer processing, allowing it to detect, react and pro-act to variable generation and changes in usage. This opens up numerous research questions and efforts to reliably and efficiently operate the distribution system to meet the challenges of renewable energy integration. Specifically, smart inverters can provide fast and continuous active and reactive power control. They also support two-way communications, which allow remote control systems to change inverter setpoints. Smart inverters can thus be utilized in tandem with traditional slow operating Volt-Var control devices to provide Volt-Var control in distribution networks with highly variable distributed solar PV generation. Such research allows the benefits resulting from the rapid growth of renewable power generation and storage to become available to the utilities and consumers.

Another big challenge for the integration of renewable energy into the electric grid is that the generation capacity, availability, and intermittency of these renewable energy sources are strongly weather and climate-dependent. Renewable energy sources like wind and solar are more resilient to the effects of climate change compared to conventional thermoelectric technologies. However, the impacts of climate change on these generation sources are more uncertain and difficult to estimate reliably. On the other hand, hydropower is vulnerable to human-induced pollutants both in the short and long term. Specifically, in the short term, pollutants such as aerosol particles can influence the hydrological cycle, reservoir inflows and can influence hydropower generation and reservoir operations. Greenhouse gases can persist in nature in the long term and can lead to an increase in temperature and sea level and a decrease in snow cover. These factors in turn influence the hydrological cycle, precipitation, evapotranspiration, soil moisture, floods, droughts, and surface runoff; ultimately impacting hydropower generation and reservoir management. To mitigate the uncertainty, it is also imperative to quantify the impact of weather and pollutants on renewable energy sources.

The literature on renewable energy integration in the smart grid can be broadly categorized into two groups: model-based and data-driven methods. Model-based methods use parametric physical models of the system to perform the task. For example, physical PV system performance models can directly calculate the behind-the-meter solar PV generation. Distribution system Volt-VAR control calculates the optimal operating schedule for voltage regulating and VAR control devices, based on the network model [129]. Model-based methods are generally theoretically rigorous and reliable. However, real-world distribution systems are often complex, and detailed physical models, system parameters, and relevant information are often unavailable. For example, the technical parameters of solar PV systems are often unknown and can change over time. Utility companies typically do not have accurate and reliable primary and secondary feeders' topology and parameter information

[375, 120]. Therefore, model-based methods can be difficult to adopt in practice.

Purely data-driven methods, on the other hand, do not employ parametric physical models. Instead, they rely solely on operational data such as smart meter data, supervisory control and data acquisition (SCADA), and weather-related data to achieve their goal. Smart meters provide a large quantity of reliable and higher temporal-resolution data. Machine learning techniques and big data analytics are therefore important technology drivers in the smart grid. However, data-driven methods have some challenges. Most data-driven methods are not physically interpretable and lack a theoretical guarantee of performance. In many cases, the pure data-driven methods require complete historical data which is often unavailable. Moreover, they often ignore crucial and readily available information. In addition, unlike model-based algorithms, the design and test of data-driven methods are not quantitative. It is also difficult to accurately reproduce the results. Consequently, it is challenging to directly adapt existing machine learning techniques to the power distribution system, which consists of a large number of critical infrastructures. As a result, maintaining a reliable operation is unlikely to be achieved by the data-driven method alone. It is often beneficial to integrate a physical model with a data-driven model to get the benefit of both worlds.

Lastly, data-based methods can be utilized for predictive maintenance of the grid. Predictive maintenance attempts to assess the health conditions of each device. This allows for the advanced detection of pending failures [342] allowing for targeted maintenance to the devices most in need. This is a cost-effective method to achieve more reliable system operations and reduce the number of sudden power supply interruptions.

1.2 Research Objectives and Contributions

In this dissertation, we answer the question of how to combine the advantages of model-based and data-driven methods to develop algorithms that have the potential to be implemented in the real world, have a performance guarantee, and are physically interpretable. Specifically, we will develop four major use cases and applications for smart grid data-driven monitoring and control:

- First, we developed an unsupervised framework to disaggregate net load measurements into solar generation and electric load estimates for individual customers without information about their exact location [184]. A hidden Markov model (HMM) regression [123] was adopted to accurately estimate electric loads for customers under different energy consumption states. The proposed algorithm seamlessly integrated a physical solar PV system performance model with a statistical model for estimating electric load. We showed that the accurate physical solar PV system performance model not only improves the accuracy of solar generation estimation but also allows us to estimate the technical parameters of the solar PV systems.

Next, we extended this work to estimate behind-the-meter solar generation for a community of customers [189]. We estimated the electric load of a community of customers simultaneously with a mixed hidden Markov model (MHMM). The MHMM allows the sharing of information across individual customers, which leads to more accurate load and solar PV generation estimates. Specifically, the MHMM captures both the population-level effects and the individual differences in the power consumption patterns among the community of customers. Furthermore, the physical PV system performance model was extended to account for the case where a customer has multiple strings of solar panels facing different directions. At last, the performance of our proposed method was compared with the state-of-the-art net load disaggregation algorithms using the data from residential customers in Austin, Texas [166].

- Second, we developed a two-timescale data-driven reinforcement learning-based Volt-VAR control method in distribution systems with high PV penetration to mitigate voltage violations and reduce network loss [186]. To tackle the frequent voltage violations caused by the highly intermittent solar PV generation, the slow operating conventional voltage regulating devices were supplemented with fast operating reactive power control of smart inverters. Specifically, on the slow timescale, a centralized model-based and optimization-based approach were adopted to determine the tap positions of voltage regulators, OLTCs, and switchable capacitor banks. On the fast timescale, a purely data-driven deep deterministic policy gradient (DDPG)-based algorithm was employed to determine the set points of real and reactive power of smart inverters. Our proposed method does not rely on secondary feeders' topology or parameter information which is often unavailable. However, it still requires knowledge of the readily available primary feeder information. Furthermore, we designed a polar action space set up to jointly determine the active and reactive power setpoints of smart inverters. The degradation costs of the smart inverters were carefully modeled in the sequential decision-making process of the VVC problem.

Next, we improved on the previous work by developing a two-timescale multi-agent reinforcement learning-based Volt-VAR control method for distribution, which does not rely on any primary or secondary feeder topology or parameter information. We proposed two hierarchically arranged sets of policies that are run at two different timescales. The two policies interact with each other via a communication medium and are learned simultaneously. On the slow timescale, a multi-agent soft actor-critic (MASAC) [62] based approach was adopted to determine the tap positions of voltage regulators, OLTCs, and switchable capacitor banks. On the fast timescale, a deep deterministic policy gradient (DDPG) [224] based algorithm was employed to determine the setpoints of the reactive power of smart inverters. The two policies cooperate with each other and the Volt-Var control is learned efficiently.

- Third, we developed an innovative and comprehensive framework for evaluating the impact of aerosols on reservoir inflow. The framework seamlessly integrated the numerical weather forecasting model (WRF-Chem) and the statistical inflow forecasting model (dynamic regression) [188]. We fitted a dynamic regression model to forecast daily inflow into the hydroelectric reservoirs. The model coefficients for the meteorological variables provide an intuitive understanding of how temperature, precipitation, and snow water equivalent influence reservoir inflow. We quantified the impact of aerosols on reservoir inflow in the Big Creek Hydroelectric System based on the proposed dynamic regression model and WRF-Chem model. The simulation results showed that the presence of aerosols resulted in a reduction of the annual reservoir inflow by 4%-14%.

Then, we took the next logical step to develop a comprehensive framework to quantify the impact of aerosols on hydropower generation and revenue [183]. To this end, we integrated the hydropower optimization toolbox, Vista Decision Support System (DSS) [12] into the framework developed in [183]. We obtained the simulations of meteorological variables with and without aerosol impacts consideration from WRF-Chem simulations conducted in the San Joaquin Valley of California. We used those to generate the inflows into the hydropower reservoirs with and without considering the impact of aerosols using the statistical inflow forecast model. Then, we fed the inflow projections with and without aerosol effects into the Vista DSS to determine the optimal operation schedules of the hydropower system for both scenarios. We, therefore, seamlessly integrated the numerical weather forecasting model (WRF-Chem), a statistical inflow forecast model, and the hydropower operation optimization toolbox. The impact of aerosols on hydropower generation and revenue was quantified for the Big Creek Hydroelectric System. The simulation results showed that aerosols lead to a significant reduction in annual hydropower generation and revenue.

- Fourth, we developed a data-driven method for the predictive maintenance of distribution transformers [185]. Predictive maintenance is a method of predicting which transformers are most likely to fail soon. This reduces maintenance costs and increases the reliability of power distribution systems. Our proposed framework only uses readily available data such as the transformers' specification, loading, location, and weather-related information. We used two suitable machine learning algorithms. The first is random forests. The second is the Random Undersampling with AdaBoost (RUSBoost) algorithm. We test these algorithms on over 700,000 distribution transformers in Southern California. This test finds that both algorithms outperform the current state of practice. Further, it finds that the RUSBoost algorithm performs better than the Random Forest model.

1.3 Thesis Organization

The remainder of the dissertation is organized as follows: we present the estimation of behind-the-meter solar generation in Chapter 2-3. In Chapter 2, we present the unsupervised framework to disaggregate the net load measurements into solar generation and electric load estimates for individual customers. In Chapter 3, we extend the work to jointly estimate the behind-the-meter solar generation for a community of customers using a Mixed hidden Markov model. We develop the reinforcement learning-based two-time Volt-Var control method in distribution systems with high PV penetration in Chapter 4-5. In Chapter 4, we develop a Volt-Var control method that does not require secondary feeders' topology or parameter information but still stilled the primary feeder information. In Chapter 5, we develop a more sophisticated method that does not rely on any primary or secondary feeder topology of parameter information. The impact of aerosols on reservoir inflow and hydropower generation will be presented in two chapters: Chapter 6 and Chapter 7. We develop a comprehensive framework to evaluate the impact of aerosols of reservoir inflow in Chapter 6 . We ultimately develop a comprehensive framework to quantify the impact of aerosols on hydropower generation and revenue in Chapter 7. In Chapter 8, we develop a data-driven method for the predictive maintenance of distribution transformers. Finally, 9 concludes this dissertation and points out future research directions.

Chapter 2

Estimation of Behind-the-Meter Solar Generation by Integrating Physical with Statistical Models

2.1 Introduction

Solar PV generation is the fastest-growing source of new energy. The introduction of the net metering policy enables customers to sell excess electricity to the utility at the retail rate and receive credit on their electricity bills. As a result, small scale residential solar PV generation constituted 33% of total solar PV generation in the United States in 2019 [359]. Moreover, 61% of total solar PV systems in the United States were connected to the distribution system in 2014 [51]. Such high penetration of solar PV poses several challenges in the distribution system operation and planning processes [317, 376]. For example, increasing solar PV generation can cause feeder over-voltage, voltage fluctuations, reverse power flow, protection system malfunction, and can exacerbate cold load pickup problem.

To mitigate these problems, it is imperative to design the system based on the amount of solar PV generation and native load in the distribution network. Thus, it is critical to develop a framework to disaggregate the net load measurements into solar PV generation and electric load. Furthermore, the technical parameters of solar PV systems need to be estimated for planning activities such as solar PV hosting capacity analysis.

The existing net load disaggregation algorithms can be classified into two groups: data-driven methods and model-based methods. The solar PV technical parameters are generally not available to the electric utilities. Detailed physical models such as PVWatts [98] developed by National Renewable Energy laboratory and PV performance modeling collaborative [337] developed by Sandia National Laboratory are capable of estimating solar generation with information of solar irradiation, solar PV location, time, solar PV size, inverter efficiency, solar PV system loss, module tilt, and module orientation. Such physics-based behind-the-meter solar generation estimations are often inaccurate due to unreliable solar PV geometry data and degradation of PV arrays. The data-driven methods do not employ parametric physical models to estimate solar PV generation. Instead, they rely solely on smart meter data, supervisory control and data acquisition (SCADA), solar irradiance, and weather-related data. The data-driven methods can be further classified into two groups: unsupervised methods and methods that need supervision such as supervised/semi-supervised methods and contextually supervised source separation methods [391].

Supervised net load disaggregation methods need historical solar PV generation and load data of all customers whereas semi-supervised methods need the solar PV generation data for a small number of customers. The contextually supervised source separation method lies between supervised and unsupervised methods. This method also needs the solar PV generation data for a small number of representative customers as a solar proxy. The studies by [60, 193, 346, 192, 324] leverage semi-supervised methods or contextually supervised source separation methods to disaggregate net loads. The supervised data-driven approach is used in [341] to forecast net load.

The net load disaggregation problem is formulated as an optimization and a signal separation problem in [60]. The net load of a customer is modeled as a composite of representative electric load and solar generation patterns. The study by [324] estimates the power generation of behind-the-meter solar photovoltaic sites using a small set of selected representative sites while providing information on the uncertainty associated with the estimated solar PV generation volumes. The studies by [193] and [346] adapt a contextually supervised source separation model to disaggregate the net load signals of individual homes located on the same distribution feeder while enforcing various constraints. The contextually supervised source separation model is used to disaggregate the net load signals of feeder-level measurements in [192]. A supervised machine learning algorithm is utilized in [220] to solve the solar PV generation capacity estimation problem as a part of the net load disaggregation method under the assumption that actual measured solar PV generation and capacity data are available for a small number of representative solar PV sites.

Although supervised and semi-supervised net load disaggregation methods show great promise, they rely on solar PV generation data, which are typically not accessible for behind-the-meter systems. The advanced metering infrastructure (AMI) measurements only provide net load data which equals the load consumption minus solar PV generation. Thus, the historical solar PV generation, load data, and the solar PV technical parameters are not available to the electric utilities. Therefore, it is critical to develop an unsupervised framework to disaggregate the net load measurements into solar PV generation and electric load.

The studies by [76, 333], and [335] all leverage unsupervised net load disaggregation methods. The net load disaggregation problem is formulated as an optimization and a signal separation problem in [76]. In this study, the electric load of a customer is modeled as a composite of representative electric patterns. An unsupervised algorithm is developed in [333] to disaggregate the net load of a group of customers who have a common point of coupling. The algorithm proposed by [335] estimates electric load by comparing periods before PV installation with similar periods after PV installation that have common weather and activity characteristics and thereby perform net load disaggregation.

Although pure data-driven methods have achieved some success, they are incapable of estimating the technical parameters of solar PV systems such as the tilt and DC size of the solar panel. These technical parameters of the solar PV systems are extremely useful for both short-term operation and long-term planning activities for electric utilities. Furthermore, the data-driven methods [76, 333, 346] often use a highly simplified linear model, which is incapable of capturing the nonlinear relationship among the solar irradiance, solar PV system geometry, and solar PV generation. In many cases, the pure data-driven methods [60, 193, 346, 324, 220] require historical solar PV generation data of a subset of customers, which can be difficult for electric utilities to obtain. Some data-driven methods [193, 346] could suffer from transposition errors if solar PV systems of different geometry are not available to serve as solar proxies. Moreover, these two algorithms also require joint estimation of a large number of hyperparameters, which makes the algorithm impractical and brittle. Some data-driven methods, such as [192, 324] only provide estimates of aggregate solar PV generation instead of the solar PV generation estimates for individual sites. The net load disaggregation algorithm proposed by [335] is built under the assumption that energy consumption habits do not significantly change once PV is installed, which may not always be true. Moreover, changes in the appliance mix or ownership of the house may also impact load patterns. Most net load forecasting algorithms only focus on the net load forecast problem and do not disaggregate the net load into electric load and solar PV generation. In addition, some of the net load forecasting algorithms only provide aggregated net load forecast [341].

In this chapter, we develop an unsupervised framework to disaggregate net load measurements into solar generation and electric load estimates for individual customers without information about their exact location. Our proposed algorithm seamlessly integrates a physical solar PV system performance model with a statistical model for estimating electric load. The accurate physical solar PV system performance model not only improves the accuracy of solar generation estimation but also allows us to estimate the technical parameters of the solar PV systems. A hidden Markov model (HMM) regression [123] is adopted to accurately estimate electric loads for customers under different energy consumption states.

The remainder of the chapter is organized as follows: Section 2.2 describes the overall framework of the study. Section 2.3 presents the technical methods used in the estimation of solar PV parameters and solar generation, electric load modeling, and the net load disaggregation algorithm along with the post-disaggregation steps. The numerical study based on our proposed algorithm and benchmark algorithms is shown in Section 2.4. Finally, Section 2.5 concludes the study.

2.2 Overall Framework

The aim of the net load disaggregation algorithm is to decompose the net load readings of a residential customer with a solar PV system into the solar PV generation and electric load. In other words, given the net load measurements for a residential customer NL_t, for time intervals $t \in \{1, 2, ..., T\}$, we need to estimate the customer's electric load L_t, and solar generation S_t for each time interval t. We do not have information about their exact location, historical PV generation or consumption, solar panel configuration, or other solar PV system parameters. However, we have the city's approximate longitude and longitude, which can be used as a proxy for the locations of all customers. According to the net load definition, the net load, electric load, and solar generation of a customer satisfy the following equality constraint at any time t:

$$NL_t = L_t - S_t; \quad L_t \geq 0,\, S_t \geq 0 \quad \forall t \tag{2.1}$$

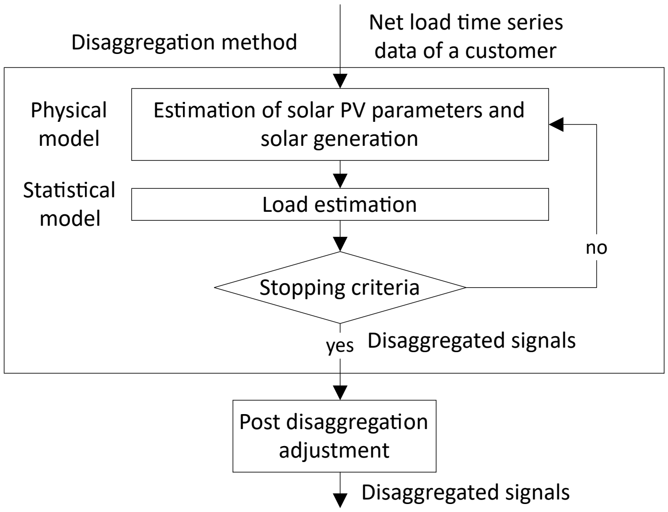

Figure 2.1: The overall framework for disaggregating net load of residential customers with solar PV systems.

The overall framework of our proposed net load disaggregation algorithm for each customer is shown in Figure 2.1. The net load includes two components: the electric load and solar generation. We estimate one of the two components one at a time while fixing the other component. The iterative estimation scheme ends when the stopping criteria are met. We discuss the algorithm in detail in Section 2.3.4. The solar PV system technical parameters are estimated by a physical model-based estimation method presented in Section 2.3.1. Solar generation is estimated by a physical model that utilizes these estimated parameters. The physical model of solar generation, called the PV system performance model, is presented in 2.3.2. The electric load of the customer is estimated based on a statistical model, which is described in Section 2.3.3. Finally, we make a post-disaggregation adjustment described in Section 2.3.4 on the disaggregated signals to ensure that electric load minus solar generation equals net load measurement at all times.

2.3 Technical Methods

In this section, we present our disaggregation methods and algorithms by integrating a physical solar PV generation model and a statistical electric load estimation model.

2.3.1 Estimation of Technical Parameters of Solar PV Systems

For the net load disaggregation algorithm, the solar PV generation, i.e., the AC output power of the PV array (P_{ac}), is estimated by a physical PV system performance model. If an estimate of the solar PV generation of a customer is available, we propose to estimate the technical parameters of the solar PV system by minimizing the sum of squared error between the input solar generation estimates and the calculated solar generation from the PV system performance model.

We denote the latest solar PV generation estimates of a customer at time t as S_t. Let $g_t\left(\boldsymbol{\theta}_S\right)$ denote the estimate for solar PV generation at time t based on the PV system performance model g_t with the technical parameters $\boldsymbol{\theta}_S$. The technical parameters include the DC rating P_{dc0}, array tilt angle θ_t, array azimuth angle θ_{az}, nominal inverter efficiency η_{nom}, and loss of the PV array l. The parameters of the solar PV system $\boldsymbol{\theta}_S = [P_{dc0}, \theta_t, \theta_{az}, \eta_{nom}, l]$ can be estimated by the following constrained optimization:

$$\begin{aligned} &\arg\min_{\boldsymbol{\theta}_s} \sum_{t=1}^{T} \left(S_t - g_t\left(\boldsymbol{\theta}_S\right)\right)^2 \\ &\text{subject to } S_t \geq 0,\ \boldsymbol{\theta}_{S,min} \leq \boldsymbol{\theta}_S \leq \boldsymbol{\theta}_{S,max} \end{aligned} \tag{2.2}$$

where T is the net load time series length, $\boldsymbol{\theta}_{S,min}$ and $\boldsymbol{\theta}_{S,max}$ denote the lower and upper limits of the PV system technical parameters respectively, which will be discussed in Section

2.4.2. The highly nonlinear nature of the PV system performance model makes Equation (2.2) a nonlinear optimization problem, which we solve by an interior-point algorithm.

2.3.2 PV System Performance Model

The PV system performance model in this study is highly nonlinear and is based on the PV performance modeling collaborative [337] and PVWatts [98] for a fixed mount system. We calculate P_{ac} by using the DC output power of the PV array P_{dc}, DC-to-AC ratio, and the nominal inverter efficiency η_{nom}. If the DC output power of the PV array is greater than the effective inverter DC input power rating $P_{dc0,inv}$, then the AC output of the inverter is capped at the AC nameplate rating of the inverter (P_{ac0}), where $P_{ac0} = \frac{P_{dc0}}{\text{DC-to-AC ratio}}$. Otherwise, if $0 < P_{dc} < P_{dc0,inv}$,

$$P_{ac} = g\left(\boldsymbol{\theta}_S\right) = \eta\left(\eta_{nom}, P_{dc}\right) P_{dc} \tag{2.3}$$

where the inverter efficiency, η, can be calculated following PVWatts [98]. P_{dc} can be calculated by using the specified DC rating P_{dc0}, cell temperature T_c, transmitted irradiance E_{tr}, and the loss in the PV array system l as follows:

$$\begin{aligned} P_{dc} &= g'\left(P_{dc0}, \theta_t, \theta_{az}, l\right) \qquad (2.4) \\ &= (1-l) \times \frac{E_{tr}\left(\theta_t, \theta_{az}\right)}{E_0} P_{dc0}\left[1 + \gamma\left(T_c\left(\theta_t, \theta_{az}\right) - T_0\right)\right] \end{aligned}$$

Here, γ and T_0 are known parameters. The operating cell temperature (T_c) can be calculated based on the Sandia module and cell temperature model [337]. The model estimates the operating cell temperature T_c from the plane of array irradiance (E_{POA}), wind speed, ambient air temperature (T_a), and the temperature difference between the module and cell. Calculation of the plane of array irradiance (E_{POA}) and transmitted irradiance (E_{tr}) requires solar irradiance data (direct normal irradiance, diffuse horizontal Irradiance, and global horizontal irradiance), solar PV installation geometry information (tilt and azimuth angle of the solar PV array), and solar position data (solar zenith and solar azimuth angle) [337]. Solar zenith and azimuth angle at time t can be calculated using the solar position algorithms [297] for known locations.

2.3.3 Hidden Markov Model Regression for Load Modeling

We propose to employ a statistical Hidden Markov model (HMM) regression [123] to improve the traditional linear regression model for the load modeling [164]. This is done by simultaneously modeling the dependence structure among the load data and incorporating the heterogeneity of the regression models over different time periods. The statistical regression model is widely used to incorporate the effects of explanatory variables, such as temperature, humidity, wind speed, hour, and day of the week to estimate the load. In this study, to capture the non-linear relationship between temperature and load, we use a 3rd-degree polynomial of temperature, denoted by $\boldsymbol{c}, \boldsymbol{c^2}$, and $\boldsymbol{c^3}$ following the proposal of Hagan et al. [150], along with the weighted moving average of the temperature of last 24 hours, $\boldsymbol{c}_{wmv}$. By empirical analysis, we use a 3rd- degree polynomial of the *hour* of the day denoted by $\boldsymbol{h}, \boldsymbol{h^2}$, and $\boldsymbol{h^3}$ to model the nonlinear relationship between *hour* and load. To capture the different effects of weekends and weekdays, we introduce a dummy variable $\boldsymbol{d}$ to indicate weekends. We also include the interaction of temperature and hour of the day, $\boldsymbol{c} \times \boldsymbol{h}$, as an explanatory variable. Explanatory variables are denoted by $\boldsymbol{X} = \left[\boldsymbol{c}, \boldsymbol{c^2}, \boldsymbol{c^3}, \boldsymbol{c}_{wmv}, \boldsymbol{d}, \boldsymbol{h}, \boldsymbol{h^2}, \boldsymbol{h^3}, \boldsymbol{c} \times \boldsymbol{h}\right]$.

The linear regression model is widely used to model the dependence of the load L_t on the explanatory variables $\boldsymbol{X}_t$ assuming a homogeneous relationship between $\boldsymbol{X}_t$ and L_t for all time periods. However, the load data can exhibit quite different patterns depending on whether a customer is present at home or not. For example, when a customer is at home, the load consists of heating, ventilation, air-conditioning, or appliance usage. On the other hand, when the customer is not at home, the load can be very low and consists of the power usages from the refrigerator and some appliances like water heaters, routers, modems, cable TV boxes, and TVs in standby mode. This change of the load pattern over time can be modeled by an HMM regression analysis.

At time t, let s_t be a *latent* state variable, $s_t = 1$ if the customer is home and $s_t = 2$, if not. Let $\boldsymbol{X}_t$ be the explanatory variables for the load L_t. In HMM regression, given s_t,

$$L_t = \boldsymbol{X}_t^T \boldsymbol{\beta}_{s_t} + \varepsilon_{s_t}, \quad \varepsilon_{s_t} \sim N\left(0, \sigma_{s_t}^2\right) \tag{2.5}$$

Note that the regression parameters $\boldsymbol{\beta}_{s_t}$ are allowed to be different for different states s_t. The dependence structure of the latent time series $\{s_t\}$ is modeled by an underlying Markov chain, $p_{ij} = P\left(s_t = j | s_{t-1} = i, s_{t-2} = k, \ldots\right) = P\left(s_t = j | s_{t-1} = i\right)$ where $i, j = 1, 2$ and p_{ij} is the transition probability from state i to state j satisfying $\sum\limits_{j=1}^{2} p_{ij} = 1$ for each i. The HMM regression has been applied in many fields [239] including econometrics, where it is known as the Markov switching regression model [136] or regime-switching model [153] with exogenous explanatory variables. A general HMM regression model can be estimated by maximum likelihood or Bayesian inference [123, 64]. We use the MS_Regress package of Matlab [286] to perform the maximum likelihood estimation.

2.3.4 Disaggregation Algorithm

We propose to disaggregate net load measurements into electric load $\hat{\mathbf{L}}$ and solar PV generation $\hat{\mathbf{S}}$ at individual homes by integrating the physical PV system performance model introduced in Section 2.3.2 and the statistical HMM regression introduced in Section 2.3.3. The algorithm for disaggregating net load for an individual customer is shown in Algorithm 1. For an initial value of the solar PV system parameters $\boldsymbol{\theta}_S$, we first estimate the solar PV generation $\hat{\mathbf{S}}$ using the PV system performance model g. For any fixed solar generation estimate $\hat{\mathbf{S}}$, we can calculate the customer's electric load $\hat{\mathbf{L}} = \mathbf{NL} + \hat{\mathbf{S}}$ and then fit an HMM regression model to $\hat{\mathbf{L}}$. Based on the updated estimation of $\hat{\mathbf{L}}$, we can calculate the solar PV generation $\hat{\mathbf{S}} = \hat{\mathbf{L}} - \mathbf{NL}$ and estimate $\boldsymbol{\theta}_S$ by running a constrained numerical optimization following Equation (2.2) using $\hat{\mathbf{S}}$ and g. We continue the above two processes until the estimated PV system parameters converge or the maximum number of iterations is reached. We repeat the same process for many initial values and select the solution that provides the lowest mean squared error for the estimated net load. Selection of initial values is discussed in Section 2.4.2.

Post-Disaggregation Adjustment

We propose to further improve the disaggregation performance by enforcing the constraint that the electricity consumption minus solar generation must be equal to the net

Algorithm 1 Algorithm for the disaggregation of net load of each customer and estimation of solar PV parameters

```
Input: Net load of a customer from AMI measurement, $\mathbf{NL}$
Output: User consumption $\hat{\mathbf{L}}$, solar generation $\hat{\mathbf{S}}$, and solar PV system parameters $\boldsymbol{\theta}_S$
    Initialization: Determine $M$ initial solar PV system technical parameters $(\boldsymbol{\theta}_S)_1^{(0)}, \ldots, (\boldsymbol{\theta}_S)_M^{(0)}$
for each starting point $m \in M$ do
    Initialize solar generation, $\hat{\mathbf{S}}_m^{(0)} = g\left((\boldsymbol{\theta}_S)_m^{(0)}\right)$
    for j=1 to maxiter do
        Estimate user consumption, $\hat{\mathbf{L}}_m^{(j)} = \mathbf{NL} + \hat{\mathbf{S}}_m^{(j-1)}$
        Fit HMM regression model, denoted by $f(\boldsymbol{X}, \boldsymbol{\theta}_L)$, to $\hat{\mathbf{L}}_m^{(j)}$ and calculate $(\boldsymbol{\theta}_L)_m^{(j)}$
        Update user consumption, $\hat{\mathbf{L}}_m^{(j)} = f\left(\boldsymbol{X}, (\boldsymbol{\theta}_L)_m^{(j)}\right)$
        Update solar generation, $\hat{\mathbf{S}}_m^{(j)} = \hat{\mathbf{L}}_m^{(j)} - \mathbf{NL}$
        Determine $(\boldsymbol{\theta}_S)_m^{(j)}$ from Equation (2.2) using $(\boldsymbol{\theta}_S)_m^{(j-1)}$ as initial value
        Update solar generation, $\hat{\mathbf{S}}_m^{(j)} = g\left((\boldsymbol{\theta}_S)_m^{(j)}\right)$
        Estimate net load, $\hat{\mathbf{NL}}_m^{(j)} = \hat{\mathbf{L}}_m^{(j)} - \hat{\mathbf{S}}_m^{(j)}$
        Calculate MSE of the net load, $E_m^{(j)}$
        if $\left|(\boldsymbol{\theta}_S)_m^{(j)} - (\boldsymbol{\theta}_S)_m^{(j-1)}\right| \leq \boldsymbol{\varepsilon}$ then
            Break
        end if
    end for
end for
Determine $m^*, j^* = \underset{m,j}{argmin}\, E_m^{(j)}$
return $\hat{\mathbf{L}} = \hat{\mathbf{L}}_{m^*}^{(j^*)}$, $\hat{\mathbf{S}} = \hat{\mathbf{S}}_{m^*}^{(j^*)}$, and $\boldsymbol{\theta}_S = (\boldsymbol{\theta}_S)_{m^*}^{(j^*)}$
```

load reading at any time. At any time t, we perform the following optimization inspired from [193] for each customer using the disaggregated signals $\hat{L}_t$ and $\hat{S}_t$ from Algorithm 1 to obtain the improved estimates. Here, α and β are user-specified parameters that denote the weights for the errors in the load and solar generation model, respectively.

$$\begin{aligned} &\underset{L_t, S_t}{\arg\min} \sum_{t=0}^{T} \alpha\left(L_t - \hat{L}_t\right)^2 + \beta\left(S_t - \hat{S}_t\right)^2 \\ &\text{subject to } L_t \geq 0,\ S_t \geq 0, \quad L_t - S_t = NL_t \end{aligned} \tag{2.6}$$

We propose two methods for determining the values of α and β. In the first variation, if the ground truth solar generation and load data are available for some customers, we determine α and β by the inverse of the variance of the error of the estimated load and solar generation for these customers:

$$\alpha = 1/Var\,(\varepsilon_{Load}), \quad \beta = 1/Var\,(\varepsilon_{PV}) \tag{2.7}$$

For the second variation, if the ground truth solar PV generation or load data are not available, we estimate the ground truth by the load and solar generation from steps 4 and 7 of Algorithm 1.

2.3.5 Error Metric

We measure the performance of net load disaggregation algorithms with three metrics: the mean squared error (MSE), mean absolute scaled error (MASE), and the coefficient of variation (CV). MASE is used instead of the mean absolute percentage error (MAPE) because many electric load and solar generation measurements are zero or close to zero, which makes MAPE extremely high even with small estimation errors. MASE scales mean absolute errors with the errors of a naive forecasting model which simply uses the last observation as a prediction. Thus, it is scale-invariant and treats all customers equally. CV is another normalized error metric defined as the root mean squared error divided by the mean actual signal. Let $y_{i,t}$ and $\hat{y}_{i,t}$ be the actual and estimated values of customer i at time t, respectively. Then, the mean MSE, MASE, and CV of N customers over a period T can be expressed as follows:

$$MSE = \frac{1}{N}\sum_{i=1}^{N}\frac{1}{T}\sum_{t=1}^{T}(y_{i,t} - \hat{y}_{i,t})^2 \tag{2.8}$$

$$MASE = \frac{1}{N}\sum_{i=1}^{N}\frac{T-1}{T}\frac{\sum\limits_{t=1}^{T}|y_{i,t} - \hat{y}_{i,t}|}{\sum_{t=2}^{T}|y_{i,t} - y_{i,t-1}|} \tag{2.9}$$

$$CV = \frac{1}{N}\sum_{i=1}^{N}\left(\sqrt{\sum_{t=1}^{T}(y_{i,t} - \hat{y}_{i,t})^2}\Bigg/\frac{1}{T}\sum_{i=1}^{T}y_{i,t}\right) \tag{2.10}$$

2.4 Numerical Study

2.4.1 Dataset for Numerical Study

The 15-minute interval net load, customer load, and solar PV generation data gathered by Pecan Street [166] are used in the numerical study. The customers are located in Austin, Texas with an approximate longitude and latitude of $(30.29^o N, -97.69^o E)$. The study period is from October 3, 2015, to October 30, 2015. We select this specific period so that we can directly compare our results with that of the consumer mixture models [76]. Within the study period, we have 197 customers with valid solar generation and electric load data. The ground truth tilt and azimuth angle of the solar PV installations are not

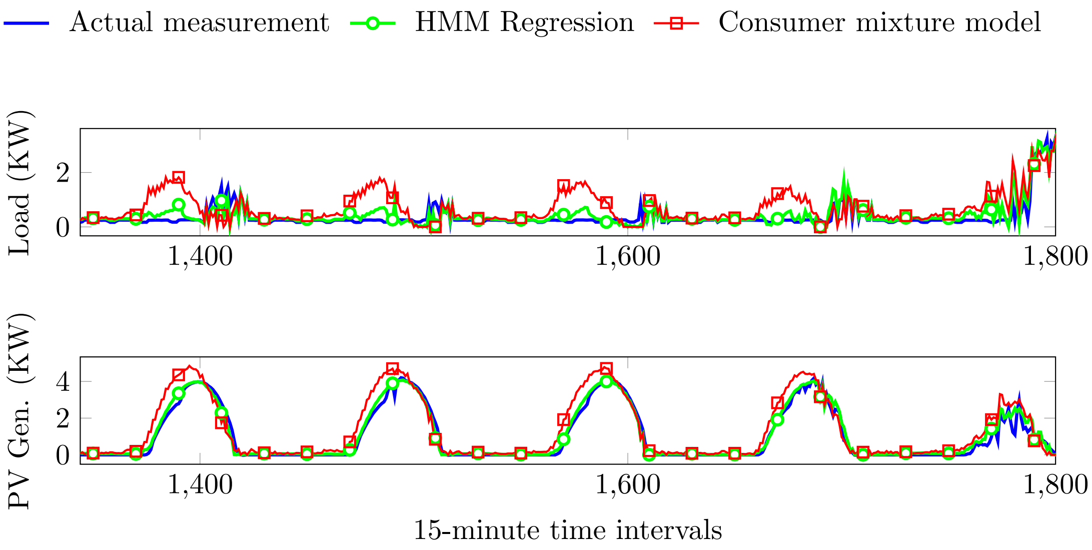

Figure 2.2: Comparison of disaggregated load and solar PV generation with actual values for a customer from 10/14/2015 to 10/19/2015

available. The DC rating of solar PV panels is available for 90% of the customers. The DC ratings are later used to validate the accuracy of our algorithm. The solar irradiance and other weather data are gathered from the National Solar Radiation Database [319]. The solar irradiance data covers the entire US with a $4km \times 4km$ grid resolution and 30-minute granularity. We select the data from the closest grid box to the approximate location of all customers $(30.29^o N, -97.69^o E)$. The 30-minute interval data are converted into 15-minute interval ones with linear interpolation. In the first version of our proposed net load disaggregation algorithm, the hyperparameters α and β in Equation (2.7) are calculated using 10% of the customers' actual electric load and solar PV generation data.

2.4.2 Experimental Setup

The technical parameters of the solar PV system are estimated by solving a constrained optimization problem. The upper and lower bounds constraining the technical

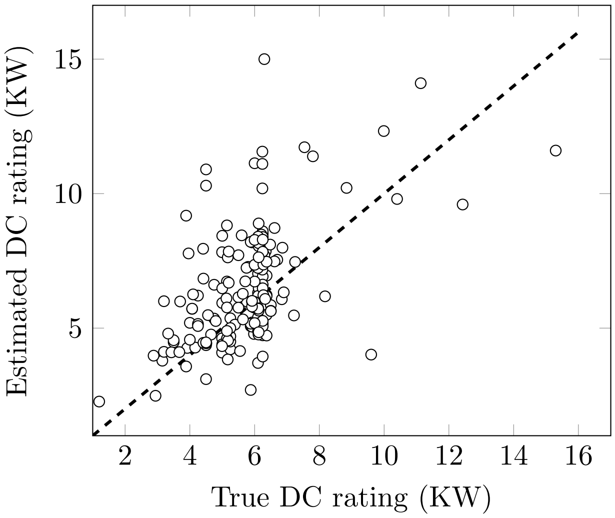

Figure 2.3: Comparison of true and estimated DC rating of PV array

parameters are set as follows. The feasible range of solar PV array tilt angle θ_T is set as $[5^o, 50^o]$. The feasible range of PV array azimuth angle θ_{AZ} is assumed to be $[0^o, 360^o]$. The feasible range of solar panel's DC rating is selected to be $[1\text{KW}, 15\text{KW}]$. The feasible range of inverter nominal efficiency η_{nom} is between 0.92 and 0.99. Finally, we select the range of PV array loss to be $[9\%, 38\%]$. The range of solar PV panel loss is obtained from the derate factor ranges provided in [246] . The DC-to-AC ratio is roughly the same for all customers. It is fixed at 1.1, the default value in PVWatts.

Note that the upper and lower bounds for solar PV panel tilt and azimuth angles are determined based on the maximum and minimum angles of 160,000 solar PV panels in California from the California Solar Initiative working data set [336]. Also, we assume that the rooftop solar PV installations being studied are fixed array systems with no tracking system. We select 8 initial solar PV system technical parameter sets for step 1 in Algorithm 1 by gradually increasing P_{dc0} in 7 steps from 1 KW to 8 KW. The other initial solar PV

Table 2.1: Comparison of various disaggregation methods

Error Metric	Variable	HMM reg. model (known error var)	HMM reg. model (unknown error var)	Consumer Mixture Model	SunDance Model
MSE	Load	**0.23**	0.23	0.38	0.49
	Solar	**0.23**	0.24	0.43	0.54
MASE	Load	0.56	**0.52**	0.74	0.81
	Solar	3.08	**2.80**	3.91	3.74
CV	Load	**0.35**	0.36	0.46	0.57
	Solar	**0.62**	0.62	0.79	0.85

system parameters $[\theta_T, \theta_{AZ}, \eta_{nom}, l]$ are set at their most common values $25^o, 180^o, 0.96$, and 14% respectively.

2.4.3 Result and Analysis

We implemented our proposed net load disaggregation method following Algorithm 1 using two variations of the post-disaggregation adjustment described in Section 2.3.4 with known and unknown error variance. The performance of our proposed model is compared against two state-of-the-art benchmark algorithms, the unsupervised consumer mixture model [76] and the SunDance algorithm [74]. Following the implementation of the consumer mixture model, the electric loads of customers without solar PVs are clustered using the K-Medoids algorithm. As the cluster medoids can change based on the initial choice of medoids, we perform 100 simulations with different initial medoids and take their mean. When implementing the SunDance model, we used a neural network to approximate the universal weather-solar effect model. The solar generation data from August 2015 to October 2015 of a house in the pecan street dataset is used for network training. The geometry of the solar PV installation is not known at the house.

Table 2.1 shows the MSE, MASE, and CV for load and solar generation estimations based on our proposed methods and the benchmark algorithms. The HMM regression model with either known or unknown error variance yields smaller errors than both the consumer mixture model [76] and the SunDance model [74]. Our proposed model with known error variance performs slightly better than the model with unknown error variance in terms of MSE and CV. However, if we consider MASE, the later model performs better.

Even without using a validation data set with actual solar and load, our proposed model without known error variance reduces the MSE by 44% compared to the consumer mixture model [76]. The improvement of our proposed model is pronounced for customers who are absent from home for a period of time as the HMM regression model is well suited to capture load behavior in different regimes. In our study, 25 out of 197 customers are absent from their residence for an extended period of time. Our proposed model reduces MSE for these customers by 63% compared to the consumer mixture model. Figure 2.2 illustrates the disaggregated load and solar PV generation signals of our proposed model and the benchmark consumer mixture model for a customer who is periodically absent from home. As shown in the figure, the load estimate from our proposed model follows the actual load data significantly more closely than the consumer mixture model during the periods of absence. The solar generation estimate is also considerably more accurate during these periods.

Our proposed model outperforms the SunDance model [74] in terms of estimation accuracy mostly due to the adoption of the more accurate physical solar PV system performance model. The SunDance model, on the other hand, relies heavily on the accurate estimation of maximum solar generation and cloud cover. If there is a lack of lower consumption periods on sunny days, then the maximum solar generation estimation will be rather unreliable. Furthermore, the cloud cover measurement data typically do not have sufficient spatial resolution at the household level. Finally, the performance of our proposed model in estimating the DC size of the solar PV systems is illustrated in Figure 2.3. As shown in the figure, the estimated solar DC ratings and the actual ones are quite similar. The four outliers in Figure 2.3 arise from an error in the dataset where the net load is not equal to load minus solar generation.

2.5 Chapter Summary

We developed an unsupervised algorithm to disaggregate net load signals into solar PV generation and electric load consumption for residential customers with solar PV systems. The iterative net load disaggregation algorithm synergistically combines a physical solar PV system performance model for solar PV generation estimation with a statistical HMM regression model for load estimation. This unique approach results in a significant reduction in solar generation and electric load estimation errors.

Chapter 3

Joint Estimation of Behind-the-Meter Solar Generation in a Community

3.1 Introduction

In the previous chapter, we developed a framework to estimate to disaggregate net load measurements into solar generation and electric load estimates for individual customers. This chapter extends the previous work to estimate behind-the-meter solar generation for a community of customers. We propose estimating the electric load of a community of customers simultaneously with a mixed hidden Markov model (MHMM). The MHMM allows the sharing of information across individual customers, which leads to more accurate load and solar PV generation estimates. Specifically, the MHMM captures both the population-level effects and the individual differences in the power consumption patterns among the community of customers. Furthermore, the physical PV system performance model is extended to account for the case where a customer has multiple strings of solar panels facing different directions. The performance of our proposed method is compared with the state-of-the-art net load disaggregation algorithms using the data from residential customers in Austin, Texas [166].

The unique contributions of this chapter are as follows:

1. An MHMM is developed to jointly estimate the electric load of a community of customers, which captures both the population-level and the individual effects.
2. The proposed net load disaggregation algorithm seamlessly integrates a statistical MHMM with a physical PV system performance model, which accounts for solar panels facing different directions.
3. The proposed behind-the-meter solar generation estimation algorithm yields significantly higher accuracy over state-of-the-art net load disaggregation algorithms including our previous work [184].

The remainder of the chapter is organized as follows: Section 3.2 provides the overall framework of the proposed algorithm. Section 3.3 presents the technical methods, which include the PV system performance model, MHMM, and the net load disaggregation algorithm. Section 3.4 shows the numerical study results. Section 3.5 states the conclusions.

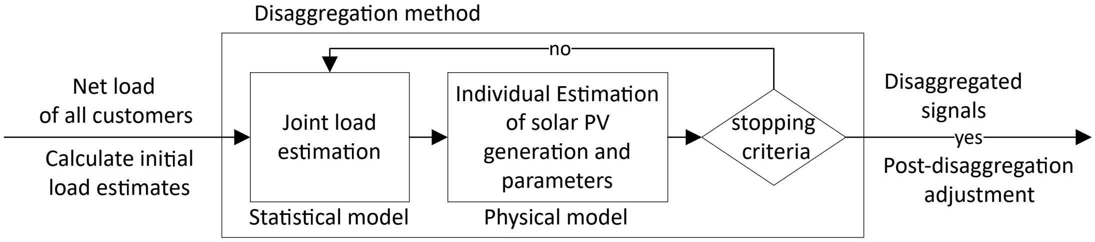

Figure 3.1: The overall framework for joint net load disaggregation for a group of residential customers with behind-the-meter solar PV systems.

3.2 Overall Framework

The net load measurement of a residential customer equals the electrical load of the customer minus the solar PV generation. Let L_{nt} be the electrical load and S_{nt} be the solar generation of a customer n at time t. Then the net load readings of the customer NL_{nt} for customers $n = 1, \ldots, N$ at time intervals $t \in \{1, 2, ..., T\}$ can be written as follows:

$$NL_{nt} = L_{nt} - S_{nt}; \quad S_{nt} \geq 0 \quad \forall t, n \tag{3.1}$$

The aim of the net load disaggregation algorithm is to decompose the net load readings NL_{nt} of a group of N residential customers with solar PV systems into the corresponding solar PV generation S_{nt} and electric load L_{nt} at each time interval t. The exact location of the customers, historical PV generation or consumption, solar panel configuration, or other solar PV system parameters are generally not available. Our proposed algorithm does not require this information.

The overall framework of the proposed net load disaggregation algorithm is shown in Fig. 3.1. First, a statistical MHMM is fit to jointly estimate the electric load of all customers with the initial estimates of the load model parameters while keeping the solar generation estimates fixed. The parameter estimation of the mixed hidden Markov model (MHMM) can be computationally intensive. Therefore, a good initial estimate of the load is needed as the starting point of the iterative net load disaggregation algorithm. The electric load estimates obtained from the iterative algorithm with HMM regression from [184] are used as the initial load estimates for the MHMM. Solar PV system parameters and solar PV generation of individual customers are then estimated with a physical model while keeping the load estimates fixed. The iterative estimation procedure continues until the stopping criteria are met. At last, a post-disaggregation adjustment is performed on the disaggregated signals to ensure that the equality constraint (3.1) relating native electric load, solar PV generation, and net load is satisfied. The joint modeling of load with MHMM and the parameter estimation procedure are described in Section 3.3.1 and 3.3.2. The physical solar PV system performance model and the estimation of the technical parameters of solar PV systems are presented in Section 3.3.3. The net load disaggregation algorithm is discussed in detail in Section 3.3.4.

3.3 Technical Methods

3.3.1 Mixed Hidden Markov Model

Many regression models are used to model the load consumption of a customer to incorporate the effect of weather and time. However, the user consumption pattern is expected to be quite different depending on whether a customer is at home or not. For example, when a customer is at home, the load may consist of heating, ventilation, air-conditioning, and other appliance usages. On the other hand, when the customer is not at home, the load can be very low and may include power usage from the refrigerator and other appliances, such as water heaters, and TVs in standby mode. To model such heterogeneous user consumption patterns, a hidden Markov model (HMM) regression [123] is used to model individual load time series of customers in [184]. However, in [184], the HMM needs to be fitted separately for each customer and thus the model is incapable of leveraging the community information to improve the load modeling.

To improve over the individual HMM regression models in [184], a *mixed hidden Markov model* (MHMM) [24] is proposed to provide a joint load estimation of all customers by modeling both the population-level and the individual effects. The individual heterogeneity can be captured by the individual-specific random effects in the MHMM representing individual deviations from the population averages.

Let L_{nt} be the load and z_{nt} be the hidden state associated with the customer n at time t, $n = 1, \ldots, N$, $t = 1, \ldots, T$. Let $z_{nt} = 1$ if the customer is at home and $z_{nt} = 2$, if not home, making the number of total states $K = 2$. Let $\boldsymbol{L}_n$ denote the T-dimensional vector of observations, i.e., load of customer n across T time points and $\boldsymbol{L}$ denote the $T \times N$-dimensional matrix of load of all customers. The vectors of hidden states, $\boldsymbol{z}_n$ and $\boldsymbol{z}$, are defined analogously. Let $\boldsymbol{x}$ be the $T \times Q$-dimensional matrix of explanatory variables or fixed effects. The explanatory variables include temperature (τ), exponential moving average of the temperature of last 24 hours (τ_{wmv}), hour of the day (h), and the interaction of temperature and hour of the day ($\tau \times h$). To capture the non-linear relationship between temperature and load, a 3rd-degree polynomial of temperature is used, denoted by $\boldsymbol{\tau}, \boldsymbol{\tau^2}$, and $\boldsymbol{\tau^3}$ following the proposal of Hagan and Behr [150]. Based on some empirical analysis, a 3rd-degree polynomial of the *hour* of the day is also used. The explanatory variable matrix $\boldsymbol{x}$ is denoted by $\boldsymbol{x} = \left[\boldsymbol{\tau}, \boldsymbol{\tau^2}, \boldsymbol{\tau^3}, \boldsymbol{\tau}_{wmv}, \boldsymbol{h}, \boldsymbol{h^2}, \boldsymbol{h^3}, \boldsymbol{\tau} \times \boldsymbol{h}\right]$.

A hidden Markov model (HMM) is defined as a pair of stochastic processes denoted by $\{\mathrm{z}_{nt}, L_{nt}\}$, where z_{nt} is an unobserved finite state Markov chain and the output process L_{nt} is related to the latent state process z_{nt}. An MHMM extends HMMs to a regression setting in a generalized linear mixed model framework. MHMM combines HMMs with a linear mixed-effect regression model in a longitudinal setting and enables the incorporation of covariates and random effects in both the conditional and/or transition model. A random intercept model is assumed for the conditional model to allow the customers to borrow information from each other and to simultaneously incorporate the heterogeneity across different customers.

Several assumptions are made for the MHMM. First, the random effects are assumed to follow a normal distribution and are independent of the hidden states. Second, given the random effects, the dependence structure of the latent time series $\{z_{nt}\}_{t=1}^{T}$ can be modeled by an underlying Markov chain. The transition probability from state j to state k for customer n is denoted by $\gamma_{njk} = P\left(z_{nt} = k | z_{n(t-1)} = j, z_{n(t-2)} = l, \ldots\right)$ $= P\left(z_{nt} = k | z_{n(t-1)} = j\right)$ where $j, k = 1, 2$ and γ_{njk} satisfies $\sum\limits_{k=1}^{2} \gamma_{njk} = 1$ for each j and n. The initial state distribution of the Markov chain is denoted by $\boldsymbol{\delta}$ and the transition matrix of all of the customers is denoted by $\mathbf{\Gamma}$. Third, conditional on the random effects, the n-th process, $\{L_{nt}\}_{t=1}^{T}$, is a HMM, and observations on different processes from different customers are independent. Therefore, given state z_{nt}, an MHMM with customer-specific random intercepts in the conditional model can be written as follows:

$$L_{nt} = a_{z_{nt}} + b_n + \boldsymbol{c}_{n,z_{nt}}\boldsymbol{x}_t + \epsilon_{nt}, \quad n = 1\dots N, \tag{3.2}$$
$$t = 1\dots T, \quad b_n \sim N\left(0, \sigma^2\right), \quad \epsilon_{nt} \sim N\left(0, \lambda^2_{z_{nt}}\right)$$

Here, $a_{z_{nt}}$ is the common state-specific intercept of all customers, $\boldsymbol{x}_t$ is the vector of explanatory variables at time t, and $\boldsymbol{c}_{n,z_{nt}}$ is the Q-dimensional vector of customer and state-specific regression coefficients of explanatory variables. Both $\boldsymbol{a}$ and $\boldsymbol{c}$ are fixed effect coefficients. Here, b_n is the customer-specific random effect common to all states and follows a normal distribution with variance σ^2. The individual error term ϵ_{nt} follows a normal distribution with state-specific variance $\lambda^2_{z_{nt}}$. Therefore, conditional on the state z_{nt} and random effect, the distribution of L_{nt} is

$$f\left(L_{nt}|z_{nt}, b_n\right) \sim N\left(a_{z_{nt}} + \boldsymbol{c}_{n,z_{nt}}\boldsymbol{x}_t + b_n, \lambda^2_{z_{nt}}\right), \quad b_n \sim N\left(0, \sigma^2\right) \tag{3.3}$$

There are a few advantages of using MHMM instead of HMM to jointly model the electric load of a community of customers. First, the random effects enter additively in the linear predictor and thus may represent the influence of omitted covariates or individual heterogeneity not captured by the observed covariates. Second, traditional HMM assumes that the observations are independent given the hidden states. To meet this assumption, an extremely large number of latent states is often required. However, in this case, the HMM becomes uninterpretable. MHMM allows for the dependence between the longitudinal observations of the same customers by means of the customer-specific random effect and hence provides more efficient estimates of fixed model parameters. As the number of latent states in MHMM is not required to be large, MHMM is relatively easy to interpret. Third, MHMM assumes that the random effects follow a common distribution which makes the estimates of the random effect shrink towards their mean (i.e., a weighted average between the overall mean effect and the individual effect). Thus, the estimation of individual effects also borrows information from each other.

Borrowing information across customers as an advantage of MHMM is further elaborated below. An advantage of joint load estimation over individual load estimation is its ability to borrow strength across customers by obtaining estimates of parameters common to all customers known as the fixed effect or population-level effect. In addition, MHMM is also able to capture the individual heterogeneity of customers through the individual-specific random effects while retaining the strength of joint load estimation. Thus, MHMM effectively treats the customers as distinct entities but from the same general population. Additionally, MHMM provides an estimate of the variance of the random effect distribution. MHMMs have been successfully applied in various scientific fields, notably, for modeling animal movement and behavior [94], lesion count in multiple sclerosis patients [24], forest tree growth [71], and teenage driving behavior [171].

3.3.2 Estimation of MHMM by MCEM Algorithm

Traditionally, the expectation–maximization (EM) algorithm has been used to estimate the parameters of a HMM. The EM algorithm is an iterative method for performing maximum likelihood estimation when some of the data are missing. Unfortunately, the basic EM algorithm cannot be applied to MHMM directly due to the existence of random effects and the complex numerical integration. The Monte Carlo expectation maximization (MCEM) algorithm is used [251] to estimate the unknown parameters of the MHMM denoted by

$$\boldsymbol{\Theta} = \left[\{a_k\}_{k=1}^{K}, \{\boldsymbol{c}_{nk}\}_{n=1,k=1}^{n=N,k=K}, \{\lambda_k^2\}_{k=1}^{K}, \boldsymbol{\delta}, \boldsymbol{\Gamma}, \sigma^2\right] \tag{3.4}$$

MCEM is a stochastic approximation method that is especially useful for cases where numerical integration and maximization are not advised, e.g., when there is a large number of random effects or a large number of parameters. Let $F_{nt} = f\left(L_{nt}|z_{nt}, b_n, \boldsymbol{\Theta}\right)$. The likelihood for N customers can be written as:

$$\begin{aligned}\mathcal{L}\left(\boldsymbol{\Theta}; \boldsymbol{L}\right) &= \int_{\boldsymbol{b}} \sum_{\boldsymbol{z}} f(\mathbf{L}|\mathbf{z}, \mathbf{b}, \boldsymbol{\Theta}) f\left(\mathbf{z}; \boldsymbol{\Theta}\right) f\left(\mathbf{b}; \boldsymbol{\Theta}\right) \mathbf{db} \\ &= \prod_{n=1}^{N} \int_{b_n} \left\{ \sum_{z_n} \delta_{z_{n1}} F_{n1} \prod_{t=2}^{T} \gamma_{z_{n(t-1)}, z_{nt}} F_{nt} \right\} f\left(b_n; \boldsymbol{\Theta}\right) db_n\end{aligned}$$

For notational convenience, the following indicator variables are defined for $t = 2, 3, \dots T$, $u_{ntj} = 1$ if and only if $z_{nt} = j$ and $v_{ntjk} = 1$ if and only if $z_{n(t-1)} = j$ and $z_{nt} = k$. Defining $F_{ntj} = f\left(L_{nt}|z_{nt} = j, b_n, \boldsymbol{\Theta}\right)$ and treating both the states of the hidden Markov chain and the random effects as missing data, the complete data log likelihood (CDLL) can be written as

$$\begin{aligned}\log \mathcal{L}_c\left(\boldsymbol{\Theta}; \mathbf{L}, \mathbf{z}, \mathbf{b}\right) &= \sum_{n=1}^{N} \left\{ \log \delta_{z_{n1}} + \sum_{t=2}^{T} \log \gamma_{z_{n(t-1)}, z_{nt}} + \sum_{t=1}^{T} \log F_{nt} + \log f\left(b_n; \boldsymbol{\Theta}\right) \right\} \\ = \sum_{n=1}^{N} &\left\{ \sum_{j=1}^{K} u_{n1j} \log \delta_{nj} + \sum_{t=1}^{T} \sum_{j=1}^{K} \sum_{k=1}^{K} v_{ntjk} \log \gamma_{njk} + \sum_{t=1}^{T} \sum_{j=1}^{K} u_{ntj} \log F_{ntj} + \log f\left(b_n\right) \right\}\end{aligned}$$

The MCEM is an iterative algorithm requiring two steps at each iteration: computation of a particular conditional expectation of the log-likelihood (E-step) and the maximization of this expectation over the relevant parameters (M-step).

In the E-step, the expectation of the complete data log likelihood (CDLL) conditional on the observed data $\boldsymbol{L}$ and parameter estimates at iteration p, $\boldsymbol{\Theta}^p$ are calculated. We replace the indicator variables by their conditional expectations given the observations $\boldsymbol{L}$ and the current parameter estimates $\boldsymbol{\Theta}^p$. The computation of the conditional expectation of CDLL is not easy due to the high-dimensional integration. The MCEM approximates the conditional expectation of the CDLL by a Monte Carlo method. Let B random samples $b_n^1, \ldots, b_n^B$ be generated from the distribution $f(\mathbf{b_n}; \boldsymbol{\Theta}^p)$. Defining $F_{ntj}^l = f\left(L_{nt} | z_{nt} = j, b_n^l, \boldsymbol{\Theta}^p\right)$, the following approximation can be obtained to the conditional expectation of the CDLL.

$$\begin{aligned} & E\left[\log \mathcal{L}_c\left(\boldsymbol{\Theta}; \mathbf{L}, \mathbf{z}, \mathbf{b} | \mathbf{L}, \boldsymbol{\Theta}^p\right)\right] \qquad (3.5) \\ & \approx \sum_{n=1}^{N} \left\{ \sum_{j=1}^{K} \hat{u}_{n1j} \log \delta_{nj} + \sum_{t=1}^{T} \sum_{j=1}^{K} \sum_{k=1}^{K} \hat{v}_{ntjk} \log \gamma_{njk} \right. \\ & \left. + \sum_{l=1}^{B} \sum_{t=1}^{T} \sum_{j=1}^{K} \hat{u}_{ntj} h(b_n^l | \boldsymbol{L}_n) \log F_{ntj}^l + \sum_{l=1}^{B} h\left(b_n^l | \boldsymbol{L}_n\right) \log f\left(b_n^l\right) \right\} \end{aligned}$$

where $\hat{u}_{n1j}$ and $\hat{v}_{ntjk}$ are defined in (3.12) and (3.12), respectively, and

$$h\left(b_n^l | \boldsymbol{L}_n\right) = \frac{f\left(\boldsymbol{L}_n | b_n^l, \boldsymbol{\Theta}^p\right)}{\sum_{l=1}^{B} f\left(\boldsymbol{L}_n | b_n^l, \boldsymbol{\Theta}^p\right)}$$

For ease of implementation of the MCEM algorithm, the forward variable is defined as follows:

$$\alpha_{nt}\left(j, b_n^l\right) = f\left(L_{n1,\ldots,}, L_{nt}, z_{nt} = j | b_n^l\right) \tag{3.6}$$

The forward variable can be computed recursively by

$$\alpha_{n1}\left(j, b_n^l\right) = \delta_{nj} f\left(L_{n1} | z_{n1} = j, b_n^l\right) \tag{3.7}$$

$$\alpha_{n(t+1)}\left(k, b_n^l\right) = \sum_{j=1}^{K} \left\{\alpha_{nt}\left(j, b_n^l\right)\gamma_{njk} \right. \tag{3.8}$$

$$\left. f\left(L_{n(t+1)} | z_{n(t+1)} = k, b_n^l\right)\right\}$$

Similarly, the backward variable is defined as follows:

$$\beta_{nt}\left(j, b_n^l\right) = f\left(L_{n(t+1)}, \ldots, L_{nT} | z_{nt} = j, b_n^l\right) \tag{3.9}$$

The backward variable can be calculated recursively by

$$\beta_{nT}\left(j, b_n^l\right) = 1 \tag{3.10}$$

$$\beta_{nt}\left(j, b_n^l\right) = \sum_{k=1}^{K} \left\{\gamma_{njk}\beta_{n(t+1)}\left(k, b_n^l\right)\ f\left(L_{n(t+1)} | z_{n(t+1)} = k, b_n^l\right)\right\} \tag{3.11}$$

The conditional expectation of the indicator variables $\hat{u}_{ntj}$ and $\hat{u}_{ntj}$ can then be defined as follows:

$$\hat{u}_{ntj} = f\left(z_{nt} = j|\boldsymbol{L}_n, \boldsymbol{\Theta}^p\right) = \frac{\sum_{l=1}^{B} \alpha_{nt}\left(j, b_n^l\right) \beta_{nt}\left(j, b_n^l\right) h(b_n^l|\boldsymbol{L}_n)}{\sum_{j=1}^{K}\sum_{l=1}^{B} \alpha_{nt}\left(j, b_n^l\right) \beta_{nt}\left(j, b_n^l\right) h\left(b_n^l|\boldsymbol{L}_n\right)}$$

$$\begin{aligned}\hat{v}_{ntjk} &= f\left(z_{n(t-1)} = j, z_{nt} = k|\boldsymbol{L}_n, \boldsymbol{\Theta}^p\right)\\ &= \frac{\sum_{l=1}^{B} \alpha_{n(t-1)}\left(j, b_n^l\right) \gamma_{njk} F_{ntk}^l \beta_{nt}\left(k, b_n^l\right) h(b_n^l|\boldsymbol{L}_n)}{\sum_{j,k=1}^{K}\sum_{l=1}^{B} \alpha_{n(t-1)}\left(j, b_n^l\right) \gamma_{njk} F_{ntk}^l \beta_{nt}\left(k, b_n^l\right) h(b_n^l|\boldsymbol{L}_n)}\end{aligned} \tag{3.12}$$

To avoid numerical underflow when α and β are very small, $\hat{u}_{ntj}$ and $\hat{v}_{ntjk}$ can be calculated using logarithms, the approximation of $\log(p+q)$ by [101] and the log-sum-exp trick.

In the M-step, the parameters $\boldsymbol{\Theta}$ are updated by maximizing the expected CDLL in (3.5) with respect to $\boldsymbol{\Theta}$. The first, second, and fourth term of (3.5) are maximized with respect to $\boldsymbol{\delta}$, $\boldsymbol{\Gamma}$ and σ^2, respectively. The third term of (3.5) is maximized with respect to $\boldsymbol{c}, \boldsymbol{a}$, and $\boldsymbol{\lambda}$. Since the conditional distribution and the random effects follow a normal distribution, closed form solutions of $\boldsymbol{\Theta}$ are available.

$$a_j = \frac{\sum_{n=1}^{N}\sum_{l=1}^{B}\sum_{t=1}^{T} \left(L_{nt} - \boldsymbol{c}_{nj}\boldsymbol{x}_t - b_n^l\right) \hat{u}_{ntj} h\left(b_n^l|\boldsymbol{L}_n\right)}{\sum_{n=1}^{N}\sum_{l=1}^{B}\sum_{t=1}^{T} \hat{u}_{ntj} h\left(b_n^l|\boldsymbol{L}_n\right)} \tag{3.13}$$

$$\boldsymbol{c}_{nj} = \frac{\sum\limits_{l=1}^{B} \sum\limits_{t=1}^{T} \left(L_{nt} - a_j - b_n^l\right) \hat{u}_{ntj} h\left(b_n^l | \boldsymbol{L}_n\right) \boldsymbol{x}_t}{\sum\limits_{l=1}^{B} \sum\limits_{t=1}^{T} \hat{u}_{ntj} h\left(b_n^l | \boldsymbol{L}_n\right) \boldsymbol{x}_t^2} \tag{3.14}$$

$$\lambda_j^2 = \frac{\sum\limits_{n=1}^{N} \sum\limits_{l=1}^{B} \sum\limits_{t=1}^{T} \left(L_{nt} - a_j - \boldsymbol{c}_{nj}\boldsymbol{x}_t - b_n^l\right)^2 \hat{u}_{ntj} h\left(b_n^l | \boldsymbol{L}_n\right)}{\sum\limits_{n=1}^{N} \sum\limits_{l=1}^{B} \sum\limits_{t=1}^{T} \hat{u}_{ntj} h\left(b_n^l | \boldsymbol{L}_n\right)} \tag{3.15}$$

$$\delta_{nj} = \hat{u}_{n1j},\ \gamma_{njk} = \frac{\sum\limits_{t=1}^{T} \hat{v}_{ntjk}}{\sum\limits_{t=1}^{T} \sum\limits_{k=1}^{K} \hat{v}_{ntjk}} \tag{3.16}$$

Once the MCEM algorithm converges and the parameter estimates are available, the random effect estimates can be calculated by the expectation of b_n for each customer,

$$\bar{b}_n = \sum_{l=1}^{B} h(b_n^l | \boldsymbol{L}_n) b_n^l \tag{3.17}$$

Then the expected load can be estimated using (3.2). The state probabilities at each time step can be estimated by calculating the filtered probabilities of regimes for each customer.

3.3.3 PV System Performance Model and Parameter Estimation

In this subsection, the physical PV system performance model is presented first. Then, the estimation method of the technical parameters of a solar PV system is described.

A PV system performance model, g calculates the AC output of a solar PV system with the relevant weather data and the solar PV system specifications. The model used in our study is based on the PV system performance modeling collaborative [337] from Sandia National Laboratory and PVWatts from NREL [97, 98]. The inputs to the model include the solar PV system specifications (system nameplate DC rating in kW P_{dc0}, tilt angle θ_t and azimuth angle θ_{az} of the PV array, nominal efficiency of the inverter η_{nom}, and loss of the PV system l), weather-related data (temperature and wind speed), and solar irradiance data (direct normal irradiance, diffuse horizontal irradiance, and global horizontal irradiance). The solar PV performance model has four main submodels, the radiation submodel, the thermal submodel, the module submodel, and the inverter submodel.

The radiation submodel translates the solar irradiation data into the energy incident on the PV module cover. First, solar position algorithms [297] can be used to calculate the sun position from the date, time, and geographic position data. The irradiance incident on the plane of the array (E_{POA}) is defined as follows.

$$E_{POA} = E_b + E_g + E_d \tag{3.18}$$

where E_b is the plane of the array (POA) beam component, E_g is the POA ground-reflected component, and E_d is the POA sky-diffuse component. The sun position data, albedo, PV array orientation, solar irradiance data, and array tracking mode are used to calculate E_b, E_g, and E_d and hence plane of array irradiance, E_{POA}. The solar irradiance data is collected from the National Solar Radiation Database (NSRDB). The physical solar model (PSM) employed by NSRDB utilizes the cloud physical and optical properties to produce cloudy-sky solar radiation [320]. For a fixed system, the angle of incidence is calculated following the standard geometrical calculation. Next, to account for reflection losses on the module cover, a correction is applied for incidence angles greater than 50^o using the polynomial correction from [337] and the transmitted irradiance, E_{tr} is calculated.

The thermal submodel calculates the operating cell temperature, T_c using the total incident POA irradiance E_{POA}, wind speed, and ambient air temperature following the Sandia module and cell temperature model.

The module submodel computes the DC output power P_{dc} by using the DC nameplate rating P_{dc0}, cell temperature T_c, transmitted POA irradiance E_{tr}, and loss of the PV array l. The loss is modeled as a percentage of DC energy. It includes the impacts of soiling, shading, mismatch, wiring, system age, etc. The reference cell temperature T_0 is 25^oC, temperature coefficient ζ is $-0.5\%/^oC$, and reference irradiance E_0 is 1000 W/m^2.

$$P_{dc} = (1-l) \times \frac{E_{tr}}{E_0} P_{dc0} \left[1 + \zeta \left(T_c - T_0\right)\right] \tag{3.19}$$

The inverter submodel calculates the AC power output of the PV system P_{ac} using P_{dc}. The AC nameplate rating of the inverter (P_{ac0}) is calculated by $P_{ac0} = \frac{P_{dc0}}{\text{DC-to-AC ratio}}$. The nominal efficiency of the inverter η_{nom} is defined as the ratio of the AC nameplate rating of the inverter P_{ac0} and the inverter DC rating $P_{dc0,inv}$. Then, the inverter efficiency η can be calculated following [98] and P_{ac} can be calculated as follows:

$$P_{ac} = \begin{cases} P_{ac0} & \text{if} P_{dc} \geq P_{dc0,inv} \\ \eta P_{dc} & \text{if} P_{dc} < P_{dc0,inv} \end{cases} \tag{3.20}$$

Next, the description of how to estimate the technical parameters of a solar PV system with multiple strings of solar panels facing different directions is provided. Although most residential houses have a single south-facing solar panel to maximize solar energy production over the year, many houses have multiple strings of solar panels often facing south and west. The west-facing solar installations may receive additional local government incentives because they produce more energy during the peak demand hours in the late afternoon. Our proposed solar PV system technical parameter estimation algorithm accounts for the cases of both single and multiple strings of solar panels.

Let $\mathbf{\Phi}$ denote a tensor of order three with dimensions $N \times M \times R$ representing the technical parameters of M panels of N customers. Let R denote the dimension of a single solar panel's parameters and $g_t\left(\mathbf{\Phi}_{mn}\right)$ denote the solar PV system's generation at time t based on a PV system performance model g. The technical parameters of the m-th solar panel of the customer n is denoted by $\mathbf{\Phi}_{mn} = [P_{dc0}, \theta_t, \theta_{az}, \eta_{nom}, l]$, which includes the DC rating, array tilt angle, array azimuth angle, nominal inverter efficiency, and loss of the PV array, respectively. The vector $\mathbf{\Phi}_n$ contains $\mathbf{\Phi}_{mn}$ for $m = 1, \ldots, M$ for customer n. The inputs to the solar PV system parameters estimator are the estimated solar PV generation S_{nt} of a customer n for time $t = 1, 2, ..., T$. Solar PV system parameters are estimated by minimizing the sum of squared error between the estimated solar PV generation S_{nt} and the calculated solar generation $g\left(\mathbf{\Phi}_{mn}\right)$ from M strings of solar panels of customer n.

$$\begin{aligned} &\underset{\mathbf{\Phi}_n}{\arg\min} \sum_{t=1}^{T} \left(S_{nt} - \sum_{m=1}^{M} g_t\left(\mathbf{\Phi}_{mn}\right) \right)^2 \\ &\text{subject to } \mathbf{\Phi}_{min} \leq \mathbf{\Phi}_{mn} \leq \mathbf{\Phi}_{max} \end{aligned} \tag{3.21}$$

where T is the time series length. $\mathbf{\Phi}_{min}$ and $\mathbf{\Phi}_{max}$ denote the lower and upper limits of the solar PV system technical parameters. The highly nonlinear nature of the solar PV system performance model makes (3.21) a nonlinear optimization problem, which can be solved by an interior-point algorithm.

3.3.4 Summary of Net Load Disaggregation Algorithm

It is proposed to disaggregate the net load measurements $\boldsymbol{NL}$ into electric load $\hat{\mathbf{L}}$ and solar PV generation $\hat{\mathbf{S}}$ for a group of residential customers by integrating the physical solar PV system performance model introduced in Section 3.3.3 and the statistical MHMM introduced in Section 3.3.1 and 3.3.2. The detailed process for joint net load disaggregation of a community of customers is shown in Algorithm 2. The MCEM estimation of the MHMM parameters can be computationally intensive. Therefore, it is necessary to have a good initial estimate of load $\hat{\mathbf{L}}^{(0)}$ as the starting point of the iterative algorithm. The initial estimates for electric load $\hat{\boldsymbol{L}}_{HMM}$ and PV system parameters $\hat{\boldsymbol{\Phi}}_{HMM}$ of all customers are set to be the estimates based on the iterative algorithm with HMM regression [184].

For each iteration i, an MHMM is fitted to the estimated load $\hat{\mathbf{L}}^{(i-1)}$. There are J_i sets of initial MHMM parameter estimates $\boldsymbol{\Theta}_0^{(i,j)}$ with $J_i = 2$ for the first iteration and $J_i = 3$ for the subsequent iterations. The first and second sets of initial MHMM parameter estimates $\boldsymbol{\Theta}_0^{(i,1)}$ and $\boldsymbol{\Theta}_0^{(i,2)}$ are obtained from fitting HMM regression to the estimated electric load $\hat{\mathbf{L}}_n^{(i-1)}$ of each customer n where $\boldsymbol{\Psi}_0^{(i,j)}$ are the initial estimates for the HMM regression parameters. Then, $\boldsymbol{\Psi}_0^{(i,1)}$ is set to be equal to be the multiple linear regression model parameters on $\boldsymbol{L}_n^{(i-1)}$ for N customers and their negatives for states $k = 1, 2$. To set $\boldsymbol{\Psi}_0^{(i,2)}$, the HMM regression is run with ten sets of initial values obtained by adding random noise to $\boldsymbol{\Psi}_0^{(i,1)}$ and then choosing the initial value set that yields the maximum log likelihood for the HMM regression. The third set of initial MHMM parameter estimates $\boldsymbol{\Theta}_0^{(i,3)}$ is equal to the MHMM parameters estimated in the previous iteration $\boldsymbol{\Theta}^{(i-1)}$. Now, the MHMM parameter estimates $\boldsymbol{\Theta}^{(i,j)}$ and the updated load estimates $\hat{\boldsymbol{L}}^{(i,j)}$ for $j = 1 \dots J_i$

are obtained.

For the j-th set of initial value, the estimated solar PV generation is calculated for each customer n as $\hat{\boldsymbol{S}}_n^{(i,j)} = \hat{\boldsymbol{L}}_n^{(i,j)} - \boldsymbol{NL}_n$. Next, the technical parameter set of M solar PV panels of customer n, $\boldsymbol{\Phi}_n^{(i,j)}$ is estimated by solving a constrained optimization following (3.21). The inputs to the optimization problem include the estimated solar PV generation $\hat{\boldsymbol{S}}_n^{(i,j)}$ and the solar PV system performance model g. The initial solar PV system parameter estimates is set to be equal to $\boldsymbol{\Phi}_n^{(i-1)}$. The solar PV generation $\hat{\boldsymbol{S}}_n^{(i,j)}$ for each customer n can then be updated by feeding the estimated solar PV parameters $\boldsymbol{\Phi}_n^{(i,j)}$ into the PV system performance model g. With the updated estimates for the load and solar generation, the net load estimate $\hat{\mathbf{NL}}_n^{(i,j)}$ and the average MSE of the customers' net load $E^{(i,j)}$ can be calculated for the j-th set of initial MHMM parameter estimates.

At the end of the i-th iteration, among the J_i sets of outputs, the one that corresponds to the lowest average MSE of the net load $E^{(i,j)}$ is calculated. The corresponding index of the initial MHMM parameter estimates is denoted as j^*. In other words, at the end of iteration i, the following variables are updated: $\hat{\boldsymbol{S}}^{(i)} = \hat{\boldsymbol{S}}^{(i,j^*)}$, $\boldsymbol{\Phi}^{(i)} = \hat{\boldsymbol{\Phi}}^{(i,j^*)}$ and $\boldsymbol{\Theta}^{(i)} = \hat{\boldsymbol{\Theta}}^{(i,j^*)}$, and $E^{(i)} = E^{(i,j^*)}$. The load estimate is then updated as $\hat{\boldsymbol{L}}^{(i)} = \boldsymbol{NL} + \hat{\mathbf{S}}^{(i)}$. The iterative algorithm continues until the average MSE of net load, $E^{(i)}$ converges or the maximum number of iterations is reached. Finally, the solution that yields the lowest average MSE for the customers' net loads is selected.

Post-disaggregation Adjustment

To further improve the net load disaggregation algorithm, the post-disaggregation adjustment is performed by enforcing the constraint that the electric load minus solar generation must be equal to the net load measurement. The following optimization problem inspired from [193] is solved for each customer n using the disaggregated signals $\hat{\boldsymbol{L}}_n$ and $\hat{\boldsymbol{S}}_n$.

$$\begin{aligned} &\underset{L_{nt},S_{nt}}{\arg\min} \sum_{t=0}^{T} \mu\Big(L_{nt} - \hat{L}_{nt}\Big)^2 + \omega\Big(S_{nt} - \hat{S}_{nt}\Big)^2 \\ &\text{subject to } S_{nt} \geq 0,\ L_{nt} \geq 0, \quad L_{nt} - S_{nt} = NL_{nt} \end{aligned} \tag{3.22}$$

Here, μ and ω are parameters that denote the weights for the errors in the load and solar generation estimates. μ and ω can be calculated as the inverse of the variance of the errors of the load and solar generation estimates.

$$\mu = 1/Var\,(\varepsilon_{Load}), \quad \omega = 1/Var\,(\varepsilon_{PV}) \tag{3.23}$$

Since the load and solar PV generation data are not available, the variance of the errors is estimated by the load and solar PV generation from steps 4 and 7 of the net load disaggregation algorithm from [184] at step 1 of Algorithm 2.

3.4 Numerical Study

3.4.1 Dataset for Numerical Study

The energy data of 193 residential customers in Austin, Texas gathered by Pecan Street Inc. [166] are used to validate our proposed net load disaggregation algorithm. The dataset includes 15-minute interval net load, electric load, and solar PV generation data. The tilt and azimuth angle information is not available. However, the solar panel's DC rating data are reported for 90% customers which can be used for validation. The study

Algorithm 2 Algorithm for joint net load disaggregation of N customers and estimation of their solar PV parameters

```
Input: A matrix of net load of customers, $\mathbf{NL}$
Output: Matrices of estimates for load $\hat{\mathbf{L}}$ and solar generation $\hat{\mathbf{S}}$, and a tensor of PV system parameters $\mathbf{\Phi}$
Initialize the matrix of load $\hat{\mathbf{L}}^{(0)} = \hat{\mathbf{L}}_{\mathbf{HMM}}$ with the load estimates from [184]. Initialize the tensor of PV parameters, $\mathbf{\Phi}^{(0)} = \hat{\mathbf{\Phi}}_{HMM}$ with estimates from [184].
for i=1 to maxiter do
  Determine $J_i$ sets of initial MHMM parameter estimates $\mathbf{\Theta}_0^{(i,j)}$. Set them equal to HMM regression model parameters $\mathbf{\Theta}_{HMM}^{(i,j)}$ based on $\hat{\mathbf{L}}^{(i-1)}$ with initial HMM regression parameters $\mathbf{\Psi}_0^{(i,j)}$ for $j = 1 \dots J_{i-1}$. Set $\mathbf{\Theta}_0^{(i,J_i)} = \mathbf{\Theta}_{HMM}^{(i,J_i)}$ if $i = 1$, $\mathbf{\Theta}_0^{(i,J_i)} = \mathbf{\Theta}^{(i-1)}$ for $i > 1$.
  for j=1 to $J_i$ do
    Fit MHMM, $f(\boldsymbol{x}, \mathbf{\Theta})$, to $\hat{\mathbf{L}}^{(i-1)}$ with initial parameter estimates $\mathbf{\Theta}_0^{(i,j)}$ and calculate $\mathbf{\Theta}^{(i,j)}$
    Update load estimates, $\hat{\mathbf{L}}^{(i,j)} = f\left(\boldsymbol{x}, \mathbf{\Theta}^{(i,j)}\right)$
    Update solar generation, $\hat{\boldsymbol{S}}^{(i,j)} = \hat{\mathbf{L}}^{(i,j)} - \mathbf{NL}$
    for customers n=1 to N do
      Determine ${\mathbf{\Phi}_n}^{(i,j)}$ from Equation (3.21) using ${\mathbf{\Phi}_n}^{(i-1)}$ as initial value
      Update solar generation, $\hat{\boldsymbol{S}}_n^{(i,j)} = g\left({\mathbf{\Phi}_n}^{(i,j)}\right)$
      Estimate net load, $\hat{\mathbf{N}}\mathbf{L}_n^{(i,j)} = \hat{\mathbf{L}}_n^{(i,j)} - \hat{\mathbf{S}}_n^{(i,j)}$ and MSE of the estimated net load, $E_n^{(i,j)}$
    end for
    Calculate $E^{(i,j)} = \frac{1}{N} \sum_{n=1}^{N} E_n^{(i,j)}$
  end for
  Determine $j^* = \underset{j}{argmin}\, E^{(i,j)}$
  Update $\hat{\mathbf{S}}^{(i)} = \hat{\mathbf{S}}^{(i,j^*)}$, $\mathbf{\Phi}^{(i)} = \mathbf{\Phi}^{(i,j^*)}$, $\mathbf{\Theta}^{(i)} = \mathbf{\Theta}^{(i,j^*)}$, and $E^{(i)} = E^{(i,j^*)}$
  Update load estimates, $\hat{\mathbf{L}}^{(i)} = \mathbf{NL} + \hat{\mathbf{S}}^{(i)}$
  if $\left|E^{(i)} - E^{(i-1)}\right| \le \varepsilon$ Break end if
end for
Determine $i^* = \underset{i}{argmin}\, E^{(i)}$
Calculate $\hat{\mathbf{L}} = \hat{\mathbf{L}}^{(i^*)}$, $\hat{\mathbf{S}} = \hat{\mathbf{S}}^{(i^*)}$, and $\mathbf{\Phi} = \mathbf{\Phi}^{(i^*)}$
return $\hat{\mathbf{L}}$, $\hat{\mathbf{S}}$, and $\mathbf{\Phi}$
```

Table 3.1: Comparison of various net load disaggregation methods

Error Metric	Variable	MHMM (S1)	HMM reg. (S1)	MHMM (S2)	HMM reg. (S2)	Consumer Mixture Model	SunDance Model	Algorithm by [333]
MSE	Solar	**0.13**	0.19	**0.12**	0.18	0.37	0.54	0.42
	Load	**0.13**	0.19	**0.12**	0.18	0.37	0.49	0.28
MASE	Solar	**2.13**	2.61	**2.11**	2.58	3.85	3.74	4.44
	Load	**0.43**	0.48	**0.42**	0.48	0.74	0.81	0.56
CV	Solar	**0.47**	0.58	**0.45**	0.57	0.77	0.85	0.78
	Load	**0.29**	0.33	**0.28**	0.32	0.46	0.57	0.43

period is selected as 10/03/2015-10/30/2015 to compare our estimates with [76]. The solar irradiance and weather-related data are collected with 4×4 km spatial and 30-minute temporal resolutions from the National Solar Radiation Database [320]. It is converted into 15-minute interval data by linear interpolation.

The approximate longitude and latitude of Austin, Texas (30.29^oN,-97.69^oE) is used as a common proxy location for all customers as their exact locations are not available. Similarly, the same weather variables are used for net load disaggregation for all of the customers. Since most of the residential rooftop solar PV systems use a fixed array, it is assumed that none of the residential solar PV systems in this study have a tracking system. Note that if the solar PV system's tracking mode information is available, then the incorporation of either 1-axis or 2-axis tracking in the PV system performance model is straightforward.

3.4.2 Experimental Setup

The proposed net load disaggregation method is implemented following Algorithm 2 under two scenarios. In the first scenario, it is assumed that every customer's solar PV system only has one string of solar panels, which means $M = 1$ and the number of solar PV technical parameters $R = 5$. In the second scenario, it is recognized that in the Pecan Street dataset, 71 out of 193 customers have two strings of solar panels facing different directions. Thus, it is assumed that these customers have two solar panels with potentially different DC ratings but the same tilt angle, nominal inverter efficiency, and loss. In this scenario $M = 2$ and $R = 7$. The rest of the customers have a single string of solar panels. Note that the data indicating one or two strings of solar panels may be erroneous. Thus, the estimated total effective DC sizes for the 71 customers [184] is compared for both one and two strings of solar panel installation assumption. If the difference between the outputs under the two assumptions is significant, then it is still assumed that the customer has a single string of solar panels. This is because customers often have larger solar panels installed on the main roof. The secondary roof usually can only support smaller solar panels. Thus, the difference between the total estimated DC ratings of solar PV systems is typically not significant. When a large difference occurs, it might suggest that the proposed iterative algorithm with two strings of solar panels setup has converged to a local optimum. This is possible given that the dimensionality of the search space is much larger for the two-string setup. Therefore, when a large difference in the DC size estimates is encountered, a single string of solar panels is assumed. Finally, 64 out of 71 customers are identified to have two strings of solar panels.

To strike a balance between computational efficiency and accuracy, the number of random samples B of the MCEM is selected to be 500. The tolerance for the convergence of the MCEM algorithm is set as $\epsilon' = 0.001$. The initial parameter estimates of the MHMM are obtained from fitting the HMM regression [184] to the individual customer's electric load data. Note that, the HMM regression is fitted using the EM algorithm [239] instead of MS regress package [286] to make the parameter estimation procedure comparable to the MCEM algorithm.

The feasible ranges of solar PV parameters P_{dc}, θ_T, θ_{az}, η_{nom}, and l are set as 1-15 kW, $5^o - 50^o$, $0^o - 360^o$, $0.92 - 0.99$ and $9\% - 40\%$, respectively [184, 336, 246]. The DC-to-AC ratio is fixed at 1.1. When testing the benchmark algorithm to perform net load disaggregation for individual customers with HMM regression [184], 8 initial solar PV system technical parameter sets are chosen for the single string of solar panel scenario by gradually increasing P_{dc0} in 7 steps from 1 kW to 8 kW. The other initial parameters were set at their most common values $[\theta_T, \theta_{az}, \eta_{nom}, l] = [25^o, 180^o, 0.96, 14\%]$. For the scenario with two strings of solar PV panels, 64 initial PV parameter sets are obtained by enumerating the two DC sizes from 1 to 8 kW. The initial estimates for θ_{az} are set at 180^o and 270^o. The tolerance for the convergence of Algorithm 2 is set as $\varepsilon = 0.001$. The performance of the proposed and benchmark algorithms is evaluated with three commonly used error metrics: mean squared error (MSE), mean absolute squared error (MASE), and coefficient of variation (CV) [184].

3.4.3 Result and Analysis

In this section, the performance of our proposed Algorithm 2 is compared with four other state-of-the-art net load disaggregation algorithms including our earlier work [184] that uses HMM regression for individual load estimation. In addition, the benefits of considering multiple strings of solar panels facing different directions are also evaluated in the numerical study.

Comparison with state-of-the-art net load disaggregation algorithms

The four state-of-the-art benchmark net load disaggregation algorithms are as follows: the unsupervised consumer mixture model [76], the SunDance algorithm [74], the algorithm proposed in [333], and our earlier behind-the-meter solar generation estimation work that uses HMM regression to model individual customer's electric load. The details of the experimental setup of the consumer mixture model and the SunDance model can be found in [184]. Since method C yields the best results among the four methods proposed in [333] for this dataset, it is used as one of the benchmarks. This method assumes electric load to be piecewise constant and models the solar PV generation by a linear combination of the solar irradiance.

The MSE, MASE, and CV for the load and solar generation estimates of the proposed algorithm and the four benchmark algorithms are reported in Table 3.1. As shown in the table, our proposed algorithm which seamlessly integrates the physical solar PV system performance model with statistical MHMM significantly outperforms all benchmark algorithms. Our proposed method reduces the MSE of the solar PV generation estimates by 67% and 33% from the consumer mixture model [76] and our earlier work that uses HMM regression [184] respectively.

There are two reasons why our proposed algorithm yields better results. First, the high fidelity physical PV system performance model incorporated in our proposed algorithm can better capture the nonlinear relationships between the solar PV generation, solar PV system specifications, and weather data. Second, MHMM is better suited to emulate the

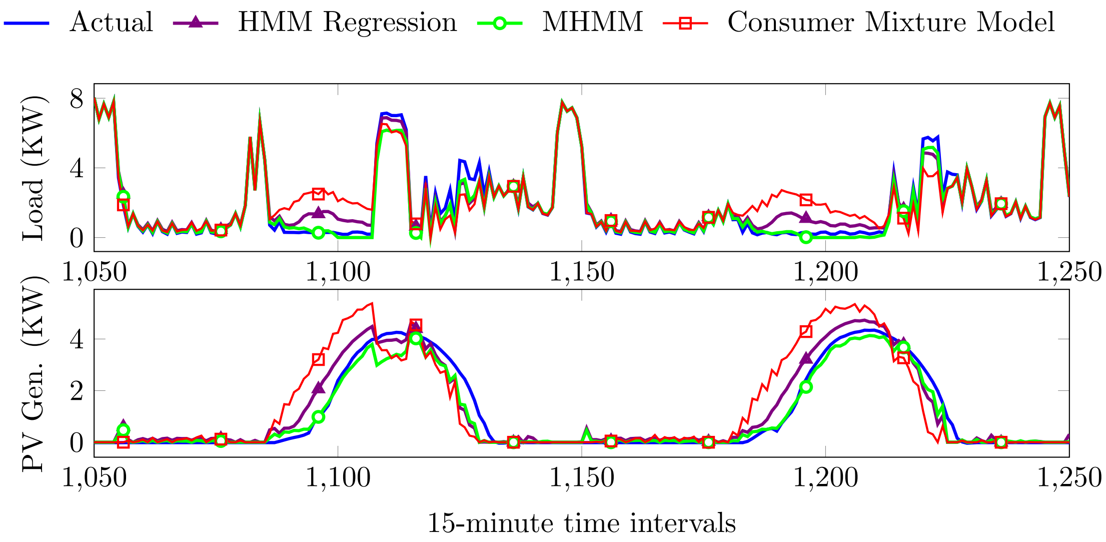

Figure 3.2: Comparison of disaggregated load and solar PV generation with actual values for a customer from 10/11/2015 to 10/12/2015

customers' energy behavior in different regimes. This is especially evident during the low load periods when the customer may be absent as depicted in Fig. 3.2. As shown in Fig. 3.2, the MHMM follows the actual load much more closely than the benchmark algorithms during the low load periods, which leads to better solar PV generation estimation. Therefore, the comparative advantage of our proposed model is more pronounced for customers who are absent from home for a long period. In the numerical study, 24 out of 193 customers are suspected to be absent from their residence for an extended period. For these customers, our proposed model with MHMM regression reduces the MSE by 71% compared to the consumer mixture model.

Comparison between MHMM and HMM regression

The proposed net load disaggregation algorithm with MHMM outperforms the algorithm with HMM regression by 33% in terms of MSE of load estimates. The MHMM provides a more accurate estimation of load compared to the HMM regression. The proposed net load disaggregation method is an iterative method that estimates the load and PV generation parameters in turn. An improved load estimate at step 6 of the algorithm leads to an improved estimate of solar PV technical parameters, which in turn leads to an improved solar PV generation estimate. Our proposed net load disaggregation algorithm with MHMM outperforms the algorithm with HMM regression by 33% in terms of MSE of solar PV generation estimates.

The improved load estimate by MHMM can be attributed to the following factors. First, MHMM jointly models the electric load of customers in a community while capturing the individual heterogeneity by incorporating the individual-specific random effects. Second, MHMM provides a more efficient estimation of the fixed model parameters. Third, MHMM enables information sharing by the population-level effect and the random effects components that follow a normal distribution with a common variance. As a result, it can be observed in this study that the algorithm with MHMM yields a more pronounced improvement for customers with unreliable intercept estimates in the HMM regression. The MHMM corrects such problems by moving these outliers toward the mean intercept. As shown in Fig. 3.3, the histogram of the intercepts from the HMM regression is skewed to the right with 54 customers having a very large intercept (> 1). The intercept estimates of the MHMM for these customers have been shifted toward the mean. The improvement in

MSE of solar PV generation estimates is 50% for these customers and only 29% for the rest of the customers.

The histograms of the MSE of the solar PV generation estimate for the algorithms with HMM regression and MHMM are shown in Fig. 3.4. It can be observed that the percentage of customers with lower MSE of solar PV generation estimates from the algorithm with MHMM is much higher than that from the algorithm with HMM regression. For example, the percentage of customers with MSE of solar PV generation estimates smaller than 0.1 kW is only 29% for the algorithm with HMM regression. By adopting the proposed algorithm with MHMM, this percentage increases to 45%.

The net load disaggregation algorithm with both HMM regression and MHMM provides accurate solar PV generation estimates both on sunny and cloudy days. In this study, October 21 to October 26 are cloudy days with low DNI. The average MSE of solar PV generation estimates is 0.10 KW for the algorithm with MHMM. The average MSE of solar PV generation estimates is 0.12 KW for the algorithm with HMM regression. For both algorithms, the MSE for the cloudy days is lower than the overall average MSE. As shown in Fig. 3.6, the PV generation estimates of the customer with the median MSE of solar PV generation from HMM regression and MHMM closely follow the actual solar PV generation.

Advantage of modeling multiple strings of solar panels

By considering the possibility of having multiple strings of solar panels facing different directions, our proposed algorithm in scenario 2 further improves the estimation accuracy when compared to scenario 1. This modeling flexibility better captures the physical

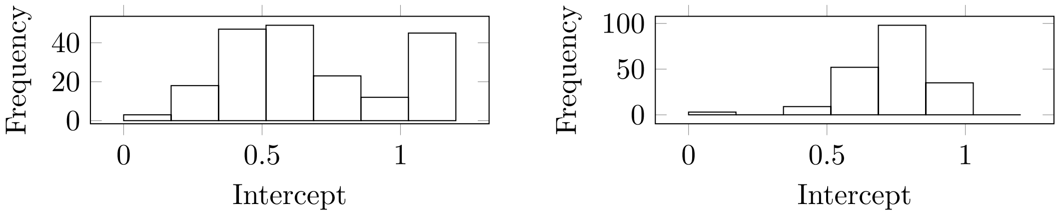

Figure 3.3: Histogram of the intercepts from the HMM regression (left, $std = 0.49$) and the MHMM(right, $std = 0.14$)

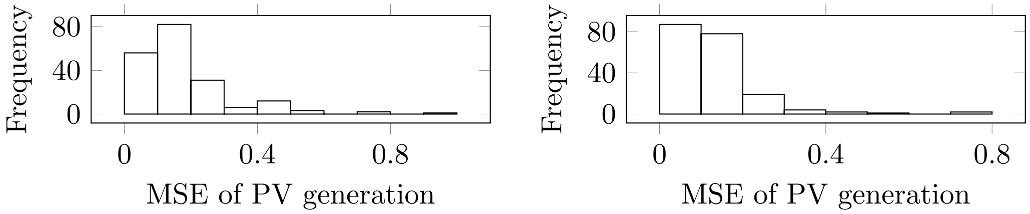

Figure 3.4: Histogram of the MSE of solar PV generation estimates for the HMM regression (left) and the MHMM (right)

configurations of real-world solar PV systems. As shown in Table 3.1, a 7% reduction in MSE of the solar generation estimates is achieved in scenario 2 over scenario 1.

Accuracy of the PV array technical parameters

The ground truth tilt and azimuth angle of the solar PV installations are not available. The DC rating of solar PV panels is available for 90% of the customers. The performance of the proposed model in estimating the DC size of the solar PV systems is illustrated in Fig. 3.5. As shown in Fig. 3.5, the estimated solar DC ratings and the actual are quite similar. The MAPE of the estimated solar DC ratings is 20% for the algorithm with HMM regression and 18% for the algorithm with MHMM.

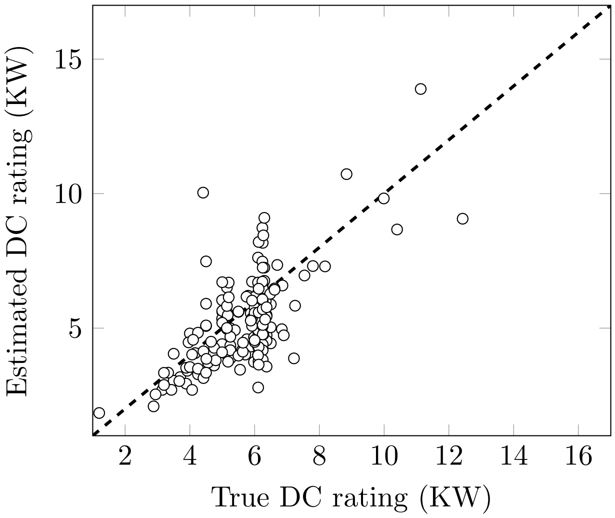

Figure 3.5: Comparison of true and estimated DC rating of PV array

Computation time and scalability

The computation time for the net load disaggregation algorithm with MHMM is 6 minutes per hour of net load data using an Intel core i9 processor. The computation time is measured for the case where the number of initial MHMM parameters J_i is 3. The number of random samples B equals 500. The tolerance for the convergence of the MCEM algorithm ϵ' is set as 0.001 and the number of customers is 193. However, 45% time is spent on solving the HMM regression problem which is used as initial parameters for the MHMM at step 3 of Algorithm 2. This process can be parallelized to save computation time since the HMM regression is estimated for each customer separately. To perform net load disaggregation for a large number of customers, one could first separate all customers into different communities based on geographical location. Then the net-load disaggregation problem can be solved for different communities in parallel, which makes the proposed

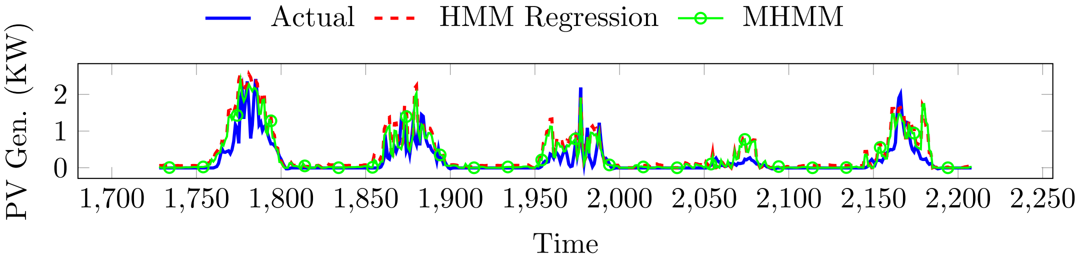

Figure 3.6: Comparison of disaggregated solar PV generation with actual values for the customer with median MSE of solar PV generation for the cloudy days from October 18 to October 23

algorithm extremely scalable.

3.5 Chapter Summary

An unsupervised algorithm is developed to disaggregate the observed net load signals of a group of residential customers with behind-the-meter solar PV systems into unknown solar PV generation and electric load. The iterative algorithm synergistically combines a physical PV system performance model for individual solar PV generation estimation with a statistical mixed hidden Markov model for joint load estimation. The mixed hidden Markov model not only models the general load consumption behavior of the entire community but also captures the individual differences with the random effects. Furthermore, the high fidelity PV system performance model considers real-world configurations with multiple strings of solar panels facing different directions. These technical advancements result in a significant reduction in the estimation error of the solar PV generation from the state-of-the-art net load disaggregation algorithms. Once the estimated solar PV systems' technical parameters are obtained with the proposed algorithm, online estimation of behind-the-meter solar PV generation becomes feasible with real-time solar irradiance data.

Chapter 4

Reinforcement Learning-based Smart Inverter Control with Polar Action Space in Power Distribution Systems

4.1 Introduction

Solar photovoltaics (PV) is projected to constitute 46% of total renewable generation by 2050, increasing from only 13% in 2018 [103] due to a rapid drop in cost [376]. However, solar energy is highly intermittent due to cloud cover and shading, fluctuating up to 15% of their nameplate ratings within one-minute intervals [370]. The increasing solar PV penetration in power distribution networks poses serious operational challenges, particularly in maintaining an appropriate feeder-wide voltage profile.

To keep the feeder voltage profile in a reasonable range, conventional Volt-VAR control (VVC) determines the optimal hourly set points for voltage regulating devices such as voltage regulators, on-load tap changers (OLTCs), and capacitor banks. However, these voltage regulating devices are slow operating mechanical equipment and are insufficient to adapt to distribution systems with fast and significant voltage fluctuations due to high solar PV penetration. Chronic voltage fluctuations can also lead to frequent operations of voltage regulating devices which will shorten their life cycles and increase maintenance costs [254].

To mitigate frequent voltage variations in distribution feeders with high solar PV penetration, smart solar PV inverter-based VVC has been studied. Smart inverters provide fast and continuous active and reactive power control with low operational costs. Besides, they support two-way communications, which allow remote control systems to change inverter setpoints. This opens up considerable opportunities for utilities to integrate distributed solar PV systems into the VVC framework. The IEEE 1547a-2020 standard allows smart inverters to participate in grid voltage regulation [18].

Previous studies on inverter control consider varying the reactive power generation of solar PV systems using centralized [111, 405, 393], distributed [355, 88, 264, 28], or local control approaches [353, 175, 109]. Centralized and distributed control solve an optimal power flow (OPF) problem to determine the inverter reactive power generation. Local control approaches calculate the reactive power generation using droop control. However, controlling only reactive power may yield low feeder power factors and cause high network currents. In fact, smart inverters can also curtail solar PV systems' active power generation to regulate feeder voltage [351, 352]. An optimization-based centralized approach is developed to determine both active and reactive power setpoints for smart inverters of solar PV systems in [87].

Recently, researchers have been developing two-timescale model-based VVC by supplementing the conventional slow timescale VVC with fast timescale smart inverter control [300, 112, 396, 218]. References [112] and [396] formulate the VVC as an OPF problem and propose to solve it using centralized optimization. The controllable devices on the slow timescale include capacitor banks [396, 112] and OLTCs [396, 218].

The model-based optimization approaches [130] rely on accurate and complete distribution network topology [375, 120] and parameter information [374]. However, the secondary feeders' phase connection information is usually not accurate [121]. To address these problems, researchers have developed data-driven control approaches for slow timescale VVC problems [371, 393, 397, 368] and fast timescale smart inverter control problem [219] using reinforcement learning (RL) algorithms. A two-timescale VVC framework is developed in [400]. For the slow timescale, deep Q-learning is used to determine the switching schedule of capacitors. For the fast timescale, an optimization-based approach is adopted to control the smart inverters. Many existing data-driven approaches need accurate line parameters and power injections at every bus which might not be available in real-time operations [394].

There are two main drawbacks of the existing data-driven VVC framework involving smart inverters. First, the existing approaches only consider changing the reactive power setpoints of smart inverters [219] and ignore the fact that active power could be curtailed for solar PV systems during certain circumstances. Second, the primary feeders' model is much more reliable than that of the secondary feeders. Thus, in the two-timescale VVC framework, the fast timescale control involving smart inverters in the secondary feeders should be data-driven and the slow timescale control involving the primary feeder can be handled with a model-based approach.

In this chapter, we fill the knowledge gap by developing a two-timescale data-driven Volt-VAR control method, which does not rely on secondary feeder information. Note that our method still requires knowledge of the primary feeder, which is often readily available. Furthermore, we design a polar action space set up to jointly determine the active and reactive power setpoints of smart inverters. Specifically, on the slow timescale, a centralized optimization-based approach is adopted to determine the tap positions of voltage regulators, OLTCs, and switchable capacitor banks. On the fast timescale, a deep deterministic policy gradient (DDPG)-based algorithm is employed to determine the set points of real and reactive power of smart inverters.

The unique contributions of this chapter are:

- We develop a reinforcement learning-based two-timescale VVC for distribution networks without requiring secondary feeders' topology or parameter information.
- We design a polar action space for reinforcement learning-based smart inverter control. This design allows joint determination of real and reactive power setpoints while explicitly enforcing the maximum power capability constraint.
- The degradation costs of the SIs are modeled in the sequential decision-making process of the VVC problem.

The rest of the chapter is organized as follows. Section 4.2 presents an overview of the two-timescale VVC problem. Section 4.3 discusses the problem formulation of the slow timescale VVC and fast timescale smart inverter control. Section 4.4 presents the proposed two-timescale VVC algorithms. Section 4.5 shows the numerical study results. Finally, Section 4.6 states the conclusions.

4.2 Two-timescale VVC Framework

We consider a power distribution system with both conventional voltage regulating devices and smart inverters. The smart inverters control the real and reactive power setpoints of solar PV systems. A generic power distribution network being modeled is shown in Fig. 4.1. The overall framework of the two-timescale VVC is shown in Fig. 4.2. In the slow timescale VVC, the optimal tap positions and switching schedules of the voltage regulator, OLTCs, and capacitor banks are determined using a centralized optimization-based method on an hourly basis τ. Within each hour, the tap and switching positions of these voltage regulating devices are kept fixed. The technical method of the slow timescale VVC is discussed in detail in Subsection 4.3.2. In the fast timescale VVC, the real and reactive power setpoints of smart inverters are determined every minute t to mitigate voltage violations caused by rapid fluctuations in the maximum potential output of solar PV systems. The smart inverter dispatch schedule is determined by the deep deterministic policy gradient algorithm which does not rely on an accurate secondary feeder model. The fast timescale VVC problem using smart inverters is formulated in Section 4.3.3.

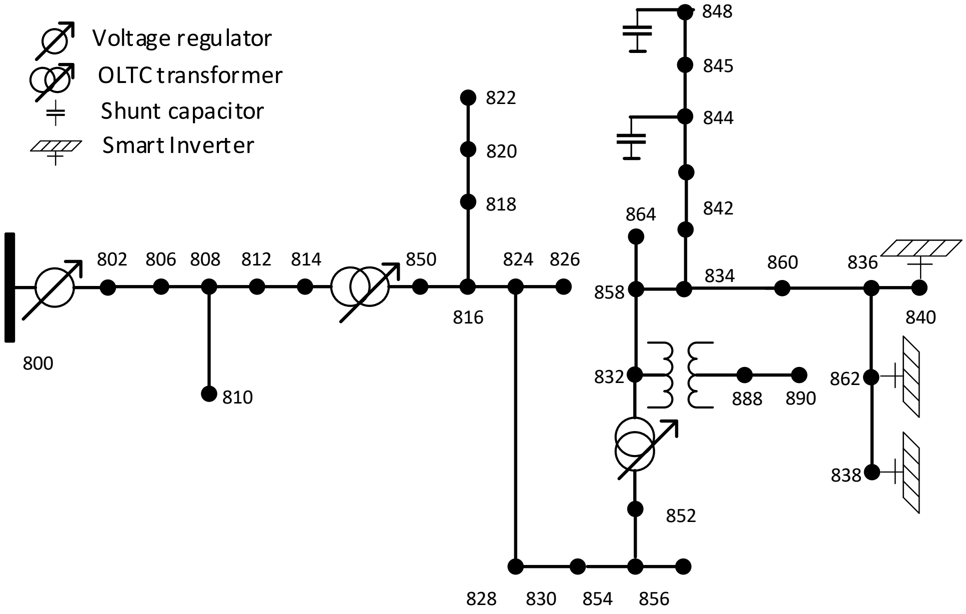

Figure 4.1: Diagram of a typical power distribution network with voltage regulating devices and smart inverters.

4.3 Problem Formulation

4.3.1 Problem Setup

Let us consider a radial distribution feeder of N buses represented by $\mathcal{G} := (\mathcal{N}, \mathcal{L})$. Here, $\mathcal{N} := \{1, \ldots, N\}$ is the collection of all nodes and $\mathcal{L} := \{(m, n) \subset \mathcal{N} \times \mathcal{N}\}$ is the collection of edges representing distribution line segments. Let r_{ij} and x_{ij} be resistance and reactance of the distribution line between node i and j. We assume that the distribution network is relatively balanced.

Let v_i denote the complex voltage phasor at node i for $i \in \mathcal{N}$ and u_i denote the square of the corresponding voltage magnitude. Let I_{ij} be the complex current flowing from node i to node j and ℓ_{ij} be the square of the corresponding current magnitude. Let P_{ij} and Q_{ij} be the real and reactive power flowing over the line connecting nodes i and j.

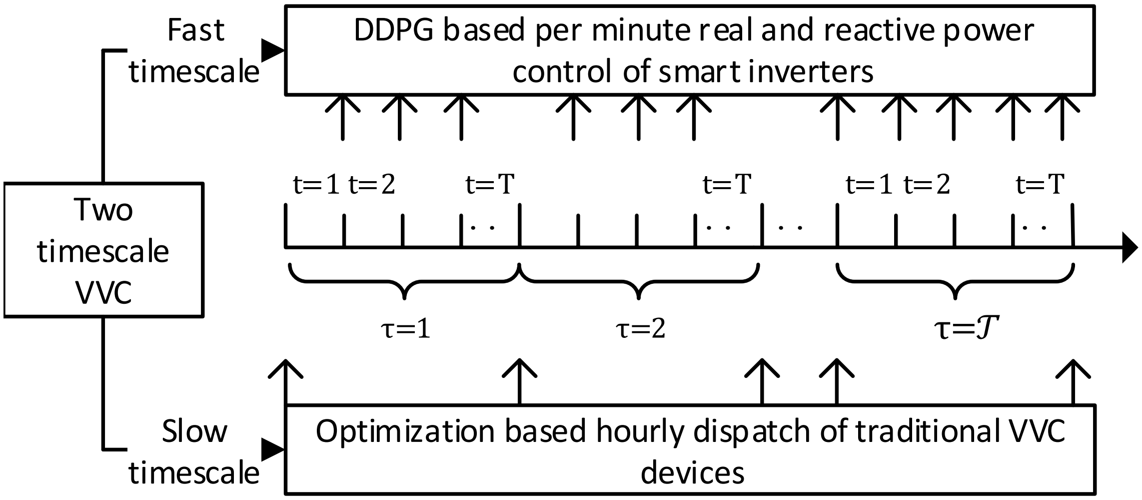

Figure 4.2: The overall framework for two-timescale VVC

Let p_i^g and q_i^g be the real and reactive power generation from the smart inverter connected solar PV system at node i, and p_i^c and q_i^c be the real and reactive power demand at node i. Let p_i^G and q_i^G be the total real and reactive power generation respectively at node i from the smart inverter connected solar PV systems and switchable capacitors. Let $p_i + jq_i$ be the net complex power injection at node i where $p_i := p_i^G - p_i^c$ and $q_i := q_i^G - q_i^c$. Let $\bar{p}_{it}^g$ be the available solar PV production at time t for smart inverter i, which is determined by solar irradiance and the smart inverters' nameplate capacity $\bar{S}_i$. At any time t, the real and reactive power generation from smart inverters, electric demand $p_{it}^g, q_{it}^g, p_{it}^c, q_{it}^c$, and the settings of voltage regulators, OLTCs, and capacitor banks determine the voltages and power flows on the distribution network.

4.3.2 Slow Timescale VVC Using Voltage Regulation Devices

For the slow timescale VVC subtask, the controllable devices include voltage regulators, OLTCs, and switchable capacitor banks. Voltage regulators are typically placed at the reference bus. Each of the voltage regulators and OLTCs has K tap positions with a step size of C^{reg} and C^{tsf} corresponding to the change in turns ratios. The series and shunt impedance of the voltage regulating devices can be neglected since their values are very small. Switchable capacitor banks are installed at different locations on the feeder to provide local voltage support. Let q_i^{cap} be the reactive power generation from the capacitor bank. Let tap_τ^{reg} and tap_τ^{tsf}, and tap_τ^{cap} indicate the tap position of the voltage regulators, OLTCs, and the switch status of the capacitor banks respectively at time τ.

For the slow timescale VVC subtask, the reactive power setpoints of smart inverters are assumed to be 0. Thus, $q_{j\tau}^{G} = q_{j\tau}^{cap}$ at every node j. The objective of the slow timescale VVC is to minimize the sum of line loss $C_e r_{ij} \ell_{ij\tau}$ and voltage deviation cost $C_V \left(u_{i\tau} - 1\right)^2$ at the beginning of each hour τ, where C_v and C_e are voltage deviation cost ($\$/volt$) and electricity price ($\$/MWh$) respectively. The slow timescale VVC is formulated as a mixed-integer nonlinear programming (MINLP) problem as follows. Note that such formulation

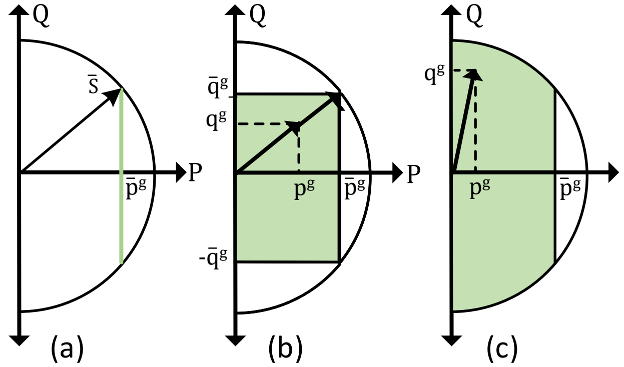

Figure 4.3: (a) Action space for reactive power control strategy, (b) Rectangular action space for inverter control with both real and reactive power, (c) Polar action space for inverter control with both real and reactive power.

might not be a feasible approach as the size of the distribution network grows.

$$\min_{\boldsymbol{X}} \sum_{(i,j)\in\mathcal{L}} C_e r_{ij} \ell_{ij\tau} + \sum_{i\in\mathcal{N}} C_v \left(u_{i\tau} - 1\right)^2 \tag{4.1}$$

$$\text{s.t. } P_{ij\tau} = \sum_{k:(j,k)\in\mathcal{L}} P_{jk\tau} + r_{ij}\ell_{ij\tau} + p^c_{j\tau} - \bar{p}^g_{j\tau} \tag{4.2}$$

$$Q_{ij\tau} = \sum_{k:(j,k)\in\mathcal{L}} Q_{jk\tau} + x_{ij}\ell_{ij\tau} + q^c_{j\tau} - q^{cap}_{i\tau} \tag{4.3}$$

$$u_{j\tau}/a^2_{ij\tau} = u_{i\tau} - 2\left(r_{ij}P_{ij\tau} + x_{ij}Q_{ij\tau}\right) + \left(r^2_{ij} + x^2_{ij}\right)\ell_{ij\tau} \tag{4.4}$$

$$u_{1\tau} = \left(u^{ref} + tap^{reg}_{\tau} \times C^{reg}\right) \tag{4.5}$$

$$\ell_{ij\tau} = \frac{P^2_{ij\tau} + Q^2_{ij\tau}}{u_{i\tau}}, \quad \forall\,(i,j) \in \mathcal{L} \tag{4.6}$$

$$\boldsymbol{X} := \left(\boldsymbol{P}_\tau, \boldsymbol{Q}_\tau, \boldsymbol{u}_\tau, \boldsymbol{\ell}_\tau, \mathbf{tap}^{reg}_\tau, \mathbf{tap}^{tsf}_\tau, \mathbf{tap}^{cap}_\tau\right) \tag{4.7}$$

where $a_{ij\tau} = 1 + tap^{tsf}_{\tau} \times C^{tsf}$ if there is an OLTC on branch (i,j) and $a_{ij\tau} = 1$ otherwise.

4.3.3 Fast Timescale VVC by Smart Inverters

Smart Inverter Control Strategies

A solar PV inverter has a maximum apparent power capability $\bar{S}_i > \max(\bar{p}^g_{it})$. There are three operational strategies for smart inverters:

Reactive Power Control Strategy If the i-th solar PV inverter allows reactive power control only, then the set of its operating points F_i^{RPC} is defined as:

$$F_i^{RPC} := \left\{ (p^g_{it}, q^g_{it}) \,\middle|\, p^g_{it} = \bar{p}^g_{it}, |q^g_{it}| \leq \sqrt{\bar{S}_i^2 - (\bar{p}^g_{it})^2} \right\}$$

Under this control strategy, the active power output is the available solar PV generation, and the reactive power output is limited by the inverter rating. The set F_i^{RPC} is represented by the vertical line segment in Fig. 4.3(a). If the inverter is not oversized, then the smart inverter can not provide reactive power compensation when $\bar{p}^g_{it} = \bar{S}_i$. With oversized inverters, the entire inverter rating can be utilized to supply reactive power when no active power is produced.

Real and Reactive Power Control with Rectangular Operating Space Under this control strategy, smart inverters are allowed to adjust both active and reactive power. However, the reactive power compensation is limited by the inverter rating and available solar PV production $\bar{p}^g_{it}$ at time t with $\bar{q}^{gR}_{it} = \sqrt{\bar{S}_i^2 - (\bar{p}^g_{it})^2}$. Thus, the smart inverter operating space is a rectangle as shown in Fig. 4.3(b). The set of possible operating points of the smart inverter is given by:

$$F_i^{RPCR} := \left\{ (p_{it}^g, q_{it}^g) \middle| 0 \leq p_{it}^g \leq \bar{p}_{it}^g, |q_{it}^g| \leq \bar{q}_{it}^{gR} \right\}$$

Under this control strategy, when $0 \leq p_{it}^g < \bar{p}_{it}^g$, active power curtailment takes place. The amount of real power curtailment p_{it}^C equals $\bar{p}_{it}^g - p_{it}^g$.

Real and Reactive Power Control with Polar Operating Space Under this strategy, solar PV inverters are allowed to adjust both active and reactive powers. The reactive power compensation is limited by the inverter rating and the actual solar PV production p_{it}^g at time t as in $\bar{q}_{it}^{gP} = \sqrt{\bar{S}_i^2 - (p_{it}^g)^2}$, which makes the inverter operating space a curtailed semi-circle as shown in Fig. 4.3(c). Here, $\bar{q}_{it}^{gP} > \bar{q}_{it}^{gR}$ when active power curtailment take place, i.e. $p_{it}^g < \bar{p}_{it}^g$. Consequently, the set of possible operating points is given by

$$F_i^{RPCP} := \left\{ (p_{it}^g, q_{it}^g) \middle| 0 \leq p_{it}^g \leq \bar{p}_{it}^g,\ |q_{it}^g| \leq \bar{q}_{it}^{gP} \right\}$$

Optimization based Fast Timescale Inverter Control

If the power distribution network model is complete and accurate, the optimal setpoints of smart inverters can be found by solving the following optimization problem at every time slot t within each interval τ. In addition to minimizing line loss and voltage deviation, the active power curtailment cost $C_c\,|\bar{p}_{it}^g - p_{it}^g|$ of each inverter is minimized where C_c is the active power curtailment cost $\$/MWh$. By relaxing the nonconvex quadratic equality constraint (4.13), the optimization problem can be converted to a Second Order

Cone Program (SOCP) defined over a convex feasible set [401]. Our numerical study shows that the non-zero duality gap issue [272] does not occur, which confirms the global optimality and exactness of the optimization-based benchmark.

$$\min_{\boldsymbol{X}} \sum_{(i,j)\in\mathcal{L}} C_e r_{ij} \ell_{ijt} + \sum_{i\in\mathcal{N}} \Big[C_v \left(u_{it} - 1\right)^2 + C_c \left|\bar{p}^g_{it} - p^g_{it}\right| \Big] \tag{4.8}$$

$$\text{s.t } \; P_{ijt} = \sum_{k:(j,k)\in\mathcal{L}} P_{jkt} + r_{ij}\ell_{ijt} + p^c_{jt} - p^g_{jt} \tag{4.9}$$

$$Q_{ijt} = \sum_{k:(j,k)\in\mathcal{L}} Q_{jkt} + x_{ij}\ell_{ijt} + q^c_{jt} - q^g_{jt} - q^{cap}_{j\tau} \tag{4.10}$$

$$u_{jt}/a^2_{ij\tau} = u_{it} - 2\left(r_{ij}P_{ijt} + x_{ij}Q_{ijt}\right) + \left(r^2_{ij} + x^2_{ij}\right)\ell_{ijt} \tag{4.11}$$

$$u_{1t} = \left(u^{ref} + tap^{reg}_{\tau} \times C^{reg}\right) \tag{4.12}$$

$$\ell_{ijt} = \left(P^2_{ijt} + Q^2_{ijt}\right)/u_{it}, \quad \forall (i,j) \in \mathcal{L} \tag{4.13}$$

$$0 \le p^g_{it} \le \bar{p}^g_{it}, -\bar{q}^g_{it} \le q^g_{it} \le \bar{q}^{gP}_{it} \quad \forall i \in \mathcal{N} \tag{4.14}$$

$$\boldsymbol{X} := \left(\boldsymbol{P}_t, \boldsymbol{Q}_t, \boldsymbol{p}^g_t, \boldsymbol{q}^g_t, \boldsymbol{u}_t, \boldsymbol{\ell}_t\right) \tag{4.15}$$

Note that the tap position variables $a_{ij\tau}$, $q^{cap}_{j\tau}$, and tap^{reg}_{τ} are taken from the last interval of the slow timescale VVC. In the future, we plan to further enhance the model predictive control (MPC)-based fast timescale VVC algorithm by taking the inverter degradation into account. This makes the baseline algorithm more consistent with the proposed reinforcement learning-based algorithm.

4.4 Two-timescale VVC using DDPG

4.4.1 Fast Timescale VVC as a Markov Decision Process

We briefly review the basics of the Markov decision process (MDP). An MDP can be defined as a tuple consists of a state space $\mathcal{S}$, an action space $\mathcal{A} = \Re^M$ (M is the dimension of the action space), an initial state distribution $p\left(s_1\right)$, a transition probability $p\left(s_{t+1}|s_t, a_t\right)$, and a reward function $R : \mathcal{S} \times \mathcal{A} \in \Re$. The agent interacts with the environment $\mathcal{E}$ according to some policy $\mu : \mathcal{S} \rightarrow A$ to generate trajectories of the form $s_1, a_1, r_1, \ldots, s_t, a_t, r_t, \ldots, s_T, a_T, r_T$, where $r_t = R(s_t, a_t)$. The return from a state is defined as the sum of discounted future reward $G_t = \sum_{i=t}^{T} \gamma^{(i-t)} R\left(s_i, a_i\right)$ with a discounting factor $\gamma \in [0, 1]$. The goal is to learn a policy which maximizes the expected return from the initial state $J = \mathbb{E}_{s \sim p(s_1)} \mathbb{E}_{\mu}[G_t | s_1 = s]$.

To formulate the fast timescale VVC problem as an MDP, the distribution system operator or controller is treated as the agent and the distribution network is treated as the environment. We define the state, action, and reward function as follows:

State The state consists of real and reactive power injection of inverters $\boldsymbol{p}_t^g, \boldsymbol{q}_t^g$, and loads $\boldsymbol{p}_t^c, \boldsymbol{q}_t^c$ at relevant nodes at time t, solar PV production potential of the inverters determined by solar irradiance and technical parameters of the respective PV systems $\bar{\boldsymbol{p}}_t^g$, voltage magnitude at each bus $|\boldsymbol{v}_t|$, and current tap positions of voltage regulating devices $tap^{reg}, tap^{tsf}, tap^{cap}$.

Action In the VVC strategy adopted in this chapter, the smart inverters are allowed to adjust both active and reactive power outputs. The active power provided by the smart inverter i can be expressed by $p^g_{it} = a_p \bar{p}^g_{it}$ where $a_p \in [0, 1]$ is a variable in the action space. It regulates the amount of active power curtailment.

Under the strategy with rectangular action space shown in Fig. 4.3(b), the reactive power injected/absorbed by inverter i is limited by the active power capacity of the inverter. It can be expressed by $|q^g_{it}| \leq \bar{q}^{gR}_{it}$ where $\bar{q}^{gR}_{it} = \sqrt{\bar{S}^2_i - (\bar{p}^g_{it})^2}$. We rewrite the equation as $q^g_{it} = a_q \bar{q}^{gR}_{it}$, where $a_q \in [-1, 1]$ is another variable in the action space. It controls the reactive power set point of the inverter.

Under the control strategy with polar action space shown in Fig. 4.3 (c), the reactive power injected/absorbed by inverter i is limited by the active power provided by inverter. It can be expressed by $|q^g_{it}| \leq \bar{q}^{gP}_{it}$ where $\bar{q}^{gP}_{it} = \sqrt{\bar{S}^2_i - (p^g_{it})^2}$. We rewrite the equation as $q^g_{it} = a_q \bar{q}^{gP}_{it}$ where $a_q \in [-1, 1]$.

Reward The reward received by the reinforcement learning agent consists of four terms as shown in (4.16): line loss, voltage violations, active power curtailment cost, and the inverter degradation cost. The line losses, voltage deviation losses, and the active power curtailment cost are formulated in the same way as in Section III-C. The inverters include power switching devices such as insulated gate bipolar transistors (IGBTs) and diodes. Change in the real and reactive power injection by the smart inverters leads to temperature swings in the switching components which can cause additional thermal stresses, ultimately leading to a reduction of the inverter lifetime. Therefore, we model the inverter degradation cost proportional to the change in the real and reactive power levels of the inverter in consecutive time steps. Let C_I be the inverter degradation cost (\$/W change in inverter real power and \$/VAR change in inverter reactive power) and $\mathcal{N}_r$ be the nodes with inverters, then the inverter degradation cost is expressed by $d_t = \sum_{i\in\mathcal{N}_r} C_I \left(\left| p^g_{i(t+1)} - p^g_{it} \right| + \left| q^g_{i(t+1)} - q^g_{it} \right| \right)$.

The reward at time t then can be written as follows:

$$\begin{aligned} r_t = -\sum_{(i,j)\in\mathcal{L}} C_e r_{ij} \ell_{ijt} - \sum_{i\in\mathcal{N}} C_v \left(u_{it} - 1\right)^2 \\ - \sum_{i\in\mathcal{N}_r} C_c \left| \bar{p}^g_{it} - p^g_{it} \right| - d_t \end{aligned} \tag{4.16}$$

4.4.2 Deep Deterministic Policy Gradient

The fast timescale VVC by smart inverters has a continuous and high dimensional action space. In addition, the complete distribution feeder parameters are not always available. Thus, we adopt the deep deterministic policy gradient (DDPG) algorithm [224], a model-free approach, to solve the fast timescale VVC problem. DDPG is an off-policy deep reinforcement learning algorithm with the actor-critic architecture and function approximators. As such, both policy and value functions are approximated by deep neural networks. The actor-network maintains a deterministic policy μ using a neural network parameterized by θ^μ. The input of the neural network is the state s and the output is a deterministic continuous action $a = \mu\left(s|\theta^\mu\right)$. To ensure exploration, noise sampled from a noise process η, e.g., an Ornstein-Uhlenbeck process [360] is added to the output: $\mu'\left(s_t\right) = \mu\left(s_t|\theta^\mu_t\right) + \eta$. The critic network approximates the corresponding Q function of the policy using the neural network parameterized by θ^Q. To improve the stability of learning, two target networks $Q'\left(s, a|\theta^{Q'}\right)$ and $\mu'\left(s|\theta^{\mu'}\right)$ are introduced to provide stable learning targets. As such, the update equations of the network are not interdependent on the values calculated by the network itself and therefore are not prone to divergence.

To further stabilize the training process, the experience tuples (s_t, a_t, r_t, s_{t+1}) are stored in a replay buffer. Then, random mini-batches of experience are sampled from the replay buffer while updating the value and policy networks. Since the target policy is deterministic, the Bellman equation can be expressed as follows:

$$Q^{\mu}\left(s_t, a_t\right) = \mathbb{E}\left[R\left(s_t, a_t\right) + \gamma\left[Q^{\mu}\left(s_{t+1}, \mu\left(s_{t+1}\right)\right)\right]\right] \tag{4.17}$$

The training of the critic network is based on minimizing the following loss function using batches of experiences with N_m number of transitions.

$$L = \frac{1}{N_m}\sum_i \left(y_i - Q\left(s_i, a_i\right)|\theta^Q\right)^2 \tag{4.18}$$

$$y_i = R\left(s_i, a_i\right) + \gamma Q'\left(s_{i+1}, \mu'\left(s_{i+1}|\theta^{\mu'}\right)|\theta^{Q'}\right) \tag{4.19}$$

The parameters of the actor network are updated using the critic network and the policy gradient algorithm with batches of experience with N_m transitions.

$$\nabla_{\theta^{\mu}} J \approx \frac{1}{N_m}\sum_i \nabla_a Q\left(s, a|\theta^Q\right)|_{s=s_i, a=\mu(s_i)} \nabla_{\theta^{\mu}}\mu\left(s|\theta^{\mu}\right)|_{s_i} \tag{4.20}$$

4.4.3 Summary of the Two-timescale VVC Algorithm

First, the slow timescale control problem is solved for each hour τ using (4.1)-(4.7) to determine the tap positions of the voltage regulators, OLTCs, and switchable capacitor banks. Within the interval τ, the switching decisions of these devices are kept fixed. Now, the fast timescale control of the smart inverters is performed for each time segment t within

Algorithm 3 Two-timescale Volt-VAR Control scheme

```
Input: Initialize actor network parameters $\theta^{\mu}$, critic network parameters $\theta^{Q}$, and empty
    replay buffer $D$. Initialize a random process $\eta$ for action exploration
Initialize target network parameter $\theta^{\mu'} \leftarrow \theta^{\mu}, \theta^{Q'} \leftarrow \theta^{Q}$
for $t = 1 \ldots T \times \mathcal{T}$ do
    Fix the tap positions of the conventional voltage regulating devices at the solution
        obtained from (4.1)-(4.7) at the corresponding hour $\tau$
    Obtain load, solar PV generation and voltage magnitude information at time $t$ to
        form state vector $s_t$.
    Feed the state vector into the actor network to generate suggested actions, i.e., the
        real and reactive power outputs of inverters. Select action $a_t = \mu\left(s_t|\theta^{\mu}\right) + \eta_t$ according
        to current policy and exploration noise.
    Execute $a_t$ in the environment.
    Gather information for the next state $s_{t+1}$. Calculate the reward $r_t$.
    Store $(s_t, a_t, r_t, s_{t+1})$ in replay buffer $\mathcal{D}$
    Randomly sample a batch of $N_m$ transitions from $\mathcal{D}$, $B = \{(s_i, a_i, r_i, s_{i+1})\}$
    Compute target $y_i$ using (4.19)
    Update Q-function by minimizing loss in (4.18)
    Update policy by one step of gradient ascent using (4.20)
    Update target networks with $\theta^{Q'} = \rho\theta^{Q} + (1-\rho)\theta^{Q'}$ and $\theta^{\mu'} = \rho\theta^{\mu} + (1-\rho)\theta^{\mu'}$
end for
```

τ. The corresponding distribution system voltage at each bus along with the load and PV generation and time stamp data is utilized to assemble the state vector s_t for the DDPG training. The state vector is provided to the agent which generates the suggested actions, i.e., the real and reactive power outputs of the inverters. The suggested actions are executed in the environment and the agent gathers the state variables from the environment which transitions to the next time period s_{t+1}. The transition (s_t, a_t, r_t, s_{t+1}) is stored. The actor and critic network is updated following Section 4.4.2 utilizing target network and experience replay till the terminal state is reached. After completing the training, the trained DDPG agent can be utilized to determine the real and reactive power setpoints of the smart inverters for the fast timescale VVC. The detailed process for the two-timescale

VVC is shown in Algorithm 1.

4.5 Numerical Study

The performance of the proposed two-timescale VVC in Algorithm 1 is tested on a modified IEEE 34 node test feeder.

4.5.1 Simulation Setup

As shown in Fig. 4.1, the IEEE 34-bus test feeder has a voltage regulator at node 800. There are two OLTCs connecting node 814 to node 850 and node 852 to node 832 respectively. Two capacitors are placed at node 844 (100 kVar) and node 847 (150 kVar). Three solar PV systems with nameplate capacity 22 KW, 67 KW, and 133 KW are added to the feeder at the nodes 840, 862, and 838 respectively. The inverters are not oversized. The solar PV penetration level of the feeder is 120%. To illustrate the algorithm's capability for active power curtailment and reactive power absorption under low load and high PV production conditions, we double the line impedances so that the benefits of active power curtailment and reactive power absorption are more pronounced.

All voltage regulators and on-load tap changers have 11 tap positions, which correspond to turns ratios ranging from 0.95 to 1.05. The capacitors can be switched on/off remotely and the number of 'tap positions' is treated as 2. In the initial state, the turns ratios of voltage regulators and on-load tap changers are 1 and the capacitors are switched off. The electricity price C_e is assumed to be \$40/MWh. The operating cost per tap change is set to be \$0.1 for all devices. The penalty coefficient C_V is set as \$1/$volt$. The inverter degradation cost C_I is set to be \$0.04/MW. One year of energy consumption and solar PV generation data from Austin, Texas in 2019 is obtained from the Pecan Street Dataset [166]. The solar PV generation data is scaled according to the corresponding nameplate capacity of the solar PV systems. Five weeks of data from the 9th to 13th week is used for training, in which the agent interacts with the environment and updates its policy and value networks. One week of data for week 14 is used for out-of-sample testing, in which the trained reinforcement learning agent takes control actions without further updating its neural networks.

4.5.2 Setup of the Benchmark and Our Proposed Algorithms

Under the model-free reinforcement learning-based control framework, we compare our proposed DDPG-based smart inverter control with polar action space with two other benchmark reinforcement learning algorithms, which have a reactive power control strategy and a real and reactive power control strategy with a rectangular operating space, respectively. We consider the following three baseline control scenarios under the model-based control assuming the accurate and complete distribution network model is available.

1. Baseline 1: No Volt-VAR control is executed.

2. Baseline 2: Only slow timescale VVC is executed following the method in Section 4.3.2. The smart inverters operate at unity power factor with no reactive power injection/absorption or active power curtailment.

3. Baseline 3: Slow timescale VVC is executed following the method in Section 4.3.2. The smart inverters are controlled following the method in Section 4.3.3.

Table 4.1: Hyperparameter settings for DDPG

Parameters	Value
Size of hidden layers	$(512, 512)$
Activation function	ReLU
Batch size	100
Discount factor	0.99
Learning rate actor and critic network	0.0001
Epoch	2
Start steps before running policy	100
Standard deviation for exploration noise	0.4

The slow timescale VVC is formulated as an MINLP problem and solved by the BONMIN solver in the OPTI toolbox [85] in MATLAB. The optimization-based fast timescale inverter control in baseline scenario 3 is implemented using the CVX toolbox [140] in MATLAB after the convex relaxation is performed. The setup of our proposed two-timescale VVC scheme with three different action space are discussed below:

1. DDPG with only reactive power control: Slow timescale VVC is executed following Section III-B. The smart inverters are controlled using DDPG with only adjustable reactive power setpoint as depicted in Fig. 4.3(a).

2. DDPG with rectangular action space: Slow timescale VVC is executed following Section 4.3.2. The smart inverters are controlled using DDPG with rectangular action space for real and reactive power setpoints as depicted in Fig. 4.3(b).

3. DDPG with polar action space: Slow timescale VVC is executed following Section 4.3.2. The inverters are controlled using DDPG with polar action space for real and reactive power setpoints as depicted in Fig. 4.3(c).

Table 4.2: Comparison of the operation costs of the proposed two-timescale VVC schemes along with three baseline scenarios in the test dataset

Operational cost ($)	Baseline1 (no VVC)	Baseline2 (slow time scale VVC)	Baseline3 (optimization based two timescale VVC)	DDPG and reactive power based two timescale VVC	DDPG based two timescale VVC with rectangular action space	DDPG based two timescale VVC with polar action space
Switching	0.00	38.20	38.20	38.20	38.20	38.20
Line loss	33.78	81.30	127.47	169.40	150.60	115.79
Voltage	3264.66	1118.60	352.73	436.12	410.18	414.47
APC	0.00	0.00	14.38	0.00	13.05	16.95
Inverter	0.75	0.75	4.16	4.10	2.80	2.37
Total	3299.20	1238.86	536.96	648.44	614.85	587.78

The feedforward neural networks of both actor and critic networks have 2 fully connected hidden layers of 512 neurons each. At the start of the training, uniform-random actions are selected before running the real policy to help exploration. The training of the agent is performed for 2 epochs. An epoch refers to one cycle through the full training dataset. The hyperparameter settings for the DDPG algorithm of all three control strategies are provided in Table 4.1.

4.5.3 Result and Analysis

To evaluate the performance of the proposed reinforcement learning-based VVC methods, we compute the line loss, voltage violation cost, active power curtailment cost (APC), switching cost of the conventional voltage regulating devices, inverter degradation cost, and the total operational cost. A lower total operational cost indicates a better control performance in voltage regulation. Table 4.2 shows the operational cost comparison of three variations of the proposed reinforcement learning-based two-timescale VVC algorithm with three model-based baseline control scenarios on the test dataset. The result is based on the trained model, which achieves the best performance out of 20 random experiments in the training dataset.

It can be observed from Table 4.2 that although the slow timescale VVC (Baseline 2) provides voltage regulation service, it is not adequate as the rapid change in the solar PV production within each hour causes high voltage violation cost. As shown in columns 4-7 of Table 4.2, all of the two-timescale VVC schemes achieved considerably lower total operational costs. In particular, among the DDPG-based smart inverter control schemes, the proposed two-timescale VVC with polar action space yields the lowest operational cost. Although the slow timescale VVC controller is not aware of the reactive power from the smart inverter in the coming hour, the formulation still improves the baseline without leading to the canceling effect of the two controllers in different timescales.

The DDPG-based two-timescale VVC with polar action space has a larger reactive power adjustment range than that of the control strategy with rectangular action space as shown in Fig 4.3. Thus, the reinforcement learning-based control with polar action space provides better voltage regulation service and consequently lower operation costs. Although the model-based fast timescale inverter control together with the slow timescale control offers the lowest operation cost, it requires complete and accurate knowledge of the secondary distribution circuit model and parameters. The DDPG-based fast timescale control on the other hand is model-free and produces relatively low total operational cost. The cost for active power curtailment and inverter degradation during the six-week training

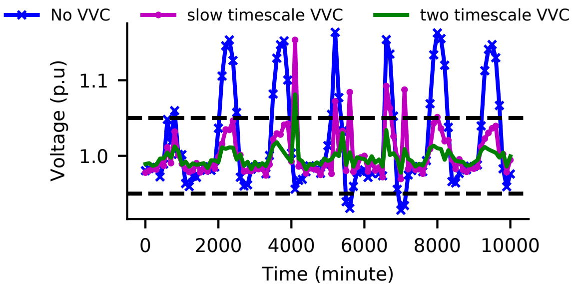

Figure 4.4: Comparison of voltage deviations at node 838 for three VVC schemes

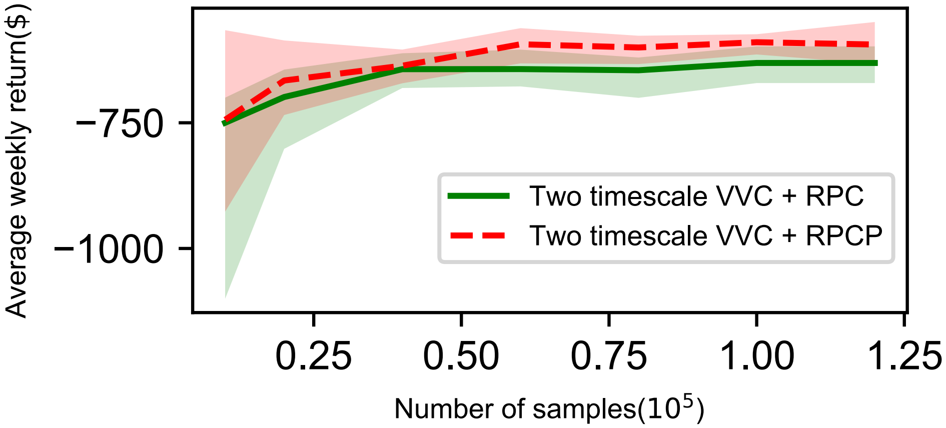

Figure 4.5: AVR vs number of samples for the two-timescale VVC schemes with polar action space and with only adjustable reactive power

period is \$633 for the customers of the 34-bus distribution network as opposed to \$91.71 if the optimization from Baseline 3 is implemented. Such training costs are inevitable in RL-based VVC methods involving smart inverter control as there are exploratory actions.

Next, we compare the voltage profiles of two baseline control scenarios and our proposed DDPG-based VVC with polar action space. The voltage magnitude time series of node 838 corresponding to no VVC, only slow timescale VVC, and the proposed two-timescale VVC with polar action space are shown in Fig. 4.4. Node 838 is selected for the comparison because it experiences the worst voltage violation when no VVC is employed. It can be seen that our proposed DDPG-based VVC with polar action space significantly improves the voltage regulation performance. Furthermore, it is capable of maintaining the voltage within 1 ± 0.05 p.u. for almost the entire operating week.

Finally, the RL algorithm employed to solve the VVC problem should be sample efficient and scalable. We demonstrate the sample efficiency of the proposed DDPG-based two-timescale VVC algorithm. The number of training samples collected versus the average weekly return (AVR) on the testing weeks are shown in Fig. 4.5. The AVR is defined as the summation of all the components of the reward function accumulated over the testing period. The middle curve shows the mean AVR averaged over 10 independent runs. The light-colored region corresponds to the error bounds. Fig. 4.5 also demonstrates the sensitivity of the test set results to the training sequence. It is observed that with about three weeks of training data, the algorithm is able to learn a very effective VVC policy. It should be noted that in Fig. 4.5, each point on the horizontal axis corresponds to a “training set”, which consists of the data from the beginning up to that point, whereas the testing dataset always starts from week 14. Thus the latter does not immediately follow the end of the training dataset. This further shows the effectiveness of the algorithm on out-of-sample data. In addition, as shown by the error bound, these results are consistent across different random initialization and training sessions.

4.6 Chapter Summary

A two-timescale Volt-VAR control scheme that does not depend on accurate secondary feeder models is proposed in this chapter. In the slow timescale control, tap positions of conventional VVC devices are determined by a model-based controller. On the fast timescale, a DDPG-based algorithm is developed to determine the real and reactive power setpoints of the smart inverters. The proposed algorithm is relatively safe to implement in the real world as the slow timescale VVC devices are set according to an optimization-based approach; only the smart inverters are allowed to perform exploratory actions. As such, there is no severe voltage violation during the training period. The proposed DDPG-based smart inverter control strategy with polar action space outperforms the strategy with the rectangular action space and the strategy with only adjustable reactive power. It is capable of maintaining the voltage within a reasonable range. In addition, it is sample efficient and only requires three weeks of training data to achieve near-optimal results.

Chapter 5

Reinforcement Learning-based Two Timescale Volt Var Control in Power Distributions Systems

5.1 Introduction

In the past decade, there has been an increasing penetration of renewable resources such as solar photovoltaic (PV) systems in power distribution networks. Globally, The share of renewables in electricity supply rose from 19% in 2008 to 26% in 2019 [21]. The global roof-mounted solar photovoltaic (PV) capacity is projected to be between 40.2 GW and 83.7 GW in 2023 [46]. Twenty-seven countries of the European Union installed 25.9 gigawatts of new solar capacity in 2021, compared to 19.3 gigawatts in 2020 [315]. In the United States, Solar photovoltaics (PV) is projected to constitute 46% of total renewable generation by 2050, increasing from only 13% in 2018 [103]. In 2017, developing countries accounted for 63% of global investment in renewable energy [31]. Consequently, distributed energy resources (DERs) including solar, wind turbines, microgrids, battery storage, electric vehicles (EVs), and load controlled by demand response (DR) has been growing in the distribution network. The growth in volume and diversity of DERs and responsive loads is transforming the operation of power systems and the design of electricity markets [372, 47, 48]. Energy consumptions from smart buildings can be coordinated across the smart grid together with other energy loads and power plants with the help of smart meters and two-way communication systems [382, 276].

While the DERs provide benefits for electricity systems, customers, and the environment, they also create new challenges for the distribution network [372] and microgrids [86, 402]. The challenges include capacity constraints, power quality issues such as voltage violations, adverse impacts on protection systems due to bidirectional power flow, and reduced hosting capacity [95]. Specifically, high solar PV penetration in the distribution network creates serious operation challenges such as over-voltages and increased line losses [254]. Moreover, the intermittent nature of solar energy due to cloud coverage and shading can cause fast, uncertain, and large voltage fluctuations in the distribution grid [254]. Thus, maintaining system voltages with acceptable limits in the distribution grid with high solar PV penetration is a major challenge [100].

Controlling the distributed energy resources to increase grid flexibility, reliability, and hosting capacity by coordinating, optimizing, and dispatching the assent in a cost-efficient manner is still an emerging topic for utilities. Pacific gas and electric company

(PG&E) has been developing a software platform called distributed resource management system (DERMS) to control the distributed energy resources [30, 95]. Southern California Edison (SCE) is designing an advanced distribution Management system (ADMS) coupled with the DER management system (DERMS) to replace their existing Distribution Management System (DMS) [19]. Both of the utilities have run pilot projects and proof-of-concept demonstrations [30, 95, 19]. The technology is still in its nascent stage and not readily available to comprehensively address utility requirements. However, the DER management systems developed by the utilities are model-based. Our proposed reinforcement learning-based Volt-VAR control algorithm addresses the limitations common to the model-based methods.

The implementation of volt-VAR control (VVC) to reduce voltage violations and network losses in the power distribution system is an integral part of DER management systems. In the conventional VVC, the operations of voltage regulating devices such as step voltage regulators, on-load tap changers (OLTC), and switchable capacitor banks are coordinated to achieve this goal. Both centralized and decentralized model-based optimization methods are widely adopted for conventional VVC [304, 22, 245, 278]. These control approaches determine the optimal hourly discrete setpoints for the voltage regulating devices by solving an optimal power flow (OPF) problem. However, these mechanical devices are usually operated at a slow-timescale e.g. hourly due to the wear and tear associated with mechanical switching. As a result, conventional VVC is not adequate for distribution systems with fast and uncertain voltage fluctuations associated with the cloud-induced fluctuation of solar PV generation. Moreover, solving the optimization-based VVC requires solving mixed-integer programming problems which can be NP-hard [301]. The computational complexity of this formulation grows exponentially with the network size and the number of VVC devices. Relaxation techniques such as McCormick relaxations [256], linearization techniques [59], and semi-definite programs [301] can be employed to formulate the problem as a convex OPF problem. However, these approaches can be computationally expensive and do not guarantee a global optimal solution.

Smart solar PV inverters, on the other hand, can provide fast and continuous active and reactive power control with low operational costs. They are equipped with two-way communications which allow remote control systems to change inverter setpoints. As a result, smart inverters can be operated at a fast-timescale e.g. every minute for VVC according to the IEEE 1547a-2020 standard [18] to mitigate frequent voltage variations in distribution feeders with high solar PV penetration. Model-based optimization approaches for smart inverter control can be broadly divided into three categories: centralized [111, 405, 87], distributed [355, 88, 264], or local control approaches [353, 109]. These control approaches determine the reactive power setpoints or both real and reactive power setpoints of PV inverters by solving an OPF problem. The nonlinear DistFlow [36] model is used for distribution system OPF formulations. Convex relaxation techniques such as second-order cone program can be applied to formulate and solve the nonconvex optimization problem [111]. Other local control approaches calculate the reactive power setpoint of smart inverters using droop control [175].

To coordinate the operation of VVC devices at different timescale, researchers developed two-timescale model-based VVC by augmenting the slow-timescale VVC of conventional voltage regulating devices with fast-timescale smart inverter control [300, 112, 396, 218]. References [112] and [396] formulate the VVC as a centralized optimization problem. The conventional VVC devices include capacitor banks [396, 112] and OLTCs [396, 218]. Reference [179] proposes bi-level Volt-VAR optimization method to achieve CVR benefits. Their proposed framework is based on mathematical optimization and decomposes the mixed-integer nonlinear programming (MINLP) into a mixed-integer linear programming (MILP) and a nonlinear programming (NLP) problem.

There is one major drawback of the existing model-based VVC methods. The model-based optimization approaches rely on accurate and complete distribution network topology and parameter information [375, 120, 130, 374]. However, it is difficult for regional electric utilities to maintain accurate reliable network models for the primary and secondary feeders. Especially, the secondary feeders' phase connection information is usually not accurate [121]. To circumvent this problem, reference [32] proposes an extremum seeking (ES) control algorithm for VVC in the distribution network by introducing sinusoidal perturbations to extract gradient information. Data-driven approaches can also eliminate the need for accurate distribution network topology and parameter information. Reference [332] uses multiple linear regression to determine a function that relates a set of local features to the optimal reactive power injection for VVC. Support vector machine-based methods have been developed for slow-timescale [308] and fast-timescale [177] VVC. Among the data-driven approaches, deep reinforcement learning (DRL) is suitable for control and optimization problems. Deep reinforcement learning can learn optimal VVC control strategies from data by learning which VVC actions yield the most return by trying them. Researchers have developed deep reinforcement learning-based algorithms for slow-timescale VVC problems [371, 393] and the fast-timescale smart inverter control problem [397, 228, 219]. Reference [371] proposes a constrained soft actor-critic-based Volt-VAR control algorithm to determine the optimal tap settings of traditional Volt-Var control devices in a model-free manner. Reference [393] proposes a batch reinforcement learning algorithm to determine the optimal tap setting of load tap changers. In the fast timescale, [397] proposes a fully distributed multi-agent-based reinforcement learning method for optimal reactive power dispatch of smart inverters. Reference [228] utilizes a multi-agent constrained soft actor-critic (MAC-SAC) reinforcement learning algorithm to coordinate the reactive power dispatch of multiple smart inverters. Reference [219] develops a DDPG based volt-VAR control algorithm for optimal reactive power dispatch of multiple smart inverters.

Data-driven approaches can be utilized to solve the two-timescale VVC problem. A two-timescale VVC framework is developed in [400]. For the slow-timescale, deep Q-learning is used to determine the switching schedule of capacitors. For the fast-timescale, an optimization-based approach is adopted to control the smart inverters. However, the model of the secondary feeders is still needed in the optimization-based fast-timescale control. In reference [229], a two-stage deep reinforcement learning method consisting of an offline and online stage in the learning process is proposed for inverter-based Volt-VAR control in active distribution networks. The operations of the slow-timescale VVC devices are scheduled in the offline stage in a model-based manner using theoretical parameters to build the approximate active distribution network model. An offline agent robust to the model mismatch is trained using a highly efficient adversarial reinforcement learning algorithm. However, the existing data-driven approaches for two-timescale VVC still use some components of the power distribution system model, which may not be available in practice. Another two-timescale data-driven VVC algorithm is developed in [187]. The deep deterministic policy gradient (DDPG) is used to learn the control policy for the fast-timescale VVC, while the primary feeder's slow-timescale VVC is done by a model-based approach. It would be advantageous to make the two-timescale VVC framework entirely model-free.

Reference [63] designed a novel physical-model-free two-timescale voltage control framework for active distribution systems. In the framework, the network is partitioned into several sub-regions, each defined as an agent. In the fast timescale, PV inverters' scheduling is modeled as Markov games and solved by a multi-agent soft actor-critic (MASAC) algorithm. In the slow timescale, OLTCs and switched capacitors are coordinated by a single agent-based SAC algorithm.

The agents in two different timescales are coordinated by the reward signal. However, the framework has two limitations. First, as the fast timescale policy is not fixed, the environment becomes non-stationary from the perspective of the slow-timescale agent. This violates the stationarity and Markovity assumptions underlying reinforcement learning and prevents the straightforward use of experience replay.

To address this problem, we propose to solve this non-stationarity problem by extending the use of centralized training and decentralized execution (CTDE) framework to the two-timescale RL setting. Second, reference [63] does not include the degradation cost of PV inverter into the objective of VVC problems. If the degradation costs of the PV inverters are not considered, there is no dependency between the reactive power control actions of the smart inverters. For this reason, the scheduling of the smart inverters at the fast timescale could be simply formulated as a contextual multi-armed bandit problem [237]. Our framework considers the inverter degradation cost thus justifies the MDP formulation.

In this paper, we take the next logical step to our previous paper [187]. We fill the knowledge gap by developing a two-timescale multi-agent reinforcement learning-based VVC algorithm, which does not rely on any primary or secondary feeder information. When we replace the model-based slow timescale VVC with DRL-based VVC, the following challenges arise: We need to design a deep reinforcement learning-based algorithm that is capable of producing actions at two different timescales. If a single deep learning agent is used, it would be challenging to ensure that the slow timescale control actions do not change within the hour. The DRL-based algorithm used by the sole agent should be capable of producing discrete actions at the slow timescale and continuous actions at the fast timescale. If two different deep reinforcement learning agents are employed, it is to be ensured that the learning environment is stationary for the agents. Additionally, the agents should have information about the actions taken by the other to learn the optimal policy. To tackle these challenges, we propose two hierarchically arranged sets of policies that are learned and executed at two different timescales. The two policies interact with each other via a communication medium and must be learned simultaneously. In the slow-timescale, a multi-agent soft actor-critic (MASAC)-based approach is adopted to determine the tap positions of voltage regulators, OLTCs, and switchable capacitor banks [62]. In the fast-timescale, a deep deterministic policy gradient (DDPG)-based algorithm is employed to determine the setpoints of the reactive power of smart inverters [224]. We design a communication scheme for the reinforcement learning agents in two different timescales to exchange information and learn the control policy concurrently and efficiently. The unique contributions of this paper are summarized below.

- We develop an entirely model-free reinforcement learning-based two-timescale VVC for distribution networks, which does not rely on any primary or secondary feeders' topology or parameter information. The hierarchically organized slow-timescale and fast-timescale reinforcement learning agents communicate with each other to learn the optimal control policies concurrently and efficiently.
- The proposed fast-timescale controller carefully considers the degradation cost of smart inverters in the sequential decision-making process of the VVC problem. As a result, the Volt-VAR control problem includes dependencies between actions at different times. Thereby justifies the use of the full MDP formulation.

The rest of the paper is organized as follows. Section 5.2 presents the overall framework of the two-timescale VVC problem. Section 5.3 provides the problem formulation of the slow-timescale VVC and fast-timescale smart inverter control. Section 5.4 presents the technical methods, which include DDPG, MASAC, and the proposed two-timescale VVC algorithm. Section 5.5 shows the numerical study results. Finally, Section 5.6 states the conclusions.

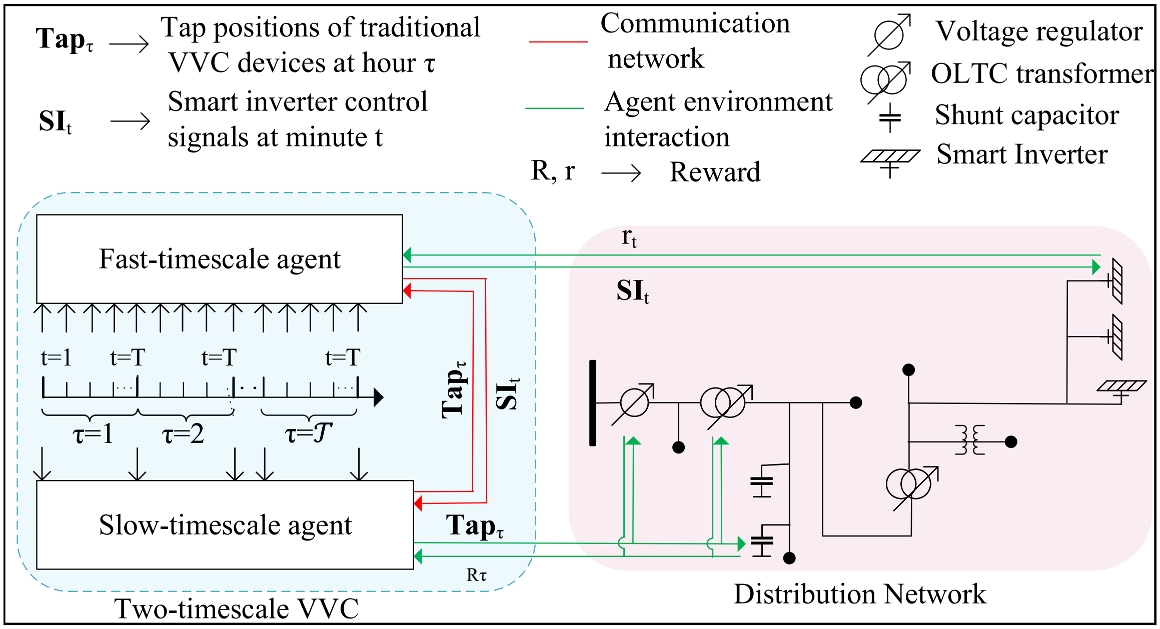

Figure 5.1: The overall framework for the proposed reinforcement learning-based two-timescale VVC

5.2 Two-timescale VVC Framework

We consider a power distribution system with both conventional voltage-regulating devices and smart inverters. The smart inverters control reactive power setpoints of solar PV systems. The overall framework of the two-timescale VVC is shown in Fig. 5.1. The framework is composed of a slow-timescale VVC subproblem and a fast-timescale VVC subproblem. Both are solved by deep reinforcement learning-based algorithms. In particular, two separate agents are set up for the slow- and fast-timescale subproblems, which communicate with each other to cooperatively achieve the global objective. The conventional voltage regulating devices are operated at a slow-timescale on an hourly basis. Within each hour, the tap and switching positions of these voltage regulating devices are kept fixed and used as part of the state space of the fast-timescale agent. In the fast-timescale VVC, the reactive power setpoints of smart inverters are determined for every minute t to mitigate voltage violations caused by rapid fluctuations in the solar PV generation. The smart inverter dispatch schedule, the tap positions, and switching schedules of the voltage regulator, OLTCs, and capacitor banks are determined jointly with a hierarchically arranged multi-agent reinforcement learning algorithm. It utilizes a soft actor-critic algorithm in the slow timescale and a deep deterministic policy gradient algorithm in the fast-timescale. Rewards collected within an hour by the fast-timescale agent are used as part of the reward collected by the corresponding slow-timescale agent. The two-timescale deep reinforcement learning-based VVC algorithm is presented in Section 5.4.2.

5.3 Problem Formulation

In this section, we first introduce the notations and problem setup. Then we discuss the mathematical formulation of the two-timescale VVC problem. Finally, we formulate the VVC problem as a multi-timescale Markov decision process (MDP).

5.3.1 Notations and Problem Setup

We consider a radial distribution feeder of N buses represented by a graph $\mathcal{G} := (\mathcal{N}, \mathcal{L})$, where $\mathcal{N} := \{1, \ldots, N\}$ is the set of nodes and $\mathcal{L} := \{(m, n) \subset \mathcal{N} \times \mathcal{N}\}$ is the collection of edges representing distribution line segments. Each line's resistance and reactance is denoted as r_{ij} and x_{ij} respectively. Let v_i be the complex voltage phasor at node $i \in \mathcal{N}$ and $u_i = |v_i|^2$. Let I_{ij}, P_{ij}, and Q_{ij} be the complex current, real and reactive power flowing from node i to node j, respectively. $\ell_{ij} = |I_{ij}|^2$ is the current magnitude squared.

In this paper, we consider N_r smart inverters and N_c conventional voltage regulating devices such as voltage regulators, OLTCs, and capacitor banks as the VVC devices. A voltage regulator is placed at the reference bus. Switchable capacitor banks and OLTCs are installed at different locations on the feeder. Each of the voltage regulators and OLTCs has K discrete tap positions with a step size of C^{reg} and C^{tsf} respectively corresponding to the change in turns ratios. The switchable capacitor banks have on/off positions. These devices are operated at a slow-timescale e.g. every hour τ. Let tap_τ^{reg} and tap_τ^{tsf}, and tap_τ^{cap} indicate the tap position of the voltage regulators, OLTCs, and the switch status of the capacitor banks at time τ, respectively. $\boldsymbol{Tap}$ groups them all.

The reactive power setpoints of the smart inverters are determined at a fast-timescale, e.g. every minute t, to mitigate the frequent voltage violations caused by the highly intermittent solar PV generation. Let $\mathcal{N}_r$ be the nodes with smart inverters. Let p_i^g and q_i^g be the real and reactive power generation from the smart inverter connected solar PV system at node i, and p_i^G and q_i^G be the total real and reactive power generation from the solar PV systems and switchable capacitors. Let $\bar{p}_{it}^g$ be the available solar PV production at time t for smart inverter i, which is determined by solar irradiance and the smart inverters' nameplate capacity $\bar{S}_i$.

Let p_i^c and q_i^c be the real and reactive power demand at node i; $p_i + jq_i$ be the net complex power injection at node i where $p_i \coloneqq p_i^G - p_i^c$ and $q_i \coloneqq q_i^G - q_i^c$. At any time t, the real and reactive power generation from smart inverters, electric demand $p_{it}^g, q_{it}^g, p_{it}^c, q_{it}^c$, and the settings of voltage regulators, OLTCs, and capacitor banks determine the voltages and power flows on the distribution network. In the next subsection, we introduce the formulation of the optimization-based VVC method.

5.3.2 Optimization-based Volt-VAR Control Methods

This subsection formulates the two-timescale VVC as an optimization problem, to clarify the control objective and act as a baseline algorithm for this study.

Slow-Timescale VVC Using Voltage Regulation Devices

The slow-timescale VVC at the beginning of each hour τ is constructed as a model predictive control (MPC) problem [61]. The tap positions at the current hour τ are determined in such a way that it minimizes the operational cost of the distribution network over a time horizon τ_h while satisfying the operational constraints at every hour. The DistFlow equations are of the form $g_s(\boldsymbol{X}) = \boldsymbol{b}$. The operational cost has three components: line real power loss, $J_{L,\tau} := \sum_{(i,j)\in\mathcal{L}} C_e r_{ij} \ell_{ij\tau}$, switching cost due to the absolute change in tap position of the N_c number of VVC devices between consecutive time steps, $J_{Tap,\tau} := \sum_j^{N_c} C_{Tap} |\boldsymbol{Tap}_{j,\tau} - \boldsymbol{Tap}_{j,\tau-1}|$, and the voltage violation cost when the voltage magnitude is not within the desirable range:

$$J_{V,\tau} = \begin{cases} C_V (u_{i\tau} - 1)^2 & \text{if } |v_i| < 0.95 \text{ or } |v_i| > 1.05 \\ 0 & \text{otherwise} \end{cases} \tag{5.1}$$

Here, C_e, C_v and C_{Tap} are electricity price ($\$/MWh$), voltage violation cost ($\$/volt$) and switching cost (\$/tap change) respectively. A voltage violation cost dependent on the magnitude of the voltage violation is chosen instead of a non-dimensional value or voltage deviation cost so that the distribution network can tolerate small voltage violations and eventually arrive at an overall lower operational cost. The MPC-based slow-timescale VVC is formulated as a mixed-integer nonlinear programming (MINLP) problem as (5.2)-(5.3).

$$\min_{\boldsymbol{Tap}_{\tau:\tau+\tau_h}} \sum_{\tau}^{\tau+\tau_h} \left(J_{L,\tau} + J_{V,\tau} + J_{Tap,\tau}\right) \tag{5.2}$$

$$\text{s.t. } \boldsymbol{g}_s\left(\boldsymbol{X}\right) = \boldsymbol{b}, \quad \boldsymbol{X}_l \leq \boldsymbol{X} \leq \boldsymbol{X}_h \tag{5.3}$$

$$\boldsymbol{X} := \left(\boldsymbol{P}_{\tau:\tau+\tau_h}, \boldsymbol{Q}_{\tau:\tau+\tau_h}, \boldsymbol{u}_{\tau:\tau+\tau_h}, \boldsymbol{\ell}_{\tau:\tau+\tau_h}, \boldsymbol{Tap}_{\tau:\tau+\tau_h}\right)$$

However, the solution is not globally optimal because the voltage violation cost is highly nonlinear. Therefore, the slow timescale problem cannot be easily relaxed into a mixed-integer second-order cone program (MISOCP). Since the convex relaxation cannot be performed easily, it is difficult to obtain the global optimal solution. However, it suffices as a baseline for our purpose.

Fast-Timescale VVC Using Smart Inverters

Smart inverters are controlled to absorb or inject power. The k-th solar PV inverter has a maximum apparent power capability $\bar{S}_k$. The active power output is set at the available solar PV production potential. The reactive power output is limited by the inverter rating. If the inverter is not oversized, then the smart inverter can not provide reactive power compensation when $\bar{p}_{kt}^{g} = \bar{S}_k$. The entire inverter rating can be utilized to supply reactive power when no active power is produced. The set of smart inverter's operating points F_k^{RPC}

is defined as:

$$F_k := \left\{ \left(p^g_{kt}, q^g_{kt}\right) \middle| p^g_{kt} = \bar{p}^g_{kt}, |q^g_{kt}| \leq \sqrt{\bar{S}_k^2 - (\bar{p}^g_{kt})^2} \right\} \tag{5.4}$$

The MPC-based fast-timescale VVC is performed at every time slot t within each interval τ. The tap positions of the conventional VVC devices are determined at the start of the hour τ by the slow-timescale VVC and kept fixed within the interval τ. The optimal setpoints of the smart inverters are determined at every minute t so that the operational cost of the distribution network over a time horizon t_h is minimized while satisfying the operational constraints at every minute.

In addition to line loss and voltage violation, the operational cost includes the inverter degradation cost. Changes in the reactive power injection by the smart inverters leads to temperature swings in the power switching devices such as insulated gate bipolar transistors (IGBTs) and diodes in the smart inverter. This can cause additional thermal stress in the inverter which ultimately reduces the inverter lifetime [334, 29]. Therefore, we model the inverter degradation cost proportional to the change in the reactive power levels of the inverter in consecutive time steps. If C_I is the inverter degradation cost (\$/watt change in inverter power), then the inverter degradation cost is expressed by $J_{I,t} := \sum_{i \in \mathcal{N}_r} C_I \left(\left| p^g_{i(t+1)} - p^g_{it} \right| + \left| q^g_{i(t+1)} - q^g_{it} \right| \right)$. The MPC-based fast-timescale VVC is formulated as follows:

$$\min_{\boldsymbol{q}^{g}_{t:t+t_h}} \sum_{t}^{t+t_h} \left(J_{L,t} + J_{V,t} + J_{I,t}\right) \tag{5.5}$$

$$\text{s.t. } \boldsymbol{g}_f\left(\boldsymbol{X}\right) = \boldsymbol{b}, \quad \boldsymbol{X}_l \leq \boldsymbol{X} \leq \boldsymbol{X}_h \tag{5.6}$$

$$\boldsymbol{X} := \left(\boldsymbol{P}_{t:t_h}, \boldsymbol{Q}_{t:t+t_h}, \boldsymbol{p}^{g}_{t:t+t_h}, \boldsymbol{q}^{g}_{t:t+t_h}, \boldsymbol{u}_{t:t+t_h}, \boldsymbol{\ell}_{t:t+t_h}\right) \tag{5.7}$$

Again, the solution is not globally optimal. However, it suffices as a baseline as the proposed Volt-VAR control algorithm does not provide a lower operational cost than the optimization-based VVC algorithm even with a local solution.

5.3.3 Formulate Volt-VAR Control as a Markov Decision Process

We briefly review the basics of the Markov decision process (MDP). An MDP can be defined as a tuple consists of a state space $\mathcal{S}$, an action space $\mathcal{A} = \Re^{M}$ (M is the dimension of the action space), an initial state distribution $p\left(s_1\right)$, a transition probability $p\left(s_{t+1}|s_t, a_t\right)$, and a reward function $R : \mathcal{S} \times \mathcal{A} \in \Re$. The agent interacts with the environment $\mathcal{E}$ according to some policy $\mu : \mathcal{S} \rightarrow A$ to generate trajectories of the form $s_1, a_1, r_1, \ldots, s_t, a_t, r_t, \ldots, s_T, a_T, r_T$, where $r_t = R(s_t, a_t)$. The return from a state is defined as the sum of discounted future reward $G_t = \sum_{i=t}^{T} \gamma^{(i-t)} R\left(s_i, a_i\right)$ with a discounting factor $\gamma \in [0, 1]$. The goal of the agent is to learn a policy which maximizes the expected return from the initial state $J = \mathbb{E}_{s \sim p(s_1)} \mathbb{E}_{\mu}[G_t | s_1 = s]$.

Fast-Timescale VVC as a Markov Decision Process

To formulate the fast-timescale VVC problem as an MDP, the distribution system operator or controller is treated as the agent and the distribution network is treated as the environment. We define the state, action, and reward function as follows:

State The state consists of reactive power injection of inverters of the previous time step $\boldsymbol{q}^g_{t-1}$, and aggregated load $\boldsymbol{p}^c_t$ at relevant nodes at time t, solar PV production potential of the smart inverters determined by solar irradiance and technical parameters of the respective solar PV systems $\bar{\boldsymbol{p}}^g_t$, voltage magnitude at each bus $|\boldsymbol{v}_t|$, and the current tap positions of voltage regulating devices $\boldsymbol{tap}^{reg}, \boldsymbol{tap}^{tsf}, \boldsymbol{tap}^{cap}$.

The current time τ can embed information about future load as electric loads consumption has a time-dependent pattern. As a result, it is beneficial to consider it as a state in the RL algorithm. The active and reactive load data at every node was not available. We only had the aggregated hourly smart meter energy consumption data from Austin Texas in 2019 from the Pecan Street Dataset. The aggregated load data is scaled and allocated to each node according to the existing spatial load distribution of the IEEE standard test cases. Since each node is assumed to have a constant power factor, we only use the aggregate load data as a state.

Action The reactive power outputs of the smart inverters are considered as actions. The reactive power injected/absorbed by inverter i is limited by the active power capacity of the inverter. It can be expressed by $|q^g_{it}| \leq \bar{q}^{gR}_{it}$ where $\bar{q}^{gR}_{it} = \sqrt{\bar{S}^2_i - (\bar{p}^g_{it})^2}$. We rewrite the equation as $q^g_{it} = a_q \bar{q}^{gR}_{it}$, where $a_q \in [-1, 1]$ is the action space.

Reward The reward received by the reinforcement learning agent consists of three terms as shown in (5.8): line loss, voltage violation costs, and the inverter degradation costs formulated in the same way as in Section 5.3.2.

$$r_t = -\left(J_{L,t} + J_{V,t} + J_{I,t}\right) \tag{5.8}$$

We consider a quadratic voltage violation cost in the reward function so that the performance of our proposed VVC algorithm can be fairly compared to the optimization-based Baseline VVC algorithms. The inverter degradation cost $J_{I,t}$ creates a dependency between the reactive power control actions of the smart inverters taken at different time steps. As a result, the scheduling of the smart inverters at the fast timescale can be directly formulated as a Markov decision process and RL algorithms can be utilized to solve the fast timescale VVC problem.

Slow-Timescale VVC as Markov Game

The slow-timescale policy should take into account the fast-timescale actions taken within the hour. Therefore, the slow-timescale policy is formulated as an ordered two-player Markov game. Markov game is a multi-agent extension of Markov decision processes. An ordered Markov game is defined by an ordered set of states S, and a collection of action sets, $A_1, \ldots, A_k$, one for each ordered agent in the environment. State transitions are controlled by the current state and one action from each agent: $S \times A_1 \times \ldots \times A_k \to S'$. Each agent i has an associated reward function, $R_i : S \times A_1 \times \ldots \times A_k \to \mathcal{R}$. Each agent i attempts to maximize its expected sum of discounted rewards, $E\left\{\sum_{j=0}^{\infty} \gamma^j r_{i,t+j}\right\}$, where $r_{i,t+j}$ is the reward received j steps into the future by agent i.

In our setup, the distribution system operator or controller is treated as the agent and the distribution network is treated as the environment. The slow-timescale agent observes the state S_τ and selects action A according to a stochastic policy π at the start of the hour τ. The fast-timescale agent receives private observations at each subsequent minute t within the hour τ denoted by $\boldsymbol{O}_{1:T} = \{O_1, \ldots, O_T\}$, selects the corresponding actions denoted by $\boldsymbol{a}_{1:T} = \{a_1, \ldots, a_T\}$, and gathers rewards $r_1, \ldots, r_T$. The slow-timescale agent receives a reward $R_\tau : S_\tau \times \boldsymbol{O}_{1:T} \times \boldsymbol{a}_{1:t}$ at the end of the hour and produces the next state $S_{\tau+1}$ according to the state transition function $\mathcal{T} : S_\tau \times A_\tau \times \boldsymbol{O}_{1:T} \times \boldsymbol{a}_{1:T} \rightarrow S_{\tau+1}$.

We define the state, action, and reward function as follows:

State The state consists of aggregated load $\boldsymbol{p}^c_\tau$, solar PV generation $\bar{\boldsymbol{p}}^g_\tau$ at the nodes with smart inverters at the start of the hour τ, current tap positions of voltage regulating devices $\boldsymbol{tap}^{reg}, \boldsymbol{tap}^{tsf}, \boldsymbol{tap}^{cap}$, and current time τ.

Action The action taken by the slow-timescale VVC agent is changing the tap positions of the conventional VVC devices from $\boldsymbol{Tap}$ to $\boldsymbol{Tap'}$. If N_c denotes the number of conventional VVC devices and $\mathcal{N}_i$ denotes the number of tap positions of device i, the size of the action space is $\prod_{i=1}^{N_c} |\mathcal{N}_i|$.

Reward The reward received by the slow-timescale reinforcement learning agent is the negative of the total operational cost at each minute t within the hour τ, i.e. the reward collected by the fast-timescale agent within the hour τ and the switching cost $J_{Tap,\tau}$:

$$R_\tau = \sum_{t=1}^{T} r_t - J_{Tap,\tau} \tag{5.9}$$

5.4 Technical Methods

In this section, we describe the proposed two-timescale reinforcement learning-based algorithm to solve the VVC problem. Section 5.4.1 reviews the DDPG algorithm to solve the fast-timescale VVC. The fast timescale VVC agent has continuous actions. Both SAC and DDPG implement a model-free policy gradient and value-based method. Both algorithms are suitable for solving the fast-timescale VVC problem. Theoretically, SAC has some advantages over DDPG. For example, DDPG suffers from instability in the form of sensitivity to hyper-parameters and propensity to converge to very poor solutions or even diverge. However, SAC is sensitive to the temperature hyperparameter which needs to be carefully tuned. In [35], the authors compared the performance of Twin delayed DDPG and SAC and found that their performance can be statistically indistinguishable in most continuous control benchmarks. In our problem setting, we obtained slightly better training and testing results by using DDPG in the fast timescale problem. Hence, we solve the fast time-scale VVC by the DDPG algorithm.

Section 5.4.2 presents the proposed two-timescale algorithm to solve the VVC problem along with the MASAC algorithm. The slow timescale agent has discrete actions. The soft actor-critic (SAC) algorithm can be modified for discrete outputs. Section 5.4.3 describes our proposed policy network architecture.

5.4.1 Review of Deep Deterministic Policy Gradient Algorithm

DDPG is an off-policy deep reinforcement learning algorithm with the actor-critic architecture and function approximators. The actor network maintains a deterministic policy μ using a neural network parameterized by θ^{μ}.

To ensure exploration, noise sampled from a noise process η, e.g., an Ornstein-Uhlenbeck process [360] is added to the output: $\mu'\left(s_t\right) = \mu\left(s_t|\theta_t^{\mu}\right) + \eta$. The critic network approximates the corresponding Q function of the policy using the neural network parameterized by θ^{Q}. To improve the stability of learning, two target networks $Q'\left(s, a|\theta^{Q'}\right)$ and $\mu'\left(s|\theta^{\mu'}\right)$ are introduced to provide stable learning targets.

In addition, the experience replay buffer is employed which stores the experience tuples (s_t, a_t, r_t, s_{t+1}) for neural network training.

Since the target policy is deterministic, the Bellman equation can be expressed as follows:

$$Q^{\mu}\left(s_t, a_t\right) = \mathbb{E}\left[R\left(s_t, a_t\right) + \gamma\left[Q^{\mu}\left(s_{t+1}, \mu\left(s_{t+1}\right)\right)\right]\right] \tag{5.10}$$

The training of the critic network is based on minimizing the following loss function using batches of experience with N_m number of transitions.

$$L = \frac{1}{N_m}\sum_i \left(y_i - Q\left(s_i, a_i|\theta^{Q}\right)\right)^2 \tag{5.11}$$

$$y_i = R\left(s_i, a_i\right) + \gamma Q'\left(s_{i+1}, \mu'\left(s_{i+1}|\theta^{\mu'}\right)|\theta^{Q'}\right) \tag{5.12}$$

The parameters of the actor network are updated using the critic network and the policy gradient algorithm with batches of experience with N_m transitions.

$$\nabla_{\theta^\mu} J \approx \frac{1}{N_m}\sum_i \nabla_a Q\left(s, a|\theta^Q\right)|_{s=s_i,a=\mu(s_i)} \nabla_{\theta^\mu}\mu\left(s|\theta^\mu\right)|_{s_i} \tag{5.13}$$

5.4.2 Proposed Reinforcement Learning-based Two-Timescale Volt-VAR Control Algorithm

To tackle the two-timescale VVC problem in a model-free manner, we propose two hierarchically arranged policies π and μ for the slow- and the-fast timescale, respectively. They are coupled via a communication medium following [198] and are learned concurrently. Two separate experience relay buffers $\mathcal{D}_\pi$ and $\mathcal{D}_\mu$ are maintained to collect the transitions at two different levels of temporal abstraction. A schematic is provided in Fig. 5.2.

At the start of each hour τ, the slow-timescale VVC agent observes the environment state S_τ and takes an action A_τ, which changes the OLTC and capacitor tap to $\boldsymbol{Tap}_\tau$. At each minute t within τ, the tap positions are kept fixed, i.e. $\boldsymbol{Tap}_{\boldsymbol{\tau}}^1 = \boldsymbol{Tap}_{\boldsymbol{\tau}}^2 = \ldots = \boldsymbol{Tap}_{\boldsymbol{\tau}}^T$. Since the taps are fixed, there is no non-stationarity from the perspective of the fast-timescale agent (but not vice versa). As such, the tap positions $\boldsymbol{Tap}_\tau$ are communicated via m to the fast-timescale agent to account for the slow-timescale policy. The fast-timescale agent produces actions $\boldsymbol{a}_t$ to control the smart inverter reactive power productions. The transitions (s_t, a_t, r_t, s_{t+1}) are stored in the experience replay buffer D_μ, which are used to train μ by the DDPG algorithm. If the fast-timescale policy is fixed, the slow-timescale VVC problem is stationary and can be solved by a single agent RL algorithm such as soft actor-critic (SAC) [148]. We briefly review SAC as follows. SAC maximizes a trade-off

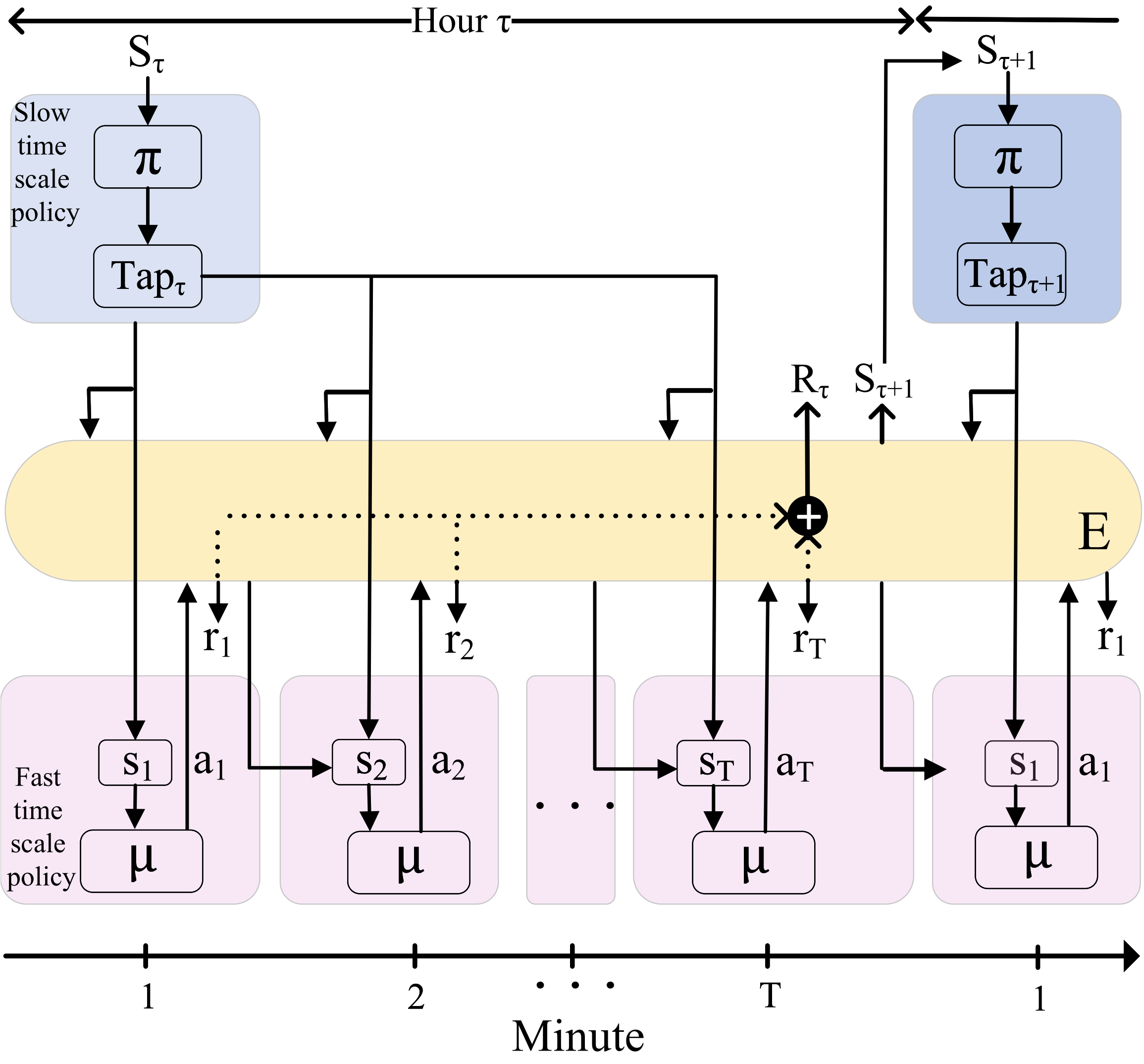

Figure 5.2: The two-timescale volt- VAR control setting

between the expected reward and the policy's entropy:

$$\pi^* = \underset{\pi}{\operatorname{argmax}} \sum_{\tau=0}^{\mathcal{T}} E_{(S_\tau, R_\tau) \sim \rho_\pi} \left[\gamma \left(R_\tau + \alpha \mathcal{H} \left(\pi \left(. | S_\tau \right) \right) \right) \right] \tag{5.14}$$

The entropy for a stochastic policy at state S_τ is defined as $\mathcal{H} \left(\pi \left(. | S_\tau \right) \right) = - \sum\limits_{A} \pi \left(A | S_\tau \right) \ln \pi \left(A | S_\tau \right)$.

Maximizing the entropy term increases the stochasticity of the policy hence encourages exploration. The trade-off between the two objectives is controlled by the non-negative temperature parameter α.

SAC makes use of three neural networks. The actor network π_ϕ parameterized by ϕ learns a stochastic policy π that maps states to actions. The critic network Q_ν parameterized by ν learns a Q-function $Q \left(S, A \right)$ that estimates the objective value of the current policy π. The value network V_ψ parameterized by ψ learns the state value function $V_\psi \left(S \right)$.

However, the fast-timescale agent's policy μ is changing within the hour τ with training and therefore the environment becomes non-stationary from the perspective of the slow-timescale agent π. This violates the stationarity and Markovity assumptions underlying reinforcement learning and prevents the straightforward use of experience replay. To address these challenges, reference [236] proposed a simple extension of actor-critic policy gradient methods where the critic is augmented with information about the policies of other agents. Their proposed Multi-agent Deep Deterministic Policy Gradient (MADDPG) algorithm extends DDPG to multi-agent settings by adopting a centralized training with decentralized execution (CTDE) framework. The primary motivation behind MADDPG is that, if the actions taken by all agents are known, the environment is stationary even if the policies change. Since the tap positions are fixed within an hour, there is no non-stationarity from the perspective of the fast timescale agent. The fixed tap positions are used as a state in the fast time-scale VVC algorithm. In that sense, the fast timescale agent can act independently and does not have a strict master-slave relation to the slow timescale agent. This leads to an algorithm that leverages the observations and actions of all agents to train a centralized action-value function, whereas the policy of each agent only depends on its own private observations. Therefore, the agents can take actions in a decentralized manner during the testing period while ensuring stable training. The CTDE framework can also be combined with the SAC algorithm, which yields the multi-agent soft actor-critic (MASAC) algorithm [379]. We further modify this algorithm to accommodate for discrete action space needed for the conventional Volt-VAR control devices.

In this paper, we take the idea of CTDE beyond its original field of application: the multi-agent RL problem. Instead, it is used to solve the non-stationarity problem of the two-timescale RL-based VVC. The pseudocode for the two-timescale VVC algorithm is shown in Algorithm 4.

In our setting, the action taken by the fast-timescale agent depends only on its own observations; the actions taken by the slow-timescale agent at the start of the hour forms part of the states of the fast-timescale policy. On the other hand, the reward obtained by the slow-timescale agent depends on its state, the actions taken by the fast-timescale agent, and the rewards obtained by the fast-timescale agent within the hour. The state transition for the slow-timescale agent depends on its state and the actions taken by the slow-timescale and fast-timescale policy.

Algorithm 4 Reinforcement learning-based two-timescale VVC scheme

```
Initialize parameters $\psi$, $\phi$, $\nu$, $\theta^{\mu}$, $\theta^{Q}$ $D_{\pi}$, $D_{\mu}$, $\mathcal{N}_{\mu}$
Initialize target networks weights $\psi' \leftarrow \psi$, $\theta^{\mu'} \leftarrow \theta^{\mu}$, $\theta^{Q'} \leftarrow \theta^{Q}$
Assemble the initial state vector $\boldsymbol{S}_1$ and $\boldsymbol{s}_1$
for $\tau = 1 \dots \mathcal{T}$ do
    Select action $\boldsymbol{A}_{\tau} = \pi_{\phi}\left(.|S_{\tau}\right)$
    Update fast-timescale state $\boldsymbol{s}_t$ by utilizing $\boldsymbol{A}_{\tau}$
    Set accumulated reward $R_{\tau} \leftarrow 0$
    for $t = 1 \dots T$ do
        Select action $\boldsymbol{a}_t = \mu\left(\boldsymbol{s}_t|\theta^{\mu}\right) + \mathcal{N}_{\mu}$ according to current fast-timescale policy and
        exploration noise
        Execute action $\boldsymbol{a}_t$, reward $r_t$, and next state $\boldsymbol{s}_{t+1}$
        Accumulate rewards $R_{\tau} \leftarrow R_{\tau} + r_t$
        Store $(\boldsymbol{s}_t, \boldsymbol{a}_t, r_t, \boldsymbol{s}_{t+1})$ in replay buffer $D_{\mu}$
        Randomly sample a random mini-batch of $N_m$ samples from $\mathcal{D}_{\mu}$
        Compute target $y_i$ using (5.12)
        Update Q-function by minimizing loss in (5.11)
        Update policy by one step of gradient ascent using (5.13)
        Update target networks with
        $\theta^{Q'} = \rho\theta^{Q} + (1-\rho)\theta^{Q'}$, $\theta^{\mu'} = \rho\theta^{\mu} + (1-\rho)\theta^{\mu'}$
    end for
    Observe next slow-timescale state $S_{\tau+1}$
    Store $\left(S_{\tau}, A_{\tau}, \boldsymbol{o}^{\tau}_{1:T}, \boldsymbol{a}^{\tau}_{1:T}, R_{\tau}, \hat{S}_{\tau+1}\right)$ in $D_{\pi}$
    Sample a random mini-batch of $\mathcal{B}$ samples from $\mathcal{D}_{\pi}$
    Update V-function by minimizing loss in (5.15)
    Update Q-function by minimizing loss in (5.17)
    Update policy by minimizing loss (5.20)
    Update target network parameters
    $\psi' = \rho\psi' + (1-\rho)\psi'$
end for
```

Let the fast-timescale actions taken by and the private observations for the inverter for all time steps within the hour τ be $\boldsymbol{a}^{\tau}_{1:T} = (a_1, \dots, a_T)^{\tau}$ and $\boldsymbol{o}^{\tau}_{1:T} = (o_1, \dots, o_T)^{\tau}$. The reward for the slow-timescale agent is calculated as the cumulative sum of the fast-timescale rewards for all time steps within the hour τ along with the switching cost, i.e. $R_{\tau} = \sum_{t=1}^{T} r^t + \sum \boldsymbol{Tap}_{\tau} - \boldsymbol{Tap}_{\tau-1}$. After the T-th fast timescale step within hour τ, the state of the environment becomes $S_{\tau+1}$. The experience replay buffer D_{π} stores the experience tuples $(\boldsymbol{S}_\tau, \boldsymbol{A}_\tau, \boldsymbol{o}^\tau_{1:T}, \boldsymbol{a}^\tau_{1:T}, R_\tau, \boldsymbol{S}_{\tau+1})$. The samples obtained from D_π are used to update the slow-timescale policy π. In order to prevent non-stationarity, following the CTDE framework, our MASAC uses the actions and observations of all agents in the action-value functions $Q\left(\boldsymbol{S}_\tau, \boldsymbol{A}_\tau, \boldsymbol{o}^\tau_{t:T}, \boldsymbol{a}^\tau_{t:T}\right)$, while the policy is only conditioned upon its own private observations $\boldsymbol{A}_\tau = \pi_\theta\left(\boldsymbol{S}_\tau\right)$.

The value network V_ψ is trained by minimizing the following approximate squared residual error calculated over sampled mini-batch $\mathcal{B}$ from the replay buffer $\mathcal{D}_\pi$.

$$J_V\left(\psi\right) = \frac{1}{|\mathcal{B}|}\sum_{\mathcal{B}}\left[\frac{1}{2}\Big(V_\psi\left(\boldsymbol{S}_\tau, \boldsymbol{o}^\tau_{1:T}, \boldsymbol{a}^\tau_{1:T}\right) - \hat{V}_\tau\Big)^2\right] \tag{5.15}$$

$$\hat{V}_\tau = Q^\nu\left(\boldsymbol{S}_\tau, \hat{\boldsymbol{A}}_\tau, \boldsymbol{o}^\tau_{1:T}, \boldsymbol{a}^\tau_{1:T}\right) - \alpha \ln \pi_\phi\left(\hat{\boldsymbol{A}}_\tau | \boldsymbol{S}_\tau\right) \tag{5.16}$$

where $\hat{\boldsymbol{A}}_\tau$ is sampled according to the current policy $\hat{\boldsymbol{A}}_\tau \sim \pi_\phi\left(.|\boldsymbol{S}_\tau\right)$. The parameters of the action-value network Q^ν are updated by minimizing the following soft Bellman residual:

$$J_Q\left(\nu\right) = \frac{1}{|\mathcal{B}|}\sum_{\mathcal{B}}\left[\frac{1}{2}\left(Q^\nu\left(\boldsymbol{S}_\tau, \boldsymbol{A}_\tau, \boldsymbol{o}^\tau_{1:T}, \boldsymbol{a}^\tau_{1:T}\right) - \hat{Q}_\tau\right)^2\right] \tag{5.17}$$

$$\hat{Q}_\tau = R_\tau + \gamma V_{\psi'}\left(\boldsymbol{S}_{\tau+1}, \boldsymbol{o}^{\tau+1}_{1:T}, \mu'\left(\boldsymbol{o}^{\tau+1}_{1:T}\right)\right), \tag{5.18}$$

where $V_{\psi'}\left(\boldsymbol{S}_{\tau+1}, \boldsymbol{o}^{\tau+1}_{1:T}, \mu'\left(\boldsymbol{o}^{\tau+1}_{1:T}\right)\right)$ is estimated using a target value network $V_{\psi'}$. The policy π_ϕ acts to maximize the expected future return along with the expected future entropy in each state, i.e. it maximizes $V(\boldsymbol{S})$. In the case of continuous actions, it is necessary to use the reparameterization trick to allow gradients to pass through the expectations operator. However, it is no longer necessary for the discrete actions which are sampled with the output distribution of the policy network. Now, with a slight abuse of notation, the policy gradient can be derived similarly to the policy gradient theorem to maximize the state-value function following [371]:

$$
\begin{aligned}
\nabla_\phi V\left(\boldsymbol{S}\right) &\approx \nabla_\phi \sum_{A} \pi_\phi\left(\boldsymbol{A}|\boldsymbol{S}\right)\left(Q\left(\boldsymbol{S},\boldsymbol{A}\right) - \alpha \ln \pi_\phi\left(\boldsymbol{A}|\boldsymbol{S}\right)\right) \\
&= \underset{A\sim\pi_\phi}{E}\left[\nabla_\phi \ln \pi_\phi\left(\boldsymbol{A}|\boldsymbol{S}\right)\left(Q\left(\boldsymbol{S},\boldsymbol{A}\right) - \alpha \ln \pi_\phi\left(\boldsymbol{A}|\boldsymbol{S}\right)\right)\right] \\
&= \underset{A\sim\pi_\phi}{E}\left[\nabla_\phi \ln \pi_\phi\left(A|S\right)\left(Q\left(\boldsymbol{S},\boldsymbol{A}\right) - V\left(\boldsymbol{S}\right) - \alpha \ln \pi_\phi\left(\boldsymbol{A}|\boldsymbol{S}\right)\right)\right]
\end{aligned}
\tag{5.19}
$$

The regularity condition $\sum_A \pi_\phi\left(\boldsymbol{A}|\boldsymbol{S}\right)\nabla_\theta \ln \pi_\phi\left(\boldsymbol{A}|\boldsymbol{S}\right) = 0$ is used to derive the second line. The loss function for updating the parameters ϕ of the policy neural network is given by (5.20), whose partial derivative is the negative of (5.19).

$$
\begin{aligned}
J_\pi\left(\phi\right) = &\frac{1}{\mathcal{B}} \sum_{\mathcal{B}} \Big[\ln \pi_\phi\left(\hat{\boldsymbol{A}}_\tau|\boldsymbol{S}_\tau\right)\Big(-Q\left(\boldsymbol{S}_\tau, \hat{\boldsymbol{A}}_\tau, \boldsymbol{o}_{1:T}^{\tau}, \boldsymbol{a}_{1:T}^{\tau}\right) \\
&+ V(\boldsymbol{S}_\tau, \boldsymbol{o}_{1:T}^{\tau}, \boldsymbol{a}_{1:T}^{\tau}) + \alpha \ln \pi_\phi\left(\hat{\boldsymbol{A}}_\tau|\boldsymbol{S}_\tau\right)\Big)\Big]
\end{aligned}
\tag{5.20}
$$

5.4.3 Policy and Value Network Architectures

The neural network architectures for the value and policy functions need to be carefully designed to handle the large input/output. First. the time series inputs $\boldsymbol{o}_{1:T}$ and $\boldsymbol{a}_{1:T}$ are passed through two separate long short-term memory (LSTM) networks [165],

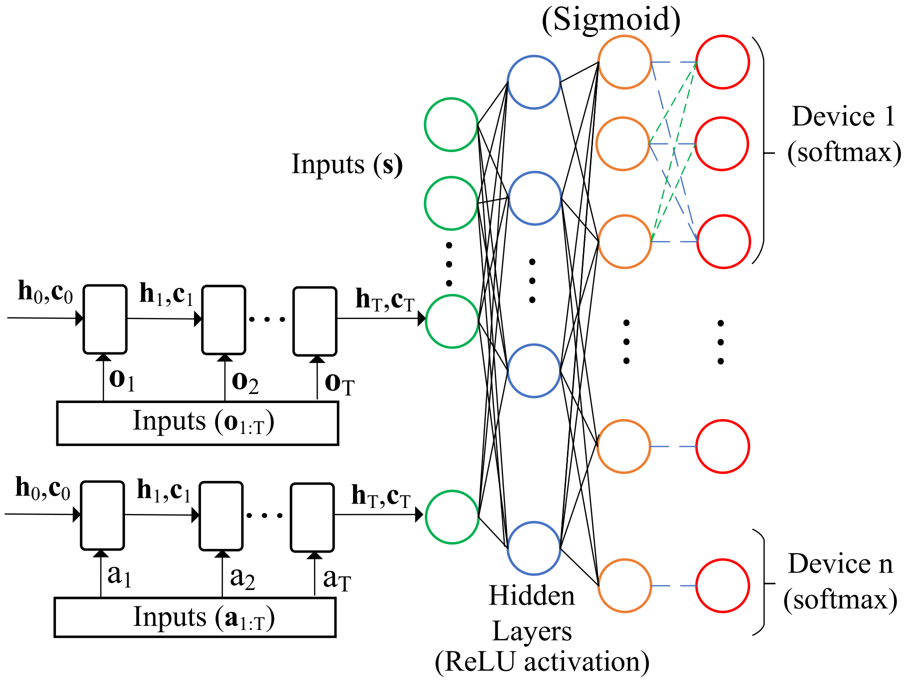

Figure 5.3: Device-decoupled structure of the policy neural network with LSTM networks for processing the action and observation time series

which convert the sequence of observations/actions to a fixed-size representation. The last cell state outputs of the LSTM networks are treated as input to the policy neural network along with the state inputs ($\boldsymbol{S}_\tau$). Then, the device-decoupled structure and the ordinal encoding architecture following [371] is used for the slow-timescale policy network. The overall architecture for the slow-timescale policy network is depicted in Figure 5.3.

5.5 Numerical Study

The performance of the proposed two-timescale VVC in Algorithm 1 is tested on a modified IEEE 123-bus test feeder.

5.5.1 Simulation Setup

The IEEE 123-bus test feeder has a voltage regulator at node 150. There are three OLTCs connecting node 9 to node 14, node 25 to node 26, and node 160 to node 67, respectively. Four capacitors are placed at node 83 (200 kVAr), node 88 (50 kVAr), node 90 (50 kVAr), and node 847 (50 kVAr). Three solar PV systems with a nameplate capacity of 801 kW, 534 kW, and 44 kW are added to the feeder at the nodes 69, 73, and 77, respectively. The inverters are not oversized and the solar PV penetration level of the feeder is 52%. To illustrate the algorithm's capability for reactive power management with highly variable load and high solar PV production conditions, we double the line impedances so that the benefits of reactive power absorption are more pronounced.

All voltage regulators and on-load tap changers have 11 tap positions, which correspond to turns ratios ranging from 0.95 to 1.05. The capacitors can be switched on/off remotely and the number of 'tap positions' is treated as 2. In the initial state, the turns ratios of voltage regulators and on-load tap changers are 1 and the capacitors are switched off. The electricity price C_e is assumed to be $\$40/MWh$. The operating cost per tap change is set to be \$0.1 for all devices. The penalty coefficient C_V is set as $\$1/volt$. The inverter degradation cost C_I is set to be $\$0.02/MW$.

One year of load and solar PV generation data from Austin, Texas in 2019 was obtained from the Pecan Street Dataset [166]. The load data is scaled and allocated to each node according to the existing spatial load distribution of the IEEE 123-bus test feeder. The solar PV generation data is scaled according to the corresponding nameplate capacity of the solar PV systems. The training dataset consists of 39 weeks of data from weeks 1 to

Table 5.1: Hyperparameter settings

Parameters	DDPG	MASAC	LSTM
Size of hidden layers	$(512, 512)$	$(512, 512)$	-
Activation function (hidden layers)	ReLU	ReLU	-
Activation function (ordinal encoding)	-	Sigmoid	-
Batch size	1000	1000	-
Discount factor	0.99	0.99	-
Learning rate actor and critic network	0.0001	0.00001	-
Standard deviation for exploration noise	0.2	-	-
Number of epoch	1	1	-
temperature parameter	-	0.2	-
Number of steps before running policy	200	500	-
Start updates after step	200	500	-
Hidden size (LSTM network for $\boldsymbol{o}_{1:T}$)	-	-	4
Hidden size (LSTM network for $\boldsymbol{a}_{1:T}$)	-	-	3

39. During the training period, the agents interact with the environment and update their policy and value networks. Two weeks of data for weeks 40 and 41 are used for out-of-sample testing, in which the trained reinforcement learning agent takes control actions without further updating the parameters of its neural networks. The hyperparameter settings for the MASAC and DDPG algorithm of the proposed two-timescale VVC are provided in Table 5.1.

5.5.2 Setup of the Baseline and Our Proposed Algorithms

Under the model-free reinforcement learning-based control framework, we compare our proposed two-timescale smart inverter control with a baseline reinforcement learning algorithm where the slow-timescale VVC and the fast-timescale VVC are trained separately. In addition, we consider three model-based control algorithms as additional baseline algorithms. Note that we assume the model-based control algorithms have an accurate and complete distribution network model, which is an unfair advantage over the RL-based algorithms.

The three model-based control algorithms and the RL-based baseline algorithm are set up as follows:

1. Baseline 1: No Volt-Var control is executed.
2. Baseline 2: Only slow-timescale VVC is executed for a look-ahead horizon of 4 hours following the method in Section 5.3.2. The smart inverters operate at unity power factor with no reactive power injection/absorption or active power curtailment.
3. Baseline 3: Slow-timescale VVC is executed for a look-ahead horizon of 4 hours following the method in Section 5.3.2. The fast-timescale VVC is executed following the method in Section 5.3.2 for a look-ahead horizon of 2 minutes. The look-ahead horizon enables the VVC algorithm to take inverter degradation and the future smart inverter control actions into account. It is assumed that the controller has perfect information for the distribution network model, load, and renewable generation forecasts.
4. Baseline 4: A two-timescale VVC where the slow-timescale VVC and the fast-timescale VVC are trained with the RL algorithm separately. The slow-timescale VVC is solved using a soft actor-critic algorithm and the fast-timescale VVC is solved using a DDPG-based algorithm. There is no communication between the two agents.

The slow-timescale VVC in baseline methods 2 and 3 is formulated as a mixed-integer nonlinear programming (MINLP) and solved by GUROBI using the YALMIP toolbox [232] in MATLAB. The optimization-based fast-timescale inverter control in baseline method 3 is solved using the Gurobi solver.

Table 5.2: Performance comparison of the Volt-VAR control algorithms in the test dataset

Operational cost ($)	Baseline 1 (no VVC)	Baseline 2 (slow-timescale VVC)	Baseline 3 (Opt-based VVC)	Baseline 4 (RL-based separately trained VVC	Proposed two-timescale VVC	Proposed two-timescale VVC w/o LSTM
Switching	0.0	33.3	33.3	37.2	0.5	1.2
Line loss	460.7	368.7	410.4	579.3	461.5	473.7
Voltage violation	13452.7	353.8	0.04	47.8	0.7	17.4
Inverter degradation	10.1	10.1	36.5	28.8	26.17	26.1
Total	13923.6	765.9	480.2	693.1	488.4	518.5

5.5.3 Operational Performance Comparison

We evaluate the performance of the proposed two-timescale reinforcement learning-based VVC methods by comparing the total operational cost with the four baseline control algorithms. A lower total operational cost indicates a better control performance in voltage regulation. The total operational cost includes the line loss, voltage violation cost, switching cost of the conventional voltage regulating devices, and inverter degradation cost. Table 5.2 shows the operational cost comparison of the proposed reinforcement learning-based two-timescale VVC algorithm with the four baseline algorithms on the test dataset. The result is based on the trained model, which achieves the best performance out of 15 random experiments in the training dataset.

It can be observed from Table 5.2 that the slow-timescale VVC (Baseline 2) alone does not provide sufficient voltage regulation as the rapid change in the solar PV production within each hour causes high voltage violation. The proposed RL-based two-timescale VVC algorithm achieves the second-lowest total operational cost among all algorithms. Although the optimization-based two-timescale VVC algorithm achieves the lowest operation cost, it requires complete and accurate knowledge of primary and secondary distribution circuit models and parameters, which are usually unavailable in practice. On the other hand, the proposed RL-based two-timescale VVC algorithm is completely model-free. However, it does not offer an improvement in operation cost compared to the optimization-based VVC methods. Finally, an ablation study is performed to demonstrate the advantage of using an LSTM network over a feedforward neural network to encode action and observation time series. The last two columns of Table 5.2 show that the adoption LSTM network in the RL-based algorithm further reduces the total operational costs.

The inverter degradation is the worst in Baseline 3 compared to the RL based algorithms because the MPC based optimization problem only has a lookahead horizon of two minutes to minimize the inverter degradation whereas the reinforcement learning algorithms has can take the future inverter degradation cost into account during the training via the reward function. As a result, the optimization-based two timescale VVC changes the reactive power output of the smart inverters frequently to achieve immediate lower operational cost which ultimately results in a bigger inverter degradation cost.

Next, we compare the voltage profiles of two baseline VVC algorithms with that of our proposed RL-based two-timescale VVC. The voltage magnitude time series of node 71 corresponding to the no VVC, slow-timescale VVC only, and the proposed two-timescale VVC are shown in Fig. 5.4. Node 71 is selected for the comparison because it experiences the worst voltage violation when no VVC is employed. It can be seen that our proposed RL-based two-timescale VVC significantly improves the voltage regulation performance. Furthermore, our proposed two-timescale VVC is capable of maintaining the voltage within

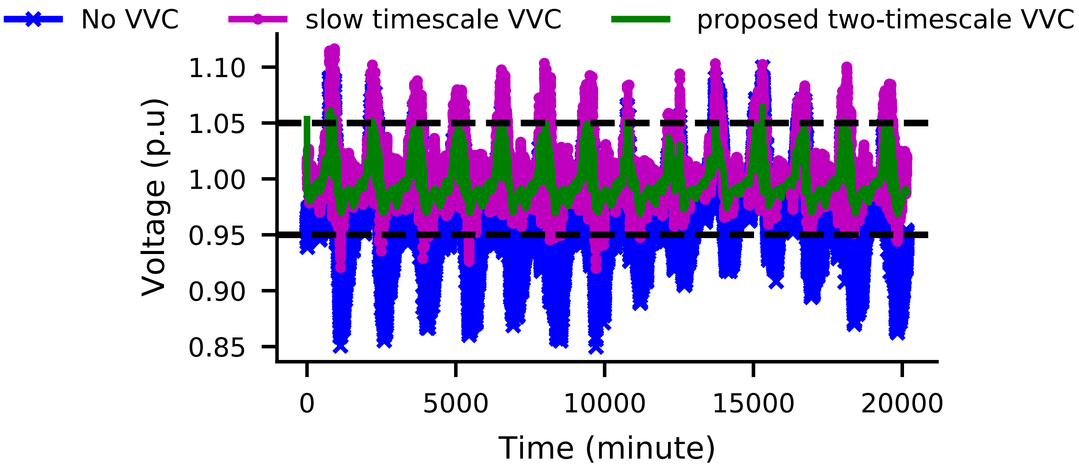

Figure 5.4: Comparison of voltage deviations at node 71 for three VVC algorithms in the test dataset

1 ± 0.05 p.u. for almost the entire operating week.

To help exploration, we follow a uniformly random policy for a certain number of steps (see Table I for the hyperparameter) before running the real policy. During this time, the load flow may not converge. If the load low does not converge, the environment is programmed to return a large bounded line loss and 0 for every node voltage, making it a large but bounded voltage violation cost. Our proposed VVC algorithm quickly learns to avoid actions that lead to non-convergence of load flow.

5.5.4 Sample and Computational Efficiency

Finally, the RL algorithm employed to solve the VVC problem should be sample efficient. Here, we demonstrate the sample efficiency of the proposed two-timescale VVC algorithm. The average biweekly return (AVR) on the testing weeks is plotted against the

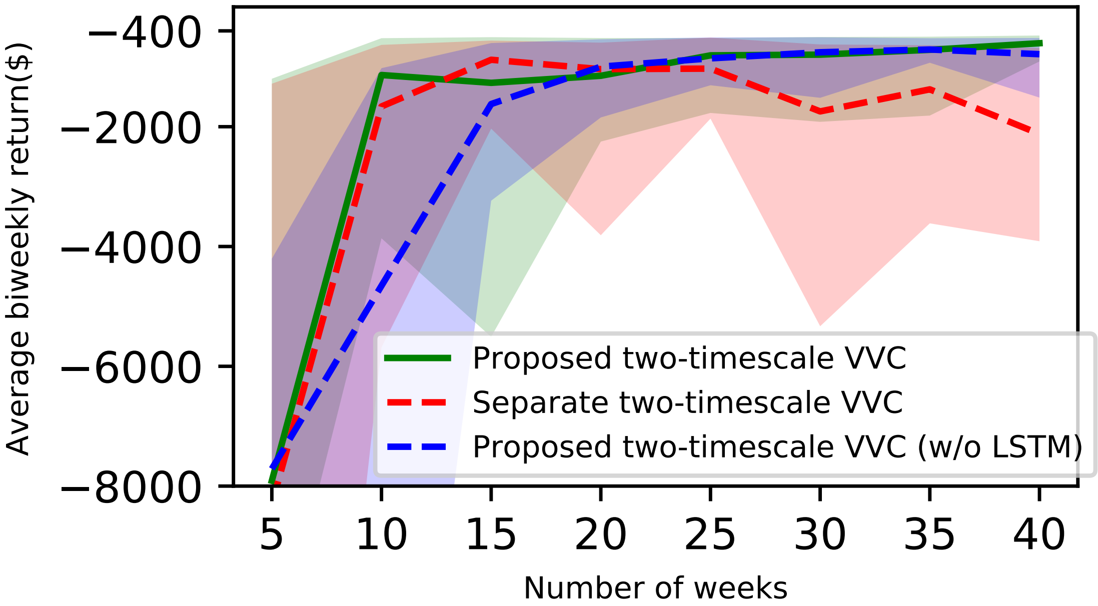

Figure 5.5: AVR vs number of weeks of training for the proposed, w/o LSTM, and separately trained VVC algorithms

number of training samples collected in Fig. 5.5. The AVR is defined as the summation of all the components of the reward function accumulated over the testing period. The colored lines show the mean AVR calculated over 15 independent runs. The light-colored region corresponds to the error bounds. It is observed that with about twenty weeks of training data, the proposed algorithm can learn a very effective VVC policy. Figure 5.6 shows the boxplot of the mean AVR calculated over 15 independent runs with 40 weeks of training data. It is observed that the results are consistent across different random initialization and training sessions. This demonstrates that the training procedure for the proposed two-timescale VVC algorithm is fairly robust.

The average computation time needed to process one hour of data for the baseline and the proposed VVC algorithms are shown in Table 5.3. The computations for the pro-

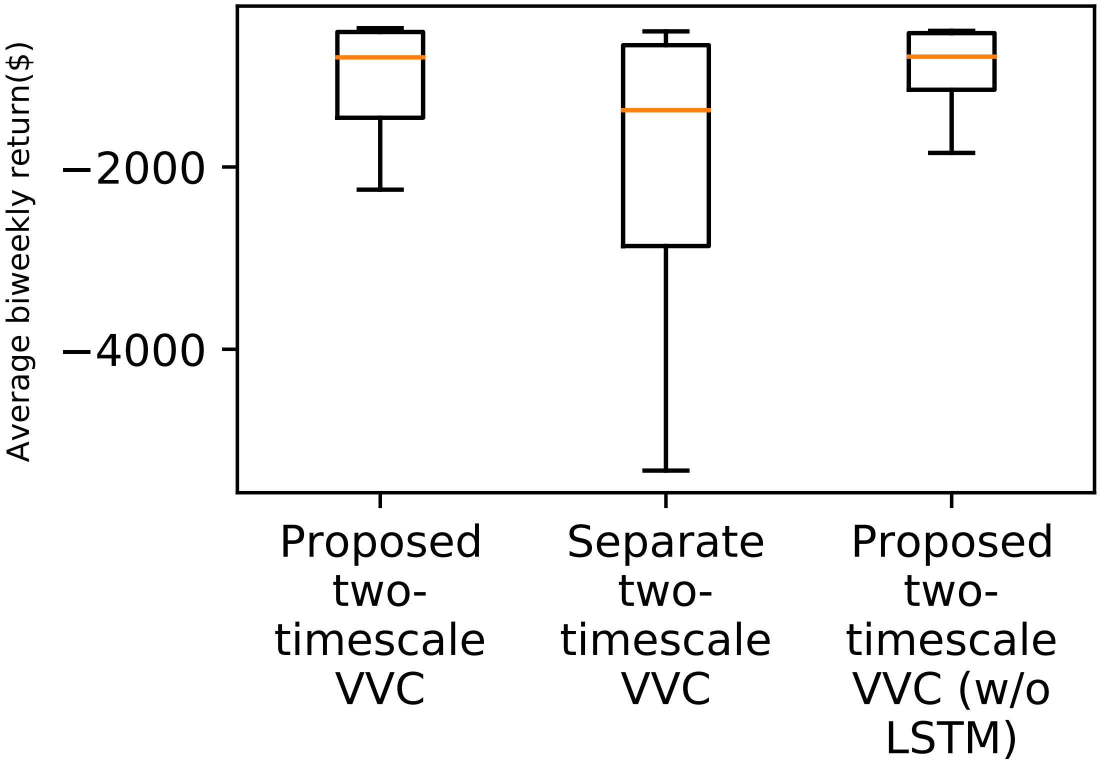

Figure 5.6: Boxplot of the AVR for the proposed, w/o LSTM, and separately trained VVC algorithms

Table 5.3: Average computation time of the baseline and proposed VVC algorithms required to process one hour of data

Computation Time (Seconds)	Opt-based slow-timescale VVC	Opt-based fast-timescale VVC	Proposed two-timescale VVC
Operational time	182	913	-
Training time	-	-	2.08
Testing time	-	-	0.63

posed VVC algorithm are performed using a 3.30GHz Intel(R) Core(TM) i9-9940X CPU and CUDA version 10.0.130 enabled GeForce RTX 2080 GPU. The training time and testing time for processing an hour of data are calculated by averaging the execution time of 10 weeks of training data and 2 weeks of testing data respectively. The convergence in our proposed two-timescale algorithm required 20 weeks of training data and is achieved in about two hours. The fast-timescale optimization-based VVC algorithm from baseline 3 is implemented using an Intel Xeon silver 4210 CPU with 15 parallel threads workers for MATLAB. Lastly, the slow-timescale VVC algorithm from baseline 2 and 3 is implemented using an Intel Core i5-5200U CPU. It can be observed from Table 5.3 that once trained, the proposed RL-based VVC algorithms can make control decisions much faster than the GUROBI solver used in the nonconvex optimization-based VVC methods. Thus, the proposed two-timescale RL-based VVC algorithm can be adopted for online implementations.

5.5.5 Robustness Analysis

Our proposed two timescale algorithm may face sample inaccuracy if the voltage reporting is not synchronized. To test the robustness of our proposed algorithm against sample inaccuracy, we introduce a 1-minute shift in the voltage with a small probability of 1% during training and testing. The performance is compared to the proposed VVC algorithm with no voltage synchronization issue in Table 5.4. It is observed that the performance declines by 16.80%. However, it is still an 18.57% improvement over the separated trained VVC in Baseline 4.

Table 5.4: Robustness analysis of the proposed VVC algorithm

Operational cost($)	Proposed two-timescale VVC	Proposed two-timescale VVC with sample inaccuracy
Switching	0.5	0.6
Line loss	461.5	505.8
Voltage violation	0.7	34.76
Inverter degradation	26.17	28.75
Total	488.4	569.91

5.6 Chapter Summary

In this paper, we propose a model-free two-timescale Volt-VAR control algorithm that does not depend on accurate primary or secondary feeder models. Two hierarchically arranged policies are run at two different timescales. In the slow-timescale, a soft actor-critic agent determines the tap positions of conventional voltage regulating devices, such as the voltage regulator, on-load tap changers, and switchable capacitor banks. On the fast-timescale, a DDPG agent determines the reactive power setpoints of the smart inverters. These two policies are coupled via a communication protocol and are learned concurrently. The proposed RL-based two-timescale VVC algorithm is capable of maintaining the voltage of the distribution grid within a reasonable range and almost achieve the same operational cost as a model-based controller with perfect network information, load, and renewable generation forecast.

Chapter 6

Impact of Aerosols on Reservoir Inflow: A Case Study for Big Creek Hydroelectric System in California

Hydroelectric power plants play a key role in supporting the integration of increasing amounts of wind and solar energy as they have a high level of operational flexibility and storage capability. Hydroelectric power plants take on important responsibilities such as flood control, navigation, irrigation, agricultural, urban water supply, and recreation in addition to enhancing the stability of power systems and security of power supply. Hence, it is important to determine the optimal operational schedule of single-stage or multistage hydroelectric power plants. An accurate and reliable reservoir inflow forecast model is in crucial need to enable optimal and efficient scheduling of hydroelectric resources [139, 241, 363]. Typically, the river runoff in the Sierra Nevada region is highly influenced by meteorological variables such as temperature, precipitation, and snow water equivalent (SWE) [66]. Since the reservoir inflows of this region are generated by the runoff captured by the reservoirs, therefore, these meteorological variables can be used as explanatory variables in reservoir inflow forecast models. In the past decade, researchers have discovered that the presence of aerosol particles in the atmosphere can exert great influence on the hydrological cycle in a region through the meteorological variables [39, 234, 290, 295].

Aerosols are a mixture of tiny particles or liquids that are suspended in air and can range from 0.001 to 10 μm in size. A discussion on the impact of aerosols on temperature, SWE, and precipitation has been provided in Section 6.6. A detailed description of the effect of aerosol on precipitation and snow water equivalent in California is provided in [385]. Reference [385] showed that aerosols reduce precipitation and SWE by 10% over mountain tops in the Sierra Nevada region. This is a result of (both anthropogenic and naturally occurring) aerosols serving as cloud condensation nuclei (CCN) which leads to an increase of non-precipitating clouds. Cloud condensation nuclei are aerosol particles that act as the initial sites for the condensation of water vapor into cloud droplets. Aerosol deposition on snow increases absorption of solar radiation, leading to warming and further reduction of SWE over mountain tops. As the level of anthropogenic aerosol particles (such as sulfate and carbonaceous aerosols) increases rapidly from preindustrial times to the present-day over urban and industrial regions, their impact is becoming more significant on the hydrological cycle and thereby on reservoir inflow [68, 69, 234, 316]. It is critical to understand and quantify the impact of aerosols on reservoir inflow as it can influence hydropower generation and reservoir operations. It should be mentioned that the atmospheric lifetime is very short, typically two to four days, making their effect on climate and weather more regional and less persistent into the future than those of the long-lived greenhouse gases [156, 366]. Aerosols show large spatial and temporal variation in atmospheric aerosol concentrations and properties. Therefore, there are large differences in their effect on climate and weather on a regional basis [156, 284, 293, 298, 312, 366]. Since inflows into the reservoirs are influenced by climatic variables, the impact of aerosols on reservoir inflows should also vary from region to region and should therefore be studied on a regional scale.

The primary objective of this chapter is to build a reservoir inflow forecast model and subsequently quantify the impact of aerosols on inflow into Florence Lake and Lake Thomas Alva Edison in the Big Creek Hydroelectric System. Since Florence Lake and Lake Edison are the higher elevation reservoirs of the system, an accurate forecast of inflow into these reservoirs can also improve the operational efficiency of the system greatly. The Big Creek Hydroelectric System resides in the San Joaquin Valley which is surrounded by the Sierra Nevada mountain range in the east. San Joaquin Valley has one of the highest pollutant concentrations in the United States due to its unique geographical location. A detailed description of the study area is provided in Section 6.2. The autoregressive integrated moving average model (ARIMA) is a well-known univariate time series model frequently used in hydrological forecasting. ARIMA models can predict a time series variable based on its own past values (AR term) and past values of the error term (MA term). Including exogenous variables in the ARIMA model improves forecasting accuracy and is commonly known as the ARIMAX model or dynamic regression model. In this chapter, we first build a statistical hydrologic model with a dynamic regression method where meteorological variables such as temperature, precipitation, and SWE are used as explanatory variables. The best parsimonious dynamic regression model is selected using the Akaike Information Criterion (AIC), residual diagnostics, and goodness-of-fit. Meteorological variables are then simulated using the WRF-Chem model with different aerosol emission levels. These simulated meteorological variables with and without aerosol impacts are fed into the dynamic regression model to quantify the impact of aerosols on reservoir inflow in the Big Creek Hydroelectric System. Detailed analysis of aerosol impacts on temperature, precipitation, and SWE in California is not the objective of this study since it has been provided in [385].

The unique contributions of this chapter are listed as follows.

1. We developed an innovative and comprehensive framework for evaluating the impact of aerosols on reservoir inflow. The framework seamlessly integrates the numerical weather forecasting model (WRF-Chem) and the statistical inflow forecasting model (dynamic regression).

2. We built a dynamic regression model to forecast daily inflow into the hydroelectric reservoirs. The model coefficients for the meteorological variables provide an intuitive understanding of how temperature, precipitation, and snow water equivalent influence reservoir inflow.

3. We quantified the impact of aerosols on reservoir inflow in the Big Creek Hydroelectric System based on the proposed dynamic regression model and WRF-Chem model. The simulation results show that the presence of aerosols resulted in a reduction of

the annual reservoir inflow by 4%-14%.

The existing research on the effect of climate change and human activities on streamflow [135, 201, 217, 365] and inflow into reservoirs [58] in the San Joaquin Basin focus on the effect of carbon dioxide and several other greenhouse gases. There are very few research papers studying the effect of natural and anthropogenic aerosols on streamflow and reservoir inflow [134]. Our study focuses on exploring the impact of aerosols on inflow at the Big Creek hydroelectric system located in the upper San Joaquin River system in the Sierra Nevada Mountains of Central California.

The remainder of the chapter is organized as follows. Section 6.1 summarizes existing studies on statistical inflow forecasting models and discusses the rationality of choosing a dynamic regression model. Section 6.2 describes the study area. Section 6.3 presents the overall framework of our study. Section 6.4 presents the technical methods used in building the dynamic regression model to forecast reservoir inflow and the WRF-Chem model. Section 6.5 describes steps of building the dynamic regression models and their goodness of fit. Section 6.6 shows the evaluation of the WRF-Chem model and the impact of aerosols on inflow into the two hydropower reservoirs. Lastly, Section 6.7 concludes the chapter by discussing the direction of future research and the limitations of the study.

6.1 Literature review

This section presents a review of research articles relevant to this chapter which can be grouped into two categories, 1) statistical inflow forecasting models and 2) impact of aerosols on reservoir inflow.

6.1.1 Statistical inflow forecasting models

The existing models for hydrological modeling and forecasting can be separated into three groups; time series models [261, 262, 282, 363, 362], regression models [125, 210, 262], and artificial neural network (ANN) models [82, 176, 199, 262, 363, 398]. Reference [262] compared regression, ARIMA and ANN models to forecast spring inflows into the Amir Kabir reservoir in the Karaj watershed. Reference [363] compared ARMA, ARIMA, and the autoregressive ANN models to forecast monthly inflows of the Dez dam reservoir. Both of these studies chose ANN as the best model. Reference [261] compared SARIMA (seasonal ARIMA) and ANN-GA (ANN combined with the genetic algorithm) models in making short-term and long-term predictions of monthly inflow into a dam where the SARIMA model outperformed the ANN-GA model, especially in forecasting low values. Reference [282] used stochastic SARIMA model to forecast monthly inflow of one or more months ahead into the planned Amopeos Reservoir in Northern Greece which helped evaluate the optimal real-time reservoir operation policies. The monthly forecasts were used to generate a synthetic series of monthly inflows that preserves the key statistics of the historical monthly inflows and their persistence Hurst coefficient, providing a probabilistic framework for reservoir design. Monthly means and the monthly standard deviations of the forecasted inflows were close to that of the measured inflows demonstrating the ability of SARIMA models to forecast monthly inflows and generate synthetic series of monthly inflows. Reference [362] investigated SARIMA and ARIMA models for long-term runoff forecasting in the United States. They found the SARIMA model to be the best model in their study with an error of $< 5\%$ for all states. Therefore, the ARIMA model can be considered an effective tool for forecasting reservoir inflow. Including exogenous covariates in the ARIMA model helps explain the dynamic relationship between the response time series and the explanatory variable time series and improves forecast accuracy. This is called a dynamic regression model. The dynamic regression model is also referred to as the ARIMAX model.

For time-series data, using a dynamic regression model is preferred over ordinary regression because, some of the underlying assumptions of the regression model, e.g. normal distribution, homoscedasticity, and no autocorrelation of error terms, are frequently violated when being applied to time series data [244]. Applying the ARIMA modeling approach to model the information contained in the error term of the regression model can take care of its autocorrelation. The transfer function in the dynamic regression model captures the time-lagged relationship of input variables and the predictor variable. Therefore, the dynamic regression model can also be thought of as a regression model with time-lagged inputs and an ARIMA model for disturbances. Lastly, though ANN models might improve forecast accuracy, it is challenging to interpret the impact of aerosols on inflow by examining the weights on the meteorological input variables. In the light of all these considerations, we decided to adopt the dynamic regression model to forecast inflow into the hydropower reservoirs.

6.1.2 Impact of aerosols on hydrology

The presence of aerosol articles have impact on the hydrological cycle through its impact on earth's radiative forcing, precipitation and snow water equivalent [42, 234, 294]. It has been shown that an increase in atmospheric aerosols primarily affects solar radiation entering earth's atmosphere, snow albedo, cloud formation, and precipitation. Aerosol effects can be differentiated in three pathways- aerosol-radiation interaction (ARI) or direct effect, aerosol-snow interaction (ASI), and aerosol-cloud interaction (ACI) or indirect effect. Reflective aerosol particles, such as nitrate and sulphate particles, scatter the solar and thermal radiation and increase planetary albedo cooling both surface and atmosphere [27, 70, 159, 181, 195, 197, 285, 292]. However, light absorbing aerosols (LAA) such as black carbon absorb radiation known as LAA, decrease planetary reflectivity and increase air temperature [172, 181]. Presence of soot particles and dust in snow darkens the surface and reduces the snow albedo through aerosol-snow interaction (ASI). Reference [79, 81, 99, 117, 142, 155, 173, 214, 247, 248, 296, 380, 381, 384, 404]. Snow albedo perturbations increase the surface air temperature and accelerate snowmelt [40, 117, 155, 211, 258, 291, 384, 392]. Further reduction of snow albedo takes place by snow albedo feedback [55, 117, 149, 155]. Snow grain size, shape and Black carbon-snow mixing type also play important roles in aerosol-snow interaction [161, 204, 227, 306, 384]. Internal mixing of light-absorbing aerosols and snow reduces snow albedo more than external mixing, which enhances the aerosol-induced snow albedo reduction. Nonspherical snow grains tend to show less aerosol-induced snow albedo reductions compared with spherical snow grains. These two opposite effects on snow albedo reductions by light-absorbing aerosols may further influence snowmelt and SWE and have merit for in-depth studies [161, 160, 227].

Aerosol-cloud interaction or indirect effect of aerosols on climate includes a change in microphysical and optical properties of cloud droplets which is related to aerosols acting as cloud condensation nuclei (CCN). Increasing the number concentration of CCN can lead to the formation of more cloud droplets, which results in a decrease in cloud droplet radius leading to higher cloud albedo [182, 357, 358]. Another effect of the decrease in cloud droplet size is the reduced precipitation through the ‘second indirect effect’ [295, 302]. This is due to the fact that small water droplets continue to drift in the air and are less likely to grow to sufficient size to fall out as precipitation. This results in prolonged cloud lifetime [23, 20, 194, 302]. Higher cloud reflectivity and increase in cloud lifetime also produce a net cooling effect on the earth’s surface by shading it from solar radiation. Absorptive aerosols can reduce low-cloud cover through the ‘semi-direct effect’ [181, 154] leading to positive radiative forcing. Glaciation aerosol effect is a possible counteracting effect where an increase in ice nuclei by anthropogenic aerosols (mineral dust and a fraction of hydrophilic soot particles) acting as ice nuclei causes supercooled liquids to freeze [235, 233]. The ice crystals quickly grow at the expense of cloud droplets since the vapor pressure over ice is lower than that over water, leading to a more frequent glaciation of supercooled clouds. The precipitation formation via the ice phase is more efficient than in warm clouds and therefore, the glaciated clouds have a shorter lifetime than supercooled water clouds leading to more precipitation. The chemical nature of the dust determines whether glaciation or warm cloud lifetime effect is larger. Reference [53] showed that the smaller mean droplet size in supercooled clouds caused by anthropogenic aerosols can significantly reduce ice particle riming efficiencies in mid-altitude orographic clouds, resulting in lower orographic snowfall rates.

Impact of aerosols on water resources

Surface runoff is a major component of the hydrological cycle. It is defined as water from precipitation, snowmelt, or other resources that flows over the land surface. Few studies were conducted to examine the impact of anthropogenic aerosols on water resources. Reference [279] studied the effect of dust radiative forcing on snow and runoff from the Upper Colorado River Basin. Disturbance of soil surfaces in the Colorado Plateau and biological crusts occurred in the mid-1800s due to dramatic growth in grazing, agriculture, and resource exploration. They used the Variable Infiltration Capacity model with post-disturbance and pre-disturbance impacts of dust on snow albedo and estimated the impact on runoff from the Upper Colorado River Basin from 1996-2003 at Lees Ferry, Arizona. Dust loading observed in 2005-2008 was used in the study. They found that the resulting short duration of snow covers leads to a three-week early peak runoff and a decreased annual runoff (5%) due to an increase in evapotranspiration from the earlier loss of snow cover. The magnitude of difference in runoff increased with the magnitude of the annual runoff. A follow-up of the study was performed by [92] developing a new snow albedo decay parametrization based on observations of levels of dust loading in 2009-2010 as they were unprecedentedly high, being on the order of five times that of 2005-2008. The extreme dust scenario caused the peak snowmelt to occur an additional three weeks earlier and further reduced the annual inflow by 1%.

In addition to studying the impact of the deposition of soot aerosol on snow on snowpack, [291] also studied its effect on the hydrological cycle in the Western United States. They performed a yearlong simulation of WRF-Chem to simulate an annual cycle of soot aerosol deposition on snow and used it to estimate snow albedo perturbations induced by the soot within the Western United States. This was followed by three regional climate simulations at Columbia River Basin (CRB), the Sacramento-San Joaquin (SSJ) River

Basin, the Central Rockies (CR), and the Sierra Nevada (SN) mountains. They used WRF in meteorology-only mode (WRF-RCM) to capture precipitation, snowpack, and runoff, but with or without the perturbed snow albedo. They found that snow albedo reduction and the snow albedo feedback accelerated snowmelt and altered the streamflow which includes a trend towards earlier melt dates. In the Western United States, the main contribution to total runoff during winter is surface runoff generated by liquid rain. During spring, both precipitation and snowmelt contribute to runoff. As a result of warming in the soot-perturbed simulation, there are significant reductions in snowpack during the snowy winter period, which are reflected in reduced snow accumulation and more runoff during winter and less snowmelt during spring. Runoff increases during late winter because the higher surface temperature in the soot-perturbed simulation causes more precipitation to come in the form of rain rather than snow. By contributing directly to runoff or by causing snowmelt, a higher percentage of rainfall versus snowfall during the cold season increases runoff. As less snow accumulates during winter, runoff as a result of snowmelt decreases during late spring. Reference [289] used a global climate model to simulate the effect of black carbon and dust in the snow on the hydrological cycle of the Tibetan Plateau. They found that surface air temperature increased by around 1^oC averaged over the Tibetan Plateau and the spring snowpack was reduced due to the presence of black carbon and dust in snow. This had a significant impact on the hydrology, with the discharge increasing during late winter and early spring and decreasing during late spring and early summer showing a trend towards earlier melt dates.

[255] developed a snow algorithm that allowed for the deposition mass flux of

different species of light-absorbing aerosols as an input variable for application in a rainfall-runoff model allowing determination of the effect of various light-absorbing aerosols at the catchment scale. They demonstrated the effect of Black Carbon deposition on snow on the hydrologic cycle through the implications for snowmelt and discharge generation on a remote southern Norwegian catchment over a period of six years. Their results indicate a significant impact of Black Carbon in the snow at the catchment with runoff increasing in the spring followed by a decrease in discharge because of a trend towards earlier melt dates and a decrease in the catchment's snow-covered area.

[132, 133] quantified the suppression of orographic precipitation by anthropogenic aerosols over hills downwind of major coastal urban areas in California and Israel and subsequently extended it in [134] to study the impact of anthropogenic aerosols on available water resources in the Sea of Galilee in northern Israel and outflows of the main springs of Jordan River where a large portion of water resources result from orographic precipitation. In [132, 133], they defined the suppression of orographic precipitation as a reduction in the orographic enhancement factor R_o, where R_o is defined as the ratio between the precipitation amounts in the hills to the precipitation in the upwind lowland. Time series of R_o from 1880-2000 based on annual precipitation from rain gauges downwind of major urban areas was compared with rain gauges sidewind of the area. A decrease in R_o with time at locations downwind of air pollution sources was explained by the increase in small-particulate air-pollution emissions with the growth of urban areas. The suppression rate was found to be 15%-20% in hilly areas in California and Israel. Such decreasing trend was not found in hills downwind of pristine areas. They applied this methodology in [134] to measure trends of the ratio of annual precipitation between hilly to upwind lowland rain gauges and subsequently quantified the trend in orographic precipitation in the catchment areas. Then, they related it to trends in runoff and spring outflows by examining the relation of the trends of the spring outflow and the recharging area of the springs, thereby correlating the loss of precipitation to loss of overall water inflow. They concluded that air pollution is the main reason behind the suppression of orographic precipitation over the hilly areas and the subsequent decreasing trend in the available water in the Sea of Galilee.

These studies of the impact of aerosols on hydrology focus only on one of the aerosol sources or pathway and few focus on reservoirs. Our study presents a complete account of the aerosol impacts from different sources through three pathways on two hydropower reservoirs in the Sierra Nevada region of California.

6.2 Study Area: San Joaquin region and Big Creek Hydroelectric Project

The Big Creek Hydroelectric Project is an extensive hydroelectric system that accounts for 12% of California's total hydroelectric generation. The project is located on the upper San Joaquin River system in the Sierra Nevada Mountains of Central California. The Sierra Nevada is a mountainous region where most precipitation is retained as snow until temperatures are sufficient for melt [66].

The hydroelectric project is owned and operated by Southern California Edison (SCE) which has a total installed capacity of 1000 MW accounting for approximately 20% of SCE's total generation capacity. The hydroelectric system includes 27 dams, 23 generating units in nine powerhouses, miles of underground tunnels, and six major reservoirs with a combined storage capacity of 560,000 acre-feet. Water from lakes in higher elevation are routed through the nine powerhouses and discharged to lakes in lower elevations which are connected through tunnels and penstocks. The water travels a combined vertical distance of 6655 feet before being discharged through the last powerhouse into the San Joaquin River. Florence Lake and Lake Thomas Alva Edison are the higher elevation reservoirs of the system having a surface elevation of 7300 and 7648 feet respectively. The dam at Florence Lake captures runoff from the South Fork San Joaquin River, diverting it through the Ward Tunnel towards the Portal Powerhouse which is the first powerhouse in the system to receive water. Lake Thomas Alva Edison is formed by the Vermillion Valley Dam constructed across Mono Creek, a tributary of the South Fork of the San Joaquin River. It discharges some of its water to the Ward Tunnel and thereby further regulates the water supply to the Portal Powerhouse. Water running through Portal Powerhouse gets discharged into Huntington Lake where it is in turn diverted to lakes of lower elevation through other powerhouses. Thus, an accurate forecast of inflow into Lake Thomas Alva Edison and Florence Lake can greatly improve the operational efficiency of the Big Creek Hydroelectric Project.

6.3 Framework

This study aims at quantifying the impact of aerosol particles on inflow into Florence Lake Reservoir and Lake Edison and calculating daily inflow forecasts for these two reservoirs. A dynamic regression model was built to forecast the inflow which uses meteorological variables like daily mean temperature, accumulative snow water equivalent, and incremental precipitation as explanatory variables. Observed inflow data and observed meteorological variables data were split into a training set and a testing set. The testing set was formed by withholding the data for the last water year from the model identification and estimation process and the rest are used as the training set. The training data set was used to estimate the model parameters. The forecasting accuracy of the model was assessed by performing out-of-sample forecasting on the testing set. Forecasts of the predictor variables considering the impact of aerosols on regional climate were calculated in the San Joaquin Valley of California using a version of Weather Research and Forecasting Model with Chemistry [141, 415] with fully coupled aerosol-meteorology-snowpack. Meteorological variable forecasts without the impact of aerosols were also calculated for the same region. Both forecasts were used as respective testing sets for calculating inflow forecasts with and without the impact of aerosols. Yearly and seasonally aggregated inflow forecasts were then compared to quantify the impact of aerosols on inflow into Lake Edison and Florence Lake. The procedure is summarized schematically in Figure 6.1.

6.4 Technical methods

In this study, we build a statistical hydrologic model with a dynamic regression method to forecast daily inflow into the hydroelectric reservoirs. Here, meteorological variables such as temperature, precipitation, and SWE are used as explanatory variables. A dynamic regression model or ARIMAX model [281], uses time-lagged explanatory variables to forecast the dependent variable while modeling the error term with an ARIMA model [54]. Reasons for choosing dynamic regression model were discussed in Section 6.1. We

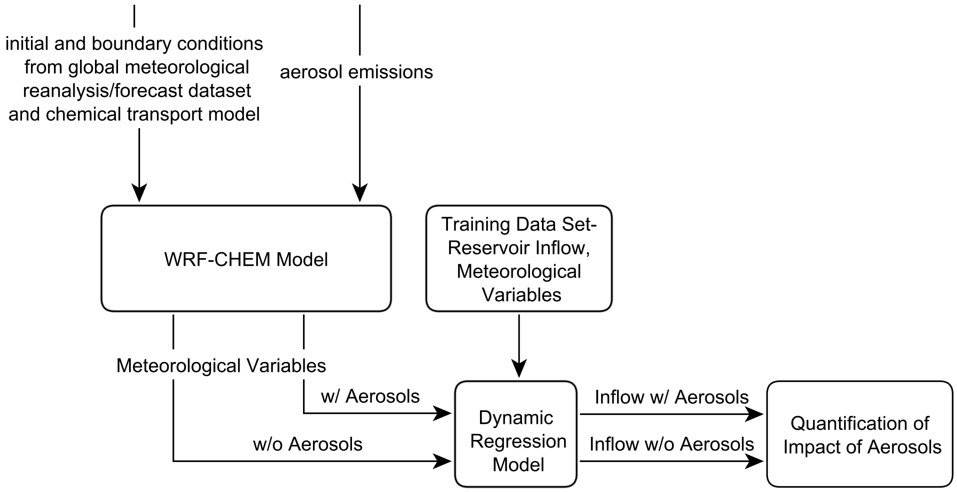

Figure 6.1: The overall framework for quantifying the impact of aerosols on reservoir inflow

conduct model building by applying relevant theory to choose the input variables and then following standard methodology for building dynamic regression models. The linear transfer function (LTF) method suggested by [281] is applied here to specify the transfer functions and the methodology described by [54] is applied to determine the ARMA order of the error time series. Finally, the coefficients of the entire model are estimated and the model is checked for adequacy. An overview of the dynamic regression model and LTF method is provided below in Section 6.4.1.

6.4.1 Dynamic regression model

. A dynamic regression model is shown in Equation (6.1). A crucial assumption in dynamic regression is that the explanatory variables are not affected by the dependent variable, i.e. there is no feedback between the variables.

$$Y_t = v\left(B\right) X_t + N_t \tag{6.1}$$

where

$Y_t =$ Dependent variable

$X_t =$ The vector of explanatory variables

$v\left(B\right) =$ Transfer function

$N_t =$ Noise time series

A free form distributed lag transfer function model like Equation (6.2) for M explanatory variables can be estimated where the noise series is approximated by a low order regular AR term proxy. The order of the transfer function, k_i is chosen based on the empirical understanding of the model.

$$Y_t = \sum_{i=1}^{M} \sum_{j=0}^{k_i} v_{i,j} X_{i,t-j} + \frac{1}{\phi\left(B\right)} a_t \tag{6.2}$$

where

$X_{i,t} =$i-th explanatory variable

$\phi\left(B\right) =$ Low-order autoregressive proxy

$a_t =$White Noise

The individual weights $v_{i,j}$ are called impulse response weights. The transfer function can be written in a parsimonious form known as a rational distributed lag transfer function model as shown in Equation (6.3).

$$Y_t = \mu + \sum_{i=1}^{M} \frac{\omega_i (B)}{\delta_i (B)} B^{b_i} X_{i,t} + N_t \tag{6.3}$$

where

$\omega_i (B) = \omega_{i,0} + \omega_{i,1} B + \omega_{i,2} B^2 ... + \omega_{i,h_i} B^{h_i}$

$\delta_i (B) = 1 - \delta_{i,1} B - \delta_{i,2} B^2 - ... - \delta_{i,r_i} B^{r_i}$

$b_i =$ Dead time for input $X_{i,t}$

It should be noted that r_i, h_i, and b_i are constants for the i-th explanatory variable. (b, r, h) are the orders of the rational distributed lag transfer function. The numerator of the transfer function model captures the lagged effect of the covariates and the denominator represents the decaying effects of the covariates. The noise series N_t may have an autocorrelated time structure that can be described by an ARIMA model.

The autoregressive (AR) component in the ARIMA model refers to the lagged values of the dependent variable time series; the moving average (MA) component refers to the lagged error terms, i.e. residuals; and the integrated component represents the number of times a time series must be differenced to achieve stationarity. A general notation for ARIMA models is ARIMA (p, d, q), where p denotes the number of autoregressive terms, q denotes the number of moving average terms, and d denotes the number of times a series must be differenced to induce stationarity. Using the general notations of an ARIMA model, the noise series can be written as:

$$N_t = \frac{\theta(B)}{\phi(B)} a_t \tag{6.4}$$

where

$\phi(B) = 1 - \phi_1 B - \cdots - \phi_p B^p$

$\theta(B) = 1 - \theta_1 B - \cdots - \theta_q B^q$

Here, a_t is assumed to be white noise. The white noise assumption implies zero mean, normal distribution, and constant variance. Finally, the dynamic regression model can be written as follows:

$$Y_t = \mu + \sum_{i=1}^{M} \frac{\omega_i(B)}{\delta_i(B)} B^{b_i} X_{i,t} + \frac{\theta(B)}{\phi(B)} a_t \tag{6.5}$$

Linear transfer function (LTF) method

The linear transfer function (LTF) method suggested by [281] was applied in this study to handle multiple inputs. The order of the rational form transfer function (b_i, r_i, h_i) for each variable i needs to be determined together with the order of ARIMA (p, d, q) model for the noise time series N_t. LTF method uses a free form distributed lag model to estimate the impulse response weights in Equation (6.2) together with an initial autoregressive proxy for the autocorrelation term of the disturbance time series N_t. If N_t is not stationary with a time-varying mean, then both the input and output time series should be differenced accordingly. A parsimonious rational form transfer function similar to Equation (6.3) is then identified by comparing the estimated impulse response weight pattern with theoretical impulse response weight patterns. The methodology described by [54] is then applied to determine the ARMA order of the error time series N_t. Finally, the coefficients of the entire model are estimated and the model is checked for adequacy.

Performance metrics

Out-of-sample forecasting was performed to assess the forecasting accuracy of the model [244]. Some of the sample data at the end of the time series were withheld as the testing dataset. They were not used in the model identification and estimation process. The fitted model was used to forecast the response variable. Root mean square error (RMSE), mean absolute error (MAE), Nash-Sutcliffe efficiency (NSE), a modified version of NSE [131, 215], percent bias (PBIAS) and RMSE-observations standard deviation ratio (RSR) [265] were used as accuracy metrics to evaluate the performance of the proposed model and the benchmark models introduced in Section 6.5.4.

[265] using three quantitative statistics, Nash-Sutcliffe efficiency (NSE), percent bias (PBIAS), and RMSE-observations standard deviation ratio (RSR) for model evaluation. In addition to the above three statistics, we used a modified version of NSE proposed by [131, 215] for model evaluation.

MAE and RMSE RMSE and MAE values signify the goodness of fit of the forecast to the observed inflow and hence can evaluate the performance of the dynamic regression model.

$$RMSE = \sqrt{\sum_{i=1}^{n} \frac{(Y_{fi} - Y_{oi})^2}{n}} \tag{6.6}$$

$$MAE = \sum_{i=1}^{n} \frac{|Y_{fi} - Y_{oi}|}{n} \tag{6.7}$$

Here, i denotes the day in a water year, Y_{fi} represents the forecasted inflow on the day i, Y_{oi} denotes the observed inflow on the day i, and n is the number of days in the water year.

NSE and modified NSE The Nash and Sutcliffe [271] coefficient (NSE) is the most widely used indicator in hydrology because of its flexibility to apply to different types of mathematical models and intuitive interpretability [257, 299, 313]. It has been used widely in streamflow and runoff predictions [83, 206, 223, 265, 274, 313]. It is a normalized measure comparing the mean square error generated by a model simulation to the variance of the observed values. NSE effectively compares the performance of a particular model to a simple model which uses the mean of the observed values as the prediction. NSE ranges from minus infinity to 1, with higher values indicating a better forecast.

$$NSE = 1 - \frac{\sum_{i=1}^{N} (Y_{oi} - Y_{fi})^2}{\sum_{i=1}^{N} \left(Y_{oi} - \bar{Y_o}\right)^2} \tag{6.8}$$

Here, $\bar{Y_o}$ is the mean of the observed inflow of the testing period. Several researchers have suggested modifications to the NSE owing to its limitations, such as using the mean of the observations as the baseline model and possible effect of outliers on NSE [131, 206, 215, 277]. Reference [131] termed the use of the mean of observed values as primitive and proposed using the daily mean value of the predictor variable for the calibration period so that the baseline model can indicate the seasonal variation of the predictor variable. This modification of NSE is also recommended by the [275]. Reference [313] recommends using benchmark models appropriate to the particular case study. The modified NSE or benchmark efficiency (BE) indicates performance improvement of the hydrologic model over the benchmark model and can be written as

$$BE = 1 - \frac{\sum\limits_{i=1}^{N} \left(Y_{oi} - Y_{fi}\right)^2}{\sum\limits_{i=1}^{N} \left(Y_{oi} - Y_{bi}\right)^2} \tag{6.9}$$

Here, Y_{bi} represents the forecasted inflow on the day i by the benchmark model. Since NSE is calculated by squaring the deviations between observation and model-calculated values, it is sensitive to extreme values leading to misevaluation of model performance [83, 206, 215, 383]. Reference [215] proposed NSE', a modification of NSE using absolute values instead of squared deviation reducing the effect of squared terms. In [216], they maintain the recommendation of NSE and NSE' because of their intuitive interpretability and having a fundamental meaning at zero. In general, NSE' has a lower value than NSE.

$$NSE' = 1 - \frac{\sum\limits_{i=1}^{N} \left|Y_{oi} - Y_{fi}\right|}{\sum\limits_{i=1}^{N} \left|Y_{oi} - \bar{Y_o}\right|} \tag{6.10}$$

PBIAS Percent bias (PBIAS) measures the average tendency of the simulated data to be larger or smaller than their observed counterparts [145]. The optimal value of PBIAS is 0 with low magnitude values indicating accurate model simulation. Positive values indicate model underestimation bias and negative values indicate model overestimation bias.

$$PBIAS = \frac{\sum\limits_{i=1}^{N} (Y_{oi} - Y_{fi}) \times 100}{\sum\limits_{i=1}^{N} Y_{oi}} \tag{6.11}$$

RSR RSR standardizes RMSE using the observation standard deviation and is calculated as the ratio of the RMSE and standard deviation of measured data with lower RSR indicating better model prediction performance.

$$RSR = \frac{RMSE}{STDEV_{obs}} = 1 - \frac{\sqrt{\sum\limits_{i=1}^{N} (Y_{oi} - Y_{fi})^2}}{\sqrt{\sum\limits_{i=1}^{N} \left(Y_{oi} - \bar{Y}_o\right)^2}} \tag{6.12}$$

6.4.2 WRF-Chem model

The WRF-Chem model [141] is a weather research and forecasting system that simulates chemistry and aerosols simultaneously with meteorology. This model has been extensively used to study regional air quality and their interactions with weather and climate (e.g., [38, 67, 114, 113, 290, 388, 389, 390, 387, 385, 416, 414, 415]). In this study, we used the WRF-Chem version 3.5.1 which includes aerosol interactions with radiation, cloud and snowpack [415]. In the WRF-Chem control (CTRL) experiment, the model is run at 4 km horizontal resolution with the model domain covering California and surrounding regions. The major components of aerosols (nitrate, ammonium, elemental carbon, primary organic matter, sulfate, sea salt, dust, water, and other inorganic matter) are simulated in the model along with their physical and chemical processes. Anthropogenic aerosol emissions are obtained from US EPA 2005 National Emissions Inventory (NEI05; US EPA, 2010). Aerosol emissions comprise SO_4, NO_3, EC, organic aerosols, and total $PM_{2.5}$ and PM_{10} masses. Anthropogenic emissions are updated every hour to account for diurnal variability. However, their seasonal variation is not considered in the simulation. Biogenic emissions are calculated online using the Model of Emissions of Gases and Aerosols from Nature (MEGAN)[143]. Biomass burning emissions are obtained from the Global Fire Emissions Database version 2.1, with 8-day temporal resolution and monthly updates [105]. However, year-to-year variability in biomass burning aerosols is not taken into account. Dust emissions are calculated using the DUST TRANsport model (DUSTRAN) scheme [325] following [387]. Sea salt emissions are derived from the PNNL-updated sea salt emission scheme that includes the correction of particles with a radius less than 0.2 μm [137] and dependence on sea surface temperature [174].

To derive aerosol optical properties (e.g. extinction, single-scattering albedo, and the asymmetry parameter for scattering) as a function of wavelength, Mie calculations [339] is used. Aerosol radiation interaction is included in the shortwave and longwave radiation schemes [115, 417]. Aerosol cloud interaction is effectively simulated in WRF-Chem [67] by linking simulated cloud droplet numbers with shortwave radiation and microphysics schemes. In this version of WRF-Chem [415], aerosol snow interaction is implemented by considering the deposition of aerosol on snow and the subsequent radiative impacts through the SNICAR (SNow, ICe, and Aerosol Radiative) model [118, 119]. The Morrison double-moment microphysics scheme [266], Rapid Radiative Transfer Model for general circulation models (RRTMG) model shortwave and longwave radiation schemes [170], Community Land

Model (CLM) Version 4 land surface scheme [212] are the physics parametrizations used in the simulations. The Yonsei University (YSU) planetary boundary layer (PBL) scheme [167] is used in the simulations. The initial and boundary conditions are provided by the European Center for Medium-Range Weather Forecasts Interim Re-Analysis [91] for meteorology and the global Model for Ozone and Related chemical Tracers, version 4 [104] for chemistry. Reference [385] showed that the model simulations reproduced the spatial and temporal variation of observed precipitation well. More details of the model setup can be found in [385].

[387, 385] evaluated the model performance on simulating aerosols and meteorological variables in California. It has been shown that the model reasonably captures the distribution and seasonal variability of aerosols from October to June, but underestimates aerosols from July to September. Since precipitation, snowpack, and inflow are mainly within October-June, the underestimation of aerosols in July-September has limited impacts on our results. The model reproduced the seasonal variations of temperature, precipitation, and SWE in California with some overestimation of temperature and SWE. In a CLEAN simulation, we turned off local aerosol emissions and set aerosols from boundary conditions as zero, but kept chemical components from boundary conditions with aerosol chemistry on. The CCN in the CLEAN experiment was on the order of 10 cm-3, representing a clean environment. The simulations of clouds, precipitation, and radiation are reasonable in the CLEAN run. Thus, meteorological variables from the WRF-Chem CTRL and WRF-Chem CLEAN simulations represent conditions with and without considering the impact of aerosols respectively. Aerosol impacts on temperature, precipitation, and SWE were investigated in [385] and discussed in the introduction and Section 6.6.

6.5 Building inflow forecasting model

In this section, we explain how to build the dynamic regression model to forecast the reservoir inflow of Florence Lake and Lake Edison which are part of the Big Creek Hydroelectric Project in California.

6.5.1 Data description

The data set contains the daily average reservoir inflow in cft/second for five consecutive water years 2010-2014. A water year or a hydrological year is a 12-month period between October 1 of one year and September 30 of the next year. To predict the reservoir inflow, we collected meteorological data such as the daily air temperature, SWE, and incremental precipitation data from the website of the California data exchange center. Data for meteorological variables, inflow, and WRF-Chem simulations used in this study can be found in [93]. The meteorological data were collected and averaged over three weather stations of Kaiser Point (KSP), Volcanic Knob (VLC), and Upper Burnt Corral (UBC) located within the 0.4×0.4^o grid box with center at $(37.32^o N, -118.97^o E)$. The study area with the grid box is shown in Figure 6.2 with the snow depth distribution map averaged over the water year 2013 overlaid on it. The observations of these meteorological variables are plotted in Figure 6.3.

Dummy Variables	Description	Season
D_1	1 if Date 03/21-04/30, 0 otherwise	Early Spring
D_2	1 if Date 05/01-05/31, 0 otherwise	Late Spring
D_3	1 if Date 06/01-06/21, 0 otherwise	Early Summer
D_4	1 if Date 06/22-09/22, 0 otherwise	Late Summer

Table 6.1: Description of dummy variables used in the dynamic regression model

6.5.2 Predictor/Variable selection

The selection of appropriate predictors or explanatory variables is essential for accurate forecast and simple model interpretation. The inflows are generated by the runoff captured by the reservoirs from the San Joaquin River. Streamflow in the Sierra Nevada region has a high correlation with temperature, SWE, and precipitation [66]. Therefore, these three variables were included in the model to forecast the inflow.

Being a mountainous region, runoff in the Sierra Nevada region is dominated by snowmelt. Maximum runoff in the San Joaquin watershed occurs during the snowmelt runoff period (April-July) [322, 340]. Accordingly, most of the reservoir inflows occur in the late spring and early summer between April and July in both Florence Lake and Lake Edison as observed in Figure 6.3. Therefore, snowmelt during this period is a useful predictor for reservoir inflow. Snowmelt can be calculated by $\max\left(SWE_{t-1} - SWE_t, 0\right)$. To handle the seasonality, four dummy variables were introduced in Table 6.1 to represent four periods in a year. These periods are early spring, late spring, early summer, and late summer. We also added interaction terms between the four meteorological variables, temperature, SWE, precipitation, and snowmelt with seasonal dummy variables to model different effects of meteorological variables in different seasons. Since there is a lag of several months between the peak snow accumulation and peak inflow in our study area as seen from Figure 6.3, lagged snow water equivalent in the late summer was included in the dynamic regression model to capture this effect. To choose the appropriate lag, stepwise regression is performed with up to 3 month lag of SWE as regressors along with current and lagged temperature, precipitation, and snowmelt as independent variables. Statistically significant lags of SWE are chosen as suitable candidates for inclusion in the final model. 80 days lagged SWE minimized the Akaike Information Criterion (AIC) of the model during the training period and is therefore chosen to be included in the final model. The complete list of variables used in building the statistical dynamic regression model is tabulated in Table 6.2.

Variables	Symbols
Reservoir Inflow	Y
Temperature	X_1
SWE	X_2
Precipitation	X_3
Snowmelt	X_4
Dummy Variables	D_1, D_2, D_3, D_4
Interaction Terms	$X_1D_1, X_1D_2, X_1D_3, X_1D_4, X_2D_1, X_2D_2,$ $X_2D_3, X_2D_4, X_3D_1, X_3D_2, X_3D_3,$ $X_3D_4, X_4D_1, X_4D_2, X_4D_3, X_4D_4$

Table 6.2: List of variables used in the dynamic regression model

6.5.3 Model Building

We explored the model performance with and without natural log transformation of the response and explanatory variables and chose untransformed variables for further model building as it offered better prediction results and model interpretation. The steps of building the dynamic regression model for the Florence Lake inflow forecast are described here. A similar procedure can be followed for Lake Edison. Building a dynamic regres-

Lag	Estimate	t-value	Lag	Estimate	t-value	p-value
0	-59.55	-0.67	8	-300.71	-4.03	$< .0001$
1	862.75	10.83	9	217.35	3.33	0.0009
2	220.73	2.88	10	-240.18	-3.94	$< .0001$
3	84.11	1.01	11	65.52	1.09	0.2769
4	548.99	6.67	12	-31.77	-0.57	0.5714
5	67.09	0.84	13	8.60	0.15	0.8773
6	-30.91	-0.42	14	-46.42	-0.81	0.4191
7	192.40	2.56	15	190.53	3.39	0.0007

Table 6.3: Impulse response weights of input variable X_4D_3

sion model has three stages, (1) model identification, (2) model estimation, and (3) model diagnostic checking.

Model identification

As the first step to identify the appropriate dynamic regression model, a free form distributed lag for the transfer function of the explanatory variables was estimated with a low order regular AR term as a proxy for the disturbance series autocorrelation pattern. A multiple regression model was formed and stepwise regression was performed to preliminarily select candidate variables and their time lags for building the free form distributed lag model. The orders of $v(B)$ for the other variables in the free form distributed lag model was determined to be 15 based on their t-test statistics. It can be argued that the inflow is zero when the explanatory variables are zero i.e. when there is no snowmelt or precipitation and the temperature is 0^oF. Therefore, no constant term was included in the model.

The disturbance series N_t was then checked for stationarity by augmented Dickey-Fuller test and found to be stationary. A parsimonious rational distributed lag transfer function model of order (b, r, h) was identified by comparing the estimated impulse response weights with theoretical impulse response weight patterns. To demonstrate the process, the estimated impulse response weights of the variable X_4D_3 which corresponds to snowmelt in early summer are shown in Table 6.3 and plotted in Figure 6.4.

There are 6 significant v weights at lag $1, 2, 4, 7, 9$ and 15 having t-value more than 2.0. This suggests that the dead time, $b_1 = 1$. Since the 6 significant impulse response weights follow an exponential decay pattern, the order of the denominator operator was determined to be $r = 1$. The number of unpatterned terms is $u = 0$. Finally, the order of the numerator operator is $h = u+r-1 = 0+1-1 = 0$. The order of the rational distributed lag transfer function for input variable snowmelt in early summer (X_4D_3) was thus determined to be $(b, r, h) = (1, 1, 0)$ and the transfer function could be written as $\frac{\omega_i}{1-\delta_i B}B$. Similar procedure was followed for other input variables, and the dynamic regression model with parsimonious rational distributed lag transfer function was determined.

Model estimation

An estimate of the parameters of the dynamic regression model was obtained at this stage. An appropriate ARMA model was identified for the error series N_t and the entire model was refit using the ARMA model for error and the transfer function for the input variables. The parameter estimates of all candidate models were estimated by maximum likelihood estimation.

First, the model was fit using only the transfer function of the input variables. The orders of AR and MA components of the model were identified by matching empirical autocorrelation patterns, e.g. autocorrelation function plot (ACF) and partial autocorrelation function (PACF) plots of the residual series with the AR and MA signature patterns. The ACF and PACF plots of the residual series are plotted in Figure 6.5. Both ACF and the PACF exhibit large spikes that gradually die out indicating that they have both autoregressive and moving averages properties. Though the ACF decays rather slowly and cuts off at lag 6, an AR order of $p = 6$ is not realistic. An AR order of $p = 1$ was selected based on the Akaike Information Criterion (AIC) and ACF of the residuals. The PACF cuts off at lag 1. Therefore, the final ARMA model for the error series was determined to be $(p, q) = (1, 1)$. At this stage, the dynamic regression model for Florence Lake can be written as (6.13).

Diagnostic checking

The Ljung-Box test for white noise was used to statistically evaluate the degree to which the residuals are free from serial correlation. For seasonal time series, the lag for Ljung-Box test is recommended to be $h = \min\left(2m, \frac{T}{5}\right)$ where m is the period of seasonality and T is the sample size. In our study, the lag was calculated to be $h = 365 \times 3/5 = 219$. Though the residuals are not perfect white noise after $lag = 25$; for a long time series, this is acceptable. Moreover, Durbin Watson Statistic was calculated to detect the presence of autocorrelation in the residuals and found to be 2 which shows that the residuals are not autocorrelated. Normality check of the model residuals was performed by checking a histogram of the residuals and the Q-Q normal plot of the residuals. The residuals were found to be approximately normally distributed and the Q-Q normal plot is approximately a straight line. The explanatory variables in the final model were checked for multicollinearity.

For all explanatory variables, the variance inflation factor (VIF) was calculated. A VIF close to 1 for an explanatory variable indicates no correlation between that predictor and the remaining explanatory variables. For all explanatory variables in this model, VIF was found to be < 1.60. Hence, there is no multicollinearity. Since there is no significant residual cross-correlation and autocorrelation left, the model is adequate. A similar procedure was followed for Lake Edison. The dynamic regression model for Florence Lake and Lake Edison can be written as Equation (6.13) and Equation 6.14.

$$\begin{aligned} Y_t = &\left(\omega_{0,0} + B\omega_{0,1} + B^2\omega_{0,2} + B^3\omega_{0,3} + B^4\omega_{0,4}\right) X_{3,t} \\ &+ \left(\omega_{1,0} + B\omega_{1,1} + B^2\omega_{1,2} + B^3\omega_{1,3}\right) X_{1,t}D_{1,t} \\ &+ \left(\omega_{2,0} + B\omega_{2,1} + B^2\omega_{2,2} + B^3\omega_{2,3}\right) X_{1,t}D_{2,t} + \frac{\omega_3}{(1-\delta_3 B)} X_{4,t}D_{2,t} \\ &+ \left(\omega_{4,0} + B\omega_{4,1} + B^2\omega_{4,2} + B^3\omega_{4,3}\right) X_{1,t}D_{3,t} + \frac{\omega_5}{(1-\delta_5 B)} X_{4,t}D_{3,t} \\ &+ \omega_6 B^{80}\left(X_{2,t}\right) D_{4,t} + \frac{\omega_7}{(1-\delta_7 B)} BX_{4,t}D_{4,t} + \frac{(1-\theta_1 B)}{(1-\phi_1 B)} a_t \end{aligned} \tag{6.13}$$

$$\begin{aligned} Y_t = &\omega_0 X_{1,t} + \omega_1 X_{3,t} + \left(\omega_{2,0} + B\omega_{2,1} + B^2\omega_{2,2} + B^3\omega_{2,3}\right) X_{1,t}D_{1,t} \\ &+ \left(\omega_{3,0} + B\omega_{3,1} + B^2\omega_{3,2} + B^3\omega_{3,3} + B^4\omega_{3,4}\right) X_{1,t}D_{2,t} \\ &+ \frac{\omega_4}{(1-\delta_4 B)} X_{4,t}D_{2,t} + \left(\omega_{5,0} + B\omega_{5,1} + B^2\omega_{5,2} + B^3\omega_{5,3}\right) X_{1,t}D_{3,t} \\ &+ \frac{\omega_6}{(1-\delta_6 B)} X_{4,t}D_{3,t} + \omega_7 B^{80}\left(X_{2,t}\right) D_{4,t} \\ &+ \frac{\omega_8}{(1-\delta_8 B)} BX_{4,t}D_{4,t} + \frac{(1-\theta_1 B)}{(1-\phi_1 B)} a_t \end{aligned} \tag{6.14}$$

The estimated parameter values of the dynamic regression models are shown in Table 6.4 and Table 6.5. The estimated parameter values of the dynamic regression models with their

Coefficient	Value	Standard error	t-value	p-value
θ_1	.07	0.04	1.91	0.06
ϕ_1	0.78	0.02	33.60	< 0.0001
$\omega_{0,0}$	14.06	8.81	1.60	0.1
$\omega_{0,1}$	6.37	9.08	0.70	0.5
$\omega_{0,2}$	9.24	9.10	1.01	0.3
$\omega_{0,3}$	7.74	9.079	0.85	0.4
$\omega_{0,4}$	12.79	8.83	1.45	0.1
$\omega_{1,0}$	1.16	1.27	0.92	0.3
$\omega_{1,1}$	6.17	1.38	4.47	< 0.0001
$\omega_{1,2}$	1.06	1.38	0.77	0.4
$\omega_{1,3}$	2.10	1.26	1.66	0.09
$\omega_{2,0}$	2.13	1.23	1.73	0.08
$\omega_{2,1}$	8.40	1.29	6.51	< 0.0001
$\omega_{2,2}$	-0.50	1.31	-0.38	0.7
$\omega_{2,3}$	0.06	1.23	0.05	0.9
ω_3	93.18	23.23	4.01	< 0.0001
δ_3	0.95	0.02	50.05	< 0.0001
$\omega_{4,0}$	0.86	1.29	0.66	0.5
$\omega_{4,1}$	3.05	1.12	2.72	0.006

t-values, p-values and standard error are shown in Table 6.4 and Table 6.5.

Coefficient	Value	Standard error	t-value	p-value
$\omega_{4,2}$	1.97	1.12	1.76	0.08
$\omega_{4,3}$	2.49	1.10	2.25	0.02
ω_5	324.03	38.22	8.48	< 0.0001
δ_5	0.79	0.03	26.68	< 0.0001
ω_6	12.92	1.94	6.66	< 0.0001
ω_7	149.15	19.66	7.59	< 0.0001
δ_7	0.92	0.01	62.27	< 0.0001

Table 6.4: Parameter estimates for inflow forecast model of Florence Lake

Coefficient	Value	Standard error	t value	p-value
θ_1	-.03	0.03	-0.89	0.4
ϕ_1	0.86	0.02	49.14	< 0.0001
ω_0	0.52	0.24	2.25	0.02
ω_1	21.55	2.75	7.85	< 0.0001
$\omega_{2,0}$	0.31	0.46	0.69	0.5
$\omega_{2,1}$	2.39	0.45	5.36	< 0.0001
$\omega_{2,2}$	0.97	0.44	2.17	0.03
$\omega_{2,3}$	0.56	0.43	1.30	0.2
$\omega_{3,0}$	1.16	0.45	2.58	.0099
$\omega_{3,1}$	2.18	0.42	5.15	< 0.0001
$\omega_{3,2}$	1.75	0.43	4.06	< 0.0001
$\omega_{3,3}$	0.64	0.42	1.51	0.1
$\omega_{3,4}$	0.47	0.37	1.27	0.2
ω_4	56.90	12.65	4.50	< 0.0001
δ_4	0.31	0.23	1.35	0.2
$\omega_{5,0}$	0.58	0.46	1.26	0.2
$\omega_{5,1}$	0.68	0.37	1.80	0.07
$\omega_{5,2}$	1.38	0.37	3.69	0.0002
$\omega_{5,3}$	2.12	0.37	5.71	< 0.0001
ω_6	126.80	14.58	8.70	< 0.0001
δ_6	0.84	0.02	34.52	< 0.0001
ω_7	2.48	0.88	2.82	0.0048
ω_8	85.75	8.24	10.40	< 0.0001
δ_8	0.94	0.008	107.91	< 0.0001

Table 6.5: Parameter estimates for inflow forecast model of Lake Edison

6.5.4 Results and analysis

Parameter estimates and interpretation

The estimated parameter values of the dynamic regression models with their t-values, p-values and standard error are shown in Table 6.4 and Table 6.5. A larger value of absolute t-statistic and low p-value (< 0.05) implies that the true parameter value is not 0. It can be observed that temperature, SWE, and precipitation play important roles in forecasting reservoir inflow. For both lakes, snowmelt during spring and summer has a strong and positive correlation with inflow. With high t-values, snowmelt is the most important variable in explaining the variability of inflow. This result is consistent with the fact that the runoff in the Sierra Nevada region is dominated by snowmelt. Prior season's SWE is also found to be a useful predictor for inflow during late summer. This can be explained by the fact that the snowpack during cold seasons plays a crucial role in runoff and subsequent reservoir inflow during warmer seasons in the Sierra Nevada region. The current season's temperature has a positive correlation with reservoir inflow in early/late spring and early summer. This is because, in higher elevation rivers, warmer temperature produces faster runoff and fewer snow [66]. Apart from early/late spring and early summer, the temperature does not have a significant impact at Florence Lake, but has a moderate impact at Lake Edison. As shown in the model fitting results, same season precipitation has a significant impact on reservoir inflow at both Florence Lake and Lake Edison. As expected, precipitation is positively correlated with inflow since a higher level of precipitation generally results in more inflow.

Lake	NSE	NSE	PBIAS	RSR	RMSE (cu ft/s)	MAE (cu ft/s)
Florence	0.97	0.82	3.79	0.18	115.91	60.09
Edison	0.97	0.82	3.54	0.17	52.49	30.88

Table 6.6: Error statistics of the dynamic regression model during calibration period 2010-2013

Performance Rating	RSR	NSE	—PBIAS—
Very good	$0.00 \leq RSE \leq 0.50$	$0.75 < NSE \leq 1.00$	$\|PBIAS\| \leq 10$
Good	$0.50 < RSE \leq 0.60$	$0.65 < NSE \leq 0.75$	$10 \leq \|PBIAS\| < 15$
Satisfactory	$0.60 < RSE \leq 0.70$	$0.50 < NSE \leq 0.65$	$15 \leq \|PBIAS\| < 25$
Unsatisfactory	$RSR > 0.70$	$NSE \leq 0.50$	$\|PBIAS\| \geq \pm 25$

Table 6.7: General performance rating for recommended statistics for a monthly time step [267]

Inflow forecast using dynamic regression model

The performance of the dynamic regression model during the calibration period is evaluated using NSE, NSE', PBIAS, RSR, RMSE, and MAE. The statistical indexes of model performance are shown in Table 6.6. Limits of acceptability of the performance metrics depend on model applications and are therefore subjective [50]. Following reference [267], the model performance at daily time step is generally considered to be good when $NSE \geq 0.75$ and satisfactory when $0.36 \leq NSE < 0.75$. Based on examples of various existing models and research data, [265] proposed general performance ratings for these statistics. Those are provided in Table 6.7. However, since typically model simulations are poorer for shorter time steps than longer time steps (e.g. daily vs monthly) [49], a less strict performance rating is required for daily time steps used in our study [265]. In general NSE' has a lower value than NSE. For NSE', the model can be considered satisfactory if NSE' ranges from 0.51 to 0.71 [107]. The value of NSE is very high and PBIAS and RSR values are very low during the calibration period indicating an excellent agreement between the observed and simulated inflows into both Florence Lake and Lake Thomas A. Edison. After calibrating the dynamic regression model with the help of historical data, the next step of the study is to simulate inflow corresponding to the future meteorological variables. The forecast period is set to 365 days. The out-of-sample forecasting ability of the model was assessed by forecasting the reservoir inflow for both lakes in the water year 2014 using a testing set containing average meteorological data for the grid box region. Actual and forecasted inflow for Lake Edison and Florence Lake are plotted in Figure 6.6. Figure 6.6 shows good agreement between observed and simulated inflow.

Statistical indexes of the model performance during the testing period are shown in Table 6.8. The NSE of Florence Lake and Lake Thomas A. Edison are 0.78 and 0.72 respectively which is considered to be good in [267]. Comparing NSE, PBIAS, and RSR value of the model with the general performance rating recommendation in [265] in [265],

Lake	Statistics	Dynamic Regression	Regression	Ratio Estimator
Florence	RMSE	100.75	114.33	136.62
	MAE	58.47	73.46	79.02
	NSE	0.78	0.57	0.72
	NSE’	0.62	0.53	0.53
	PBIAS	0.16	31.47	-26.20
	RSR	0.46	0.65	0.53
Edison	RMSE	44.52	50.97	67.85
	MAE	27.84	38.12	38.31
	NSE	0.72	0.54	0.67
	NSE’	0.58	0.40	0.51
	PBIAS	-8.85	44.32	-31.28
	RSR	0.53	0.68	0.57

Table 6.8: Forecast error statistics (cft/second) for water year 2014

it can be concluded that, for daily step, the fit of the dynamic regression model during the testing period is very good for both Florence Lake and Lake Thomas A. Edison. The modified NSE proposed by [131] is Benchmark efficiency (BE) calculated using the daily mean value of the predictor variable for the calibration period as the baseline model. It is found to be 0.90-0.91 showing very high performance of the dynamic regression model compared to the baseline model. The NSE value also indicates the good performance of the model. The small root mean square error in Table 6.8 also indicates that the dynamic regression model is capable of producing a reasonable forecast of inflows into the reservoirs. Moreover, the errors in the annual inflow forecast for Florence Lake and Lake Edison are only 0.15% and 10% respectively.

For further comparison, we included a benchmark model, which is a multiple regression model containing the same explanatory variables as the dynamic regression model. The time-lagged relationships were incorporated by including the time-lagged variables as separate explanatory variables. The inflow of the previous day was also included as an explanatory variable. Statistics indexes of the multiple regression model are shown in Table 6.8. Another benchmark estimator would be a ratio estimator based on the same day inflow from last year, which can be written as Equation (6.15).

$$Y_t = Y_{t-365} \times \frac{\text{Peak SWE}_{\text{current year}}}{\text{Peak SWE}_{\text{previous year}}} \tag{6.15}$$

The values of all the performance metrics indicate that the dynamic regression model consistently outperforms the benchmark multiple regression model and the ratio estimator. PBIAS values of the regression model and the ratio estimator are not satisfactory for both

Florence Lake and Lake Thomas A. Edison. Moreover, the dynamic regression model is more parsimonious compared to the multiple regression model. From the visual comparison of the observed and simulated inflow in Figure 6.6, low error in annual inflow forecast, the value of the statistical indexes, and their comparison with regression and the ratio estimator, it can be concluded that the dynamic regression model is very good at forecasting reservoir inflows.

Robustness analysis of the dynamic regression model

Global sensitivity analyis A global sensitivity analysis of the dynamic regression model was performed with the purpose of assessing the robustness of the model and simulation results. Input values of the model were perturbed within their reasonable range and subsequent changes in model output were studied[41, 78, 350, 361]. Changes in input values automatically cause perturbations in parameter estimates of the dynamic regression model. Little change in resultant output values indicates the robustness of the model to perturbations of inputs and parameter estimates and shows the uncertainty of the output variables to be relatively small [361].

A qualitative global sensitivity analysis (GSA) was performed in this study by visual inspection of model predictions. All input values were varied simultaneously within the entire allowable ranges of the input space and the effect on the output was studied [41, 287]. This allowed GSA to evaluate the relative contributions of each input factor to the model output variable and account for effects of nonlinear interactions between different inputs [80, 41, 158, 309]. Though local sensitivity analysis where inputs are varied one at a time (OAT) is more common, it assumes a linear relationship between inputs and outputs, making it only a perfunctory sensitivity analysis for most models [311]. GSA does not assume any such specific relationship between inputs and model predictions and therefore, is recommended for any kind of model [311, 243, 303].

We followed the General Probabilistic Framework (GPF) based on Monte Carlo simulation for the global sensitivity analysis of deterministic models proposed by [41]. The flowchart for the GPF can be found in [41]. As is the norm, output in the sensitivity analysis does not refer to the entire range of temporal inflow variable produced by the model [287]. Rather, it is measured as the variability induced in the model performance measure, RMSE of the testing set. In the first step, all sources of uncertainty in the input meteorological variables, U_{xi} were characterized. Since meteorological data were taken as the average of three weather stations- namely KSP, UBC, and VLC, uncertainty may arise due to variability of meteorological variables between the calculated average and actual value at the location of Florence Lake and Lake Edison. Errors and approximations in input data measurement are other sources of uncertainty. Since meteorological variable measurements are not available at Florence Lake and Lake Edison, to account for the uncertainty, a grid box of 0.5×0.5^o with center at $(37.32^oN, -118.97^oE)$ was considered. Two more weather stations, Huntington Lake (HNT) and Tamarack Summit (TMR), are located within the grid box along with the three existing weather stations. The average of the meteorological variables in these five weather stations was calculated. In accordance with the comparison between data from the average of three weather stations and five weather stations, a random error was introduced to the daily nominal value of each variable. Measurement differences in the meteorological variables depend on the type of water year and season.

As such, unnaturally big variability can be introduced if random values are taken from the probability distribution of the difference time series. To preserve the temporal correlation of the meteorological variables, a random variable following uniform distribution on the interval [0, 1] was multiplied with $X_{5\ stations} - X_{3\ stations}$ where X denotes meteorological variables. The resultant random error was added to the meteorological variables data to produce the perturbed inputs. Each variable was physically constrained to avoid unrealistic values (e.g. negative value for precipitation and SWE).

The realization of each uncertainty was then associated with a scalar input factor $F_i = 1...128$ for $i = 1..3$. The three input factors were assumed to be independent. To minimize the number of model runs, a quasi-randomized, low-discrepancy sampling design called Sobol sequence was used to sample the three discrete uniform distributions according to the method present in [41, 310]. No correlations among the three input factors were considered in the sampling design. The simulations were run using a number of sampling points N=128 which corresponds to a number of total number of model runs $N_R = N(2\times3+2) = 1024$. A combination of MATLAB and SAS codes was run to perform the sensitivity analysis.

Result and analysis Figure 6.7 shows the probability distribution of the RMSE of forecasted inflow with perturbed inputs at Florence Lake and Lake Edison in the water year 2014. Out of the 1024 model runs performed in the sensitivity analysis, the model which produces median RMSE is selected for analysis of results. Forecasts of the selected perturbed input model are plotted in Figure 6.8 along with actual inflows and forecasts of reference model for both lakes in the water year 2014. The annual inflow of the selected

Lake	Actual (acre ft)	Reference Model (acre ft)	Perturbed Model (acre ft)
Florence	99979	99818	94872
Edison	49339	54062	49270

Table 6.9: Annual reservoir inflow for the selected perturbed input model with median RMSE and reference model in water year 2014

perturbed input model is compared with the observed and reference model inflow forecast for the water year 2014 in Table 6.9. Here, the reference model is the inflow forecast model with unperturbed inputs. Annual inflow for the perturbed model has less than 5% error for both Florence Lake and Lake Edison. The RMSE results and forecasts show a generally good performance of the model under perturbed inputs which shows the robustness of the model to perturbed inputs and parameter estimates.

The sensitivity analysis of the dynamic regression model was also performed with respect to the number of water years used. Two models were estimated using three and four water years in the training set respectively for both lakes. The water years 2013 and 2014 work as the corresponding testing sets. Parameter estimates of both models are compared for changes in sign. No parameter estimate changes sign between these two simulations for both Florence Lake and Lake Edison. The annual inflow error is 15% and 5% respectively at Florence Lake and Lake Edison when four water years of data are used in the training set to forecast inflow of the water year 2013. Therefore, it can be argued that the model is robust against the increase in the amount of training data.

6.6 Quantifying the impact of aerosols on reservoir inflow

6.6.1 Evaluation of the WRF-Chem simulation

We investigate the WRF-Chem model performance in our region of interest (the black box in Figure 6.2). WRF-Chem CTRL and WRF-Chem CLEAN simulation are WRF-Chem models with and without considering the impact of aerosols respectively. As shown in Figure 6.9, the meteorological variables simulated from the WRF-Chem model are reasonably close to the observed variables. The WRF-Chem model results are highly correlated with the observed meteorological variables for both water years. The correlation coefficients between the observed and WRF-Chem CTRL simulations for temperature and SWE range from 0.88-0.97 for 2013. The correlation coefficient for precipitation ranges from 0.66-0.73 which is adequate for our model since it has lesser impact on inflow as shown in Table 6.4 and Table 6.5. Both visual inspection of Figure 6.9 and one-way ANOVA show that the WRF-Chem model underestimates temperature and precipitation in our interested region. The model underestimates the SWE from December to March and overestimates the SWE from April to June.

The meteorological variables simulated from the WRF-Chem CTRL and WRF-Chem CLEAN models are highly correlated. The RMSE of the simulated meteorological variables with the observed variables is shown in Table 6.10. It can be observed from Table 6.10 that the meteorological variables from the WRF-Chem CTRL simulations are closer to the observed meteorological variables than those of the WRF-Chem CLEAN simulations. In general, the temperature from WRF-Chem CTRL simulations is higher than those of

Year	Simulation	Temperature (^0F)	SWE (inch)	Precipitation (inch)
2013	CTRL	4.86	2.10	0.20
	CLEAN	4.91	2.61	2.61
2014	CTRL	5.78	2.48	0.23
	CLEAN	5.93	2.85	0.25

Table 6.10: RMSE of WRF-Chem simulated meteorological variables with respect to observed variables

the CLEAN simulations because aerosol deposition increases the impurity of snow [385]. Precipitation and SWE from WRF-Chem CTRL simulations are lower than the CLEAN simulations. In order to understand how the aerosols affect these two variables, [385] examine the effects of ARI, ACI, and ASI separately and found that ACI plays a dominant role in increasing cloud water but reducing precipitation, leading to reduced SWE. An increase of non-precipitating clouds can be explained by the fact that more CCN are available for the formation of clouds with smaller cloud droplets when more aerosols are present in the atmosphere. More detailed analysis on aerosol impacts on precipitation and snowpack in our region of interest can be found in [385]. Higher temperature, snow albedo effect, and feedback lead to higher snowmelt with aerosols in the late spring. However, snowmelt is lower with aerosols during early/late summer because of lower prior season's SWE and higher snowmelt in the late spring. From the correlation coefficient of WRF-Chem CTRL and CLEAN simulations and ANOVA, the difference between the simulated SWE and precipitation in the CTRL and CLEAN simulations is larger in 2013 compared to 2014. In other words, the impact of aerosols on these meteorological variables is stronger in 2013 within the grid box.

6.6.2 Quantification of the impact of aerosols on reservoir inflow

The impact of aerosols on reservoir inflow was quantified for two water years 2013 and 2014. In order to quantify the impact of aerosols on inflow, we ran a dynamic regression model using the meteorological variables simulated from both the WRF-Chem CTRL and CLEAN models as inputs of the testing data set. The actual inflow (red) is compared with simulated inflow from observed meteorological variables (blue) and WRF-Chem simulated meteorological variables (green and purple) in Figure 6.10. The inflows simulated by the meteorological variables from the CTRL simulations match well with the actual inflow. The difference in inflow between the CTRL and CLEAN simulations ($Inflow_{CTRL}$-$Inflow_{CLEAN}$) represents the impact of aerosols which is plotted in Figure 6.11. The observed inflow and meteorological data for 2010-2012 are used as the training set while simulating inflow for the water year 2013.

It can be observed from Figure 6.11 that for the same year, the impact of aerosols on inflow is consistent in direction and similar in magnitude in both lakes. After simulating inflow for both water years under CTRL and CLEAN conditions, annual and seasonal inflow with and without considering the impact of aerosols were calculated. The impact of aerosols on inflow into reservoirs was then calculated by Equation (6.16).

$$\frac{Inflow_{\text{w/ Aerosols}} - Inflow_{\text{w/o Aerosols}}}{Inflow_{\text{w/o Aerosols}}} \times 100\% \tag{6.16}$$

The impact of aerosols on annual and seasonal inflow is tabulated in Table 6.12. For seasonal analysis, we first define the four seasons- fall is defined as the period of 10/01-

12/21, winter is defined as 12/22-03/20, spring is defined as 03/21-05/31, and summer is defined as 06/01-09/30.

It can be observed from Figure 6.11 that the difference between WRF-Chem CTRL and CLEAN inflow is negligible during the low inflow period. Inflow during the fall and winter season is extremely low in both Florence Lake and Lake Thomas Alva Edison. During this period, the main contribution to reservoir inflows comes from surface runoff generated by rainfall. As winter is the wet season in this region, most of the rainfall occurs during fall and winter. We also modeled the inflows during this period by temperature since temperature influences precipitation and snow accumulation. From Figure 6.9, it can be observed that precipitation forecast with and without considering the impact of aerosols (WRF-Chem and WRF-Chem CTRL) have up to 6% difference. Temperature forecast from WRF-Chem and WRF-Chem CTRL have up to 4% difference. Extremely low inflow combined with a small difference in key meteorological variables, temperature, and precipitation leads to a small difference between inflows with and without considering the impact of aerosols.

The impact of aerosols is pronounced during the high inflow period from May to June. In general, aerosols lead to slightly higher inflow in the late spring and significantly lower inflow during summer (11%-26% reduction) as seen from Figure 6.11 and Table 6.12. These results can be explained by the seasonal variation of the impact of aerosols on the meteorological variables. During spring, the presence of aerosols leads to enhanced solar absorption by dust aerosol leading to higher temperature and snowmelt which translate into a higher inflow. On the other hand, aerosols lead to lower precipitation which results in a small reduction in the inflow. The aggregated effect of aerosols on inflow through temperature, snowmelt, and precipitation is the slightly higher inflow in the spring. Lower prior season's SWE and lower current season's snowmelt together with lower precipitation result in lower inflow in summer. Low inflow in summer due to the impact of aerosol creates the sudden dip in Figure 6.11 from May to June. This is consistent with the observation in [385] that over mountaintops in the Sierra Nevada region, surface runoff slightly increases in spring and decreases after April. It is helpful to mention again that Florence Lake and Lake Thomas A. Edison are higher elevation lakes that generate inflow by capturing runoff from the San Joaquin River. The presence of aerosols suppresses the precipitation which leads to lower inflow for Florence Lake during fall and winter. In Lake Edison, inflow in fall and winter is simulated using precipitation and temperature. Aerosols lead to lower precipitation and higher temperature which translate into lower inflow in fall and slightly higher inflow in winter. The overall effect of aerosols is a reduction in annual inflow by 4%-14% for both lakes as shown in Table 6.11 and Table 6.12. Reference [385] observed a 10% decrease in surface runoff from October to June in the mountaintops of the Sierra Nevada region due to the impact of aerosols which agrees with our calculated annual impact on reservoir inflow in the region.

The impact of aerosols is more significant in the water year 2013 than in the water year 2014 for both lakes. This is because the impact of aerosols on the meteorological variables is more pronounced in the water year 2013 as seen from the mean of the meteorological variables from CTRL and CLEAN simulations. The annual impact of aerosols is stronger in Florence Lake. This is because the fall and winter inflow are simulated using only precipitation for Florence Lake. For Lake Edison, the fall and winter inflow are simulated using

Lake	Year	Actual (acre ft)	CTRL (acre ft)	CLEAN (acre ft)
Florence	2013	117390	113610	13163
	2014	99980	119740	125410
Edison	2013	58572	61004	66240
	2014	49339	55446	58247

Table 6.11: Annual reservoir inflow under different aerosol conditions.

Lake	Year	Annual	Fall	Winter	Spring	Summer
Florence	2013	-14%	-11%	-5%	-.01%	-26%
	2014	-4%	-2%	-1%	2%	-11%
Edison	2013	-8%	-1%	0.2%	1%	-18%
	2014	-5%	-0.4%	0.3%	0.6%	-11%

Table 6.12: Impact of aerosols (%) on annual and seasonal reservoir inflow

both precipitation and temperature. The higher temperature effect from aerosols offsets some of the reduction in inflow in Lake Edison. Therefore, the annual impact of aerosols on inflow is lower in Lake Edison.

6.6.3 Robustness analysis of the estimation of the impact of aerosols

It can be observed that the difference between CTRL and CLEAN inflows is between 4% and 15%. On the other hand, the difference between annual observed and simulated inflow varies between 0.1%-17% at Lake Florence and 7%-9% at Lake Thomas A. Edison which is in the same range as the impact of aerosols on inflows. However, in Section 6.5.4, it was shown that the dynamic regression model built is robust against perturbations of input variables and the number of water years used in the training set.

Moreover, the most significant impact of aerosols occurs in the late spring and summer when the WRF-Chem simulations of SWE have a large error. Therefore, forecasts of inflow in the water year 2013 and 2014 and the impact of aerosol on inflow were calculated with perturbed testing set inputs to gain more confidence in the impact of aerosol results. To account for the discrepancy between the observed meteorological variables and WRF-Chem CTRL simulation outputs, the difference between these two time series was calculated for all of the meteorological variables. A random error was introduced to the daily values of the meteorological variables of the WRF-Chem simulated testing set. To preserve the temporal correlation of the meteorological variables, a random variable following uniform distribution in the interval $[0, 1]$ was multiplied with $X_{obs} - X_{WRF-Chem\ CTRL}$ where X denotes meteorological variables. The resultant random error was added to the meteorological variables of the testing set to generate the perturbed inputs. Both CTRL and CLEAN simulations were perturbed by the same error. Input meteorological variables of the training set are not perturbed. The dynamic regression model was then simulated with the perturbed WRF-Chem CTRL and CLEAN testing sets for Florence Lake for both water years. 1024 model runs were performed in the same fashion as Section 6.5.4. Out of the 1024 models, the model which produced the median RMSE was selected for analysis of results. The difference in inflow between the CTRL and CLEAN simulations was then calculated and plotted in Figure 6.12 for the selected model.

It can be observed that, for all of the simulations, the sign and magnitude of the difference in inflow with the selected perturbed input model are similar to the reference model. Here, the reference model denotes the unperturbed input model. The annual and seasonal impacts of aerosol are compared to the reference model in Table 6.13 which shows that they are similar. Therefore, it can be safely argued that the difference between the inflows arises from the difference between meteorological variables with and without the

Lake	Year	Model	Annual	Fall	Winter	Spring	Summer
Florence	2013	Reference	-14%	-11%	-6%	-.07%	-26%
		Perturbed	-13%	-10%	-5%	0.05%	-23%
	2014	Reference	-4%	-2%	-1%	2%	-11%
		Perturbed	-4%	-0.10%	-0.09%	2%	-10%
Edison	2013	Reference	-8%	-1%	0.2%	1%	-18%
		Perturbed	-8%	-1%	0.1%	1%	-17%
	2014	Reference	-5%	-0.4%	0.3%	0.6%	-11%
		Perturbed	-5%	-0.2%	0.4%	0.7%	-10%

Table 6.13: Comparison of impact of aerosols on annual and seasonal reservoir inflow for the reference and selected perturbed input model with median RMSE

impact of aerosol.

6.7 Summary and conclusion

A comprehensive framework to quantify the impact of aerosols on reservoir inflow was developed by synergistically combining the WRF-Chem model and a dynamic regression model. The dynamic regression model can also be leveraged to perform a one-year ahead daily inflow forecast. A case study was conducted using Florence Lake and Lake Thomas Alva Edison of the Big Creek Hydroelectric Project. The dynamic regression model was found to be adequate and performed well compared to the benchmark models.

We investigated the impact of aerosols on the inflow into these hydropower reservoirs over two water years. The simulation results show that the presence of aerosols significantly reduces the annual inflow into the hydropower reservoirs of the Big Creek Hydroelectric Project. Moreover, aerosols significantly reduce the amount of inflow in the summer when the marginal economic value of water is extremely high. The presence of aerosols also slightly increases the inflow in the spring when the run-off risk is high. Therefore, it can be concluded that the presence of aerosol is detrimental to the optimal utilization of hydroelectric power systems. The change in inflow due to the impact of aerosol in different seasons with different water and electricity demands can assist the reservoir operators in determining the optimal operation policy for the reservoirs. Further scarcity of reservoir inflow during dry seasons can motivate the San Joaquin River region water resources planners to focus their efforts on mitigation strategies. The findings from this research can provide another justification for stricter environmental regulations to reduce anthropogenic aerosol emissions.

A forecast of the inflow into the hydropower reservoirs obtained from this study can assist in optimizing the cascaded hydropower system. The framework for evaluating the impact of aerosols on reservoir inflow is easily extendable to reservoirs located in other regions. The time series of the meteorological variables and reservoir inflows need for dynamic regression model building are usually available from the nearby weather stations. WRF-Chem simulations of the relevant meteorological variables with and without aerosol can be performed in other regions with a similar experimental setup. With these data available, the impact of aerosols on inflow into the reservoirs located in other regions can be evaluated in a similar fashion.

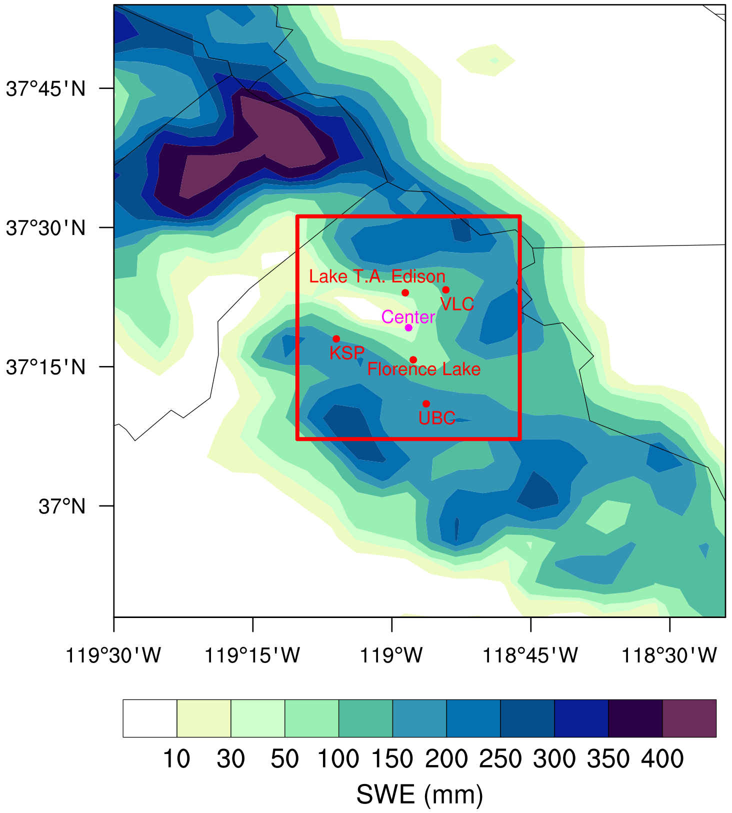

Figure 6.2: Study area with grid box and weather stations identified. Snow depth distribution averaged over water year 2013 is overlaid on the map

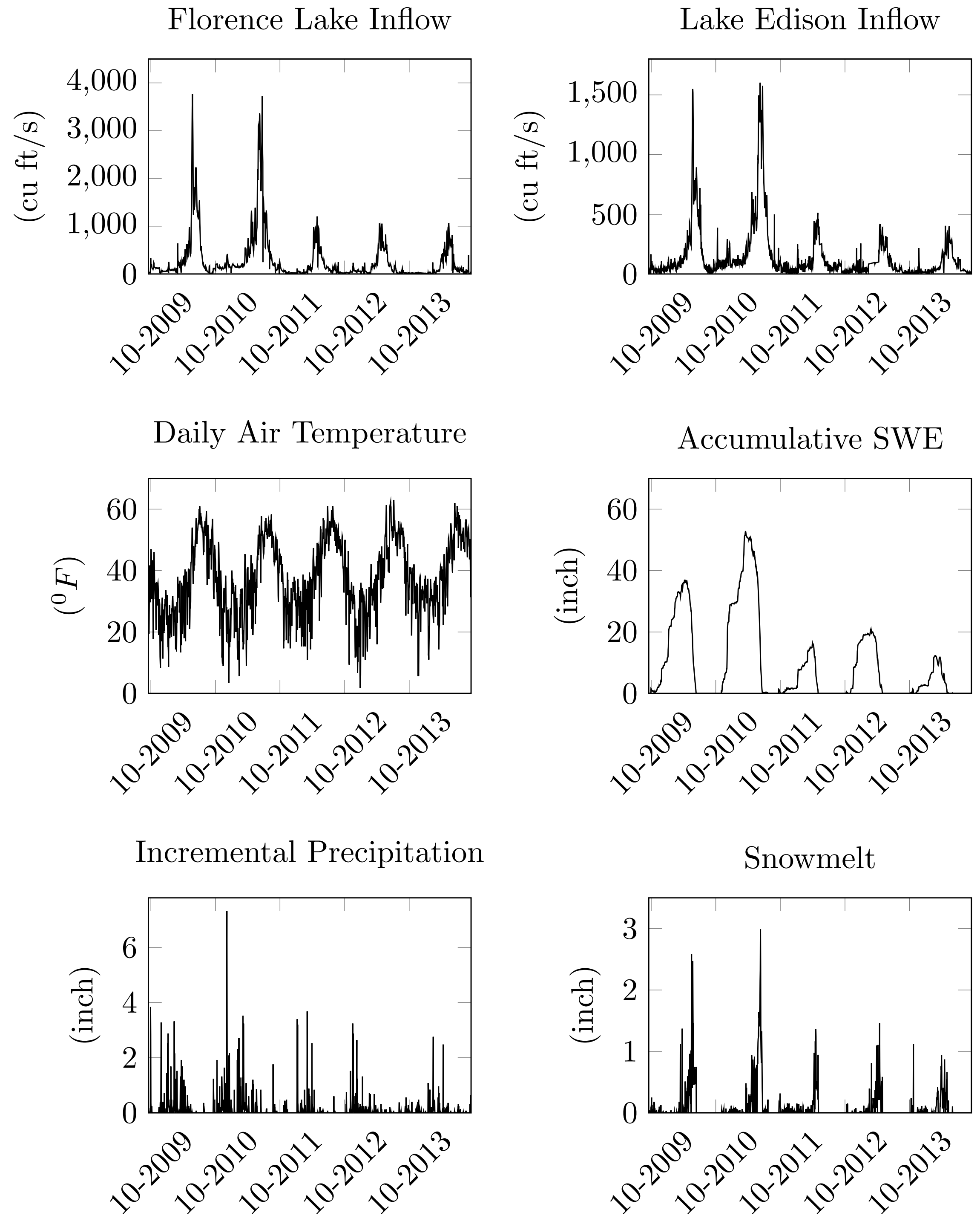

Figure 6.3: Response variables (inflow at Florence Lake and Lake Edison) and the explanatory variables (average temperature, SWE, incremental precipitation and snowmelt at weather stations- UBC, KSP and VLC) for water year 2010-2014

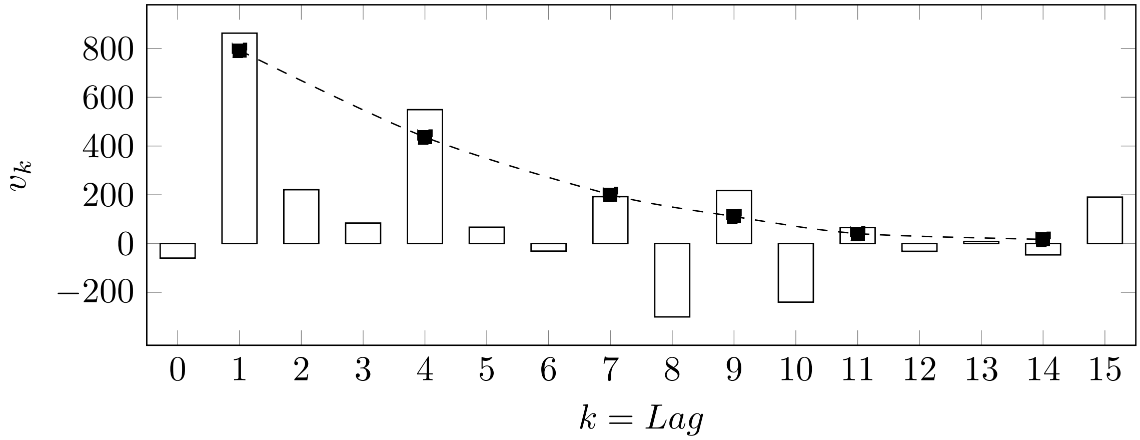

Figure 6.4: Impulse response weights of input variable X_4D_3

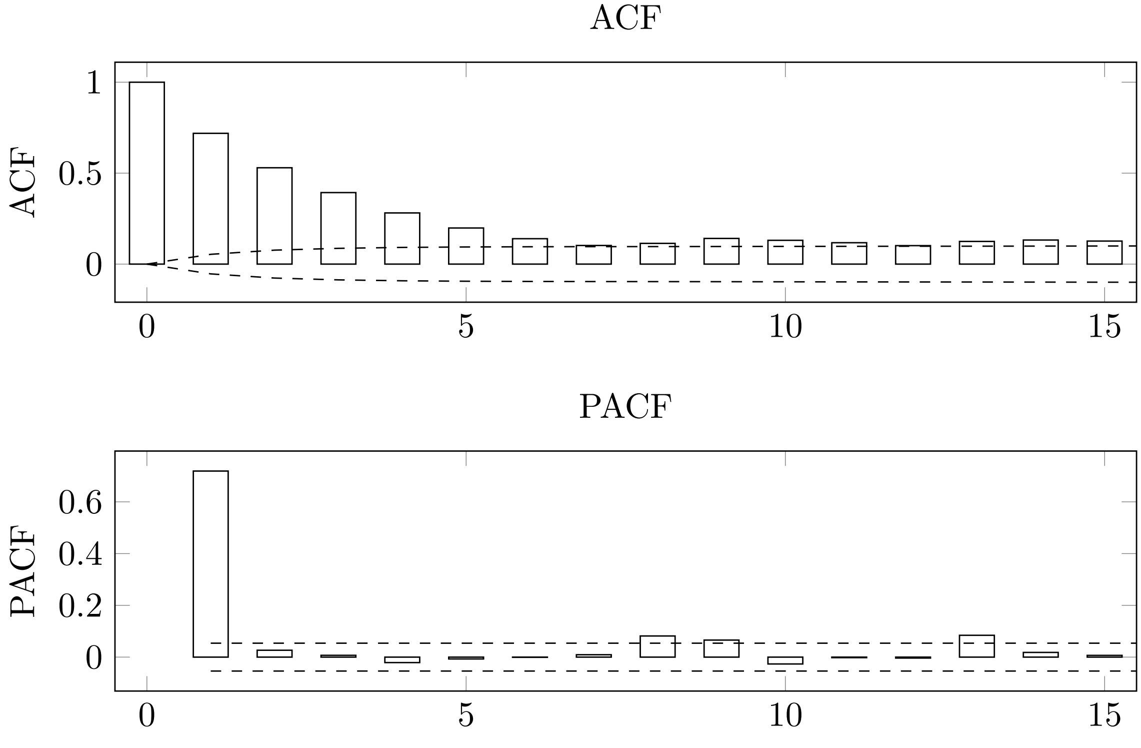

Figure 6.5: ACF and PACF of noise series N_t

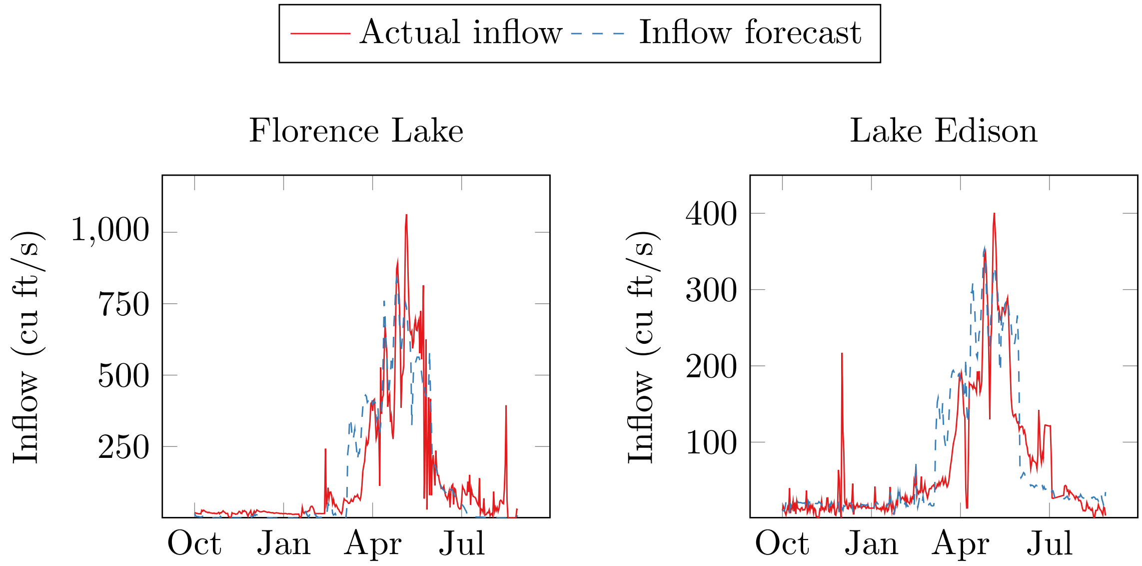

Figure 6.6: Comparison of actual inflow and inflow forecast with observed meteorological variables in water year 2014

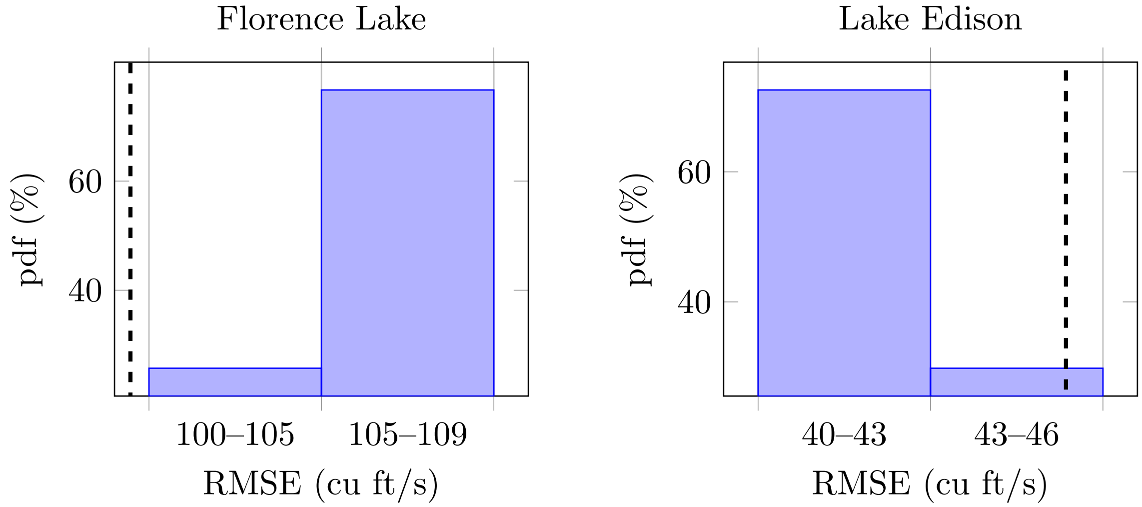

Figure 6.7: Probability distribution function (%) of the RMSE of forecasted inflow with perturbed inputs in water year 2014. RMSE of the reference model is indicated with the dashed line

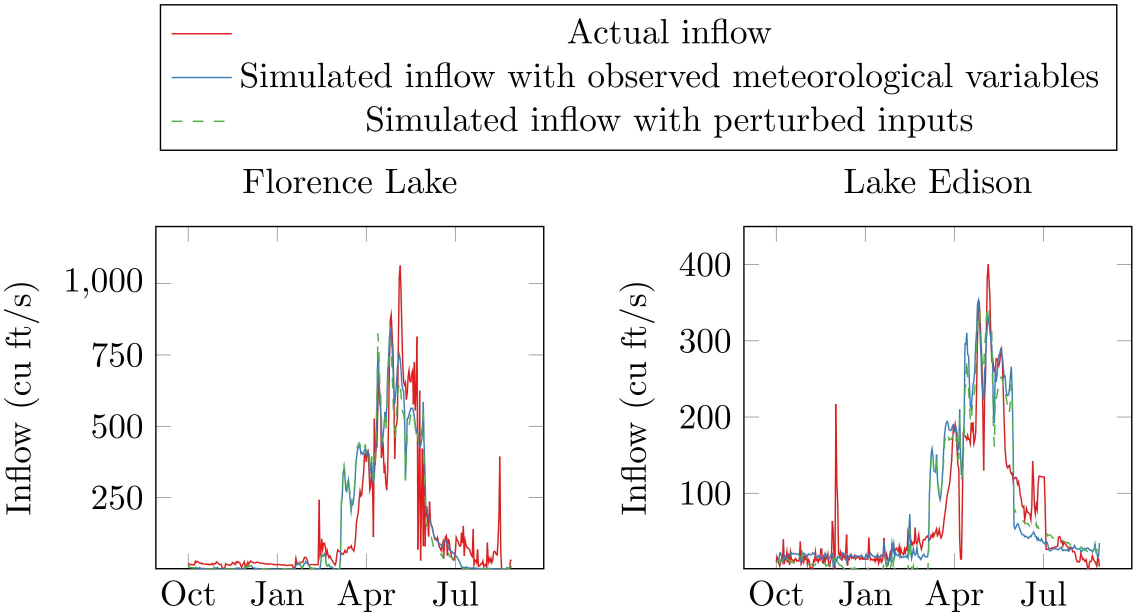

Figure 6.8: Comparison of actual inflow, simulated inflow from observed meteorological variables (reference) and simulated inflow from the selected perturbed input model with median RMSE in water year 2014

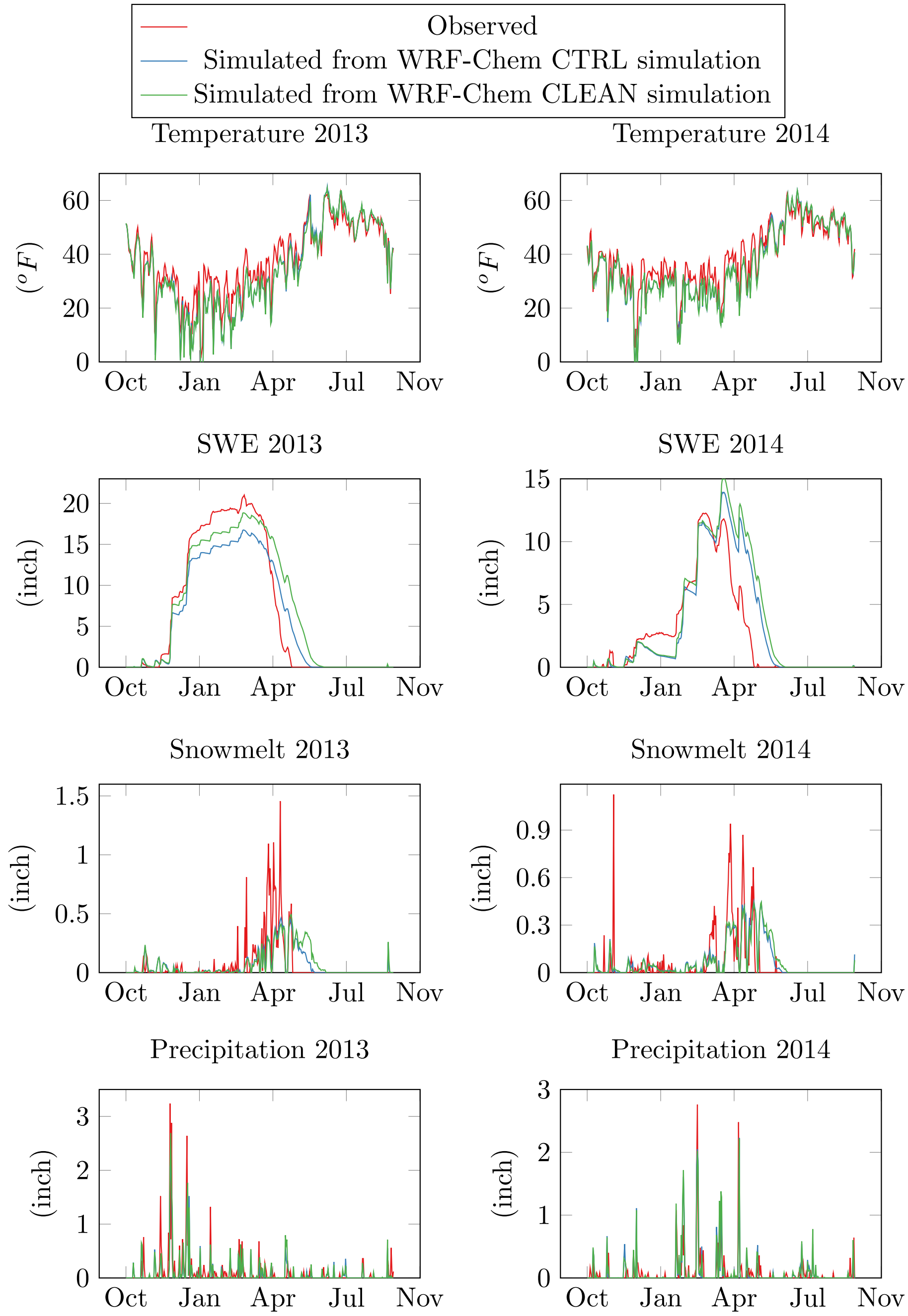

Figure 6.9: Comparison of observed and WRF-Chem CTRL and CLEAN simulated meteorological variables

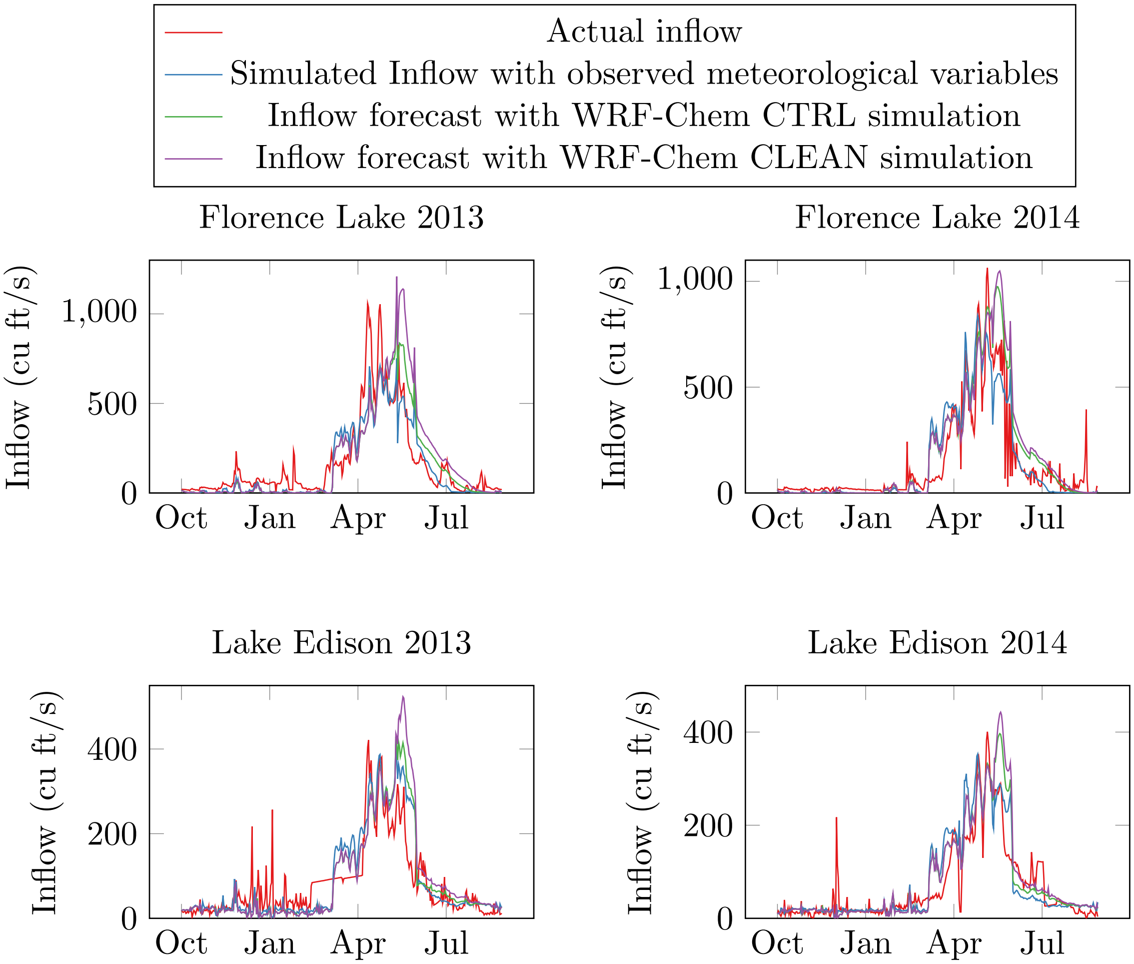

Figure 6.10: Comparison of actual inflow, simulated inflow from observed meteorological variables and WRF-Chem CTRL and CLEAN simulated meteorological variables

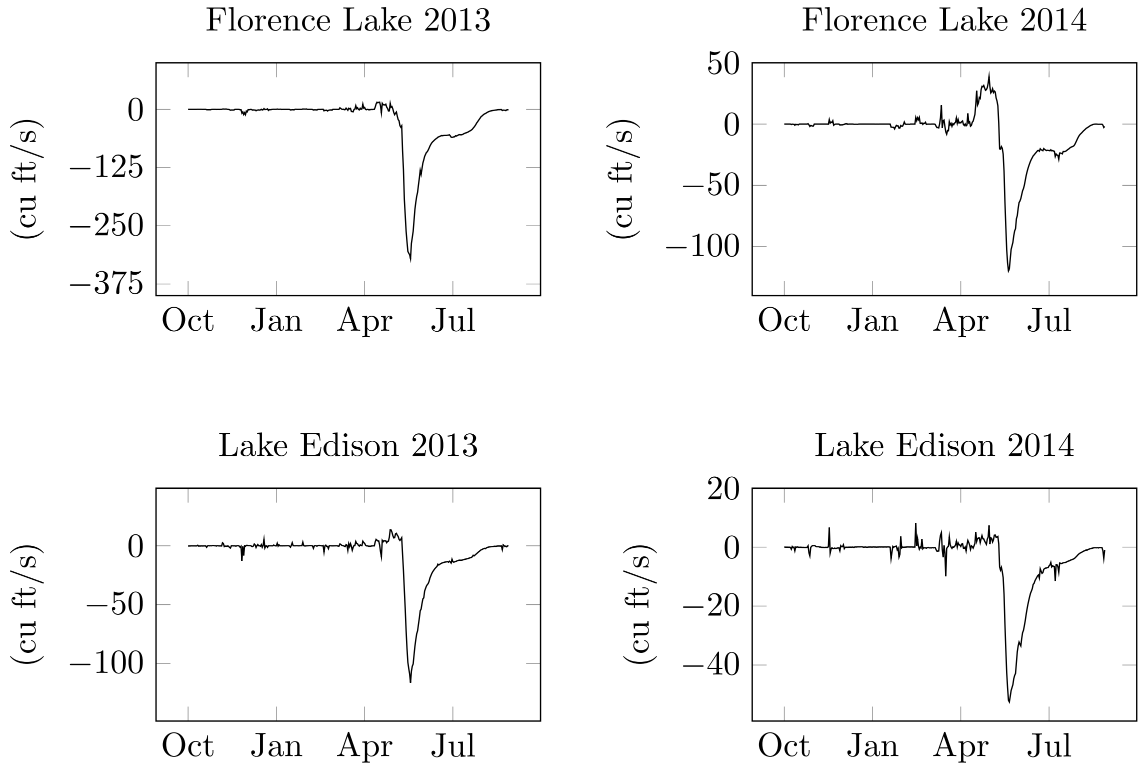

Figure 6.11: The impact of aerosols on reservoir inflow ($Inflow_{CTRL} - Inflow_{CLEAN}$)

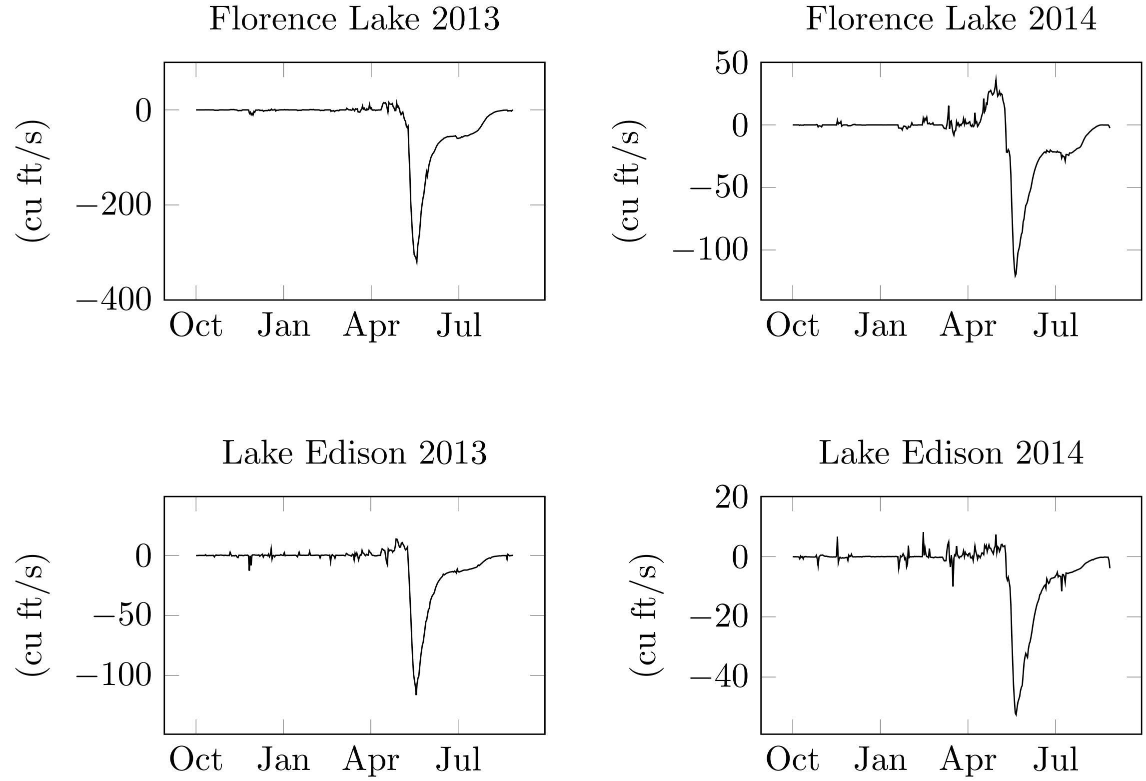

Figure 6.12: The impact of aerosols on reservoir inflow ($Inflow_{CTRL} - Inflow_{CLEAN}$) for the selected perturbed input model with median RMSE

Chapter 7

Climate, Water, Energy Nexus: Impact of Aerosols on Hydropower Generation in California

7.1 Introduction

Water and energy are intrinsically interconnected. Water is required for nearly all forms of energy production and electricity generation. On the other hand, energy is needed for the treatment, recycling, transportation, and distribution of water [152]. Climate change and increased demand for water and energy are creating scarcity and uncertainty in water and energy systems. The strong interdependence between the systems means that disturbance in one of the systems will likely lead to vulnerabilities within the other system. To mitigate these vulnerabilities, it is imperative to closely study the interplay among the water, climate, and energy systems.

Hydropower generation is a crucial link in the climate-water-energy nexus. Climate change causes rises in average temperature, shifts in precipitation, snowmelt, and runoff patterns, disruptions in the availability of water, and increases in climate variability. The shifts in precipitation, snowmelt, and runoff patterns, in turn, affect the scheduling of hydropower plant operations. Aerosols are a large source of uncertainty in climate change projections. They influence the hydrological cycle through their impacts on meteorological variables, for example, snow water equivalent (SWE), precipitation, and temperature [39, 290]. We have provided a detailed literature review of aerosol impacts on these meteorological variables in [183]. In general, light-absorbing aerosols increase air temperature and reflective aerosols decrease the air temperature. Over the mountain tops in the Sierra Nevada region, aerosols lower precipitation and SWE by 10% [386]. We have provided a thorough description of aerosol effects on SWE and precipitation in California in [386]. Meteorological variables, in turn, can significantly influence inflows into the hydropower reservoirs and water availability for hydropower generation. It is, therefore, important to able to explain and quantify the impact of aerosols on hydropower generation and revenue for the purpose of vulnerability assessment.

The objective of this chapter is to quantify the impact of aerosols on hydropower generation and revenue of the Big Creek Hydroelectric Project. The project is located in the Sierra Nevada Mountains of Central California. This evaluation requires a regional scale assessment because the impact of aerosols on climate differs by region. In the previous chapter, we developed a comprehensive framework to quantify the impact of aerosols on inflows into higher elevation hydropower reservoirs [183]. We integrated the Weather Research and Forecasting Model with Chemistry (WRF-Chem) with a statistical inflow forecast model. We performed the case study in the Big Creek Hydroelectric Project. We showed that aerosols reduced the annual reservoir inflow by 4-14%. Aerosols reduced the inflows during summer significantly when the marginal value of water is high. They also increased the spring inflow slightly when run-off risk is high. Hence, it is hypothesized that the presence of aerosols can be unfavorable for optimally utilizing hydroelectric power plants.

In this study, we take the next logical step to quantify the impact of aerosols on hydropower generation and revenue. To this end, we integrate the hydropower optimization toolbox, Vista Decision Support System (DSS) [12] into the framework developed in [183]. We obtain the simulations of meteorological variables with and without aerosol impacts consideration from WRF-Chem simulations conducted in the San Joaquin Valley of California. We use those to generate the inflows into the hydropower reservoirs with and without considering the impact of aerosols using the statistical inflow forecast model. Then, we feed the inflow projections with and without aerosol effects into the Vista DSS to determine the optimal operation schedules of the hydropower system for both scenarios.

The unique contributions of this study are listed as follows:

1. This chapter develops a comprehensive framework to evaluate the impact of aerosols on hydropower generation and revenue by seamlessly integrating the numerical weather forecasting model (WRF-Chem), a statistical inflow forecast model, and the hydropower operation optimization toolbox.

2. The impact of aerosols on hydropower generation and revenue is quantified for

the Big Creek Hydroelectric System. The simulation results show that aerosols lead to a significant reduction in annual hydropower generation and revenue.

There are a number of researches on climate change effects on hydropower generation and revenue. However, they tend to study the effects of carbon dioxide and several other greenhouse gases. The impact of climate change on the Upper American River Project and the Big Creek Hydroelectric Project, which are two high elevation hydropower systems in California, are estimated in [367]. They simulated the operations of the two hydroelectric projects with historical data and data generated from four climate change scenarios. The climate change scenarios result in reduced runoff and earlier runoff that causes a reduction in hydropower generation for both hydropower systems. The hydropower generation in 137 high elevation systems is explored in [240] under three climate change scenarios: wet warm, dry warm, and warming only. They found that dry warming and warming only climate change scenarios reduced average hydropower revenues whereas wet warming scenarios increased revenue. Other studies are limited to large lower elevation reservoirs in California ([365, 347]). Our study differs from the existing ones by studying the impact of aerosols on hydropower generation in a higher elevation hydroelectric system in California.

The rest of the chapter is organized as follows. Section 7.2 describes the overall framework of the study. Section 7.3 describes the hydropower plant operation optimization problem. Section 7.4 describes the technical methods: the WRF-Chem Model, the statistical inflow forecast model, and Vista DSS. Section 7.5 presents the case study. Section 7.6 shows the impacts of aerosols on hydropower generation and revenue. Finally, Section 7.7 concludes the chapter.

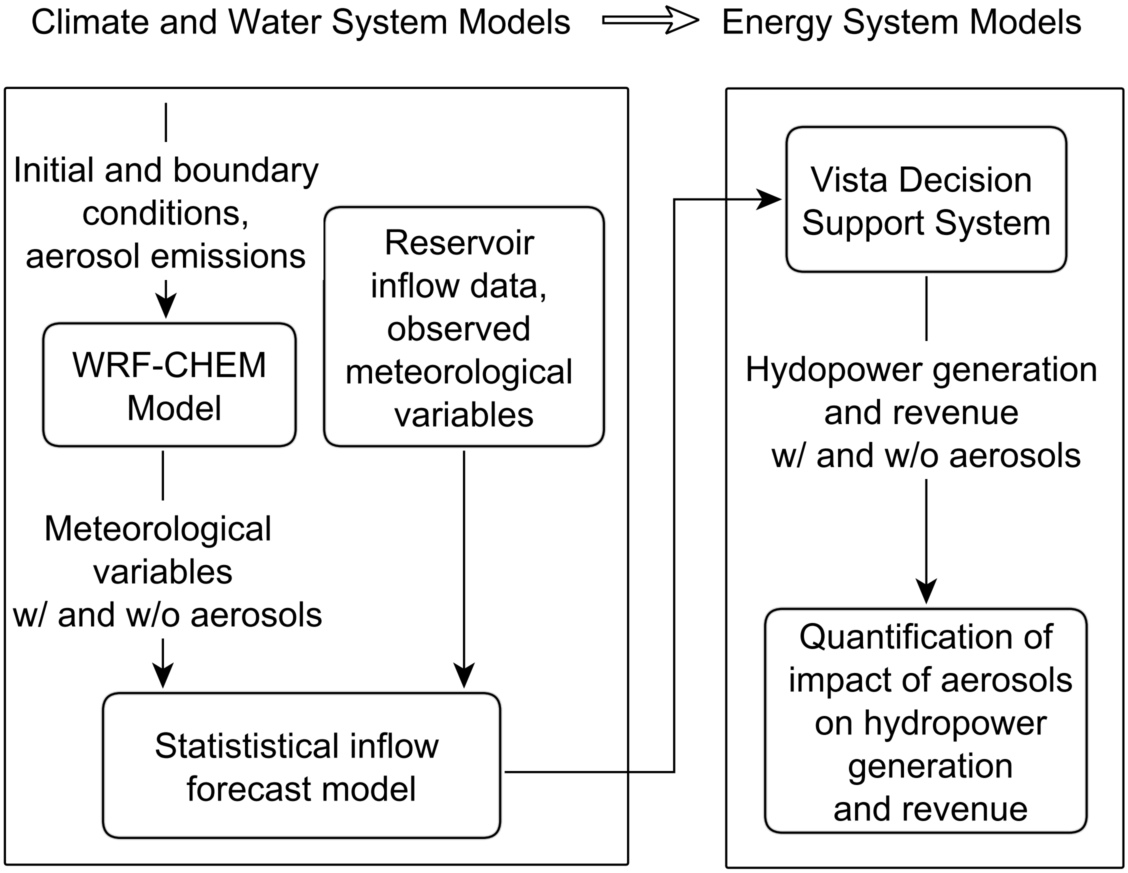

Figure 7.1: Overall framework for quantifying the impact of aerosols on hydropower generation and revenue

7.2 Framework

Figure 7.1 shows the framework for quantifying the impact of aerosols on hydropower generation and revenue. The workflow is as follows. First, we run a version of the Weather Research and Forecasting Model with Chemistry and fully coupled aerosol-meteorology-snowpack module [141, 415]. The outputs of the model include, with and without considering the impacts of aerosols, the meteorological variables, such as daily mean temperature, accumulative snow water equivalent, and incremental precipitation in the San Joaquin Valley of California. Then, we feed these meteorological variables, along with historical reservoirs inflow data, into the statistical inflow forecast model. These statistical models produce reservoirs inflows with and without considering the aerosol impacts, which we, in turn, feed into the hydropower operation optimization model. The Vista DSS then conducts hydroelectric system optimization over a one-year horizon to maximize the generation revenue of the hydropower facility. Finally, we quantify the impact of aerosols on hydropower generation and revenue by comparing the hydropower generation and revenue results with and without considering aerosols.

7.3 Problem Formulation

In order to estimate the impact of aerosols on hydropower generation in a hydro year, we use Vista DSS to optimize the generation schedule of the cascaded hydropower system. The goal is to maximize the hydropower system's revenue from providing energy, spinning reserve, frequency regulation up, and frequency regulation down services subject to physical, operational, and contractual constraints. The decision variables include the generation units' status and the amount of generation from each powerhouse. The optimization algorithm assumes that the cascaded hydroelectric system is a price taker in the electricity market. The inputs to the optimization include the inflows to various reservoirs and prices for energy and ancillary services. The hydropower plant operation optimization problem is formulated as follows.

$$
\begin{aligned}
Max \sum_{n=1}^{N}\sum_{t=1}^{T} \{ & U_{nt} \times (P_{nt} \times f_t + c_t^{res} \times P_{nt}^{res} \\
& + c_t^{reg,up} \times P_{nt}^{reg,up} + c_t^{reg,down} \times P_{nt}^{reg,down}) \\
& - F(U_{nt}, P_{nt}, P_{nt}^{res}, P_{nt}^{reg,up}, P_{nt}^{reg,down})\}
\end{aligned}
$$

subject to

$$P_n^{\min} \leq P_{nt} \leq P_n^{\max}, \quad n = 1, \ldots, N, \quad t = 1, \ldots, T$$

and other operational and contractual constraints.

U_{nt} denotes the up/down status of generation unit n at hour t (0: unit down, 1: unit up). P_{nt} denotes the power generation of unit n at hour t. P_{nt}^{res}, $P_{nt}^{reg,up}$, and $P_{nt}^{reg,down}$ are the spinning reserve capacity, frequency regulation up, and frequency regulation down capacity respectively, scheduled for unit n at hour t. f_t represents the forecasted energy price (\$/MWh) for hour t. c_t^{res}, $c_t^{reg,up}$, and $c_t^{reg,down}$ denote the forecasted price (\$/MW) for spinning reserve service, frequency regulation up service, and frequency regulation down service for hour t. F is the operation and maintenance cost of the cascaded hydroelectric system. $P_n^{\min}$ and $P_n^{\max}$ denote the minimum and maximum rated capacity of unit n. N is the number of generation units and T is the number of hours in a water year.

7.4 Technical methods

7.4.1 Vista Decision Support System

In order to maximize the revenue from operating a hydroelectric project, it is crucial to determine the optimal operation schedules of various powerhouses and reservoirs. At the same time, hydroelectric projects often have multiple additional functions, such as irrigation, flood control, navigation, water supply, and recreation. Vista DSS is a toolbox that assists in both planning and operation of the hydroelectric systems to ultimately maximize the value of hydropower generation while helping hydroelectric systems to serve additional functions such as water management and flood control. We present three key modules of the Vista DSS below. The first module is used to develop a representation of the physical system. The second module models individual powerhouses. The third module describes the physical, operational, and contractual constraints.

Physical System Representation

A water resource system can be disaggregated into a number of hydraulically independent basins for modeling purposes. A hydraulic system consists of rivers and watersheds. Nodes are points of interest in the water resource system being modeled. For example, nodes can represent reservoirs, tailwater junctions, river junctions, sources, and sinks. Reservoir and river junction nodes combine a number of inflow and outflow channels in the network. An arc is a directed line segment that joins an upstream node to a downstream node. There are four types of arcs: inflow, power, spillway, and river reach. Inflow arcs represent inflow into the river system to be modeled, power arcs represent one or more turbines and their associated flow, spillway arcs represent the total flow through spillway structures, and river reach arcs indicate physical conveyances such as natural or man-made channels.

Physical structures in a river system such as reservoir and hydropower plants are represented mathematically along with estimated parameters. A storage reservoir is represented by its full supply level (FSL), dead storage level (DSL), and the coefficients of the polynomial defining the storage elevation-volume relation. River reach arcs are used to model flow travel time and attenuation en route. The Muskingum-Cunge channel flow routing method is employed here which assumes that storage in a single river reach is related to its inflows and outflows. The routing coefficients are determined by fitting the routing equation to the observed field data so that the sum of weighted residual errors is minimized. Channel water levels data are collected from the flow gauges, which are converted into discharge by a stage-discharge rating curve. Spillway discharge is modeled as a function of reservoir elevation and spillway opening.

Hydropower Plant Modeling

The power generation from a single generating unit is defined by a power polynomial. The power equation represents a fundamental relationship between discharge, net head, and efficiency.

$$\mathrm{P} = \mathrm{C}\times\eta_p\times\mathrm{Q}\times\mathrm{h}_n \tag{7.1}$$

where P is the generated power, C is a coefficient, η_p is the overall generating efficiency, Q is the turbine discharge, and h_n is the net head. Based on this theoretical relationship, the power polynomial for each unit can be approximated by a third-order equation that represents unit power generation as a function of the head and the discharge along with all the head-losses acting on that unit.

$$P = a + b \times Q + c \times Q^2 + d \times Q^3 \tag{7.2}$$

where P is the power produced by one unit, Q is the discharge flowing through the unit, and a, b, c, d are functions of unit gross head h.

$$a = a_1 + a_2 \times h + a_3 \times h^2 \tag{7.3}$$

Here, $b, c,$ and d have similar relationships with the unit gross head, h. The estimation of the power polynomial coefficients can be formulated as a multiple linear regression problem. The solution should satisfy these two conditions: (i) the second derivative of efficiency with respect to discharge should be less than 0 and (ii) the derivative of power with respect to discharge should be greater than or equal to 0 over a unit's discharge range.

Constraints

There are three types of constraints in the Vista DSS: physical, operational, and contractual constraints. Physical constraints represent mandatory physical operating limits such as the size of the lake, limitations of generation units and tunnels, and minimum and maximum turbine limits. Operational constraints include limitations for reservoir elevation, discharge speed, and scheduled releases. The contractual constraints model the restrictions on hydroelectric project operations due to water rights, minimum fish flows, recreational requirements, etc. Every imposed constraint lowers the total revenue of the hydroelectric project. However, these operational and contractual constraints can be violated at a cost. The constraints are prioritized by their relaxation cost.

7.5 Case Study

We conduct the case study in the Big Creek Hydroelectric System of California.

7.5.1 Simulation of Hydropower Reservoir Inflows

Historic inflows for Lake T. A. Edison and Florence Lake are available for the water years 2010-2015. A water year or a hydrological year is a time period of 12 months between October 1 of a given year through September 30 of the next year. We divide the observed inflows and meteorological variables into a training set and a test set. We form the test set by withholding the data for the last water year, i.e., the water year 2015, from the model identification and estimation process. The rest of the data work as the training set. We collect the meteorological data and average those over three weather stations located within a 0.4×0.4^o grid box with center at $(37.32^oN, -118.97^oE)$. They are- Kaiser Point (KSP), Volcanic Knob (VLC), and Upper Burnt Corral Coral (UBC). The WRF-Chem CTRL and CLEAN simulations of the meteorological variables are available for the water year 2015 at the grid box location. We compute inflow forecasts into these two lakes with and without aerosols for the water year 2015 using a dynamic regression model.

We assume that inflows from the Bear Creek are about 90% of the Lake Edison inflows as the two inflows are highly correlated. The historic inflow data for Huntington

Lake, Shaver Lake, Redinger Lake, and Mammoth lake are not available before the water year 2015. We utilize the statistical inflow forecast model of Florence Lake as a proxy because its location is physically closer to these lakes compared to Lake Edison. We use the WRF-Chem CTRL and CLEAN simulations of meteorological variables performed at 0.4×0.4^o grid boxes with center at the location of Huntington Lake, Shaver Lake, Mammoth pool, and Redinger lake to estimate the inflows into these lakes respectively with and without aerosol impacts. We assume that the ratio of simulated inflows with and without the impact of aerosols to the observed inflows for these lakes are the same as that of the Florence lake. The inflows at one of these Lakes L can be calculated as follows.

$$Y^L = \frac{Y^{FL}\left(X_{\text{WRF-Chem simulations at lake } L}\right)}{Y^{FL}_{OBS}} \times Y^L_{OBS}$$

where Y^L denotes the estimated inflows with or without considering the impact of aerosols at Lake L, Y^{FL} represents the simulated inflows with or without considering impact of aerosols at Florence Lake, X denotes WRF-Chem CTRL or CLEAN simulations of meteorological variables performed at a 0.4×0.4^o grid box having center at the location of lake L, Y^L_{OBS} is observed inflow at Lake L, and Y^{FL}_{OBS} is observed inflow at Florence Lake.

7.5.2 Calculating the Impact of Aerosols on Hydropower Generation and Revenue

We use the Vista DSS to optimize the operation schedule of hydropower plants over a one hydro year horizon to maximize the Big Creek Hydroelectric Project's revenue. Because both 2014 and 2015 are dry years, no recreational requirements for reservoir elevation levels are placed on Huntington Lake. We assume that the impact of aerosols on the side flows into Dam 5, Dam 6, and Pittman is negligible given that these inflows are extremely small in dry years and cannot be stored.

We feed the inflow forecasts into the lakes into the Vista DSS which determines the optimal generation schedules for the water year 2015 which maximizes the revenue of the hydroelectric system while meeting the physical and operational constraints. The optimization algorithm has a weekly time step. We formulate the hydro operation optimization problem as a mixed-integer linear programming problem by approximating non-linear constraints as linear ones.

7.6 Result and analysis

7.6.1 The Impact of Aerosols on Hydropower Reservoir Inflows

We quantify the impact of aerosols on reservoir inflows for water year 2015. The percentage change in inflows caused by aerosols can be calculated by Equation (7.4).

$$\frac{Inflow_{\text{w/ Aerosols}} - Inflow_{\text{w/o Aerosols}}}{Inflow_{\text{w/o Aerosols}}} \times 100\% \tag{7.4}$$

As shown in Table 7.1 and Table 7.2, the presence of aerosols results in a reduction in annual inflows by 1-10% for all of the lakes. The presence of aerosols leads to lower annual inflows due to reduced SWE, precipitation, and snowmelt. Significantly lower annual inflows can be observed for Lake Edison and Florence Lake due to the impact of aerosols. However, the reduction in inflows is not as significant in the other reservoirs with lower elevations. This happens because the impact of aerosols on SWE is very strong around the higher elevation reservoirs having a 22% difference between the WRF-Chem CTRL and CLEAN simulations whereas the impact is in the order of 1-6% in the lower elevation reservoirs. Note that, the reservoir inflows in the Big Creek Hydroelectric Project are snowmelt dominated [183].

We define the four seasons four seasonal analysis as follows: 10/01-12/21 is defined as fall, 12/22-03/20, is defined as winter, 03/21-05/31 is defined and spring, and finally 06/01-09/30 is defined as summer. As shown in Table 7.2, the impact of aerosols on inflows is more significant in the summer. Significantly lower inflows can be observed during summer in Lake Edison and Florence Lake due to the impact of aerosols. Lower prior season's SWE, lower current season's snowmelt, and lower precipitation result in lower inflows in summer for Lake Edison and Florence Lake. The impact of aerosols on inflows during summer is less significant for the other reservoirs with lower elevation due to the weak influence of aerosols on SWE and snowmelt in lower elevation reservoirs. The impacts of aerosols on inflows are much smaller for all lakes in spring. In spring, dust aerosols enhance solar absorption which leads to a higher temperature, snowmelt, and inflows. On the other hand, in spring, aerosols lead to lower precipitation which results in a reduction of the inflows. The aggregated effect of aerosols on inflows through temperature, snowmelt, and precipitation is a small reduction in inflows in the spring. Although the percentage change in inflows caused by aerosols in fall and winter is high, the magnitude of change in inflows is small. This is because the levels of inflows are very low in fall and winter. A detailed discussion of the impact of aerosols on inflows into the reservoirs can be found in Chapter 6.

Table 7.1: Annual reservoir inflows under different aerosol conditions

Lake	CTRL ($acreft$)	CLEAN ($acreft$)
Edison	47,683	50,353
Florence	85,541	92,793
Huntington	34,756	35,804
Mammoth	222,732	225,737
Redinger	4,689	4,791
Shaver	8,097	8,245

Table 7.2: The impact of aerosols (%) on annual and seasonal reservoir inflows

Lake	Annual	Fall	Winter	Spring	Summer
Edison	-5	-1	-0.5	1	-15
Florence	-10	-8	-12	-0.5	-23
Huntington	-3	-6	-8	-1	-7
Mammoth	-1	-5	-11	-0.8	-1
Redinger	-2	-6	-10	-1	0
Shaver	-2	-8	-5	-1	-1

7.6.2 The Impact of Aerosols on Hydropower Generation and Revenue

We calculate the impact of aerosols on hydropower generation and revenue for the Big Creek Hydroelectric Project for the water year 2015. Table 7.3 shows the results. In the water year 2015, aerosols reduced Big Creek's generation by 89,356 MWh and revenue by approximately \$2.8 million. This is equivalent to a 6% reduction in hydropower

Table 7.3: Impact of aerosols on hydropower generation and revenue in water year 2015.

	Period	CTRL	CLEAN	Difference	(%)
MWH	Annual	1,502,330	1,591,686	89,356	-6
	Fall	89,907	99,135	9,228	-9
	Winter	189,796	193,647	3,851	-2
	Spring	231,395	267,710	36,315	-13
	Summer	991,232	1,031,216	39,984	-4
Revenue ($)	Annual	70,954,360	73,818,350	2,863,990	-4
	Fall	6,868,430	7,291,490	423,060	-6
	Winter	11,275,690	11,321,170	45,480	-0.4
	Spring	8,866,110	9,821,320	955,210	-10
	Summer	43,944,160	45,384,410	1,440,250	-3

generation and a 4% reduction in revenue. Note that, 2015 is the driest year on record. Hence, the revenue generated is very low for the size of the hydropower plant. The loss of hydropower generation and revenue are caused by the reduction in annual inflows due to aerosols. Aerosols reduced inflows to higher elevation reservoirs by 5-10% and inflows to lower elevation reservoirs by 1-2%. The reduction in inflows to higher elevation reservoirs is more important for a cascaded hydroelectric project. This explains why the loss in hydropower generation is around 6%. The percentage reduction in revenue is smaller than that of the power generation. This is because the loss in hydropower generation can be somewhat offset by the efficient scheduling and operation of the hydroelectric project. These findings are consistent with the findings in [240].

It can be seen that the impact of aerosols on generation and revenue is small during low inflow periods (fall and winter). The impact is high during high inflow periods (spring and summer). This finding is in agreement with the result that the impact of aerosols on inflows is more significant during high inflow seasons. Although there is a significant reduction in inflows into the two higher elevation reservoirs (15-23%) in summer, the percentage reduction in generation and revenue are not as significant. This is because both the water years 2014 and 2015 are dry years. The reservoirs have plenty of unused storage capacity to mitigate the impact of aerosols on generation in summer by storing inflows in spring.

The impact of aerosols on the Big Creek Hydroelectric Project's revenue from providing energy, spinning reserve, frequency regulation up, and frequency regulation down services are shown in Table 7.4. It can be seen from the table that the reductions in revenue

Table 7.4: Impact of aerosols on hydropower generation revenue based on revenue type in water year 2015

Products (revenue)	CTRL($)	CLEAN ($)	Difference ($)
Energy	47,886,920	50,292,810	2,405,890
Spinning reserve	6,717,860	6,719,640	1,780
Regulation up	9,774,540	9,784,180	9,640
Regulation down	6,575,040	7,021,720	446,680

from providing energy and frequency regulation down services are more significant than that of spinning reserve and frequency regulation up services. The significant reduction in energy revenues can be explained by lower inflows due to the presence of aerosols. The amount of frequency regulation down service provision of a generator is limited by its energy schedule. Hence, there is a significant reduction in frequency regulation down service revenue.

7.7 Chapter Summary

We develop a comprehensive framework to quantify the impact of aerosols on hydropower generation and revenue by synergistically combining the WRF-Chem model, a statistical inflow forecast model, and the hydropower operation optimization model, Vista DSS. We conduct a case study to quantify the impact of aerosols on the Big Creek Hydroelectric Project's generation and revenue in California. The results show that aerosols reduce inflows into high elevation reservoirs by 6-10% and low elevation reservoirs by 1-3% in a water year. The presence of aerosols leads to a reduction in hydropower generation by 89,356 MWh (6%) which is a staggering $2.8 million loss in revenue in a water year. The results reported in this chapter show the necessity to implement stricter environmental regulations to reduce anthropogenic aerosol emissions.

Chapter 8

Data-driven Predictive Maintenance of Distribution Transformers

8.1 Introduction

Aging infrastructure is the undoing of a reliable electric grid. Unhealthy hardware can result in power outages, raise the costs of power, and start fires. Equipment failure caused 15% of electric disturbances reported to the Department of Energy of the United States in 2015. The current electric transmission and distribution infrastructure in the United States is aging. Many electric grid equipments are approaching or have surpassed their useful life. 70% of power transformers are 25+ years old. 60% of circuit breakers are 30+ years old, and over 60% of distribution poles are $30 - 50$ years old. This far surpasses their useful lives of 25 years, 20 years and 50 years [14]. One critical hardware component susceptible to failure is the distribution transformer. There are many ways for a transformer to fail. For example, high ambient temperatures and excessive loading may damage a transformer. A deficient power supply or exposure to a hostile environment can destroy one. Something as simple as poor workmanship can see a transformer's demise [178]. Yet the most common cause of transformer failure is age. The average age of the distribution transformers in the United States is even higher than the transformers in the transmission system. Thus, proper maintenance of distribution transformers is essential.

Current equipment maintenance strategies fall into three main categories. The first is 'run-to-failure'. In this category, interventions occur only after a transformer has already failed. The second category is preventive maintenance. Here, maintenance actions are carried out according to a planned schedule. The final category, predictive maintenance, is the most cost-effective. Predictive maintenance attempts to assess the health conditions of each device. This allows for the advanced detection of pending failures [342]. The detection, in turn, allows for targeted maintenance to the devices most in need. Currently, electric utilities practice run-to-failure maintenance management for distribution transformers. Employing predictive maintenance instead would be beneficial. It would help to achieve more reliable system operations and reduce the number of sudden power supply interruptions. These benefits are shared by both predictive maintenance and preventative maintenance. But predictive maintenance further reduces costs by avoiding unnecessary maintenance operations.

Existing predictive maintenance research and practice focuses on large power transformers. The methods assess transformer health via dissolved gas analysis (DGA). DGA is a well-known diagnostic technique in the industry [259, 411]. It works by monitoring the concentration of certain gases in the insulation oil of a transformer. The concentration of the dissolved gases is characteristic of the insulation's decomposition. Gases used in DGA include hydrogen (H_2), methane (CH_4), ethane (C_2H_6), acetylene (C_2H_2), ethylene (C_2H_4), carbon monoxide (CO) and carbon dioxide (CO_2). DGA has also been combined with data-centric machine learning techniques. Tested techniques include artificial neural networks (ANN) [411, 378, 406, 270] [406] [378] and fuzzy logic [270]. Support vector machines, the extreme learning machine (ELM), and deep belief networks have been employed as well [116, 408, 326]. These methods identify patterns in historical DGA data to assess transformer health. Many such studies formulate the failure prediction problem as a supervised classification task. The results of such methods are excellent. An evaluation of 15 standard machine-learning algorithms was performed in [259]. The authors of this study separated their results based on false alarm rates. With a false alarm rate of 1%, the researchers were able to detect between 30% and 50% of faulty transformers. When allowed a false alarm rate of 10%, they could detect 80% to 85% of faulty transformers.

Dissolved gas analysis, however, requires semiconductor gas sensors on each transformer. Installing these is feasible for transmission systems that do not have many transformers. High voltage power transformers make up $< 3\%$ of all transformers in the United States. But distribution systems have far more. Thus, these installations are prohibitively expensive for distribution systems. But there are ways of predicting transformer failure which is less direct. For example, environmental conditions play a causal role in transformer failure. Thus, data related to these conditions contain information about a transformer's health. This is verified somewhat in reference [259]. The reference supplements DGA data with transformer-specific features like age and nominal power. Such data are low-cost and readily available. It thus enables cheap predictive maintenance.

This study focuses on the predictive maintenance of distribution transformers. Machine learning techniques are applied to model the dependency between low-cost data and transformer health. The random under-sampling with boosting (RUSBoost) algorithm is adopted to handle data imbalance. The unique contribution of this chapter is that it just uses *just* low-cost transformer-specific and environmental-related features.

The rest of this chapter is organized as follows: In Section 8.2, an overall framework of the failure prediction problem is presented. Section 8.3 describes the technical methods used in the study. Section 8.4.1 presents the case study by describing the dataset and application of the machine learning algorithms on the dataset. The performance of the failure prediction models is reported in Section 8.5. Finally, Section 8.6 concludes the chapter.

8.2 Framework

The aim of this study is to predict if a distribution transformer will fail in a given horizon. We perform such prediction via transformer-specification, loading, location, and weather-related data. The dataset is first divided by year into a training set, a validation set, and a testing set. Transformer failure information within each period acts as a binary label. The convention that a 1 indicates failure and a 0 indicates a non-failure is used. Thus, the failure prediction problem is formulated as a supervised binary classification task. We will denote the dataset as $(\mathbf{X}, \mathbf{y})$. This consists of pairs $(\mathbf{x_i}, y_i)$ of features $\mathbf{x_i}$ and failure labels y_i.

As with most real data, there are a few challenges involved in dealing with this dataset. First, there is missing data. Thus imputing those will be necessary. Second, the dimensionality of the data involved in this study is high. Thus feature selection is important for obtaining better learning performance. Third, the dataset is of mixed type, i.e. the features can be either continuous or categorical. Thus a tree-based model may be useful. Lastly, transformer failures are rare events. This creates an imbalance in the dataset. As a result, traditional algorithms can create suboptimal classification models [162]. We employed random under-sampling with boosting to ease the class imbalance problem.

The study focuses on keeping the number of false predictions small. If the number of false predictions is high, then the cost of their premature replacement will exceed the cost of their sudden failure. As a result, the 'match in top N' (MITN) metric is suitable for assessing the quality of a given method. To calculate this metric, predicted failures are first ranked by likelihood. The N transformers deemed most likely to fail are then placed in a set L. Transformers that ended up failing in the given horizon are then placed in a set F. The MITN metric is then the carnality of $L \cap F$. The workflow is summarized in Figure 8.1

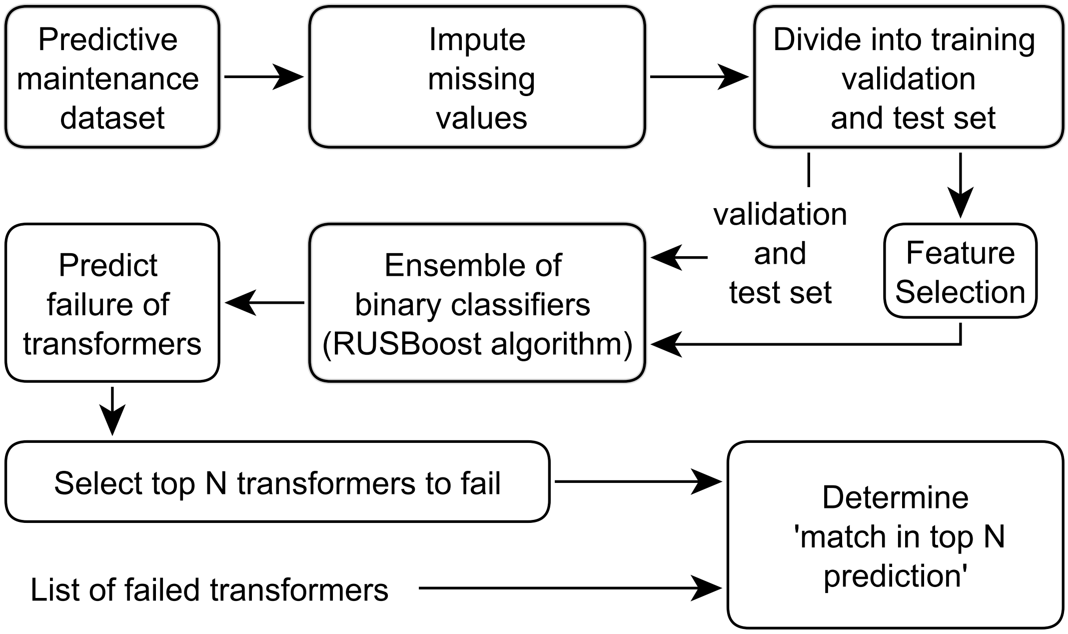

Figure 8.1: Work flow for failure prediction of distribution transformers

8.3 Technical methods

8.3.1 Data Preprocessing

Treating missing values

Existing methods for dealing with missing values can be divided into two categories. The first category simply removes instances with missing data. But this has drawbacks such as substantial data loss and biased instance sampling. The second category attempts to instead impute missing data [209]. Some popular single imputation strategies are mean imputation, hot-deck imputation, and predictive imputation [209] . In the first, missing values are replaced by the mean of the observed values in that variable. In the second, missing values are replaced by ”nearby” data values from the same dataset. The third encompasses more sophisticated procedures for handling missing data. These methods treat a missing variable as a new classification or regression variable. All other relevant variables become predictors of this new variable. Commonly used techniques are decision trees, artificial neural networks, and random forests. However, single imputation methods might ignore the variance associated with the imputation process. Multiple imputation schemes can address this problem [305]. Using a random forest as a prediction model for imputation is a promising approach. It can handle mixed data types, high dimensionality, and address complex interactions. A random forest also forms a multiple imputation scheme intrinsically. This is due to the averaging of the many trees found in the forest. The MissForest method [338] is an iterative imputation method based on random forests. It has been shown to outperform well-known methods such as parametric MICE [323]. Imputation error can be determined from the out-of-bag error estimates of the random forests.

Feature Selection

High dimensional data has always presented a challenge to existing machine learning methods. Feature selection reduces the dimensionality by choosing a subset of the features. This helps our methods perform better. It increases learning accuracy, lowers computational costs, and improves model interpretability. Supervised feature selection methods are chosen to use. Existing methods can be classified into filter models, wrapper models, hybrid models, and embedded models [203].

In filter methods, the relevancy of each feature is ranked. The highly ranked features are selected for inclusion in the dataset. Filter methods can also rank feature subsets instead of individual features. Popular ranking metrics include the Pearson correlation coefficient and mutual information. The PCC is calculated easily from the dataset. Mutual information, however, must be estimated. A common nonparametric estimation method follows from nearest neighbor distances [205].

Wrappers models use an interaction between feature selection and a predetermined classification algorithm. These models include sequential forward and backward selection [203]. In sequential forward selection, features are added until classification performance converges. In sequential backward selection, features are removed instead of added. Though wrapper methods have better performance, they are computationally expensive.

Hybrid models achieve both efficiency and accuracy. They first select several candidate variables by incorporating statistical criteria. They then choose the subset of features with the highest classification accuracy. Embedded models perform feature selection during the modeling algorithm's execution. These methods are embedded in the algorithm as part of the training process. Common embedded algorithms include various types of decision tree algorithms: CART, C4.5, and random forest. Decision trees inherently estimate the suitability of features. The features found at the top of a binary decision tree are the best at separating instances for the task at hand. This characteristic can be exploited for feature selection.

8.3.2 Learning algorithms

We have used the random forest classification algorithm [57] in this study. A random forest is an ensemble of decision trees. Each tree is generated by randomly sampling features iteratively.

8.3.3 Dealing with Imbalanced Dataset

When a dataset is imbalanced, learning algorithms will under-perform on the minority class. Data re-sampling and boosting are two techniques that ease the data imbalance problem. Under-sampling removes examples from the majority class. It has the benefit of reduced training time due to the reduced number of training data points. But it has the drawback of losing useful information. Boosting builds an ensemble of models by assigning higher weights to difficult instances. In imbalanced problems, these difficult instances are the minority examples. Predictions are then made using a weighted average of each of the separate models. Random undersampling with Boosting [318] (RUSBoost) integrates these methods. In RUSBoost, instances are removed randomly from the majority class until balanced. An iteration of the boosting method is then performed. The under-sampled training data is then re-sampled according to the instance's assigned weight. This process is repeated for several iterations. RUSBoost with the AdaBoost.M.2 boosting algorithm [122] is adopted in this study. The Random forest classifier is selected as the base learner in the AdaBoost.M.2 algorithm.

8.4 Case Study

Predictive maintenance is performed for one of the largest utility companies, Southern California Edison. This company's distribution transformers are becoming old. 35% of them were approaching or had surpassed the useful life of 35 years by 2016. Thus employing predictive maintenance to these transformers would be beneficial for the company. The prediction horizon in this study is two years.

8.4.1 Dataset Description

The predictive maintenance dataset contains over $700,000$ transformers in the Los Angeles, Mono, Fresno, Riverside, San Bernardino, Orange, Kern, Tulare, and Ventura counties of California. The dataset covers the years 2012 to 2016. There are 42 categorical, and 30 continuous variables. Features fall into four broad categories. The first is data related to transformer specification. These include line and phase voltages, KVA ratings, primary ratings, secondary voltages, overhead/underground locations, ages, manufacturers, models, subtypes, used/new condition indicators, main line indicators, and commercial use indicators. The second type is data related to transformer loading. These include average loading (%), peak loading (%), and the percent of the time the transformer is overloaded. The third type is data related to location. These include longitude, latitude, district, region, fire zone indicator, corrosion zone indicator, and flood zone indicator. The fourth type is data related to weather. In addition to these, four new features were created for the study. The first is denoted as 'primary category'. It is a bucketing of the transformer ratings into three categories - low, medium, and high. The last three are groupings of KVA ratings, manufacturers, and models by survival rate.

Weather-related variables include temperature (^oF), relative humidity (%), rain (mm), wind speed ($mile/hour$), resultant wind speed ($mile/hour$) and solar radiation (Wh/m^2). Hourly weather-related data are available from 24 weather stations. Statistics of the weather-related variables from each station were used as features. The statistics used were the maximum, minimum, average, and standard deviation. Three new features were created for each weather-related variable. These are counters of exceedance beyond

Table 8.1: Threshold values for weather-related variables

Weather-related Variables	Thresholds (Th1, Th2, Th3)
Temperature (high)	75, 85 and 95
Temperature (low)	50, 40 and 30
Humidity	75, 85 and 95
Wind speed	6.5, 10 and 15
Resultant wind speed	6, 10 and 15
Rain	0.01, 0.07 and 0.15

three threshold values. Three similar additional features were created for temperature. These count the number of times temperature falls below the three threshold values. The thresholds values are provided in Table 8.1.

Some extra information is available which was not directly used as a feature. These are the reason for removal and the date of removal. Some transformers failed due to reasons which cannot be predicted. For example, a transformer may fail due to a lightning surge or an animal attack. These transformers are given a 'transformer failure' label of 0. The removal date helps divide the dataset into training, validation, and test sets. Finally, a unique equipment number for each transformer is available.

8.4.2 Data Preprocessing

Training, validation and test set

First, the dataset is divided by year into a training, validation, and testing dataset. Data from 2012-2014 are divided into a training set and a validation set. The training set contains 70% of the instances and a validation set contains the other 30%. Both the training set and the validation set contain two sets of data. One set is for 2012-2013 and the other is for 2013-2014. Only age changes between these two sets, and it only changes by 1. However,

Table 8.2: List of selected features

Feature type	Feature
Transformer specification	Age, KVA, Manufacturer group, Model group, Overhead/Underground indicator, Subtype, Primary rating group, Used/New condition indicator
Loading	Average loading, Peak loading, Percent time overloaded
Location	Region, Corrosion zone indicator
Weather	Rain above Th2, Humidity over Th2, Wind speed above Th3

the label may change as well. Each changed label will introduce a tomek link - that is, a minimally distanced nearest neighbor pair with opposite class [13]. Tomek links create unwanted overlapping between classes. Therefore, transformers that failed in 2014 are not included in the 2012-2013 set. Data from 2015-2016 work as the testing set.

Dealing with missing values

Some attributes have values missing at random in the predictive maintenance dataset. The rate of missing data is in the range of $1\% - 20\%$. Weather-related variables are imputed via the closest weather station. For the rest of the missing data, the MissForest method is used. This method far outperformed Artificial Neural Networks for this task.

Feature selection

Several feature selection methods are used in this study. The first is sequential forward and backward selection. The second is Mutual Information based filtering. The Top n features of a binary decision tree are also selected. Some selected features were common to all of these methods. The final set of features is selected empirically using a random forest classifier. The final set consists of 16 features. The features are listed in Table 8.2

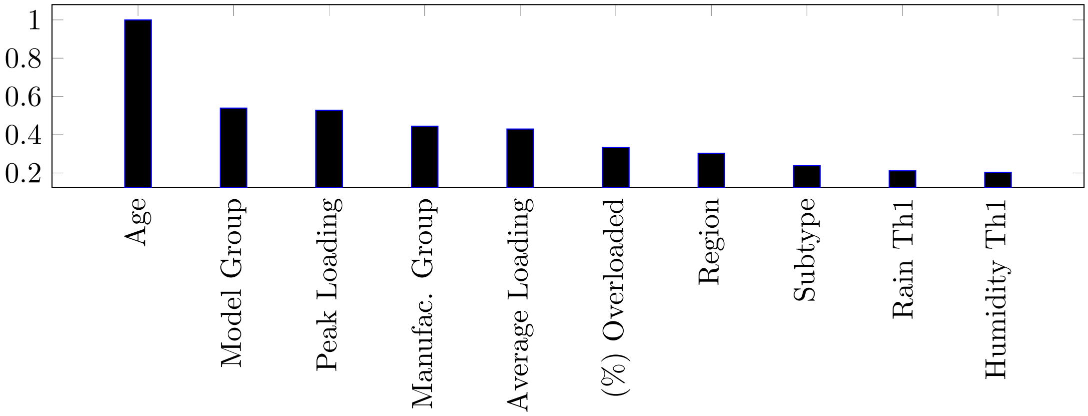

Figure 8.2: Variable importance measures from base random forest classifier

8.4.3 Application of learning algorithm

A random forest and a RUSBoost classifier are trained on the training dataset. To tune the hyperparameters of the random forest model, a grid of ranges is defined first. The validation set performance. The MITN metric is calculated for the validation and testing set.

8.5 Result and analysis

We have calculated the variable importance measures for the input features are calculated. They are plotted in Figure 8.2. The transformer's age was found to be the most influential variable. This confirms intuition. Other important features are Peak and average loading, transformer model, and manufacturer group. This signifies the impact of transformer loading and workmanship.

The MITN is calculated for the Random forest and RUSBoost algorithm with $N = 1000$. Both the Random Forest and RUSBoost algorithm outperforms the traditional

Table 8.3: Comparison of age-based, random forest and RUSBoost model in 'match in top 1000' metric

Set	Age-based	Random Forest	RUSBoost
Validation	50	462	471
Test	50	312	359

age-based rule. Comparison of the Random forest, the RUSBoost algorithm, and the age-based rule is shown in Table 8.3. The age-based rule has a match rate of 50 in the top 1000 transformers. The match rate of the Random Forest Model is 462 in the validation set and 312 in the test set. RUSBoost slightly outperformed the Random forest algorithm. It had a match rate of 471 and 359 in the validation and test datasets respectively. This makes RUSBoost our preferred algorithm in the task of failure prediction.

The achieved level of performance is acceptable for distribution transformers. The achieved MITN outweighs the cost of installing gas sensors for every transformer. We note that there is some imprecise labeling of the transformers. This is evident in the fact that several "reasons for removals" were recorded as "other". With more precise labeling, higher performance may be achieved. Overall, it is concluded that the machine learning-based predictive maintenance utilizing the selected features far outperforms the traditional age-based method and can be used for failure prediction.

8.6 Chapter Summary

In this chapter, the problem of failure prediction of distribution transformers is addressed where traditional dissolved gas analysis is not economically feasible. The problem of predicting distribution transformer failure is formulated as a binary classification problem. The proposed method is very cost-effective as only readily available and low-cost transformer specification, loading, and weather-related data are used. Both random forecast and Random undersampling with boosting (RUSBoost) algorithm are tested through the large-scale case study. 'Match in top 1000' was used as the performance metric. RUSBoost slightly outperforms random forest making it our preferred algorithm for predicting distribution transformer failures. Both random forest and RUSBoost algorithm outperform traditional age-based prediction techniques by a good margin.

Chapter 9

Conclusions

9.1 Summary of Thesis

In this dissertation, we develop four different frameworks to facilitate the integration of renewable energy into the electric grid. The achievements of this dissertation work are summarized as follows:

- In Chapter 2-3, we present unsupervised frameworks for estimating solar PV generation by disaggregating the net load readings to tackle the challenge of behind-the-meter solar PV generation. In Chapter 2, we develop an unsupervised framework to disaggregate net load measurements into solar generation and electric load estimates for individual customers without information about their exact location. Specifically, our algorithm iteratively estimates solar PV generation with a physical model and electric load with the Hidden Markov model regression. In Chapter 3, we present an unsupervised framework for joint disaggregation of the net load readings of a group of customers into the solar PV generation and electric load. The electric loads for a group of customers are estimated jointly by a mixed hidden Markov model (MHMM) which enables modeling the general load consumption behavior present in all customers while acknowledging the individual differences. At the same time, the new model can capture the change in load patterns over a time period by the hidden Markov states. Both of the proposed frameworks synergistically combine a physical PV system performance model with a statistical model for load estimation. The proposed algorithms are also capable of estimating the key technical parameters of the solar PV systems. Our proposed methods are validated against net load and solar PV generation data gathered from residential customers located in Austin, Texas. The validation results show that our proposed method in Chapter 2 reduces the mean squared error by 44% compared to the state-of-the-art disaggregation algorithm. The behind-the-meter solar generation estimation algorithm proposed in Chapter 3 yields significantly higher accuracy over state-of-the-art net load disaggregation algorithms including our proposed algorithm in Chapter 2. It reduces the mean squared error of the state-of-the-art net-load disaggregation baseline algorithm used in Chapter 2 by 67%.

- To tackle the challenge of voltage regulation under high solar photovoltaics (PV) penetration, we develop reinforcement learning-based two-timescale Volt-VAR control (VVC) frameworks in Chapter 4-5. In Chapter 4, the slow timescale control of voltage regulating devices is achieved by a model-based approach. The fast time-scale control of smart inverters is attained with a reinforcement learning-based method.

The deep deterministic policy gradient (DDPG) algorithm is adopted to control the setpoints of both the real and reactive power of smart inverters. The control policy of smart inverters is learned from the historical operational data without relying on accurate distribution network secondary circuit parameters. In Chapter 4, we propose a completely model-free two-timescale Volt-VAR control scheme that does not depend on accurate primary or secondary feeder models. Two hierarchically arranged agents are set up for the slow timescale and fast timescale problem which are coupled through a communication medium. The two sets of policies are learned concurrently by a deep deterministic policy gradient and multi-agent soft actor-critic based algorithm respectively. Simulation results on the IEEE 34-bus feeder show that the proposed framework in Chapter 4 can determine near-optimal set points of smart inverters in real-time operations. Compared with existing reinforcement learning-based smart inverter control, our approach achieves lower line losses, voltage deviations, and active power curtailment. Comprehensive numerical studies performed with the IEEE 123-bus distribution test feeders show that the proposed framework in 5 can determine near-optimal control actions of conventional Volt-Var control devices and set points of smart inverters in real-time operations.

- In Chapter 6-7, we quantify the impact of aerosols on reservoir inflows and hydropower generation. In Chapter 6, we develop a comprehensive framework was developed to quantify the impact of aerosols on reservoir inflow by integrating the Weather Research and Forecasting Model with chemistry (WRF-Chem) and a dynamic regression model. The statistical dynamic regression model produces forecasts for reservoir inflow based on the meteorological output variables from the WRF-Chem model. In Chapter 6, we take the next logical step to explore the impact of aerosols on hydropower generation and revenue. A comprehensive framework is developed to quantify the impact of aerosols on hydropower generation and revenue by integrating the Weather Research and Forecasting Model with Chemistry, a statistical hydrologic forecasting model, and the hydropower operation optimization toolbox. We perform the case studies on the Big Creek Hydroelectric Project in the San Joaquin Region. We conclude that the presence of aerosols is detrimental to the optimal utilization of hydroelectric power systems. It causes a reduction of annual hydropower generation causing a $2.8 million loss in annual revenue.

- In Chapter 8, we present a method for the predictive maintenance of distribution transformers, i.e. method of predicting which transformers are most likely to fail soon. Once predicted, such transformers may be subject to maintenance or replacement. This practice reduces the costs and increases the reliability of power distribution systems. The practice is common in transmission systems. In that domain, physical methods such as dissolved gas analysis see fantastic results. Data-driven techniques utilizing DGA data are also popular. But such methods are cost-prohibitive for distribution systems. Instead, we proposed to utilize a data-driven framework for the task which only uses readily available data. Such data include the transformers' specification, loading, location, and weather-related information. Such data inspire the use of two suitable machine learning algorithms. The first is random forests. The second is the Random Undersampling with AdaBoost (RUSBoost) algorithm. We test these algorithms on over 700,000 distribution transformers in Southern California. This test finds that both algorithms outperform the current state of practice. Further, it finds that the RUSBoost algorithm performs better than the Random Forest.

9.2 Limitations and Future Research Directions

Some additional research questions need to be addressed. In the future, we plan to explore the following topics:

- Further improvement can be achieved by leveraging more granular solar irradiance data in our proposed net load disaggregation algorithm developed in Chapter 2. Several interesting extensions of our proposed joint net load disaggregation algorithm developed in Chapter 3 can be explored in the future. First, a semi-parametric mixed hidden Markov model can be developed to further improve the computational efficiency of the proposed algorithm. Second, in the current model, the customer-specific random effect and its variance are assumed to be independent of the hidden states. The mixed hidden Markov model can be improved by assuming that the random effect variance depends on the hidden states. Third, a robust version of the proposed net-load disaggregation algorithm can be developed to improve estimation accuracy in the presence of outliers. Finally, a mixed effect model to jointly estimate load in several communities with a community-specific random effect along with the customer-specific random effect will be of interest.
- Our proposed reinforced learning algorithm approximates the value function, action-value functions, and policy networks with neural networks. With a large number of

traditional VVC devices and smart inverters, the number of input features and outputs in the neural networks will increase along with the size of the hidden layers. However, neural networks are scalable and capable of handling thousands of outputs. Therefore, in theory, our proposed algorithm will be able to handle a large network. However, there are many challenges associated with large-scale systems. For example, a large amount of training data would be required. The performance may degrade with a large number of features. As such, feature selection techniques should be carefully employed. The training will be slow and computationally intensive. In the future, We plan to test our proposed VVC algorithm with necessary modifications for large-scale implementation on the 8500 node test feeder.

There are several drawbacks to the proposed VVC algorithm. First, Our proposed framework assumes a time-invariant distribution network topology. If the distribution network topology changes, then it will be required to train the RL network from scratch. In the future, we plan to develop RL-based Volt-VAR control algorithms that can be easily adapted to handle updated network topology and voltage controllers. This way, the RL-based controller does not have to be trained entirely from scratch. Second, if the observability of the system is incomplete, our proposed VVC algorithm will work as long as the critical parts of the network have observability. Lastly, integrating the existing local controllers for OLTCs, considering the hourly reactive power dispatch of PVs along with the traditional VVC devices, or formulating the two-timescale problem as a multi-time optimization problem will further improve the performance of the baselines. One very useful extension to the model-free two timescale reinforcement learning-based Volt-Var control method is to adopt an incremental learning scheme for the reinforcement learning method so that the new incrementally available data can be readily utilized to extend the existing model's expertise instead of training from scratch.

- There are a few limitations to the framework developed in Chapter 6 and 7. The limited historical reservoir inflow data prevented us from capturing the long-term trend in reservoir inflow and evaluating the long-term impact of aerosols on the reservoir inflow. The daily temperature, snow water equivalent, and precipitation records for 2010-2014 were not available at the weather stations located at Florence Lake and Lake Thomas Alva Edison. These additional observations could have improved the quality of the inflow forecast. The quantification of the impact of aerosols on inflows into reservoirs strongly depends on the accurate estimation of the difference in meteorological variables between the WRF-Chem CTRL and CLEAN simulations. WRF-Chem model run in a higher resolution in the grid box could deliver more accurate results. At last, a rigorous outlier detection algorithm can be applied to the inflow data, which can further improve the forecast performance of the dynamic regression model. In the future, we plan to integrate the year ahead inflow forecast of Florence Lake and Lake Edison into the long-term scheduling of the Big Creek Hydroelectric Project.

- There are several drawbacks to the predictive maintenance framework developed in Chapter 8. Failure information of the transformers was only available for four years. Data spanning a longer period of time could better help the machine learning algorithm capture the trend in transformer failures. The loading-related data were available for only one year. Availability of historic load information can improve the classifier performance as it is an important feature in modeling the failure of the transformers. Rigorous record keeping of the distribution transformers' information can reduce the occurrence of missing values in the dataset and therefore improve the classifier performance. Recording the exact reason(s) for transformer removal can help alleviate the label noise problem. In the future, we plan to build machine learning models to estimate the remaining lifetime of the distribution transformers. Accurate estimation of the remaining useful life of transformers could facilitate the development of a more cost-effective maintenance strategy for electric utilities.

Bibliography

[1] DiGrad: Multi-task reinforcement learning with shared actions.

[2] Economic and technical analysis of reactive power provision from distributed energy resources in microgrids | Elsevier Enhanced Reader.

[3] Equilibrium and dynamics of local voltage control in distribution systems - IEEE Conference Publication.

[4] IEEE Xplore Full-Text PDF:.

[5] Learning to control in power systems_ Design and analysis guidelines for concrete safety problems | Elsevier Enhanced Reader.

[6] Options for control of reactive power by distributed photovoltaic generators - IEEE journals & magazine.

[7] Real-time Voltage Control Using Deep Reinforcement Learning. | OpenReview.

[8] Reliability challenges of automotive power electronics | Elsevier Enhanced Reader.

[9] Renewable power generation costs in 2019. *International Renewable Energy Agency*, page 144.

[10] Thermal Loading and Lifetime Estimation for Power Device Considering Mission Profiles in Wind Power Converter - IEEE Journals & Magazine.

[11] Transitioning to Physics-of-Failure as a Reliability Driver in Power Electronics - IEEE Journals & Magazine.

[12] Vista Decision Support System. `https://www.hatch.com/en/Expertise/Services-and-Technologies/Vista-Decision-Support-System`.

[13] Two modifications of CNN. *IEEE Transactions on Systems, Man, and Cybernetics*, SMC-6(11):769–772, November 1976.

[14] Failure to act: The economic impact of current investment trends in electricity infrastructure. Technical report, American Society of Civil Engineers, 2011.

[15] Transmission and distribution (T&D) Volume 4 – infrastructure replacement programs. Technical report, Southern California Edison, Rosemead, Caifornia, 2013.

[16] Annual energy outlook 2019 with projections to 2050. Technical report, US Energy Information Administration, Office of Energy Analysis, U.S. Department of Energy, Washington, DC 20585, January 2019.

[17] Global Energy Review 2020. page 55, 2020.

[18] IEEE Standard for interconnection and interoperability of distributed energy resources with associated electric power systems interfaces–Amendment 1: To provide more flexibility for adoption of abnormal operating performance category III. *IEEE Std 1547a-2020 (Amendment to IEEE Std 1547-2018)*, pages 1–16, April 2020.

[19] Reimagining the grid. Technical report, Southern Califonria Edison, 2020.

[20] Andrew S Ackerman, Michael P Kirkpatrick, David E Stevens, and Owen B Toon. The impact of humidity above stratiform clouds on indirect aerosol climate forcing. *Nature*, 432(7020):1014–1017, 2004.

[21] International Energy Agency. *Global Energy Review 2019: The latest trends in energy and emissions in 2019*. OECD, June 2020.

[22] Hamed Ahmadi, José R. Martí, and Hermann W. Dommel. A Framework for Volt-VAR Optimization in Distribution Systems. *IEEE Transactions on Smart Grid*, 6(3):1473–1483, May 2015.

[23] Bruce A Albrecht. Aerosols, cloud microphysics, and fractional cloudiness. *Science*, 245(4923):1227–1231, 1989.

[24] Rachel MacKay Altman. Mixed hidden Markov models: an extension of the hidden Markov model to the longitudinal data setting. *Journal of the American Statistical Association*, 102(477):201–210, 2007.

[25] AZ Amin. Global energy transformation: A roadmap to 2050. *International Renewable Energy Agency*, 2019.

[26] Sean Anderson, Patricia Hidalgo-Gonzalez, Roel Dobbe, and Claire J. Tomlin. Distributed Model Predictive Control for Autonomous Droop-Controlled Inverter-Based Microgrids. In *2019 IEEE 58th Conference on Decision and Control (CDC)*, pages 6242–6248, Nice, France, December 2019. IEEE.

[27] Meinrat O Andreae, Chris D Jones, and Peter M Cox. Strong present-day aerosol cooling implies a hot future. *Nature*, 435(7046):1187, 2005.

[28] K. E. Antoniadou-Plytaria, I. N. Kouveliotis-Lysikatos, P. S. Georgilakis, and N. D. Hatziargyriou. Distributed and decentralized voltage control of smart distribution networks: Models, methods, and future research. *IEEE Transactions on Smart Grid*, 8(6):2999–3008, November 2017.

[29] Anup Anurag, Yongheng Yang, and Frede Blaabjerg. Thermal performance and reliability analysis of single-phase PV inverters with reactive power injection outside feed-in operating hours. *IEEE Trans. Emerg. Sel. Topics Power Electron.*, 3(4):870–880, December 2015.

[30] Kristen B. Ardani, Eric O'Shaughnessy, and Paul D. Schwabe. Coordinating distributed energy resources for grid services: A case study of pacific gas and electric. 2018.

[31] Channing Arndt, Doug Arent, Faaiqa Hartley, Bruno Merven, and Alam Hossain Mondal. Faster than you think: Renewable energy and developing countries. *Annual Review of Resource Economics*, 11(1):149–168, 2019.

[32] Daniel B. Arnold, Matias Negrete-Pincetic, Michael D. Sankur, David M. Auslander, and Duncan S. Callaway. Model-free optimal control of VAR resources in distribution systems: An extremum seeking approach. *IEEE Trans. Power Syst.*, 31(5), September 2016.

[33] Himani Arora, Rajath Kumar, Jason Krone, and Chong Li. Multi-task Learning for Continuous Control. *arXiv:1802.01034 [cs, stat]*, February 2018.

[34] Kyri Baker, Andrey Bernstein, Emiliano Dall'Anese, and Changhong Zhao. Network-cognizant voltage droop control for distribution grids. *IEEE Transactions on Power Systems*, 33(2):2098–2108, 2018.

[35] Philip J. Ball and Stephen J. Roberts. Offcon^3: What is state of the art anyway?, 2021.

[36] M.E. Baran and F.F. Wu. Network reconfiguration in distribution systems for loss reduction and load balancing. *IEEE Transactions on Power Delivery*, 4(2):1401–1407, April 1989.

[37] Sean Barker, Aditya Mishra, David Irwin, Emmanuel Cecchet, and Prashant Shenoy. Smart: An open data set and tools for enabling research in sustainable homes. page 6.

[38] J. C. Barnard, J. D. Fast, G. Paredes-Miranda, W. P. Arnott, and A. Laskin. Technical note: Evaluation of the WRF-Chem "Aerosol chemical to aerosol optical properties" Module using data from the MILAGRO campaign. *Atmos. Chem. Phys.*, 10(15):7325–7340, August 2010.

[39] T. P. Barnett, J. C. Adam, and D. P. Lettenmaier. Potential impacts of a warming climate on water availability in snow-dominated regions. *Nature*, 438(7066):303–309, November 2005.

[40] Tim P Barnett, Jennifer C Adam, and Dennis P Lettenmaier. Potential impacts of a warming climate on water availability in snow-dominated regions. *Nature*, 438(7066):303–309, 2005.

[41] G. Baroni and S. Tarantola. A general probabilistic framework for uncertainty and global sensitivity analysis of deterministic models: a hydrological case study. *Environmental Modelling & Software*, 51(Supplement C):26–34, January 2014.

[42] Mary Barth, Joseph P. McFadden, Jielun Sun, Christine Wiedinmyer, Patrick Chuang, Don Collins, Robert Griffin, Michael Hannigan, Thomas Karl, Si-Wan Kim, Sonia Lasher-Trapp, Samuel Levis, Marcy Litvak, Natalie Mahowald, Katharine Moore, Sreela Nandi, Eiko Nemitz, Athanasios Nenes, Mark Potosnak, Timothy M. Raymond, James Smith, Christopher Still, and Craig Stroud. Coupling between Land Ecosystems and the Atmospheric Hydrologic Cycle through Biogenic Aerosol Pathways. *Bulletin of the American Meteorological Society*, 86(12):1738–1742, 2005.

[43] Andrew G Barto and Sridhar Mahadevan. Recent Advances in Hierarchical Reinforcement Learning. *Discrete Event Dynamic Systems*, page 37.

[44] T. Basso. IEEE 1547 and 2030 standards for distributed energy resources interconnection and interoperability with the electricity grid. Technical Report NREL/TP-5D00-63157, 1166677, December 2014.

[45] Benjamin Bayer, Patrick Matschoss, Heiko Thomas, and Adela Marian. The German experience with integrating photovoltaic systems into the low-voltage grids. *Renewable Energy*, 119:129–141, April 2018.

[46] A. Beauvais, N. Chevillard, M.G Paredes, M. Heisz, R. Rossi, M. Schmela, and SolarPower Europe. Global market outlook for solar power 2018–2022. *Africa-EU Renewable Energy Cooperation Programme (RECP), Solar Power Europe: Brussels, Belgium*, 2018.

[47] Juan Carlos Bedoya, Chen-Ching Liu, Gayathri Krishnamoorthy, and Anamika Dubey. Bilateral electricity market in a distribution system environment. *IEEE Transactions on Smart Grid*, 10(6):6701–6713, November 2019.

[48] Juan Carlos Bedoya, Mohammad Ostadijafari, Chen-Ching Liu, and Anamika Dubey. Decentralized transactive energy for flexible resources in distribution systems. *IEEE Transactions on Sustainable Energy*, 12(2):1009–1019, April 2021. Conference Name: IEEE Transactions on Sustainable Energy.

[49] Engel Bernard, Storm Dan, White Mike, Arnold Jeff, and Arabi Mazdak. A Hydrologic/Water Quality Model Applicati11. *JAWRA Journal of the American Water Resources Association*, 43(5):1223–1236, October 2007.

[50] Keith Beven. A manifesto for the equifinality thesis. *Journal of Hydrology*, 320(1):18–36, March 2006.

[51] M Bolinger and J Seel. Utility-scale solar 2014: An empirical analysis of project cost, performance, and pricing trends in the United States. Technical Report LBNL-1000917, Lawrence Berkeley National Lab., United States, 2015.

[52] V. Borozan, M.E. Baran, and D. Novosel. Integrated volt/VAr control in distribution systems. In *2001 IEEE Power Engineering Society Winter Meeting. Conference Proceedings (Cat. No.01CH37194)*, volume 3, pages 1485–1490 vol.3, January 2001.

[53] Borys Randolph D., Lowenthal Douglas H., Cohn Stephen A., and Brown William O. J. Mountaintop and radar measurements of anthropogenic aerosol effects on snow growth and snowfall rate. *Geophysical Research Letters*, 30(10), May 2003.

[54] George E. P. Box, Gwilym M. Jenkins, Gregory C. Reinsel, and Greta M. Ljung. *Time Series Analysis: Forecasting and Control.* John Wiley & Sons, June 2015. Google-Books-ID: lCy9BgAAQBAJ.

[55] Richard E Brandt, Stephen G Warren, and Antony D Clarke. A controlled snowmaking experiment testing the relation between black carbon content and reduction of snow albedo. *Journal of Geophysical Research: Atmospheres*, 116(D8), 2011.

[56] JE Braun and JC Mitchell. Solar geometry for fixed and tracking surfaces. *Solar energy*, 31(5):439–444, 1983.

[57] Leo Breiman. Random forests. *Machine Learning*, 45(1):5–32, October 2001.

[58] Levi D. Brekke, Norman L. Miller, Kathy E. Bashford, Nigel W. T. Quinn, and John A. Dracup. Climate change impacts uncertainty for water resources in the San Joaquin River Basin, California. *J. Am. Water Resour. Assoc.*, 40(1):149–164, February 2004.

[59] Enrique Briglia, Sebastián Alaggia, and Fernando Paganini. Distribution network management based on optimal power flow: Integration of discrete decision variables. In *2017 51st Annu. Conf. Inf. Sci. and Syst. (CISS)*, pages 1–6, 2017.

[60] F. Bu, K. Dehghanpour, Y. Yuan, Z. Wang, and Y. Zhang. A data-driven game-theoretic approach for behind-the-meter pv generation disaggregation. *IEEE Transactions on Power Systems*, 35(4):3133–3144, 2020.

[61] Eduardo F Camacho and Carlos Bordons Alba. *Model predictive control.* Springer science & business media, 2013.

[62] Di Cao, Junbo Zhao, Weihao Hu, Fei Ding, Qi Huang, Zhe Chen, and Frede Blaabjerg. Data-driven multi-agent deep reinforcement learning for distribution system decentralized voltage control with high penetration of pvs. *IEEE Transactions on Smart Grid*, 2021.

[63] Di Cao, Junbo Zhao, Weihao Hu, Nanpeng Yu, Fei Ding, Qi Huang, and Zhe Chen. Deep reinforcement learning enabled physical-model-free two-timescale voltage control method for active distribution systems. *IEEE Transactions on Smart Grid*, 13(1):149–165, 2022.

[64] Olivier Cappé, Eric Moulines, and Tobias Rydén. *Inference in hidden Markov models.* Springer series in statistics. Springer, 2005.

[65] P. M. S. Carvalho, P. F. Correia, and L. A. F. M. Ferreira. Distributed Reactive Power Generation Control for Voltage Rise Mitigation in Distribution Networks. *IEEE Transactions on Power Systems*, 23(2):766–772, May 2008.

[66] Daniel R. Cayan, Laurence G. Riddle, and Edward Aguado. The influence of precipitation and temperature on seasonal streamflow in California. *Water Resour. Res.*, 29(4):1127–1140, April 1993.

[67] E. G. Chapman, W. I. Gustafson Jr., R. C. Easter, J. C. Barnard, S. J. Ghan, M. S. Pekour, and J. D. Fast. Coupling aerosol-cloud-radiative processes in the WRF-Chem model: Investigating the radiative impact of elevated point sources. *Atmos. Chem. Phys.*, 9(3):945–964, February 2009.

[68] R. J. Charlson, J. Langner, H. Rodhe, C. B. Leovy, and S. G. Warren. Perturbation of the northern hemisphere radiative balance by backscattering from anthropogenic sulfate aerosols*. *Tellus A*, 43(4):152–163, August 1991.

[69] R. J. Charlson, S. E. Schwartz, J. M. Hales, R. D. Cess, J. A. Coakley, J. E. Hansen, and D. J. Hofmann. Climate forcing by anthropogenic aerosols. *Science*, 255(5043):423–430, January 1992.

[70] Robert J Charlson and SE Schwartz. Climate forcing by anthropogenic aerosols. *Science*, 255(5043):423, 1992.

[71] Florence Chaubert-Pereira, Yann Guédon, Christian Lavergne, and Catherine Trottier. Markov and semi-Markov switching linear mixed models used to identify forest tree growth components. *Biometrics*, 66(3):753–762, 2010.

[72] Dong Chen, Joseph Breda, and David Irwin. Staring at the sun: a physical black-box solar performance model. In *Proceedings of the 5th Conference on Systems for Built Environments - BuildSys '18*, pages 53–62, Shenzen, China, 2018. ACM Press.

[73] Dong Chen and David Irwin. Black-box Solar Performance Modeling: Comparing Physical, Machine Learning, and Hybrid Approaches. 45(2):6, 2017.

[74] Dong Chen and David Irwin. SunDance: Black-box behind-the-meter solar disaggregation. In *Proceedings of the Eighth International Conference on Future Energy Systems*, pages 45–55. ACM, 2017.

[75] W. Chen, C. Pan, Y. Yun, and Y. Liu. Wavelet networks in power transformers diagnosis using dissolved gas analysis. *IEEE Transactions on Power Delivery*, 24(1):187–194, January 2009.

[76] C. M. Cheung, W. Zhong, C. Xiong, A. Srivastava, R. Kannan, and V. K. Prasanna. Behind-the-meter solar generation disaggregation using consumer mixture models. In *2018 IEEE International Conference on Communications, Control, and Computing Technologies for Smart Grids (SmartGridComm)*, pages 1–6, October 2018.

[77] Yinlam Chow, Ofir Nachum, Aleksandra Faust, Edgar Duenez-Guzman, and Mohammad Ghavamzadeh. Lyapunov-based safe policy optimization for continuous control. *arXiv:1901.10031 [cs, stat]*, February 2019. arXiv: 1901.10031.

[78] M. L. Chu-Agor, R. Muñoz-Carpena, G. Kiker, A. Emanuelsson, and I. Linkov. Exploring vulnerability of coastal habitats to sea level rise through global sensitivity and uncertainty analyses. *Environmental Modelling & Software*, 26(5):593–604, May 2011.

[79] Petr Chỳlek, V Ramaswamy, and Vandana Srivastava. Albedo of soot-contaminated snow. *Journal of Geophysical Research: Oceans*, 88(C15):10837–10843, 1983.

[80] Lorenzo Ciannelli, Kung-Sik Chan, Kevin M. Bailey, and Nils Chr. Stenseth. Nonadditive effects of the environment on the survival of a large marine fish population. *Ecology*, 85(12):3418–3427, December 2004.

[81] Antony D Clarke and Kevin J Noone. Soot in the Arctic snowpack: A cause for perturbations in radiative transfer. *Atmospheric Environment (1967)*, 19(12):2045–2053, 1985.

[82] P. Coulibaly, F. Anctil, and B. Bobée. Daily reservoir inflow forecasting using artificial neural networks with stopped training approach. *J. Hydrol.*, 230:244–257, May 2000.

[83] Robert E. Criss and William E. Winston. Do Nash values have value? Discussion and alternate proposals. *Hydrological Processes*, 22(14):2723–2725, July 2008.

[84] Qiming Cui, Kai Liang, Hongyu Gao, Guodong Chen, Naiyu Wang, Shaoyu Jin, Changqing Zhong, Shuting Cui, Daojun Sun, Jie Fang, Chengwei Han, Bin Xu, Yuhong An, and Minghu Xu. Research of the transformer fault diagnosis expert system based on esta and deep learning neural network programmed in matlab. 01 2016.

[85] Jonathan Currie and David I. Wilson. OPTI: Lowering the Barrier Between Open Source Optimizers and the Industrial MATLAB User. In Nick Sahinidis and Jose Pinto, editors, *Foundations of Computer-Aided Process Operations*, Savannah, Georgia, USA, 8–11 January 2012.

[86] Emiliano Dall'Anese, Hao Zhu, and Georgios B. Giannakis. Distributed optimal power flow for smart microgrids. *IEEE Transactions on Smart Grid*, 4(3):1464–1475, September 2013. Conference Name: IEEE Transactions on Smart Grid.

[87] Emiliano Dall'Anese, Sairaj V. Dhople, and Georgios B. Giannakis. Optimal dispatch of photovoltaic inverters in residential distribution systems. *IEEE Transactions on Sustainable Energy*, 5(2):487–497, April 2014.

[88] Emiliano Dall'Anese, Sairaj V Dhople, Brian B Johnson, and Georgios B Giannakis. Decentralized optimal dispatch of photovoltaic inverters in residential distribution systems. *IEEE Transactions on Energy Conversion*, 29(4):957–967, 2014.

[89] Emiliano Dall'Anese, Sairaj V Dhople, Brian B Johnson, and Georgios B Giannakis. Decentralized optimal dispatch of photovoltaic inverters in residential distribution systems. *IEEE Transactions on Energy Conversion*, 29(4):957–967, 2014.

[90] J. W. Davidson, D. A. Savic, and G. A. Walters. Symbolic and numerical regression: experiments and applications. *Inform. Sci.*, 150(1–2):95–117, March 2003.

[91] D. P. Dee, S. M. Uppala, A. J. Simmons, P. Berrisford, P. Poli, S. Kobayashi, U. Andrae, M. A. Balmaseda, G. Balsamo, P. Bauer, P. Bechtold, A. C. M. Beljaars, L. van de Berg, J. Bidlot, N. Bormann, C. Delsol, R. Dragani, M. Fuentes, A. J. Geer, L. Haimberger, S. B. Healy, H. Hersbach, E. V. Hólm, L. Isaksen, P. Kållberg, M. Köhler, M. Matricardi, A. P. McNally, B. M. Monge-Sanz, J.-J. Morcrette, B.-K. Park, C. Peubey, P. de Rosnay, C. Tavolato, J.-N. Thépaut, and F. Vitart. The ERA-Interim reanalysis: configuration and performance of the data assimilation system. *Q. J. Roy. Meteorol. Soc.*, 137(656):553–597, April 2011.

[92] J. S. Deems, T. H. Painter, J. J. Barsugli, J. Belnap, and B. Udall. Combined impacts of current and future dust deposition and regional warming on Colorado River Basin snow dynamics and hydrology. *Hydrol. Earth Syst. Sci.*, 17(11):4401–4413, November 2013.

[93] California Department of Water Resources. Reservoir inflow at Florence Lake and lake Thomas A. Edison in California, meteorological variables at weather stations KSP, VLC, UBC, TMR and HTT for water year 2010-14 and WRF-Chem Simulations of meteorological variables for two aerosol scenarios at Big Creek Hydroelectric Project for water year 2013 and 2014, 2017.

[94] Stacy L DeRuiter, Roland Langrock, Tomas Skirbutas, Jeremy A Goldbogen, John Calambokidis, Ari S Friedlaender, Brandon L Southall, et al. A multivariate mixed hidden Markov model for blue whale behaviour and responses to sound exposure. *The Annals of Applied Statistics*, 11:362–392, 2017.

[95] Rustom Dessai and Franz Stadtmueller. EPIC final report: EPIC 2.02 – distributed energy resource management system. Technical report, Pacific Gas and Electric Company, 2019.

[96] Roel Dobbe, Patricia Hidalgo-Gonzalez, Stavros Karagiannopoulos, Rodrigo Henriquez-Auba, Gabriela Hug, Duncan S. Callaway, and Claire J. Tomlin. Learning to control in power systems: Design and analysis guidelines for concrete safety problems. *Electric Power Systems Research*, 189:106615, December 2020.

[97] Aron P Dobos. PVWatts version 1 technical reference. Technical report, National Renewable Energy Laboratory, Golden, CO, USA, 2013.

[98] Aron P Dobos. PVWatts version 5 manual. Technical report, National Renewable Energy Laboratory, Golden, CO, USA, 2014.

[99] SJ Doherty, SG Warren, TC Grenfell, AD Clarke, and RE Brandt. Light-absorbing impurities in Arctic snow. *Atmospheric Chemistry and Physics*, 10(23):11647–11680, 2010.

[100] J. Driesen and R. Belmans. Distributed generation: challenges and possible solutions. In *2006 IEEE Power Eng. Soc. General Meeting*, page 8, 2006.

[101] Richard Durbin, Sean Eddy, Anders Krogh, and Graeme Mitchison. *Biological Sequence Analysis: Probabilistic Models of Proteins and Nucleic Acids.* Cambridge University Press, Cambridge, U.K., 1998.

[102] Carlo D'Eramo, Davide Tateo, Andrea Bonarini, Marcello Restelli, and Jan Peters. Sharing knowledge in multi-task deep reinforcement learning. page 18, 2020.

[103] EIA. Annual energy outlook 2020: with projections to 2050. *United States Energy Information Administration*, 2020.

[104] L. K. Emmons, S. Walters, P. G. Hess, J.-F. Lamarque, G. G. Pfister, D. Fillmore, C. Granier, A. Guenther, D. Kinnison, T. Laepple, J. Orlando, X. Tie, G. Tyndall, C. Wiedinmyer, S. L. Baughcum, and S. Kloster. Description and evaluation of the model for ozone and related chemical tracers, version 4 (MOZART-4). *Geosci. Model Dev.*, 3(1):43–67, January 2010.

[105] Oak Ridge National Laboratory Environmental Sciences Division. Global fire emissions database, version 2 (gfedv2.1), 2013.

[106] eurostat. Renewable energy on the rise: 37% of eu's electricity, 2022.

[107] F. Licciardello, D. A. Zema, S. M. Zimbone, and R. L. Bingner. Runoff and Soil Erosion Evaluation by the AnnAGNPS Model in a Small Mediterranean Watershed. *Transactions of the ASABE*, 50(5):1585–1593, 2007.

[108] J. Fan, L. R. Leung, P. J. DeMott, J. M. Comstock, B. Singh, D. Rosenfeld, J. M. Tomlinson, A. White, K. A. Prather, P. Minnis, J. K. Ayers, and Q. Min. Aerosol impacts on California winter clouds and precipitation during CalWater 2011: local pollution versus long-range transported dust. *Atmos. Chem. Phys.*, 14(1):81–101, January 2014.

[109] M. Farivar, L. Chen, and S. Low. Equilibrium and dynamics of local voltage control in distribution systems. In *52nd IEEE Conference on Decision and Control*, pages 4329–4334, December 2013.

[110] M. Farivar, R. Neal, C. Clarke, and S. Low. Optimal inverter VAR control in distribution systems with high PV penetration. In *2012 IEEE Power and Energy Society General Meeting*, pages 1–7, San Diego, CA, July 2012. IEEE.

[111] Masoud Farivar, Christopher R. Clarke, Steven H. Low, and K. Mani Chandy. Inverter VAR control for distribution systems with renewables. In *2011 IEEE International Conference on Smart Grid Communications (SmartGridComm)*, pages 457–462, Brussels, Belgium, October 2011. IEEE.

[112] Masoud Farivar, Russell Neal, Christopher Clarke, and Steven Low. Optimal inverter VAR control in distribution systems with high PV penetration. In *2012 IEEE Power and Energy Society General Meeting*, pages 1–7, July 2012.

[113] J. D. Fast, J. Allan, R. Bahreini, J. Craven, L. Emmons, R. Ferrare, P. L. Hayes, A. Hodzic, J. Holloway, C. Hostetler, J. L. Jimenez, H. Jonsson, S. Liu, Y. Liu, A. Metcalf, A. Middlebrook, J. Nowak, M. Pekour, A. Perring, L. Russell, A. Sedlacek, J. Seinfeld, A. Setyan, J. Shilling, M. Shrivastava, S. Springston, C. Song, R. Subramanian, J. W. Taylor, V. Vinoj, Q. Yang, R. A. Zaveri, and Q. Zhang. Modeling regional aerosol and aerosol precursor variability over California and its sensitivity to emissions and long-range transport during the 2010 CalNex and CARES campaigns. *Atmos. Chem. Phys.*, 14(18):10013–10060, September 2014.

[114] J. D. Fast, W. I. Gustafson Jr., L. K. Berg, W. J. Shaw, M. Pekour, M. Shrivastava, J. C. Barnard, R. A. Ferrare, C. A. Hostetler, J. A. Hair, M. Erickson, B. T. Jobson, B. Flowers, M. K. Dubey, S. Springston, R. B. Pierce, L. Dolislager, J. Pederson, and R. A. Zaveri. Transport and mixing patterns over Central California during the carbonaceous aerosol and radiative effects study (CARES). *Atmos. Chem. Phys.*, 12(4):1759–1783, February 2012.

[115] Fast Jerome D., Gustafson William I., Easter Richard C., Zaveri Rahul A., Barnard James C., Chapman Elaine G., Grell Georg A., and Peckham Steven E. Evolution of ozone, particulates, and aerosol direct radiative forcing in the vicinity of Houston using a fully coupled meteorology-chemistry-aerosol model. *Journal of Geophysical Research: Atmospheres*, 111(D21), November 2006.

[116] Sheng-wei Fei and Xiao-bin Zhang. Fault diagnosis of power transformer based on support vector machine with genetic algorithm. *Expert Systems with Applications*, 36(8):11352–11357, October 2009.

[117] Mark G Flanner, Charles S Zender, James T Randerson, and Philip J Rasch. Present-day climate forcing and response from black carbon in snow. *Journal of Geophysical Research: Atmospheres*, 112(D11), 2007.

[118] Flanner Mark G. and Zender Charles S. Snowpack radiative heating: Influence on Tibetan Plateau climate. *Geophysical Research Letters*, 32(6), March 2005.

[119] Flanner Mark G. and Zender Charles S. Linking snowpack microphysics and albedo evolution. *Journal of Geophysical Research: Atmospheres*, 111(D12), June 2006.

[120] Brandon Foggo and Nanpeng Yu. A comprehensive evaluation of supervised machine learning for the phase identification problem. *World Acad. Sci. Eng. Technol. Int. J. Comput. Syst. Eng*, 12(6), 2018.

[121] Brandon Foggo and Nanpeng Yu. Improving supervised phase identification through the theory of information losses. *IEEE Transactions on Smart Grid*, 11(3):2337–2346, 2019.

[122] Yoav Freund and Robert E Schapire. Experiments with a new boosting algorithm. page 9.

[123] Moshe Fridman. Hidden Markov model regression. Technical report, Institute of Mathematics, University of Minnesota, 1993.

[124] Scott Fujimoto, Herke van Hoof, and David Meger. Addressing Function Approximation Error in Actor-Critic Methods. *arXiv:1802.09477 [cs, stat]*, October 2018. arXiv: 1802.09477.

[125] Giorgio Galeati. A comparison of parametric and non-parametric methods for runoff forecasting. *Hydrol. Sci. J.*, 35(1):79–94, February 1990.

[126] Lingwen Gan, Na Li, Ufuk Topcu, and Steven Low. Branch Flow Model for Radial Networks: Convex Relaxation. page 8.

[127] Oktoviano Gandhi, Carlos D. Rodríguez-Gallegos, Naga Brahmendra Yadav Gorla, Monika Bieri, Thomas Reindl, and Dipti Srinivasan. Reactive Power Cost From PV Inverters Considering Inverter Lifetime Assessment. *IEEE Transactions on Sustainable Energy*, 10(2), April 2019.

[128] Oktoviano Gandhi, Carlos D. Rodríguez-Gallegos, Wenjie Zhang, Dipti Srinivasan, and Thomas Reindl. Economic and technical analysis of reactive power provision from distributed energy resources in microgrids. *Applied Energy*, 210, January 2018.

[129] Yuanqi Gao, Wei Wang, and Nanpeng Yu. Consensus multi-agent reinforcement learning for volt-var control in power distribution networks. *IEEE Transactions on Smart Grid*, 12(4):3594–3604, 2021.

[130] Yuanqi Gao and Nanpeng Yu. Deep reinforcement learning in power distribution systems: Overview, challenges, and opportunities. In *2021 IEEE power & energy society innovative smart grid technologies conference (ISGT)*, pages 1–5. IEEE, 2021.

[131] M. Garrick, C. Cunnane, and J.E. Nash. A criterion of efficiency for rainfall-runoff models. *Journal of Hydrology*, 36(3-4):375–381, February 1978.

[132] Amir Givati and Daniel Rosenfeld. Quantifying precipitation suppression due to air pollution. *J. Appl. Meteorol.*, 43(7):1038–1056, July 2004.

[133] Amir Givati and Daniel Rosenfeld. Separation between cloud-seeding and air-pollution effects. *J. Appl. Meteorol.*, 44(9):1298–1314, September 2005.

[134] Amir Givati and Daniel Rosenfeld. Possible impacts of anthropogenic aerosols on water resources of the Jordan River and the Sea of Galilee. *Water Resour. Res.*, 43(10):W10419, October 2007.

[135] Peter H. Gleick and Elizabeth L. Chalecki. The impacts of climatic changes for water resources of the Colorado and Sacramento–San Joaquin River Basins1. *J. Am. Water Resour. Assoc.*, 35(6):1429–1441, December 1999.

[136] Stephen M Goldfeld and Richard E Quandt. A Markov model for switching regressions. *Journal of Econometrics*, 1(1):3–15, 1973.

[137] Gong S. L. A parameterization of sea-salt aerosol source function for sub- and supermicron particles. *Global Biogeochemical Cycles*, 17(4), October 2003.

[138] John W. Gorman and R. J. Toman. Selection of variables for fitting equations to data. *Technometrics*, 8(1):27–51, 1966.

[139] A. S. Gragne, A. Sharma, R. Mehrotra, and K. Alfredsen. Improving real-time inflow forecasting into hydropower reservoirs through a complementary modelling framework. *Hydrol. Earth Syst. Sci.*, 19(8):3695–3714, August 2015.

[140] Michael Grant and Stephen Boyd. CVX: Matlab software for disciplined convex programming, version 2.1. `http://cvxr.com/cvx`, March 2014.

[141] Georg A. Grell, Steven E. Peckham, Rainer Schmitz, Stuart A. McKeen, Gregory Frost, William C. Skamarock, and Brian Eder. Fully coupled "online" chemistry within the WRF model. *Atmos. Environ.*, 39(37):6957–6975, December 2005.

[142] Thomas C Grenfell, Bonnie Light, and Matthew Sturm. Spatial distribution and radiative effects of soot in the snow and sea ice during the sheba experiment. *Journal of Geophysical Research: Oceans*, 107(C10), 2002.

[143] A. Guenther, T. Karl, P. Harley, C. Wiedinmyer, P. I. Palmer, and C. Geron. Estimates of global terrestrial isoprene emissions using MEGAN (Model of Emissions of Gases and Aerosols from Nature). *Atmos. Chem. Phys.*, 6(11):3181–3210, August 2006.

[144] Swaroop S. Guggilam, Emiliano Dall'Anese, Yu Christine Chen, Sairaj V. Dhople, and Georgios B. Giannakis. Scalable Optimization Methods for Distribution Networks With High PV Integration. *IEEE Transactions on Smart Grid*, 7(4), July 2016.

[145] Gupta Hoshin Vijai, Sorooshian Soroosh, and Yapo Patrice Ogou. Status of Automatic Calibration for Hydrologic Models: Comparison with Multilevel Expert Calibration. *Journal of Hydrologic Engineering*, 4(2):135–143, April 1999.

[146] Tuomas Haarnoja, Aurick Zhou, Pieter Abbeel, and Sergey Levine. Soft Actor-Critic: Off-Policy Maximum Entropy Deep Reinforcement Learning with a Stochastic Actor. *arXiv:1801.01290 [cs, stat]*, August 2018.

[147] Tuomas Haarnoja, Aurick Zhou, Pieter Abbeel, and Sergey Levine. Soft Actor-Critic: Off-Policy Maximum Entropy Deep Reinforcement Learning with a Stochastic Actor. *arXiv:1801.01290 [cs, stat]*, August 2018. arXiv: 1801.01290.

[148] Tuomas Haarnoja, Aurick Zhou, Kristian Hartikainen, George Tucker, Sehoon Ha, Jie Tan, Vikash Kumar, Henry Zhu, Abhishek Gupta, Pieter Abbeel, et al. Soft actor-critic algorithms and applications. *arXiv preprint arXiv:1812.05905*, 2018.

[149] Odelle L Hadley and Thomas W Kirchstetter. Black-carbon reduction of snow albedo. *Nature Climate Change*, 2(6):437–440, 2012.

[150] M. T. Hagan and S. M. Behr. The time series approach to short term load forecasting. *IEEE Transactions on Power Systems*, 2(3):785–791, Aug 1987.

[151] L.M. Hajagos and B. Danai. Laboratory measurements and models of modern loads and their effect on voltage stability studies. *IEEE Transactions on Power Systems*, 13(2):584–592, May 1998.

[152] Ait Mimoune Hamiche, Amine Boudghene Stambouli, and Samir Flazi. A review of the water-energy nexus. *Renewable and Sustainable Energy Reviews*, 65:319–331, November 2016.

[153] James D. Hamilton. Regime switching models. In *Macroeconometrics and Time Series Analysis*, pages 202–209. Palgrave Macmillan UK, 2010.

[154] J Hansen, Mki Sato, and R Ruedy. Radiative forcing and climate response. *Journal of Geophysical Research: Atmospheres*, 102(D6):6831–6864, 1997.

[155] James Hansen and Larissa Nazarenko. Soot climate forcing via snow and ice albedos. *Proceedings of the National Academy of Sciences of the United States of America*, 101(2):423–428, 2004.

[156] Hans-Christen Hansson and Jonas Bhend. Causes of Regional Change—Aerosols. In *Second Assessment of Climate Change for the Baltic Sea Basin*, Regional Climate Studies, pages 441–452. Springer, Cham, 2015.

[157] Jack Harmer, Linus Gisslén, Jorge del Val, Henrik Holst, Joakim Bergdahl, Tom Olsson, Kristoffer Sjöö, and Magnus Nordin. Imitation learning with concurrent actions in 3D games. *arXiv:1803.05402 [cs, stat]*, September 2018.

[158] Elizabeth B. Harper, John C. Stella, and Alexander K. Fremier. Global sensitivity analysis for complex ecological models: A case study of riparian cottonwood population dynamics. *Ecological Applications: A Publication of the Ecological Society of America*, 21(4):1225–1240, June 2011.

[159] James Haywood and Olivier Boucher. Estimates of the direct and indirect radiative forcing due to tropospheric aerosols: A review. *Reviews of geophysics*, 38(4):513–543, 2000.

[160] Cenlin He, Kuo-Nan Liou, and Yoshi Takano. Resolving Size Distribution of Black Carbon Internally Mixed With Snow: Impact on Snow Optical Properties and Albedo. *Geophysical Research Letters*, 45(6):2697–2705, March 2018.

[161] Cenlin He, Yoshi Takano, Kuo-Nan Liou, Ping Yang, Qinbin Li, and Fei Chen. Impact of Snow Grain Shape and Black Carbon–Snow Internal Mixing on Snow Optical Properties: Parameterizations for Climate Models. *Journal of Climate*, 30(24):10019–10036, September 2017.

[162] H. He and E. A. Garcia. Learning from imbalanced data. *IEEE Transactions on Knowledge and Data Engineering*, 21(9):1263–1284, September 2009.

[163] He Cenlin, Liou Kuo-Nan, Takano Yoshi, Yang Ping, Qi Ling, and Chen Fei. Impact of Grain Shape and Multiple Black Carbon Internal Mixing on Snow Albedo: Parameterization and Radiative Effect Analysis. *Journal of Geophysical Research: Atmospheres*, 123(2):1253–1268, January 2018.

[164] Jennifer Hinman and Emily Hickey. Modeling and forecasting short-term electricity load using regression analysis. *Journal of Institute for Regulatory Policy Studies*, pages 1–51, 2009.

[165] Sepp Hochreiter and Jürgen Schmidhuber. Long short-term memory. *Neural computation*, 9(8):1735–1780, 1997.

[166] Chris Holcomb. Pecan street inc.: A test-bed for NILM. In *International Workshop on Non-Intrusive Load Monitoring*, 2012.

[167] Song-You Hong, Yign Noh, and Jimy Dudhia. A New Vertical Diffusion Package with an Explicit Treatment of Entrainment Processes. *Monthly Weather Review*, 134(9):2318–2341, September 2006.

[168] Mian Huang, Qinghua Ji, and Weixin Yao. Semiparametric hidden Markov model with non-parametric regression. *Communications in Statistics-Theory and Methods*, 47(21):5196–5204, 2018.

[169] Hyeong Soo Chang, P.J. Fard, S.I. Marcus, and M. Shayman. Multitime scale markov decision processes. *IEEE Transactions on Automatic Control*, 48(6):976–987, June 2003.

[170] Iacono Michael J., Delamere Jennifer S., Mlawer Eli J., Shephard Mark W., Clough Shepard A., and Collins William D. Radiative forcing by long-lived greenhouse gases: Calculations with the AER radiative transfer models. *Journal of Geophysical Research: Atmospheres*, 113(D13), July 2008.

[171] John C Jackson, Paul S Albert, and Zhiwei Zhang. A two-state mixed hidden Markov model for risky teenage driving behavior. *The annals of applied statistics*, 9(2):849, 2015.

[172] Mark Z Jacobson. Strong radiative heating due to the mixing state of black carbon in atmospheric aerosols. *Nature*, 409(6821):695–697, 2001.

[173] Mark Z Jacobson. Climate response of fossil fuel and biofuel soot, accounting for soot's feedback to snow and sea ice albedo and emissivity. *Journal of Geophysical Research: Atmospheres*, 109(D21), 2004.

[174] L. Jaeglé, P. K. Quinn, T. S. Bates, B. Alexander, and J.-T. Lin. Global distribution of sea salt aerosols: new constraints from in situ and remote sensing observations. *Atmos. Chem. Phys.*, 11(7):3137–3157, April 2011.

[175] Pedram Jahangiri and Dionysios C. Aliprantis. Distributed Volt/Var control by PV inverters. *IEEE Transactions on Power Systems*, 28(3):3429–3439, August 2013.

[176] S. K. Jain, A. Das, and D. K. Srivastava. Application of ANN for reservoir inflow prediction and operation. *J. Water Resour. Plann. Man.*, 125(5):263–271, 1999.

[177] Mana Jalali, Vassilis Kekatos, Nikolaos Gatsis, and Deepjyoti Deka. Designing reactive power control rules for smart inverters using support vector machines. *IEEE Trans. Smart Grid*, 11(2):1759–1770, March 2020.

[178] S. T. Jan, R. Afzal, and A.J. khan. Transformer failures, causes & impact. In *International Conference Data Mining, Civil and Mechanical Engineering*. International Institute of Engineers, February 2015.

[179] Rahul Ranjan Jha, Anamika Dubey, Chen-Ching Liu, and Kevin P. Schneider. Bi-Level Volt-VAR optimization to coordinate smart inverters with voltage control devices. *IEEE Trans. Power Syst.*, 34(3):1801–1813, May 2019.

[180] Zilong Jiao and Jae Oh. Asynchronous Multitask Reinforcement Learning with Dropout for Continuous Control. In *2019 18th IEEE International Conference On Machine Learning And Applications (ICMLA)*, pages 529–534, December 2019.

[181] BT Johnson, KP Shine, and PM Forster. The semi-direct aerosol effect: Impact of absorbing aerosols on marine stratocumulus. *Quarterly Journal of the Royal Meteorological Society*, 130(599):1407–1422, 2004.

[182] A Jones, DL Roberts, and A Slingo. A climate model study of indirect radiative forcing. *Nature*, 370:450–453, 1994.

[183] F. Kabir, N. Yu, W. Yao, L. Wu, J.H. Jiang, G. Yu, and H. Su. Impact of aerosols on reservoir inflow: a case study for Big Creek Hydroelectric System in California. *Hydrological Processes*, August 2018.

[184] F. Kabir, N. Yu, W. Yao, R. Yang, and Y. Zhang. Estimation of behind-the-meter solar generation by integrating physical with statistical models. In *2019 IEEE International Conference on Communications, Control, and Computing Technologies for Smart Grids (SmartGridComm)*, pages 1–6, 2019.

[185] Farzana Kabir, Brandon Foggo, and Nanpeng Yu. Data driven predictive maintenance of distribution transformers. In *2018 China International Conference on Electricity Distribution (CICED)*, pages 312–316, 2018.

[186] Farzana Kabir, Yuanqi Gao, and Nanpeng Yu. Reinforcement learning-based smart inverter control with polar action space in power distribution systems. In *2021 IEEE Conference on Control Technology and Applications (CCTA)*, pages 315–322, 2021.

[187] Farzana Kabir, Nanpeng Yu, and Yuanqi Gao. Reinforcement learning-based smart inverter control with polar action space in power distribution systems. In *2021 IEEE Conf. Control Technol. and Appl. (CCTA)*. IEEE, 2021.

[188] Farzana Kabir, Nanpeng Yu, Balakrishna Sastry, and Vibhu Kaushik. Climate, water, energy nexus: Impact of aerosols on hydropower generation in california. In *2019 IEEE PES GTD Grand International Conference and Exposition Asia (GTD Asia)*, pages 235–240, 2019.

[189] Farzana Kabir, Nanpeng Yu, Weixin Yao, Rui Yang, and Yingchen Zhang. Joint estimation of behind-the-meter solar generation in a community. *IEEE Transactions on Sustainable Energy*, 12(1):682–694, 2021.

[190] Christos Kaplanis, Claudia Clopath, and Murray Shanahan. Continual reinforcement learning with multi-timescale replay. *arXiv:2004.07530 [cs, stat]*, April 2020.

[191] Emre C. Kara, Ciaran M. Roberts, Michaelangelo Tabone, Lilliana Alvarez, Duncan S. Callaway, and Emma M. Stewart. Towards Real-Time Estimation of Solar Generation From Micro-Synchrophasor Measurements. July 2016.

[192] Emre C. Kara, Ciaran M. Roberts, Michaelangelo Tabone, Lilliana Alvarez, Duncan S. Callaway, and Emma M. Stewart. Disaggregating solar generation from feeder-level measurements. *Sustainable Energy, Grids and Networks*, 13:112–121, March 2018.

[193] Emre Can Kara, Michaelangelo Tabone, Ciaran Roberts, Sila Kiliccote, and Emma M. Stewart. Estimating behind-the-meter solar generation with existing measurement infrastructure: Poster abstract. In *Proceedings of the 3rd ACM International Conference on Systems for Energy-Efficient Built Environments*, pages 259–260. ACM, 2016.

[194] Yoram J Kaufman, Ilan Koren, Lorraine A Remer, Daniel Rosenfeld, and Yinon Rudich. The effect of smoke, dust, and pollution aerosol on shallow cloud development over the atlantic ocean. *Proceedings of the National Academy of Sciences of the United States of America*, 102(32):11207–11212, 2005.

[195] Yoram J Kaufman, Didier Tanré, and Olivier Boucher. A satellite view of aerosols in the climate system. *Nature*, 419(6903):215–223, 2002.

[196] Amanpreet Kaur, Hugo TC Pedro, and Carlos FM Coimbra. Impact of onsite solar generation on system load demand forecast. *Energy conversion and management*, 75:701–709, 2013.

[197] JT Kiehl and BP Briegleb. The relative roles of sulfate aerosols and greenhouse gases in climate forcing. *Science*, 260(5106):311–314, 1993.

[198] Ozsel Kilinc and Giovanni Montana. Multi-agent deep reinforcement learning with extremely noisy observations. In *32nd Conf. Neural Inf. Process. Syst. (NIPS)*, 2018.

[199] Ismail Kilinç and Kerem Ciğizoğlu. Reservoir management using artificial neural networks. *Proc. 14th. Reg. Director. DSI (State Hydraulic Works)*, 2003.

[200] Chang-Jin Kim and Charles R Nelson. State-space models with regime switching. 1999.

[201] Noah Knowles and Daniel R. Cayan. Potential effects of global warming on the Sacramento/San Joaquin watershed and the San Francisco estuary. *Geophys. Res. Lett.*, 29(18):1891, September 2002.

[202] Jonas Koenig, Simon Malberg, Martin Martens, Sebastian Niehaus, Artus Krohn-Grimberghe, and Arunselvan Ramaswamy. Multi-stage reinforcement learning for object detection. *arXiv:1810.10325 [cs, stat]*, October 2018.

[203] Ron Kohavi and George H. John. Wrappers for feature subset selection. *Artificial Intelligence*, 97(1-2):273–324, December 1997.

[204] A. Kokhanovsky. Spectral reflectance of solar light from dirty snow: a simple theoretical model and its validation. *The Cryosphere*, 7(4):1325–1331, August 2013.

[205] Alexander Kraskov, Harald Stoegbauer, and Peter Grassberger. Estimating mutual information. *Physical Review E*, 69(6), June 2004. arXiv: cond-mat/0305641.

[206] P. Krause, D. P. Boyle, and F. Bäse. Comparison of different efficiency criteria for hydrological model assessment. *Advances in Geosciences*, 5:89–97, December 2005.

[207] Lakshman Krishnamurthy, Robert Adler, Phil Buonadonna, and Jasmeet Chhabra. Design and deployment of industrial sensor networks: Experiences from a semiconductor plant and the North Sea. page 12.

[208] Tejas D. Kulkarni, Karthik R. Narasimhan, Ardavan Saeedi, and Joshua B. Tenenbaum. Hierarchical Deep Reinforcement Learning: Integrating Temporal Abstraction and Intrinsic Motivation. *arXiv:1604.06057 [cs, stat]*, May 2016. arXiv: 1604.06057.

[209] Kamakshi Lakshminarayan, Steven A. Harp, and Tariq Samad. Imputation of missing data in industrial databases. page 17.

[210] U. Lall and K. Bosworth. Multivariate Kernel Estimation of Functions of Space and Time Hydrologic Data. In Keith W. Hipel, A. Ian McLeod, U. S. Panu, and Vijay P. Singh, editors, *Stochastic and Statistical Methods in Hydrology and Environmental Engineering*, number 10/3 in Water Science and Technology Library, pages 301–315. Springer Netherlands, 1994.

[211] William KM Lau, Maeng-Ki Kim, Kyu-Myong Kim, and Woo-Seop Lee. Enhanced surface warming and accelerated snow melt in the Himalayas and Tibetan plateau induced by absorbing aerosols. *Environmental Research Letters*, 5(2):025204, 2010.

[212] Lawrence David M, Oleson Keith W, Flanner Mark G, Thornton Peter E, Swenson Sean C, Lawrence Peter J, Zeng Xubin, Yang Zong-Liang, Levis Samuel, Sakaguchi Koichi, Bonan Gordon B, and Slater Andrew G. Parameterization improvements and functional and structural advances in Version 4 of the Community Land Model. *Journal of Advances in Modeling Earth Systems*, 3(1), March 2011.

[213] Yeonok Lee, Debashis Ghosh, and Yu Zhang. Regression hidden Markov modeling reveals heterogeneous gene expression regulation: a case study in mouse embryonic stem cells. *BMC genomics*, 15(1):1, 2014.

[214] Julia Lee-Taylor and Sasha Madronich. Calculation of actinic fluxes with a coupled atmosphere–snow radiative transfer model. *Journal of Geophysical Research: Atmospheres*, 107(D24), 2002.

[215] David R. Legates and Gregory J. McCabe Jr. Evaluating the use of "goodness-of-fit" Measures in hydrologic and hydroclimatic model validation. *Water Resources Research*, 35(1):233–241, January 1999.

[216] Legates David R. and McCabe Gregory J. A refined index of model performance: a rejoinder. *International Journal of Climatology*, 33(4):1053–1056, April 2012.

[217] Dennis P. Lettenmaier and Thian Yew Gan. Hydrologic sensitivities of the Sacramento-San Joaquin River Basin, California, to global warming. *Water Resour. Res.*, 26(1):69–86, January 1990.

[218] Changfu Li, Vahid R. Disfani, Hamed Valizadeh Haghi, and Jan Kleissl. Optimal voltage regulation of unbalanced distribution networks with coordination of OLTC and PV generation. In *2019 IEEE Power Energy Society General Meeting (PESGM)*, pages 1–5, August 2019.

[219] Changfu Li, Chenrui Jin, and Ratnesh Sharma. Coordination of PV smart inverters using deep reinforcement learning for grid voltage regulation. In *2019 18th IEEE International Conference On Machine Learning And Applications (ICMLA)*, pages 1930–1937. IEEE, December 2019.

[220] Kangping Li, Fei Wang, Zengqiang Mi, Mahmoud Fotuhi-Firuzabad, Neven Duić, and Tieqiang Wang. Capacity and output power estimation approach of individual behind-the-meter distributed photovoltaic system for demand response baseline estimation. *Applied Energy*, 253:113595, November 2019.

[221] Peng Li, Haoran Ji, Chengshan Wang, Jinli Zhao, Guanyu Song, Fei Ding, and Jianzhong Wu. Coordinated Control Method of Voltage and Reactive Power for Active Distribution Networks Based on Soft Open Point. *IEEE Transactions on Sustainable Energy*, 8(4):1430–1442, October 2017.

[222] Siyuan Li, Rui Wang, Minxue Tang, and Chongjie Zhang. Hierarchical reinforcement learning with advantage-based auxiliary rewards. *arXiv:1910.04450 [cs]*, October 2019.

[223] Zhaofu Li, Chuan Luo, Kaixia Jiang, Rongrong Wan, and Hengpeng Li. Comprehensive Performance Evaluation for Hydrological and Nutrients Simulation Using the Hydrological Simulation Program–Fortran in a Mesoscale Monsoon Watershed, China. *International Journal of Environmental Research and Public Health*, 14(12), December 2017.

[224] Timothy P Lillicrap, Jonathan J Hunt, Alexander Pritzel, Nicolas Heess, Tom Erez, Yuval Tassa, David Silver, and Daan Wierstra. Continuous control with deep reinforcement learning. *arXiv preprint arXiv:1509.02971*, 2015.

[225] Timothy P. Lillicrap, Jonathan J. Hunt, Alexander Pritzel, Nicolas Heess, Tom Erez, Yuval Tassa, David Silver, and Daan Wierstra. Continuous control with deep reinforcement learning. *ICLR*, July 2019.

[226] Timothy P. Lillicrap, Jonathan J. Hunt, Alexander Pritzel, Nicolas Heess, Tom Erez, Yuval Tassa, David Silver, and Daan Wierstra. Continuous control with deep reinforcement learning. *arXiv:1509.02971 [cs, stat]*, July 2019.

[227] Liou K. N., Takano Y., He C., Yang P., Leung L. R., Gu Y., and Lee W. L. Stochastic parameterization for light absorption by internally mixed BC/dust in snow grains for application to climate models. *Journal of Geophysical Research: Atmospheres*, 119(12):7616–7632, June 2014.

[228] Haotian Liu and Wenchuan Wu. Online multi-agent reinforcement learning for decentralized inverter-based Volt-VAR control. *IEEE Trans. Smart Grid*, 2(4), July 2021.

[229] Haotian Liu and Wenchuan Wu. Two-stage deep reinforcement learning for inverter-based volt-var control in active distribution networks. *IEEE Trans. Smart Grid*, 12(3):2037–2047, May 2021.

[230] M. B. Liu, Claudio A. Canizares, and W. Huang. Reactive Power and Voltage Control in Distribution Systems With Limited Switching Operations. *IEEE Transactions on Power Systems*, 24(2):889–899, May 2009.

[231] Yutian Liu, Peng Zhang, and Xizhao Qiu. Optimal volt/var control in distribution systems. *International Journal of Electrical Power & Energy Systems*, 24(4):271–276, May 2002.

[232] Johan Lofberg. YALMIP: A toolbox for modeling and optimization in matlab. In *2004 IEEE Int. Conf. Robot. and Automation (IEEE Cat. No. 04CH37508)*, pages 284–289. IEEE, 2004.

[233] U. Lohmann and J. Feichter. Global indirect aerosol effects: a review. *Atmos. Chem. Phys.*, 5(3):715–737, March 2005.

[234] Ulrike Lohmann. Impact of aerosols on the hydrological cycle. *Water and the Environment*, 12:104–219, 2005.

[235] Lohmann U. A glaciation indirect aerosol effect caused by soot aerosols. *Geophysical Research Letters*, 29(4):11–1, February 2002.

[236] Ryan Lowe, Yi Wu, Aviv Tamar, Jean Harb, Pieter Abbeel, and Igor Mordatch. Multi-agent actor-critic for mixed cooperative-competitive environments. *31st Conf. Neural Inf. Process. Syst. (NIPS)*, 2017.

[237] Tyler Lu, Dávid Pál, and Martin Pál. Contextual multi-armed bandits. In *Proceedings of the Thirteenth international conference on Artificial Intelligence and Statistics*, pages 485–492. JMLR Workshop and Conference Proceedings, 2010.

[238] Ke Ma, Marco Liserre, Frede Blaabjerg, and Tamas Kerekes. Thermal Loading and Lifetime Estimation for Power Device Considering Mission Profiles in Wind Power Converter. *IEEE Transactions on Power Electronics*, 30(2):590–602, February 2015.

[239] Iain L MacDonald and Walter Zucchini. *Hidden Markov and other models for discrete-valued time series.* Chapman & Hall, 1997.

[240] Kaveh Madani and Jay R. Lund. Estimated impacts of climate warming on California's high-elevation hydropower. *Climatic Change*, 102(3):521–538, October 2010.

[241] H. Madsen, B. Richaud, and C. B. Pedersen. A real-time inflow forecasting and reservoir optimization system for optimizing hydropower production. *Waterpower XVI*, 2009.

[242] M. A. Mahmud, M. J. Hossain, H. R. Pota, and A. B. M. Nasiruzzaman. Voltage control of distribution networks with distributed generation using reactive power compensation. In *IECON 2011 - 37th Annual Conference of the IEEE Industrial Electronics Society*, pages 985–990, November 2011. ISSN: 1553-572X.

[243] Vardit Makler-Pick, Gideon Gal, Malka Gorfine, Matthew R. Hipsey, and Yohay Carmel. Sensitivity analysis for complex ecological models – A new approach. *Environmental Modelling & Software*, 26(2):124–134, February 2011.

[244] Spyros Makridakis, Steven C. Wheelwright, and Rob J. Hyndman. *Forecasting methods and applications.* John Wiley & Sons, 2008.

[245] Moein Manbachi, Abhinav Sadu, Hassan Farhangi, Antonello Monti, Ali Palizban, Ferdinanda Ponci, and Siamak Arzanpour. Real-time co-simulation platform for smart grid Volt-VAR optimization using IEC 61850. *IEEE Trans. Smart Grid*, 12(4):1392–1402, August 2016.

[246] Bill Marion, J Adelstein, K ea Boyle, H Hayden, B Hammond, T Fletcher, B Canada, D Narang, A Kimber, L Mitchell, et al. Performance parameters for grid-connected PV systems. In *Conference Record of the Thirty-first IEEE Photovoltaic Specialists Conference, 2005.*, pages 1601–1606. IEEE, 2005.

[247] AA Marks and MD King. The effects of additional black carbon on the albedo of Arctic sea ice: variation with sea ice type and snow cover. *The Cryosphere*, 7(4):1193, 2013.

[248] AA Marks and MD King. The effect of snow/sea ice type on the response of albedo and light penetration depth (e-folding depth) to increasing black carbon. *The Cryosphere*, 8(5):1625, 2014.

[249] J. Martinec and A. Rango. Merits of Statistical Criteria for the Performance of Hydrological Models1. *JAWRA Journal of the American Water Resources Association*, 25(2):421–432, April 1989.

[250] José R. Martí, Hamed Ahmadi, and Lincol Bashualdo. Linear Power-Flow Formulation Based on a Voltage-Dependent Load Model. *IEEE Transactions on Power Delivery*, 28(3):1682–1690, July 2013.

[251] Antonello Maruotti. Mixed hidden Markov models for longitudinal data: An overview. *International Statistical Review*, 79:427–454, 2011.

[252] Karl Mason, Matthew J Reno, Logan Blakely, Sadegh Vejdan, and Santiago Grijalva. A deep neural network approach for behind-the-meter residential pv size, tilt and azimuth estimation. *Solar Energy*, 196:260–269, 2020.

[253] San Mateo. Berkeley, CA (US); Emre can Kara,. page 33.

[254] B. Mather, S. Shah, B. Norris, J. Dise, L. Yu, D. Paradis, F. Katiraei, R. Seguin, D. Costyk, J. Woyak, J. Jung, K. Russell, and R. Broadwater. NREL/SCE high penetration pv integration project: FY13 annual report. Technical Report NREL/TP-5D00-61269, 1136232, National Renewable Energy Laboratory (NREL), Golden, CO (United States), June 2014.

[255] F. N. Matt, J. F. Burkhart, and J.-P. Pietikäinen. Modelling hydrologic impacts of light absorbing aerosol deposition on snow at the catchment scale. *Hydrol. Earth Syst. Sci.*, 22(1):179–201, January 2018.

[256] G. McCormick. Computability of global solutions to factorable nonconvex programs: Part I — convex underestimating problems. *Math.Program.*, 10:147–175, 1976.

[257] McCuen Richard H., Knight Zachary, and Cutter A. Gillian. Evaluation of the Nash–Sutcliffe Efficiency Index. *Journal of Hydrologic Engineering*, 11(6):597–602, November 2006.

[258] Jing Ming, Cunde Xiao, Helene Cachier, Dahe Qin, Xiang Qin, Zhongqi Li, and Jianchen Pu. Black carbon (bc) in the snow of glaciers in west China and its potential effects on albedos. *Atmospheric Research*, 92(1):114–123, 2009.

[259] P. Mirowski and Y. LeCun. Statistical machine learning and dissolved gas analysis: A review. *IEEE Transactions on Power Delivery*, 27(4):1791–1799, October 2012.

[260] Joseph Modayil, Adam White, and Richard S. Sutton. Multi-timescale nexting in a reinforcement learning robot. *arXiv:1112.1133 [cs]*, June 2012. arXiv: 1112.1133.

[261] Hamid Moeeni, Hossein Bonakdari, Seyed Ehsan Fatemi, and Amir Hossein Zaji. Assessment of stochastic models and a hybrid artificial neural network-genetic algorithm method in forecasting monthly reservoir inflow. *INAE Lett.*, 2(1):13–23, April 2017.

[262] K Mohammadi, HR Eslami, and Sh Dayyani Dardashti. Comparison of regression, ARIMA and ANN models for reservoir inflow forecasting using snowmelt equivalent (a case study of Karaj). *J. Agric. Sci. Technol*, 7(12):17–30, January 2005.

[263] Rahul Mohan, Tim Cheng, Abhay Gupta, Vivek Garud, and Ye He. Solar Energy Disaggregation using Whole-House Consumption Signals. page 4.

[264] D. K. Molzahn, F. Dörfler, H. Sandberg, S. H. Low, S. Chakrabarti, R. Baldick, and J. Lavaei. A survey of distributed optimization and control algorithms for electric power systems. *IEEE Transactions on Smart Grid*, 8(6):2941–2962, November 2017.

[265] D. N. Moriasi, J. G. Arnold, M. W. Van Liew, R. L. Bingner, R. D. Harmel, and T. L. Veith. *Model evaluation guidelines for systematic quantification of accuracy in watershed simulations.* 2007.

[266] H. Morrison, G. Thompson, and V. Tatarskii. Impact of Cloud Microphysics on the Development of Trailing Stratiform Precipitation in a Simulated Squall Line: Comparison of One- and Two-Moment Schemes. *Monthly Weather Review*, 137(3):991–1007, March 2009.

[267] Yuri G Motovilov, Lars Gottschalk, Kolbjørn Engeland, and Allan Rodhe. Validation of a distributed hydrological model against spatial observations. *Agricultural and Forest Meteorology*, 98-99:257–277, December 1999.

[268] Mahera Musallam and C. Mark Johnson. An Efficient Implementation of the Rainflow Counting Algorithm for Life Consumption Estimation. *IEEE Transactions on Reliability*, 61(4):978–986, December 2012.

[269] Ofir Nachum, Mohammad Norouzi, Kelvin Xu, and Dale Schuurmans. Bridging the Gap Between Value and Policy Based Reinforcement Learning. *arXiv:1702.08892 [cs, stat]*, November 2017. arXiv: 1702.08892.

[270] R. Naresh, V. Sharma, and M. Vashisth. An integrated neural fuzzy approach for fault diagnosis of transformers. *IEEE Transactions on Power Delivery*, 23(4):2017–2024, October 2008.

[271] J. E. Nash and J. V. Sutcliffe. River flow forecasting through conceptual models part I — A discussion of principles. *Journal of Hydrology*, 10(3):282–290, April 1970.

[272] Nawaf Nazir and Mads Almassalkhi. Voltage positioning using co-optimization of controllable grid assets in radial networks. *IEEE Transactions on Power Systems*, pages 1–1, 2020.

[273] U. P. Networks. Smart meter energy consumption data in london households.

[274] Huiseong Noh, Jongso Lee, Narae Kang, Dongryul Lee, Hung Soo Kim, and Soojun Kim. Long-Term Simulation of Daily Streamflow Using Radar Rainfall and the SWAT Model: A Case Study of the Gamcheon Basin of the Nakdong River, Korea, 2016.

[275] World Meteorological Organization. *Intercomparison of Models of Snowmelt Runoff.* Secretariat of the World Meteorological Organization, 1986.

[276] Mohammad Ostadijafari, Anamika Dubey, and Nanpeng Yu. Linearized price-responsive HVAC controller for optimal scheduling of smart building loads. *IEEE Transactions on Smart Grid*, 11(4):3131–3145, July 2020.

[277] Ludovic Oudin, Vazken Andréassian, Thibault Mathevet, Charles Perrin, and Claude Michel. Dynamic averaging of rainfall-runoff model simulations from complementary model parameterizations. *Water Resources Research*, 42(7), July 2006.

[278] Antonio Padilha-Feltrin, Darwin Alexis Quijano Rodezno, and José Roberto Sanches Mantovani. Volt-VAR multiobjective optimization to peak-load relief and energy efficiency in distribution networks. *IEEE Trans. Power Del.*, 30(2):618–626, April 2015.

[279] Thomas H. Painter, Jeffrey S. Deems, Jayne Belnap, Alan F. Hamlet, Christopher C. Landry, and Bradley Udall. Response of Colorado River runoff to dust radiative forcing in snow. *Proceedings of the National Academy of Sciences*, 107(40):17125–17130, October 2010.

[280] Bryan Palmintier, Robert Broderick, Barry Mather, Michael Coddington, Kyri Baker, Fei Ding, Matthew Reno, Matthew Lave, and Ashwini Bharatkumar. On the path to sunshot. emerging issues and challenges in integrating solar with the distribution system. Technical report, National Renewable Energy Lab. (NREL), Golden, CO (United States), 2016.

[281] Alan Pankratz. *Forecasting with Dynamic Regression Models.* John Wiley & Sons, January 2012. Google-Books-ID: ZCmFI5U1j6cC.

[282] Dimitris M. Papamichail and Pantazis E. Georgiou. Seasonal ARIMA inflow models for reservoir sizing. *J. Am. Water Resour. Assoc.*, 37(4):877–885, August 2001.

[283] J. Park, S. Nam, and J. Park. Control of a ULTC Considering the Dispatch Schedule of Capacitors in a Distribution System. *IEEE Transactions on Power Systems*, 22(2):755–761, May 2007.

[284] Joyce E Penner, MO Andreae, H Annegarn, L Barrie, J Feichter, D Hegg, A Jayaraman, R Leaitch, D Murphy, J Nganga, et al. Aerosols, their direct and indirect effects. In *Climate Change 2001: The Scientific Basis. Contribution of Working Group I to the Third Assessment Report of the Intergovernmental Panel on Climate Change*, pages 289–348. Cambridge University Press, 2001.

[285] Joyce E Penner, Johannes Quaas, Trude Storelvmo, Toshihiko Takemura, Olivier Boucher, Huan Guo, Alf Kirkevåg, Jón Egill Kristjánsson, and Øyvind Seland. Model intercomparison of indirect aerosol effects. *Atmospheric Chemistry and Physics*, 6(11):3391–3405, 2006.

[286] Marcelo Perlin. MS_regress - the MATLAB package for Markov regime switching models. *Available at SSRN 1714016*, 2015.

[287] Francesca Pianosi, Keith Beven, Jim Freer, Jim W. Hall, Jonathan Rougier, David B. Stephenson, and Thorsten Wagener. Sensitivity analysis of environmental models: A systematic review with practical workflow. *Environmental Modelling & Software*, 79(Supplement C):214–232, May 2016.

[288] Doina Precup and Richard S Sutton. Multi-time models for reinforcement learning. page 7.

[289] Y. Qian, M. G. Flanner, L. R. Leung, and W. Wang. Sensitivity studies on the impacts of Tibetan Plateau snowpack pollution on the Asian hydrological cycle and monsoon climate. *Atmos. Chem. Phys.*, 11(5):1929–1948, March 2011.

[290] Yun Qian, William I. Gustafson, L. Ruby Leung, and Steven J. Ghan. Effects of soot-induced snow albedo change on snowpack and hydrological cycle in western United States based on Weather Research and Forecasting chemistry and regional climate simulations. *J. Geophys. Res.-Atmos.*, 114(D3):D03108, February 2009.

[291] Yun Qian, William I Gustafson, L Ruby Leung, and Steven J Ghan. Effects of soot-induced snow albedo change on snowpack and hydrological cycle in western United States based on weather research and forecasting chemistry and regional climate simulations. *Journal of Geophysical Research: Atmospheres*, 114(D3), 2009.

[292] Johannes Quaas, Olivier Boucher, Nicolas Bellouin, and Stefan Kinne. Satellite-based estimate of the direct and indirect aerosol climate forcing. *Journal of Geophysical Research: Atmospheres*, 113(D5), 2008.

[293] S. Ramachandran and Ribu Cherian. Regional and seasonal variations in aerosol optical characteristics and their frequency distributions over India during 2001–2005. *Journal of Geophysical Research*, 113(D8), April 2008.

[294] V. Ramanathan, P. J. Crutzen, J. T. Kiehl, and D. Rosenfeld. Aerosols, Climate, and the Hydrological Cycle. *Science*, 294(5549):2119–2124, December 2001.

[295] V. Ramanathan, P. J. Crutzen, J. Lelieveld, A. P. Mitra, D. Althausen, J. Anderson, M. O. Andreae, W. Cantrell, G. R. Cass, C. E. Chung, A. D. Clarke, J. A. Coakley, W. D. Collins, W. C. Conant, F. Dulac, J. Heintzenberg, A. J. Heymsfield, B. Holben, S. Howell, J. Hudson, A. Jayaraman, J. T. Kiehl, T. N. Krishnamurti, D. Lubin, G. McFarquhar, T. Novakov, J. A. Ogren, I. A. Podgorny, K. Prather, K. Priestley, J. M. Prospero, P. K. Quinn, K. Rajeev, P. Rasch, S. Rupert, R. Sadourny, S. K. Satheesh, G. E. Shaw, P. Sheridan, and F. P. J. Valero. Indian Ocean Experiment: An integrated analysis of the climate forcing and effects of the great Indo-Asian haze. *J. Geophys. Res.-Atmos.*, 106(D22):28371–28398, November 2001.

[296] HJ Reay, JL France, and MD King. Decreased albedo, e-folding depth and photolytic oh radical and no2 production with increasing black carbon content in Arctic snow. *Journal of Geophysical Research: Atmospheres*, 117(D14), 2012.

[297] Ibrahim Reda and Afshin Andreas. Solar position algorithm for solar radiation applications. *Solar Energy*, 76(5):577–589, 2004.

[298] Leighton A. Regayre, Kirsty J. Pringle, Lindsay A. Lee, Alexandru Rap, Jo Browse, Graham W. Mann, Carly L. Reddington, Ken S. Carslaw, Ben B. B. Booth,

and Matthew T. Woodhouse. The Climatic Importance of Uncertainties in Regional Aerosol–Cloud Radiative Forcings over Recent Decades. *Journal of Climate*, 28(17):6589–6607, May 2015.

[299] Axel Ritter and Rafael Muñoz-Carpena. Performance evaluation of hydrological models: Statistical significance for reducing subjectivity in goodness-of-fit assessments. *Journal of Hydrology*, 480:33–45, February 2013.

[300] B. A. Robbins, C. N. Hadjicostis, and A. D. Domínguez-García. A two-stage distributed architecture for voltage control in power distribution systems. *IEEE Transactions on Power Systems*, 28(2):1470–1482, May 2013.

[301] Brett A. Robbins, Hao Zhu, and Alejandro D. Domínguez-García. Optimal tap setting of voltage regulation transformers in unbalanced distribution systems. *IEEE Trans. Power Syst.*, 31(1):256–267, 2016.

[302] Daniel Rosenfeld. Suppression of rain and snow by urban and industrial air pollution. *Science*, 287(5459):1793–1796, 2000.

[303] Rafael Rosolem, Hoshin V. Gupta, W. James Shuttleworth, Xubin Zeng, and Luis Gustavo Gonçalves de Gonçalves. A fully multiple-criteria implementation of the Sobol method for parameter sensitivity analysis. *Journal of Geophysical Research: Atmospheres*, 117(D7):D07103, April 2012.

[304] I. Roytelman, B.K. Wee, and R.L. Lugtu. Volt/Var control algorithm for modern distribution management system. *IEEE Trans. Power Syst.*, 10(3):1454–1460, August 1995.

[305] Donald B. Rubin. *Multiple Imputation for Nonresponse in Surveys.* John Wiley & Sons, June 2004. Google-Books-ID: bQBtw6rx_mUC.

[306] Petri Räisänen, Risto Makkonen, Alf Kirkevåg, and Jens B. Debernard. Effects of snow grain shape on climate simulations: sensitivity tests with the Norwegian Earth System Model. *The Cryosphere; Katlenburg-Lindau*, 11(6):2919–2942, 2017.

[307] A. Salami and P. Pahlevani. Neural network approach for fault diagnosis of transformers. In *2008 International Conference on Condition Monitoring and Diagnosis*, pages 1346–1349, April 2008.

[308] Diogo Salles, Adriano C. Pinto, and Walmir Freitas. Integrated volt/Var control in modern distribution power systems based on support vector machines. *Int. Trans. Elect. Energy Syst.*, 26(10):2216–2229, 2016.

[309] A. Saltelli, S. Tarantola, and K. P.-S. Chan. A quantitative model-independent method for global sensitivity analysis of model output. *Technometrics*, 41(1):39–56, February 1999.

[310] Andrea Saltelli, Paola Annoni, Ivano Azzini, Francesca Campolongo, Marco Ratto, and Stefano Tarantola. Variance based sensitivity analysis of model output. Design and estimator for the total sensitivity index. *Computer Physics Communications*, 181(2):259–270, February 2010.

[311] Andrea Saltelli, Paola Annoni, and Beatrice D'Hombres. How to avoid a perfunctory sensitivity analysis. *Procedia - Social and Behavioral Sciences*, 2(6):7592–7594, January 2010.

[312] Bjørn H. Samset. Aerosols and Climate - Oxford Research Encyclopedia of Climate Science. page 25, 2018.

[313] Bettina Schaefli and Hoshin V. Gupta. Do Nash values have value? *Hydrological Processes*, 21(15):2075–2080, July 2007.

[314] U. Scheuermann. Reliability challenges of automotive power electronics. *Microelectronics Reliability*, 49(9):1319–1325, September 2009.

[315] Michael Schmela and SolarPower Europe. Solar power europe (2021): Eu market outlook for solar power 2021-2025. Technical report, Smart Energy, 2021.

[316] Stephen E. Schwartz. The whitehouse effect- Shortwave radiative forcing of climate by anthropogenic aerosols: an overview. *J. Aerosol Sci.*, 27(3):359–382, April 1996.

[317] Rich Seguin, Jeremy Woyak, David Costyk, Josh Hambrick, and Barry Mather. High-penetration PV integration handbook for distribution engineers. Technical Report No. NREL/TP-5D00-63114, National Renewable Energy Laboratory, Golden, CO, United States, January 2016.

[318] Chris Seiffert, Taghi M. Khoshgoftaar, Jason Van Hulse, and Amri Napolitano. RUSBoost: A hybrid approach to alleviating class imbalance. *IEEE Transactions on Systems, Man, and Cybernetics - Part A: Systems and Humans*, 40(1):185–197, January 2010.

[319] Manajit Sengupta, Yu Xie, Anthony Lopez, Aron Habte, Galen Maclaurin, and James Shelby. The National Solar Radiation Data Base (NSRDB). *Renewable and Sustainable Energy Reviews*, 89:51–60, 2018.

[320] Manajit Sengupta, Yu Xie, Anthony Lopez, Aron Habte, Galen Maclaurin, and James Shelby. The National Solar Radiation Data Base (NSRDB). *Renewable and Sustainable Energy Reviews*, 89:51–60, June 2018.

[321] Tomonobu Senjyu, Yoshitaka Miyazato, Atsushi Yona, Naomitsu Urasaki, and Toshihisa Funabashi. Optimal distribution voltage control and coordination with distributed generation. *IEEE Trans. Power Del.*, 23(2):1236–1242, April 2008.

[322] Mark C. Serreze, Martyn P. Clark, Richard L. Armstrong, David A. McGinnis, and Roger S. Pulwarty. Characteristics of the western United States snowpack from snowpack telemetry(SNOTEL) data. *Water Resour. Res.*, 35(7):2145–2160, 1999.

[323] Anoop D Shah, Jonathan W Bartlett, James Carpenter, Owen Nicholas, and Harry Hemingway. Comparison of random forest and parametric imputation models for imputing missing data using mice: a CALIBER study. *American journal of epidemiology*, 179(6):764–774, 2014.

[324] Hamid Shaker, Hamidreza Zareipour, and David Wood. Estimating power generation of invisible solar sites using publicly available data. *IEEE Transactions on Smart Grid*, 7(5):2456–2465, September 2016.

[325] William J. Shaw, K. Jerry Allwine, Bradley G. Fritz, Frederick C. Rutz, Jeremy P. Rishel, and Elaine G. Chapman. An evaluation of the wind erosion module in DUSTRAN. *Atmos. Environ.*, 42(8):1907–1921, March 2008.

[326] X Shi, Y Zhu, X Ning, L Wang, G Sun, and G Chen. Transformer fault diagnosis based on deep auto-encoder network. 36:122–126, May 2016.

[327] Yue Shi and Mesut Baran. A coordinated Volt/Var control scheme for distribution system with high der penetration. page 8.

[328] David Silver, Guy Lever, Nicolas Heess, Thomas Degris, Daan Wierstra, and Martin Riedmiller. Deterministic Policy Gradient Algorithms. page 9.

[329] A. Singhal, V. Ajjarapu, J. C. Fuller, and J. Hansen. Real-time local volt/var control under external disturbances with high PV penetration. *IEEE Transactions on Smart Grid*, pages 1–1, 2018.

[330] Ankit Singhal. Volt/var control with high solar PV penetration in distribution systems and its impact on the transmision grid. page 137.

[331] J. W. Smith, W. Sunderman, R. Dugan, and B. Seal. Smart inverter volt/var control functions for high penetration of PV on distribution systems. In *2011 IEEE/PES Power Systems Conference and Exposition*, pages 1–6, March 2011.

[332] Oscar Sondermeijer, Roel Dobbe, Daniel Arnold, Claire Tomlin, and Tamás Keviczky. Regression-based inverter control for Decentralized optimal power flow and voltage regulation. In *Proc. IEEE PES Gen. Meeting*, 2016.

[333] F. Sossan, L. Nespoli, V. Medici, and M. Paolone. Unsupervised disaggregation of photovoltaic production from composite power flow measurements of heterogeneous prosumers. *IEEE Transactions on Industrial Informatics*, 14(9):3904–3913, Sep. 2018.

[334] Sumith Madampath Sreechithra, Panida Jirutitijaroen, and Akshay Kumar Rathore. Impacts of reactive power injections on thermal performances of PV inverters. In *IECON 2013 - 39th Annu. Conf. IEEE Ind. Electron. Soc.*, pages 7175–7180, November 2013.

[335] Wendell Stainsby, Daniel Zimmerle, and Gerald P. Duggan. A method to estimate residential PV generation from net-metered load data and system install date. *Applied Energy*, 267:114895, June 2020.

[336] California Distributed Generation Statistics. The California Solar Initiative - CSI working data set, 2019. `https://www.californiadgstats.ca.gov/downloads/`.

[337] Joshua S Stein. The photovoltaic performance modeling collaborative (PVPMC). In *38th IEEE Photovoltaic Specialists Conference*, pages 003048–003052. IEEE, 2012.

[338] Daniel J. Stekhoven and Peter Bühlmann. MissForest - nonparametric missing value imputation for mixed-type data. *Bioinformatics*, 28(1):112–118, January 2012. arXiv: 1105.0828.

[339] Steven Ghan, Nels Laulainen, Richard Easter, Richard Wagener, Seth Nemesure, Elaine Chapman, Yang Zhang, and Ruby Leung. Evaluation of aerosol direct radiative forcing in MIRAGE. *Journal of Geophysical Research: Atmospheres*, 106(D6):5295–5316, March 2001.

[340] Iris T. Stewart, Daniel R. Cayan, and Michael D. Dettinger. Changes in snowmelt runoff timing in western North America under a 'Business as Usual' climate change scenario. *Clim. Change*, 62(1-3):217–232, January 2004.

[341] Mingyang Sun, Tingqi Zhang, Yi Wang, Goran Strbac, and Chongqing Kang. Using Bayesian deep learning to capture uncertainty for residential net load forecasting. *IEEE Transactions on Power Systems*, 35(1):188–201, January 2020. Conference Name: IEEE Transactions on Power Systems.

[342] G. A. Susto, A. Schirru, S. Pampuri, S. McLoone, and A. Beghi. Machine learning for predictive maintenance: A multiple classifier approach. *IEEE Transactions on Industrial Informatics*, 11(3):812–820, June 2015.

[343] Richard S. Sutton and Andrew G. Barto. *Reinforcement learning: an introduction.* Adaptive computation and machine learning series. The MIT Press, Cambridge, Massachusetts, second edition edition, 2018.

[344] Richard S. Sutton, Doina Precup, and Satinder Singh. Between MDPs and semi-MDPs: A framework for temporal abstraction in reinforcement learning. *Artificial Intelligence*, 112(1-2):181–211, August 1999.

[345] Richard S. Sutton, Doina Precup, and Satinder Singh. Between MDPs and semi-MDPs: A framework for temporal abstraction in reinforcement learning. *Artificial Intelligence*, 112(1-2):181–211, August 1999.

[346] Michaelangelo Tabone, Sila Kiliccote, and Emre Can Kara. Disaggregating solar generation behind individual meters in real time. In *Proceedings of the 5th Conference on Systems for Built Environments*, pages 43–52. ACM, 2018.

[347] Stacy K. Tanaka, Tingju Zhu, Jay R. Lund, Richard E. Howitt, Marion W. Jenkins, Manuel A. Pulido, Mélanie Tauber, Randall S. Ritzema, and Inês C. Ferreira. Climate warming and water management adaptation for California. *Climatic Change*, 76(3-4):361–387, June 2006.

[348] W. H. Tang, J. Y. Goulermas, Q. H. Wu, Z. J. Richardson, and J. Fitch. A probabilistic classifier for transformer dissolved gas analysis with a particle swarm optimizer. *IEEE Transactions on Power Delivery*, 23(2):751–759, April 2008.

[349] Arash Tavakoli, Fabio Pardo, and Petar Kormushev. Action Branching Architectures for Deep Reinforcement Learning. *arXiv:1711.08946 [cs]*, January 2019.

[350] Lorenzo Tomassini, Peter Reichert, Reto Knutti, Thomas F. Stocker, and Mark E. Borsuk. Robust bayesian uncertainty analysis of climate system properties using markov chain monte carlo methods. *Journal of Climate*, 20(7):1239–1254, April 2007.

[351] R. Tonkoski, L. A. C. Lopes, and T. H. M. El-Fouly. Coordinated active power curtailment of grid connected PV inverters for overvoltage prevention. *IEEE Transactions on Sustainable Energy*, 2(2):139–147, April 2011.

[352] Reinaldo Tonkoski and Luiz A. C. Lopes. Impact of active power curtailment on overvoltage prevention and energy production of PV inverters connected to low voltage residential feeders. *Renewable Energy*, 36(12):3566–3574, 2011.

[353] K. Turitsyn, P. Sulc, S. Backhaus, and M. Chertkov. Local control of reactive power by distributed photovoltaic generators. In *2010 First IEEE International Conference on Smart Grid Communications*, pages 79–84, October 2010.

[354] K. Turitsyn, P. Sulc, S. Backhaus, and M. Chertkov. Options for control of reactive power by distributed photovoltaic generators. *Proceedings of the IEEE*, 99(6), June 2011.

[355] Konstantin Turitsyn, Petr Šulc, Scott Backhaus, and Michael Chertkov. Distributed control of reactive power flow in a radial distribution circuit with high photovoltaic penetration. *IEEE PES general meeting*, pages 1–6, 2010.

[356] Mosaddek Hossain Kamal Tushar and Chadi Assi. Volt-VAR Control Through Joint Optimization of Capacitor Bank Switching, Renewable Energy, and Home Appliances. *IEEE Transactions on Smart Grid*, 9(5):4077–4086, September 2018.

[357] S Twomey. Pollution and the planetary albedo. *Atmospheric Environment (1967)*, 8(12):1251–1256, 1974.

[358] S Twomey. Aerosols, clouds and radiation. *Atmospheric Environment. Part A. General Topics*, 25(11):2435–2442, 1991.

[359] Brady Tyra. Electric power monthly. Technical report, US Energy Information Administration, Washington, DC, United States, June 2020.

[360] G. E. Uhlenbeck and L. S. Ornstein. On the theory of the Brownian motion. *Phys. Rev.*, 36:823–841, Sept. 1930.

[361] Laura Uusitalo, Annukka Lehikoinen, Inari Helle, and Kai Myrberg. An overview of methods to evaluate uncertainty of deterministic models in decision support. *Environmental Modelling & Software*, 63(Supplement C):24–31, January 2015.

[362] Mohammad Valipour. Long-term runoff study using SARIMA and ARIMA models in the United States. *Meteorol. Appl.*, 22(3):592–598, 2015.

[363] Mohammad Valipour, Mohammad Ebrahim Banihabib, and Seyyed Mahmood Reza Behbahani. Comparison of the ARMA, ARIMA, and the autoregressive artificial neural network models in forecasting the monthly inflow of Dez dam reservoir. *J. Hydrol.*, 476:433–441, January 2013.

[364] Hado van Hasselt and Marco A. Wiering. Reinforcement Learning in Continuous Action Spaces. In *2007 IEEE International Symposium on Approximate Dynamic Programming and Reinforcement Learning*, pages 272–279, Honolulu, HI, USA, April 2007. IEEE.

[365] Nathan T. VanRheenen, Andrew W. Wood, Richard N. Palmer, and Dennis P. Lettenmaier. Potential implications of PCM climate change scenarios for Sacramento–San Joaquin River Basin hydrology and water resources. *Clim. Change*, 62(1-3):257–281, January 2004.

[366] B Verheggen and E P Weijers. Climate change and the impact of aerosol. page 32, 2010.

[367] S. Vicuna, R. Leonardson, M. W. Hanemann, L. L. Dale, and J. A. Dracup. Climate change impacts on high elevation hydropower generation in California's Sierra Nevada: a case study in the Upper American River. *Climatic Change*, 87(1):123–137, March 2008.

[368] J. G. Vlachogiannis and N. D. Hatziargyriou. Reinforcement learning for reactive power control. *IEEE Transactions on Power Systems*, 19(3):1317–1325, August 2004.

[369] Tiago Soares Vítor, Eduardo Nobuhiro Asada, and José Carlos de Melo Vieira. Optimal Volt/Var control applied to modern Distribution Systems. In Mariana Resener, Steffen Rebennack, Panos M. Pardalos, and Sérgio Haffner, editors, *Handbook of Optimization in Electric Power Distribution Systems*, Energy Systems, pages 1–56. Springer International Publishing, Cham, 2020.

[370] Gang Wang, Vassilis Kekatos, Antonio J. Conejo, and Georgios B. Giannakis. Ergodic energy management leveraging resource variability in distribution grids. *IEEE Transactions on Power Systems*, 31(6):4765–4775, November 2016.

[371] W. Wang, N. Yu, Y. Gao, and J. Shi. Safe off-policy deep reinforcement learning algorithm for volt-var control in power distribution systems. *IEEE Transactions on Smart Grid*, 11(4):3008–3018, 2020.

[372] Wei Wang and Nanpeng Yu. Chordal conversion based convex iteration algorithm for three-phase optimal power flow problems. *IEEE Transactions on Power Systems*, 33(2):1603–1613, March 2018.

[373] Wei Wang, Nanpeng Yu, Jie Shi, and Yuanqi Gao. Volt-VAR control in power distribution systems with deep reinforcement learning. In *2019 IEEE International Conference on Communications, Control, and Computing Technologies for Smart Grids (SmartGridComm)*, pages 1–7, Beijing, China, October 2019. IEEE.

[374] Wenyu Wang and Nanpeng Yu. Parameter estimation in three-phase power distribution networks using smart meter data. In *2020 International Conference on Probabilistic Methods Applied to Power Systems (PMAPS)*, pages 1–6. IEEE, 2020.

[375] Wenyu Wang, Nanpeng Yu, Brandon Foggo, Joshua Davis, and Juan Li. Phase identification in electric power distribution systems by clustering of smart meter data. In *2016 15th IEEE International Conference on Machine Learning and Applications (ICMLA)*, pages 259–265. IEEE, 2016.

[376] Wenyu Wang, Nanpeng Yu, and Raymond Johnson. A model for commercial adoption of photovoltaic systems in California. *Journal of Renewable and Sustainable Energy*, 9(2):025904, 2017.

[377] Yi Wang, Ning Zhang, Qixin Chen, Daniel S. Kirschen, Pan Li, and Qing Xia. Data-driven probabilistic net load forecasting with high penetration of behind-the-meter PV. *IEEE Transactions on Power Systems*, 33(3):3255–3264, May 2018.

[378] Zhenyuan Wang, Yilu Liu, and P. J. Griffin. A combined ANN and expert system tool for transformer fault diagnosis. *IEEE Transactions on Power Delivery*, 13(4):1224–1229, October 1998.

[379] Zihao Wang, Yanxin Zhang, Chenkun Yin, and Zhiqing Huang. Multi-agent deep reinforcement learning based on maximum entropy. In *2021 IEEE 4th Adv. Inf. Manage. Commun. Electron. and Automation Control Conf. (IMCEC)*, volume 4, pages 1402–1406, 2021.

[380] Stephen G Warren. Impurities in snow: Effects on albedo and snowmelt. *Annals of Glaciology*, 5(1):177–179, 1984.

[381] Stephen G Warren and Antony D Clarke. Soot in the atmosphere and snow surface of Antarctica. *J. Geophys. Res*, 95(181):l–1816, 1990.

[382] Tianshu Wei, Qi Zhu, and Nanpeng Yu. Proactive demand participation of smart buildings in smart grid. *IEEE Transactions on Computers*, 65(5):1392–1406, May 2016. Conference Name: IEEE Transactions on Computers.

[383] Cort J. Willmott, Scott M. Robeson, and Kenji Matsuura. A refined index of model performance. *International Journal of Climatology*, 32(13):2088–2094, November 2012.

[384] Warren J Wiscombe and Stephen G Warren. A model for the spectral albedo of snow. i: Pure snow. *Journal of the Atmospheric Sciences*, 37(12):2712–2733, 1980.

[385] L. Wu, Y. Gu, J. H. Jiang, H. Su, N. Yu, C. Zhao, Y. Qian, B. Zhao, K.-N. Liou, and Y.-S. Choi. Impacts of aerosols on seasonal precipitation and snowpack in California based on convection-permitting WRF-Chem simulations. *Atmos. Chem. Phys.*, 18(8):5529–5547, April 2018.

[386] L. Wu, Y. Gu, J. H. Jiang, H. Su, N. Yu, C. Zhao, Y. Qian, B. Zhao, K.-N. Liou, and Y.-S. Choi. Impacts of aerosols on seasonal precipitation and snowpack in California based on convection-permitting WRF-Chem simulations. *Atmos. Chem. Phys.*, 18(8):5529–5547, April 2018.

[387] L. Wu, H. Su, O. V. Kalashnikova, J. H. Jiang, C. Zhao, M. J. Garay, J. R. Campbell, and N. Yu. WRF-Chem simulation of aerosol seasonal variability in the San Joaquin Valley. *Atmos. Chem. Phys. Discuss.*, 17(12):7291–7309, November 2017.

[388] Longtao Wu, Hui Su, and Jonathan H. Jiang. Regional simulations of deep convection and biomass burning over South America: 1. Model evaluations using multiple satellite data sets. *J. Geophys. Res.-Atmos.*, 116(D17):D17208, September 2011.

[389] Longtao Wu, Hui Su, and Jonathan H. Jiang. Regional simulations of deep convection and biomass burning over South America: 2. Biomass burning aerosol effects on clouds and precipitation. *J. Geophys. Res.-Atmos.*, 116(D17):D17209, September 2011.

[390] Longtao Wu, Hui Su, and Jonathan H. Jiang. Regional simulation of aerosol impacts on precipitation during the East Asian summer monsoon. *J. Geophys. Res.-Atmos.*, 118(12):6454–6467, June 2013.

[391] Matt Wytock and J. Zico Kolter. Contextually supervised source separation with application to energy disaggregation. In *Proceedings of the Twenty-Eighth AAAI Conference on Artificial Intelligence*, AAAI'14, pages 486–492. AAAI Press, 2014.

[392] Baiqing Xu, Junji Cao, James Hansen, Tandong Yao, Daniel R Joswia, Ninglian Wang, Guangjian Wu, Mo Wang, Huabiao Zhao, and Wei Yang. Black soot and the survival of Tibetan glaciers. *Proceedings of the National Academy of Sciences*, 106(52):22114–22118, 2009.

[393] Hanchen Xu, Alejandro D Domínguez-García, and Peter W Sauer. Optimal tap setting of voltage regulation transformers using batch reinforcement learning. *IEEE Transactions on Power Systems*, 35(3):1990–2001, 2019.

[394] Hanchen Xu, Alejandro D. Domínguez-García, and Peter W. Sauer. Data-driven coordination of distributed energy resources for active power provision. *IEEE Transactions on Power Systems*, 34(4):3047–3058, 2019.

[395] Hanchen Xu, Alejandro D. Domínguez-García, and Peter W. Sauer. Data-driven coordination of distributed energy resources for active power provision. *IEEE Trans. Power Syst.*, 34(4):3047–3058, July 2019.

[396] Y. Xu, Z. Y. Dong, R. Zhang, and D. J. Hill. Multi-timescale coordinated Voltage/Var control of high renewable-penetrated distribution systems. *IEEE Transactions on Power Systems*, 32(6):4398–4408, November 2017.

[397] Y. Xu, W. Zhang, W. Liu, and F. Ferrese. Multiagent-based reinforcement learning for optimal reactive power dispatch. *IEEE Transactions on Systems, Man, and Cybernetics, Part C (Applications and Reviews)*, 42(6):1742–1751, November 2012.

[398] Z. X. Xu and J. Y. Li. Short-term inflow forecasting using an artificial neural network model. *Hydrol. Process.*, 16(12):2423–2439, August 2002.

[399] Jiachen Yang, Alireza Nakhaei, David Isele, Kikuo Fujimura, and Hongyuan Zha. CM3: Cooperative multi-goal multi-stage multi-agent reinforcement learning. *arXiv:1809.05188 [cs, stat]*, January 2020.

[400] Qiuling Yang, Gang Wang, Alireza Sadeghi, Georgios B. Giannakis, and Jian Sun. Two-timescale voltage regulation in distribution grids using deep reinforcement learning. In *2019 IEEE International Conference on Communications, Control, and Computing Technologies for Smart Grids (SmartGridComm)*, pages 1–6, October 2019.

[401] Qiuling Yang, Gang Wang, Alireza Sadeghi, Georgios B. Giannakis, and Jian Sun. Two-Timescale voltage control in distribution grids using deep reinforcement learning. *IEEE Transactions on Smart Grid*, 11(3):2313–2323, May 2020.

[402] Zaiyue Yang, Rui Wu, Jinfeng Yang, Keyu Long, and Pengcheng You. Economical operation of microgrid with various devices via distributed optimization. *IEEE Transactions on Smart Grid*, 7(2):857–867, March 2016.

[403] Zhaoyang Yang, Kathryn Merrick, Hussein Abbass, and Lianwen Jin. Multi-task deep reinforcement learning for continuous action control. In *Proceedings of the Twenty-Sixth International Joint Conference on Artificial Intelligence*, pages 3301–3307, Melbourne, Australia, August 2017. International Joint Conferences on Artificial Intelligence Organization.

[404] Hao Ye, Rudong Zhang, Jinsen Shi, Jianping Huang, Stephen G Warren, and Qiang Fu. Black carbon in seasonal snow across northern Xinjiang in northwestern China. *Environmental Research Letters*, 7(4):044002, 2012.

[405] Hen-Geul Yeh, Dennice F. Gayme, and Steven H. Low. Adaptive VAR control for distribution circuits with photovoltaic generators. *IEEE Transactions on Power Systems*, 27(3):1656–1663, August 2012.

[406] Jiao-Hong Yi, Jian Wang, and Gai-Ge Wang. Improved probabilistic neural networks with self-adaptive strategies for transformer fault diagnosis problem. *Advances in Mechanical Engineering*, 8(1):1687814015624832, January 2016.

[407] Nanpeng Yu, Sunil Shah, Raymond Johnson, Robert Sherick, Mingguo Hong, and Kenneth Loparo. Big data analytics in power distribution systems. In *2015 IEEE*

Power & Energy Society Innovative Smart Grid Technologies Conference (ISGT), pages 1–5. IEEE, 2015.

[408] H Yuan, G Wu, and B Gao. Fault diagnosis of power transformer using particle swarm optimization and extreme learning machine based on dga. 52:176–180 and 187, 11 2016.

[409] Baosen Zhang, Albert Y.S. Lam, Alejandro D. Dominguez-Garcia, and David Tse. An optimal and distributed method for voltage regulation in power distribution systems. *IEEE Transactions on Power Systems*, 30(4):1714–1726, July 2015.

[410] Cuo Zhang, Yan Xu, Zhaoyang Dong, and Jayashri Ravishankar. Three-stage robust inverter-based Voltage/Var control for distribution networks with high-level PV. *IEEE Transactions on Smart Grid*, 10(1):782–793, January 2019.

[411] Y. Zhang, X. Ding, Y. Liu, and P. J. Griffin. An artificial neural network approach to transformer fault diagnosis. *IEEE Transactions on Power Delivery*, 11(4):1836–1841, October 1996.

[412] Ying Zhang and Yingchen Zhang. Deep Reinforcement Learning Based Volt-VAR Optimization in Smart Distribution Systems. page 9, 2019.

[413] Zhizheng Zhang, Jiale Chen, Zhibo Chen, and Weiping Li. Asynchronous episodic deep deterministic policy gradient: Towards continuous control in computationally complex environments. *arXiv:1903.00827 [cs, stat]*, March 2019. arXiv: 1903.00827.

[414] C. Zhao, S. Chen, L. R. Leung, Y. Qian, J. F. Kok, R. A. Zaveri, and J. Huang. Uncertainty in modeling dust mass balance and radiative forcing from size parameterization. *Atmos. Chem. Phys.*, 13(21):10733–10753, November 2013.

[415] C. Zhao, Z. Hu, Y. Qian, L. Ruby Leung, J. Huang, M. Huang, J. Jin, M. G. Flanner, R. Zhang, H. Wang, H. Yan, Z. Lu, and D. G. Streets. Simulating black carbon and dust and their radiative forcing in seasonal snow: a case study over North China with field campaign measurements. *Atmos. Chem. Phys.*, 14(20):11475–11491, October 2014.

[416] C. Zhao, X. Liu, L. R. Leung, B. Johnson, S. A. McFarlane, W. I. Gustafson Jr., J. D. Fast, and R. Easter. The spatial distribution of mineral dust and its shortwave radiative forcing over North Africa: modeling sensitivities to dust emissions and aerosol size treatments. *Atmos. Chem. Phys.*, 10(18):8821–8838, September 2010.

[417] C. Zhao, X. Liu, L. Ruby Leung, and S. Hagos. Radiative impact of mineral dust on monsoon precipitation variability over West Africa. *Atmos. Chem. Phys.*, 11:1879–1893, March 2011.

[418] Xiaoyang Zhou, Nanpeng Yu, Weixin Yao, and Raymond Johnson. Forecast load impact from demand response resources. In *2016 IEEE Power and Energy Society General Meeting (PESGM)*, pages 1–5. IEEE, 2016.